

Static Misalignment Effects in a Self-Tracking Laser Vibrometry System for Rotating Bladed Disks

by

Richard Allan Lomenzo, Jr., B.S., M.S.

Dissertation submitted to the Faculty of the
Virginia Polytechnic Institute and State University
in partial fulfillment of the requirements for the degree of

Doctor of Philosophy

in

Mechanical Engineering

Dr. Al Wicks
Dr. Andy Barker
Dr. Jose' Carlos Lopez-Dominguez
Dr. Gordon Kirk
Dr. Harry Robertshaw

16 October 1998

Blacksburg, Virginia

Static Misalignment Effects in a Self-Tracking Laser Vibrometry System for Rotating Bladed Disks

Richard Allan Lomenzo, Jr., Ph.D.

Virginia Polytechnic Institute and State University, 1998

Supervisor: Dr. Al Wicks

ABSTRACT

The application of laser Doppler vibrometry to high speed rotating structures has been hampered by technical limitations. Whereas full-field three-dimensional velocity measurements can be made on stationary structures, the capability on rotating structures is limited to low speed, one-dimensional, steady state operation. This work describes the implementation of a self-tracking laser vibrometry system which overcomes many of the limitations of current techniques for vibration measurements on rotating structures. A model of the self-tracker is developed and used to predict the effects of static misalignments on the position and velocity errors. These predictions are supported by experimental results and simplified models of the self-tracker.

Dedicated to everyone who helped along the way, especially my family who stood by me throughout my dozen years at Virginia Tech.

Acknowledgments

Throughout my many years at Virginia Tech, I have encountered many people. Some helped, some hindered, but all contributed to my growth. I thank them all.

RICHARD ALLAN LOMENZO, JR.

Virginia Polytechnic Institute and State University

16 October 1998

Contents

Abstract	ii
Acknowledgments	iv
List of Tables	xi
List of Figures	xiii
Chapter 1 Introduction	1
1.1 Motivation	3
1.2 Objective	4
1.3 Approach	5
1.4 Contribution	6
1.5 Scope of Work	6

1.6	Summary	8
Chapter 2 Vibration Measurements for Rotating Bladed Disks		9
2.1	Blade Tip Sensors	12
2.2	Holographic Interferometry	13
2.3	Laser Doppler Vibrometry	17
2.3.1	Stationary Beam Approach	17
2.3.2	Tracking Beam Approach	19
2.3.3	Self-Tracking Approach	22
2.4	Summary	25
Chapter 3 Laser Doppler Vibrometry		27
3.1	Laser Doppler Vibrometry for Diffuse Surfaces	28
3.2	Laser Doppler Vibrometry for Reflective Surfaces	34
3.2.1	Frequency Shift Due to a Moving Particle	34
3.2.2	Frequency Shift for a Moving Mirror	36
3.2.3	Frequency Shift for a Rotating Mirror	41
3.3	Extraction of Velocity Signal from Frequency Shift	51

3.3.1	Laser Source	52
3.3.2	Interferometer	54
3.3.3	Photodetectors	62
3.3.4	Demodulator	64
3.4	Path Length Changes Versus Velocity	67
3.5	Speckle Noise	71
3.6	Speckle Noise Prediction	76
3.7	Summary	83
Chapter 4 Component Models and Analysis Techniques		86
4.1	Bladed Disk Model	87
4.2	Self-Tracker Model	89
4.3	Analysis Procedure	90
4.3.1	Position Analysis	92
4.3.2	Determining Location and Orientation of Planes	97
4.3.3	Coordinate Frame Transformations	98
4.3.4	Definition of Coordinate Frames	99
4.3.5	Definition of Transformations	103

4.3.6	Velocity Analysis	106
4.4	Summary	108
Chapter 5	Experimental Apparatus and Setup	109
5.1	Tracking System	110
5.2	Rotating Structure Description	113
5.3	Shaft Encoder	116
5.4	Position Sensitive Photodetector	116
5.5	Data Acquisition Systems	121
5.5.1	Photodetector Data	122
5.5.2	Velocity Data	122
5.6	Set-Up Procedure	123
5.6.1	Traverse System Alignment	123
5.6.2	Laser to Structure Alignment	128
5.6.3	Characterization of Ideal Alignment Case	129
5.7	Summary	133
Chapter 6	Ideal Alignment Case	134

6.1	Ideal Alignment Model	134
6.1.1	Ideal Alignment Position Analysis	138
6.1.2	Alternative Position Analysis	144
6.1.3	Ideal Alignment Case Velocity Analysis	146
6.1.4	Characteristics of Ideal Alignment Case	150
6.2	Single Point Capability	151
6.2.1	Radial Scan Capability	153
6.2.2	Azimuthal Scan Capability	153
6.2.3	Experimental Verification of Ideal Alignment Performance	154
6.2.4	Summary	154
Chapter 7 Misalignment Cases		156
7.1	Definition of Misalignment Cases	158
7.2	Contributors to Position and Velocity Errors	161
7.3	Translational Misalignments	163
7.3.1	Simulation Results	167
7.3.2	Analytical Verification	188
7.3.3	Experimental Verification	193

7.4	Rotational Misalignments	199
7.4.1	Simulation Results	201
7.4.2	Experimental Verification	221
7.4.3	Analytical Verification of Rotational Misalignment Effects	223
7.5	Combined Static Displacement and Rotation	232
7.5.1	Simulation Results	233
7.6	Summary	243
Chapter 8 Conclusions		245
8.1	Self-Tracker Capabilities	245
8.2	Recommendations for Future Work	246
Bibliography		247
Vita		251

List of Tables

3.1	Velocity Amplitudes for Vibrating Mirror	38
3.2	Once Per Rev Velocity Amplitudes for Rotating Mirror	47
3.3	Effect of Diffuse Surface Tilt Angle on Measured Velocity	49
3.4	Vibrometer Ranges and Frequency Shifts	64
7.1	Model Parameters	162
7.2	Translational Misalignment Magnitude Effects	187
7.3	Translational Misalignment Direction Effects	188
7.4	Rotational Misalignment Magnitude Effects	221
7.5	Rotational Misalignment Directional Effects	222
7.6	Slideway Translations and Rotations	228
7.7	Rotational Misalignment Position Errors	230

7.8	Rotational Misalignment Velocity Errors	232
7.9	Combined Translational and Rotational Misalignment Effects	243

List of Figures

1.1	Schematic of Self-Tracking System	2
2.1	Hologram of Turbine Blades (taken from Gasvik)	14
2.2	Schematic of Holography System (taken from Gasvik)	15
3.1	Relationship Between True and Measured Velocity	29
3.2	Measured Velocity Components, Cases (a)-(c)	31
3.3	Measured Velocity Components, Cases (d)-(f)	32
3.4	Particle Scattering Schematic	35
3.5	Particle Scattering Geometry	36
3.6	Frequency Shift for Moving Mirror	37
3.7	Measured Velocity for Moving Mirrors, Cases (a)-(c)	39
3.8	Measured Velocity for Moving Mirrors, Cases (d)-(e)	40

3.9	Geometry for Rotating Mirror, 0° Rotation Angle	42
3.10	Geometry for Rotating Mirror, 90° Rotation Angle	43
3.11	Component of Mirror Velocity in Laser Beam Plane	44
3.12	Frequency Spectra for Rotating Mirror Velocity, Positive Displacements . . .	45
3.13	Frequency Spectra for Rotating Mirror Velocity, Negative Displacements . .	46
3.14	Diffuse Surface Tilt	48
3.15	Frequency Spectra for Path Length Change, Negative Tilt Angles	49
3.16	Frequency Spectra for Path Length Change, Positive Tilt Angles	50
3.17	Once Per Rev Velocity Amplitudes for Tilted Surface	51
3.18	Schematic of Laser Vibrometer	53
3.19	Velocity Direction Resolution	63
3.20	Velocity Versus Path Length Change, Macroscopic View	68
3.21	Velocity Versus Path Length Change, Microscopic View	69
3.22	Speckle Pattern Formation (adapted from Dainty)	72
3.23	Speckle Pattern (taken from Dainty)	72
3.24	Discretization of Continuous Speckle Pattern	74
3.25	Vector Sum of Discrete Speckles	75

3.26	Speckle From Rotating Disk	78
3.27	Fixed Disk With Moving Laser Spot	79
3.28	Autocorrelation of Intensity Signal	80
3.29	Simulated Effect of Laser Path on Speckle Noise Spectrum	82
3.30	Actual Effect of Laser Path on Speckle Noise Spectrum	84
4.1	Simplified Model of Bladed Disk	88
4.2	Origins and Directions of Laser Beam Segments	93
4.3	Reflection From Plane Mirror	96
4.4	Fixed Angle Transformations	98
4.5	Preferred Locations and Orientations of Coordinate Frames	100
5.1	Self-Tracker Test Rig	110
5.2	Vertex Mirror Mount	111
5.3	Self-Tracker Traverse System	111
5.4	Vibrometer Adjustment Platform	112
5.5	Fold Mirror Mount	113
5.6	Rotating Structure Test Rig	114
5.7	Rotating Structure Adjustments	115

5.8	PSD Op-Amp Circuit	118
5.9	Actual Versus Calculated Positions for Linear Relationship	119
5.10	Actual Versus Calculated Positions for Polynomial Relationship	120
5.11	Self-Tracker Component Locations	124
5.12	Cross Hair Target for Fold Mirror Alignment	127
5.13	Laser Path for Ideal Alignment	130
5.14	Laser Path on Shaft End	131
6.1	Two-dimensional Laser Path	139
6.2	Laser Beam Path	142
6.3	Laser Beam Path	143
6.4	Unfolding of Laser Path	145
6.5	Unfolding of Laser Path	151
7.1	Static Misalignments	159
7.2	Introduction of Translational Misalignments	163
7.3	Shift in Target Point Path due to Translational Misalignment	164
7.4	Measurement Point Path on Target Plane	165
7.5	Vertex Motion for Translational Misalignment	166

7.6	Translational Misalignment, Magnitude Effects, $d_X=-5$ mm	168
7.7	Translational Misalignment, Magnitude Effects, $d_X=-4$ mm	169
7.8	Translational Misalignment, Magnitude Effects, $d_X=-3$ mm	170
7.9	Translational Misalignment, Magnitude Effects, $d_X=-2$ mm	171
7.10	Translational Misalignment, Magnitude Effects, $d_X=-1$ mm	172
7.11	Translational Misalignment, Magnitude Effects, $d_X=0$ mm	173
7.12	Translational Misalignment, Magnitude Effects, $d_X=1$ mm	174
7.13	Translational Misalignment, Magnitude Effects, $d_X=2$ mm	175
7.14	Translational Misalignment, Magnitude Effects, $d_X=3$ mm	176
7.15	Translational Misalignment, Magnitude Effects, $d_X=4$ mm	177
7.16	Translational Misalignment, Magnitude Effects, $d_X=5$ mm	178
7.17	Translational Misalignments, Directional Effects, $d_X=2$ mm, $d_Y=0$ mm . . .	179
7.18	Translational Misalignments, Directional Effects, $d_X=1.414$ mm, $d_Y=1.414$ mm	180
7.19	Translational Misalignments, Directional Effects, $d_X=0$ mm, $d_Y=2$ mm . . .	181
7.20	Translational Misalignments, Directional Effects, $d_X=-1.414$ mm, $d_Y=1.414$ mm	182
7.21	Translational Misalignments, Directional Effects, $d_X=-2$ mm, $d_Y=0$ mm . . .	183

7.22	Translational Misalignments, Directional Effects, $d_X=-1.414$ mm, $d_Y=-1.414$ mm	184
7.23	Translational Misalignments, Directional Effects, $d_X=0$ mm, $d_Y=-2$ mm	185
7.24	Translational Misalignments, Directional Effects, $d_X=1.414$ mm, $d_Y=-1.414$ mm	186
7.25	Velocity Resolution for Translational Misalignment	189
7.26	Simplified Model for Translational Misalignment Position Errors	189
7.27	Measured Position Errors for Negative Translational Misalignments	194
7.28	Measured Position Errors for Positive Translational Misalignments	195
7.29	Measured Velocity Errors for Negative Translational Misalignments	196
7.30	Measured Velocity Errors for Positive Translational Misalignments	197
7.31	Once Per Rev Measured Velocity for Translational Misalignments	198
7.32	Introduction of Rotational Misalignments	199
7.33	Effect of Rotational Misalignment	200
7.34	Rotational Misalignments, Magnitude Effects, $\beta=-1.0$ mrad	202
7.35	Rotational Misalignments, Magnitude Effects, $\beta=-0.8$ mrad	203
7.36	Rotational Misalignments, Magnitude Effects, $\beta=-0.6$ mrad	204
7.37	Rotational Misalignments, Magnitude Effects, $\beta=-0.4$ mrad	205

7.38	Rotational Misalignments, Magnitude Effects, $\beta=-0.2$ mrad	206
7.39	Rotational Misalignments, Magnitude Effects, $\beta=0$ mrad	207
7.40	Rotational Misalignments, Magnitude Effects, $\beta=0.2$ mrad	208
7.41	Rotational Misalignments, Magnitude Effects, $\beta=0.4$ mrad	209
7.42	Rotational Misalignments, Magnitude Effects, $\beta=0.6$ mrad	210
7.43	Rotational Misalignments, Magnitude Effects, $\beta=0.8$ mrad	211
7.44	Rotational Misalignments, Magnitude Effects, $\beta=1.0$ mrad	212
7.45	Rotational Misalignments, Directional Effects, $\gamma=0.0$ mrad, $\beta=0.4$ mrad . .	213
7.46	Rotational Misalignments, Directional Effects, $\gamma=0.283$ mrad, $\beta=0.283$ mrad	214
7.47	Rotational Misalignments, Directional Effects, $\gamma=0.4$ mrad, $\beta=0.0$ mrad . .	215
7.48	Rotational Misalignments, Directional Effects, $\gamma=0.283$ mrad, $\beta=-0.283$ mrad	216
7.49	Rotational Misalignments, Directional Effects, $\gamma=0.0$ mrad, $\beta=-0.4$ mrad . .	217
7.50	Rotational Misalignments, Directional Effects, $\gamma=-0.283$ mrad, $\beta=-0.283$ mrad	218
7.51	Rotational Misalignments, Directional Effects, $\gamma=-0.4$ mrad, $\beta=0.0$ mrad . .	219
7.52	Rotational Misalignments, Directional Effects, $\gamma=-0.283$ mrad, $\beta=0.283$ mrad	220
7.53	Rotational Misalignments	223
7.54	Measured Position Errors for Negative Rotational Misalignments	224

7.55	Measured Position Errors for Positive Rotational Misalignments	225
7.56	Measured Velocity Errors for Negative Rotational Misalignments	226
7.57	Measured Velocity Errors for Positive Rotational Misalignments	227
7.58	Once Per Rev Measured Velocity for Rotational Misalignments	228
7.59	Simplified Model for Rotational Misalignments	229
7.60	Velocity Error for Rotational Misalignments	231
7.61	Combined Misalignments, $\beta=0.4$ mrad, $d_X=2$ mm, $d_Y=0$ mm	235
7.62	Combined Misalignments, $\beta=0.4$ mrad, $d_X=1.414$ mm, $d_Y=1.414$ mm	236
7.63	Combined Misalignments, $\beta=0.4$ mrad, $d_X=0$ mm, $d_Y=2$ mm	237
7.64	Combined Misalignments, $\beta=0.4$ mrad, $d_X=-1.414$ mm, $d_Y=1.414$ mm . . .	238
7.65	Combined Misalignments, $\beta=0.4$ mrad, $d_X=-2$ mm, $d_Y=0$ mm	239
7.66	Combined Misalignments, $\beta=0.4$ mrad, $d_X=-1.414$ mm, $d_Y=-1.414$ mm . . .	240
7.67	Combined Misalignments, $\beta=0.4$ mrad, $d_X=0$ mm, $d_Y=-2$ mm	241
7.68	Combined Misalignments, $\beta=0.4$ mrad, $d_X=1.414$ mm, $d_Y=-1.414$ mm . . .	242

Chapter 1

Introduction

The application of laser Doppler vibrometry to high speed rotating structures has been hampered by technical limitations. Whereas full-field three-dimensional velocity measurements can be made on stationary structures, the capability on rotating structures is limited to low speed, one-dimensional, steady state operation. This work describes the implementation of a novel technique for applying laser Doppler vibrometry to rotating structures. The proposed self-tracking technique begins to bridge the gap between the emerging capability for rotating structures and the well developed capability for stationary structures.

The self-tracking technique departs from previous approaches by using a simple mechanical connection between the structure and the tracking system in place of the more common electro-mechanical connection. It is this fundamental difference, mechanically linking the pointing of the measurement beam to the structure's rotation, as opposed to making the link electrically, that sets the self-tracker apart from current techniques. The direct mechanical connection allows the rotating structure to point the measurement beam itself, tracking the measurement point theoretically at any speed, without the need for external electronics or moving parts. It is from this characteristic, using the structure itself to provide the tracking

mechanism, that the proposed technique gets its name.

The self-tracking system consists of two mirrors, a large plane mirror placed in front of the structure, and a small plane mirror attached to the rotating bladed disk. A schematic of the self-tracker is shown in Figure 1.1.

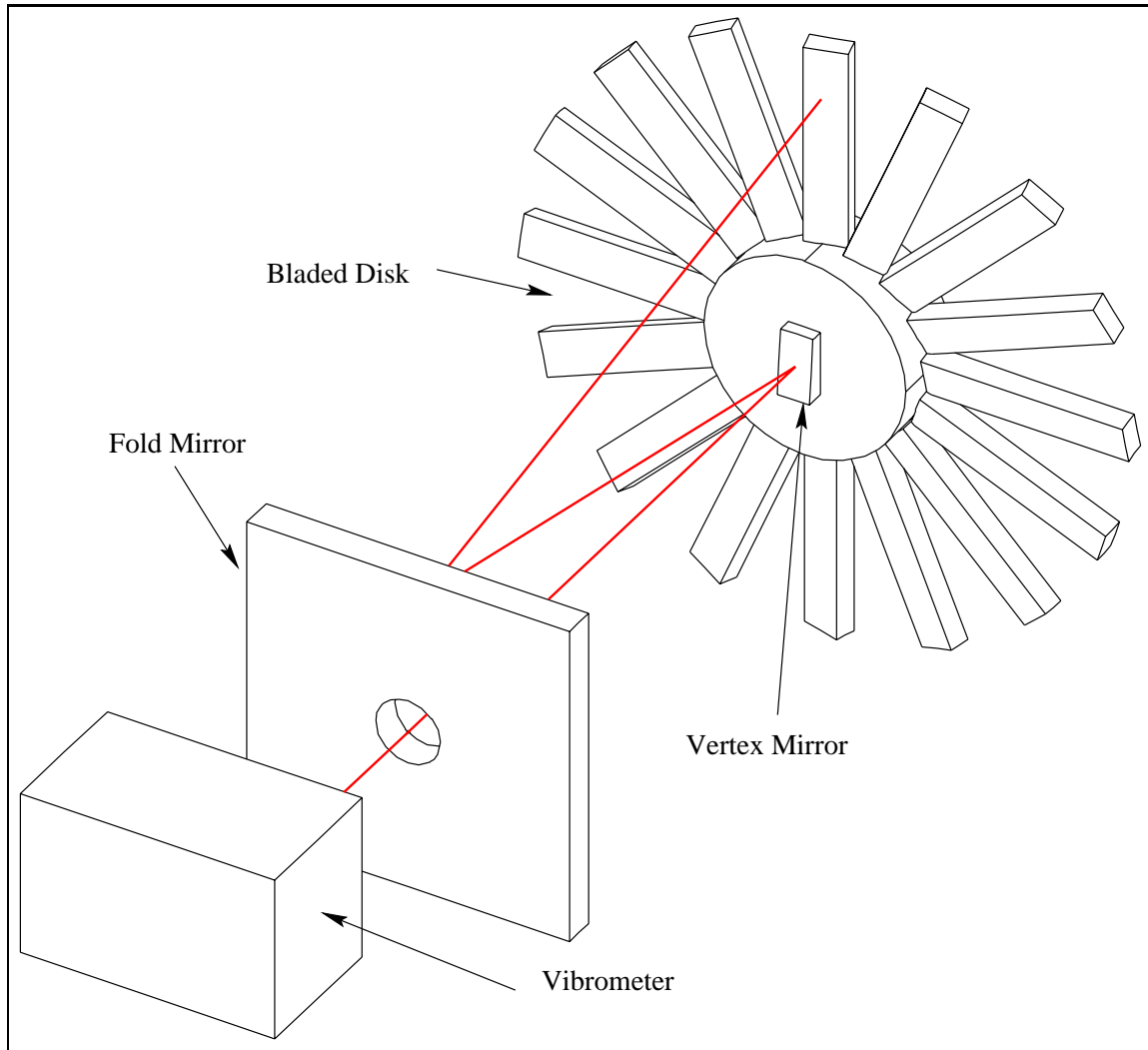


Figure 1.1: Schematic of Self-Tracking System

In the self-tracker, the vibrometer's laser beam is reflected by the vertex mirror back to the fold mirror. The fixed orientation of the vertex mirror relative to the bladed disk locks the motion of the reflected beam to the bladed disk's rotation. Once reflected from the

vertex mirror, the beam is directed towards the fold mirror which reflects the beam back towards the bladed disk, with its motion still locked to the disk's rotation. The location of the laser spot on the blade is fixed with the rotation angle of the disk and is independent of the disk's rotational speed. The capability to direct the laser beam to a fixed measurement point regardless of rotational speed, including transient operation, is a direct consequence of mounting the vertex mirror to the rotating structure.

One complication encountered in the self-tracker and other laser based tracking techniques is misalignment between the tracking system and the structure. Misalignment of the bladed disk relative to the the vibrometer and fold mirror introduces errors in the location of the measurement point as well as errors in the measured velocity. While these errors are also present in other tracking systems, the effects of the misalignments have not been quantified for any tracking system. One reason for this lack of investigation is related to the fact that other tracking techniques are limited in their capability due to their limited speed range. Thus in these cases the effects of misalignments, though noted, have been overshadowed by the limited speed range. By overcoming the constraints on operating conditions related to rotational speed, the self-tracker brings the concerns of misalignments to the forefront.

1.1 Motivation

Current tracking techniques for laser vibrometry are hampered by two limitations, the ability to track a point over a broad speed range and the effect of component misalignments on the position and velocity errors. Since the the self-tracker overcomes the speed range limitations, misalignment effects become the next important limitation. Therefore to advance the use of laser vibrometry on rotating structures, the effects of component misalignments in the self-tracker system must be characterized. This research effort addresses the problem of characterizing the effects of component misalignment in the self-tracker system.

1.2 Objective

This research presents a self-tracking laser vibrometry system for rotating structures with the expressed purpose of characterizing the misalignment effects. The characterization is centered around addressing two fundamental questions:

- What effects do static misalignments have on the tracking error?
- What effects do static misalignments have on the velocity error?

To determine how misalignments effect the self-tracker's tracking error, the locations of the target and measurement points must be found. The target point is defined as a fixed point on the blade where the vibration measurement is to be made. The measurement point is the actual point where the measurement is made. The difference between these two points defines the tracking error.

To determine how misalignments affect the self-tracker's velocity error, several parameters must be found. First, the velocity of each moving surface encountered by the laser beam along its path from the vibrometer to the measurement point must be found. For the self-tracker this consists of two surfaces, the vertex mirror and the blade. Secondly, the relative orientations of the surface velocities and laser beam directions must be known. For the interaction of the laser beam with the vertex mirror this requires three direction vectors, one for the incident laser beam, one for the reflected laser beam, and a third for the velocity direction. For the interaction of the laser beam with the blade the direction of the incident laser beam and the direction of the velocity vector is required. Thirdly, the motion of the measurement point on the structure contributes a component to the vibrometer output in the form of speckle noise. Therefore the path traced out by the measurement beam on the blade must be known. With knowledge of these three contributors, the total vibrometer output

can be found. The difference between the vibrometer output and the vibratory velocity of the blade constitutes the velocity error.

Therefore, the primary objectives of the research are to

- Develop a mathematical model capable of predicting the position and velocity errors
- Construct an apparatus which allows measurement of the position and velocity errors
- Exercise both the model and the apparatus to characterize the self-tracker's performance

Successful completion of these objectives will result in a body of knowledge useful in the application of the self-tracker to vibration measurements on rotating bladed disks.

1.3 Approach

To address the three research objectives, several general tasks are performed. First current techniques for vibration measurements on rotating structures are reviewed to identify the benefits and limitations of each technique. Next, the self-tracking technique is described with specific attention to the benefits of the self-tracking technique over other current scanning techniques. Third, the operation of the laser vibrometer is described, illustrating the phenomena responsible for vibrometer output. Next, models are developed of both the rotating bladed disk system and the self-tracker. These models are used to predict the performance of the self-tracker under several specific alignment conditions. To verify the model predictions, an instrumented test rig is developed. For each alignment condition, the predicted position and velocity errors are confirmed within the hardware limitations of the test rig. Completion of these tasks satisfies the research objectives and illustrates the utility of the self-tracker as an effective vibration measurement tool for rotating structures.

1.4 Contribution

This research adds to the currently published body of literature related to vibrometry measurements on rotating structures in three ways. First, it implements a new tracking approach which departs from the fundamental approaches currently used. Second, it provides a structured technique for analyzing the position and velocity errors of the self-tracker, a topic alluded to in the literature for current techniques, but not rigorously developed. Third, it presents experimental verification of the analysis procedure for several situations commonly encountered in the use of the self-tracker. These contributions serve as the foundation for the analysis of static misalignments considered here as well as a starting point for future analysis of dynamic misalignments.

1.5 Scope of Work

While there are a multitude of research issues created by the introduction of the self-tracker, only the misalignment effects are addressed here. In general the misalignments effects can be due to either static or dynamic misalignment of the structure and self-tracker components. This work focuses on static misalignment effects only. Furthermore, it is possible for each of the components to be statically misaligned relative to each other. Instead of looking at every possible instance of misalignment, only misalignment of the structure relative to the fold mirror and vibrometer is considered here. This limitation assumes that the vibrometer and fold mirror are properly aligned to each other and can be treated as a fixed assembly. This condition can be met by careful construction of a common support structure for the fold mirror and vibrometer. Thus the proper alignment condition could be built into the vibrometer/fold mirror assembly and the entire assembly treated as a single component. Therefore the misalignments considered are those between the combined vibrometer/fold mirror assembly and the rotating bladed disk.

Four static alignment cases are considered. First, the operation of the self-tracker under ideal alignment conditions is discussed. Next, two fundamental misalignment cases are presented; translational misalignment from the ideal alignment case, and rotational misalignment from the ideal alignment case. Last, the combined effects of translational and rotational misalignments are considered. With these final constraints placed on the cases to be studied, the specific research task can be defined as follow:

- Review current non-contacting measurement techniques for rotating structures, concentrating on tracking techniques for laser vibrometry
- Describe the operation of the laser vibrometer, illustrating the phenomena which cause a response from the vibrometer, and concentrating on
 - Velocity of diffuse surfaces
 - Velocity of reflective surfaces
 - Variation of speckle patterns
- Develop three-dimensional models of the bladed disk and the self-tracker for predicting the position and velocity errors
- Construct a test rig for verifying the errors predicted by the model
- Characterize the performance of the self-tracking system under four alignment conditions
 - Ideal alignment
 - Translational misalignment
 - Rotational misalignment
 - Combined translational and rotational misalignment
- Identify future work for further development of the self-tracker

1.6 Summary

A self-tracking technique for laser vibrometry on a rotating bladed disk which overcomes the limitations of current tracking techniques has been described. The predominant research goal is to identify the effects of static misalignment on the position and velocity errors. A research plan has been outlined for predicting these effects using analytical models and verifying the predictions using an instrumented test rig. The following chapters present the work performed to carry out this research.

Current techniques for vibration measurements on rotating bladed disks are reviewed in Chapter 2. This review highlights the capabilities and limitations of several non-contacting techniques and presents the scenarios in which the self-tracking system excels. The transducer used with the self-tracking system, a laser Doppler vibrometer, is described in Chapter 3. The description illustrates phenomena encountered in the self-tracker that cause vibrometer response. The general modeling and analysis techniques for determining the position and velocity errors in the self-tracker are presented in Chapter 4. This is followed in Chapter 5 by a description of the test rig used to verify the predicted results. The performance characteristics of the self-tracker for the ideal alignment condition are developed and described in Chapter 6. This is followed by a discussion of the three misalignment cases in Chapter 7. Finally, concluding remarks on the self-tracker's performance and recommendations for future work are presented in Chapter 8.

Chapter 2

Vibration Measurements for Rotating Bladed Disks

While there are several ways to classify vibration transducers, the most natural distinction to make in the context of this work is that between contacting and non-contacting transducers. Contacting techniques are those in which the transducer is attached to the structure, such as strain gages and accelerometers. Non-contacting techniques avoid contact between the transducer and the structure. Each of these techniques have their own advantages and disadvantages.

The most significant advantage of contacting transducers is that the attachment point on the structure can be easily determined and remains fixed during the structure's rotation. Thus there is no uncertainty in the measurement location. Unfortunately the fact that the transducer is attached to the structure is the major downside to these transducers.

Attaching transducers to structures tends to change the response of the structure due to a number of effects. One of the most common effects is mass loading. This is generally a concern for transducers whose mass is significant relative to the mass of the structure.

This is especially true in the case of applying accelerometers to thin flexible structures. The additional mass causes shifts in the natural frequencies and mode shapes, whether the structure is rotating or non-rotating. This effect can be magnified in rotating structures where the additional mass experiences centrifugal accelerations. A second effect experienced in turbo-machinery is interruption of the flow field over the structure. This causes forces to be exerted on the structure that would not be present in the absence of the transducer. Additionally, since the transducer is exposed to the flow, its life may be greatly diminished. This is typically an issue for strain gages attached to turbine or compressor blades where the success of a test is measured by the number of gages that survive the test.

Even if the above problems can be solved, a second hurdle, the requirement for running power and signal leads to the transducer must be overcome. This requirement can usually be overcome by the use of telemetry or sliprings. The downside to this approach is the added complexity and cost of the measurement system as well as degradation of the measurement signals. Although these approaches are used with strain gages, they are not as flexible as non-contacting techniques.

Non-contacting transducers eliminate most of the problems encountered with contacting transducers, but typically at the expense of knowing the exact measurement point location. One application where this trade-off is most beneficial is in the vibration measurement of high-speed rotating structures. Kadambi et al. (1989) reviews current non-contacting measurement techniques for in-use operation of rotating structures. This points out a dichotomy of non-contacting transducers; those suitable for in-use operation and those suitable for testing. The differences in the capabilities of these two techniques are directly related to the roles that they fill. In general, transducers for in-use operation are used to monitor the health of a rotating structure. These signals can be used to determine problems with the machine and alert the operator to perform some corrective action. Potentially hazardous conditions can typically be identified based on single point measurements. However, dynamic characterization requires multi-point measurements which are most easily performed in a laboratory

environment. It is in this arena where optical methods excel.

The two most common optical techniques for vibration measurements are laser holography and laser vibrometry. Like most non-contacting techniques, these too are plagued by uncertainties in the location of the measurement point. This results in uncertainty in the location of the measurement point for non-rotating and rotating structures. While this problem is not significant in holography, it is one of the biggest concerns in laser vibrometry for rotating structures. Additionally the uncertainty in the measurement location also introduces errors in the measured velocity. To eliminate these effects, special steps must be taken to properly configure these systems.

With the complications brought about by making measurements on rotating structures, the obvious question to ask is 'Why not measure the vibration with the part stationary?' There are two motivations for measuring vibration on structures while they are rotating.

First, the dynamic behavior of structures changes under rotating conditions. The most obvious effect is the generation of centrifugal acceleration which creates axial forces in the structure. These forces stiffen the part, increasing the natural frequencies and flattening the mode shapes. The dynamic properties experienced under rotating conditions will be different than those measured under non-rotating conditions. This effect is increased as the stiffness of the structure decreases. Since aerodynamic considerations dictate thin blades, bladed disks are significantly affected by centrifugal loading. This effect may be even greater on highly swept or twisted blades, where centrifugal loads tend to untwist the blades, further changing their dynamic performance. Therefore for dynamic characterization, it is not plausible to perform the measurements under non-rotating conditions.

Second, it may not be possible to synthesize the loading conditions on a non-rotating blade that are generated on a rotating blade. In the case of axial flow compressors and turbines, aerodynamic forces are present during rotation that are not present during static testing. These forces may be distributed over the blade surface and typically can not be synthesized

on non-rotating structures. Furthermore, these forces may not be measurable. In this case measurements on the rotating structure can be used to determine the loading conditions through the study of the inverse problem.

To address the special requirements of rotating structures a number of vibration measurement techniques have been developed. Three of the most commonly applied techniques are blade tip sensors, laser holography, and laser vibrometry.

2.1 Blade Tip Sensors

Blade tip sensors, the simplest non-contacting transducers for rotating bladed disks, measure blade vibrations as the blade passes a fixed point in space. The sensors are typically oriented to point along a radial line of the bladed disk. The output of these transducers consists of a pulse as the blade passes the transducer. Given a measured rotational speed and a rigid structure, the time it takes for a blade to make one rotation, and therefore the time between pulses, should be fixed. For vibrating blades, this time will change and can be used to measure the vibration amplitude. By measuring the time between pulses and monitoring the rotational speed of the structure, the vibrational amplitude can be deduced. This technique is widely used as an in-use monitoring tool for gas turbines and has been described in varying levels of detail by a number of authors including Watkins, Kaydoya, and Nava. While the basic principle described can be applied to several transducer technologies, the two most common transducers used are inductive and optical probes.

Inductive probes sense the presence of the blade based on the electrical interaction between the bladed material and the flux lines created by the probe. Optical probes sense the presence of the blade by reflecting light off the blade tip. In each case, as the blades of a rotating disk pass the sensor, the probe produces a series of pulses corresponding to the passage of the blades. While the basic principle of applying blade tip sensors is relatively

straightforward, it has several limitations.

First, measurements can only be made at the blade tip. Secondly, the technique requires significant signal processing with varying levels of complexity for detecting synchronous and non-synchronous vibrations. Some of these limitation can be overcome through the use of arrays of sensors strategically placed around the circumference of the structure. The limited amount of information that can be gathered from blade tip sensors makes them more applicable for in-use monitoring than in design and development.

2.2 Holographic Interferometry

Holographic interferometry is a non-contacting optical technique which measures the displacement amplitudes of vibrating structures based on the interference between two images. An image of the displacement field is generated by combining a reference image of the non-displaced structure with images of the displaced structure. The addition of these images generates fringe patterns due to the interference between the two images. Output consists of an image of the displacement amplitudes of the vibrating part. Though these images can be calibrated to give actual displacements, they are typically used to qualitatively assess dynamic performance. Some representative holograms of non-rotating turbine blades are shown in Figure 2.1.

A typical holographic interferometry setup is shown in Figure 2.2.

Holographic interferometry relies on a reference image first being captured. To create this reference image, the structure is illuminated with an expanded beam of laser light as shown in Figure 2.2 (a). The laser beam is first sent through a beam splitter creating two beams of laser light. The first beam is used to illuminate the structure with the light reflected from the structure directed towards an imaging surface. The second beam is also directed towards

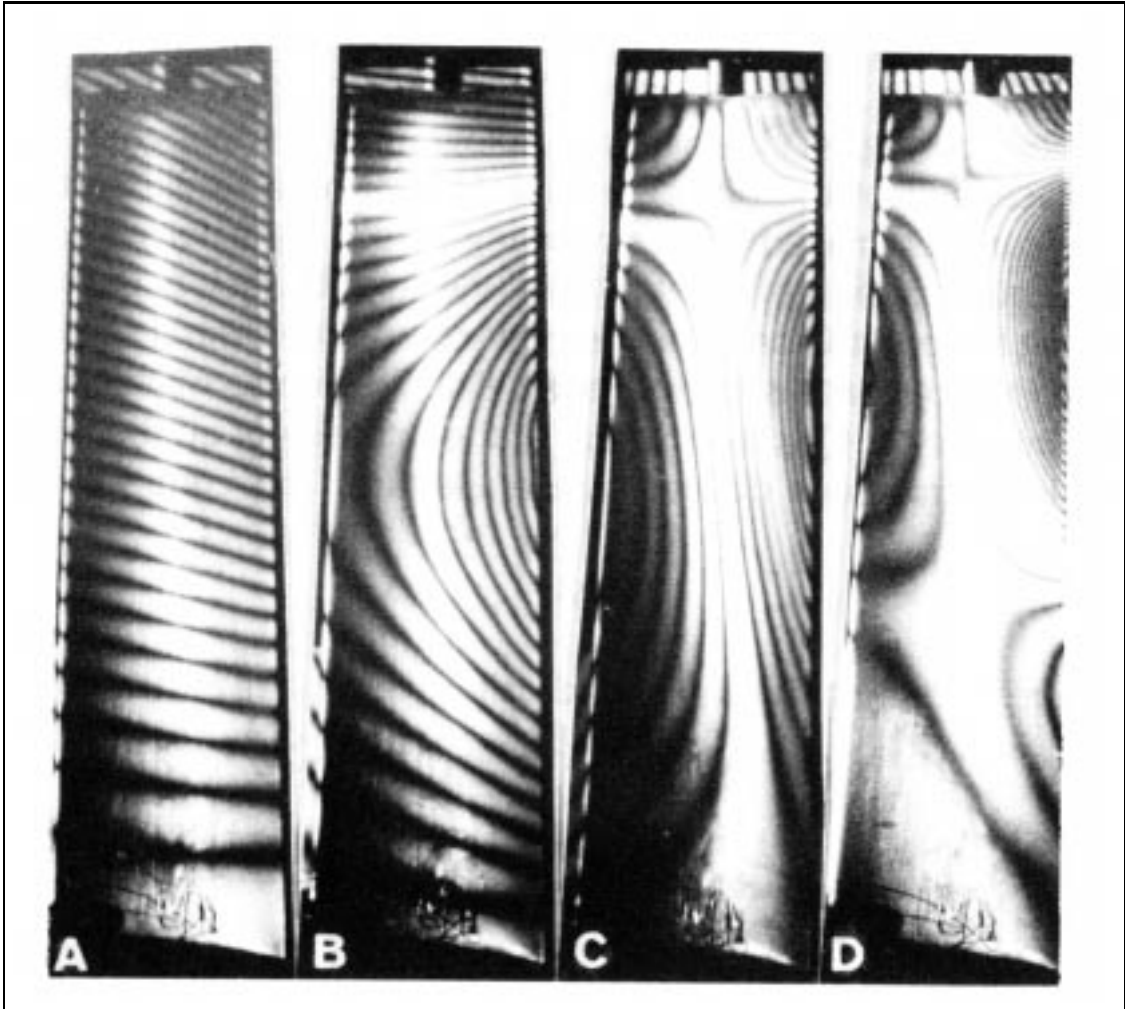


Figure 2.1: Hologram of Turbine Blades (taken from Gasvik)

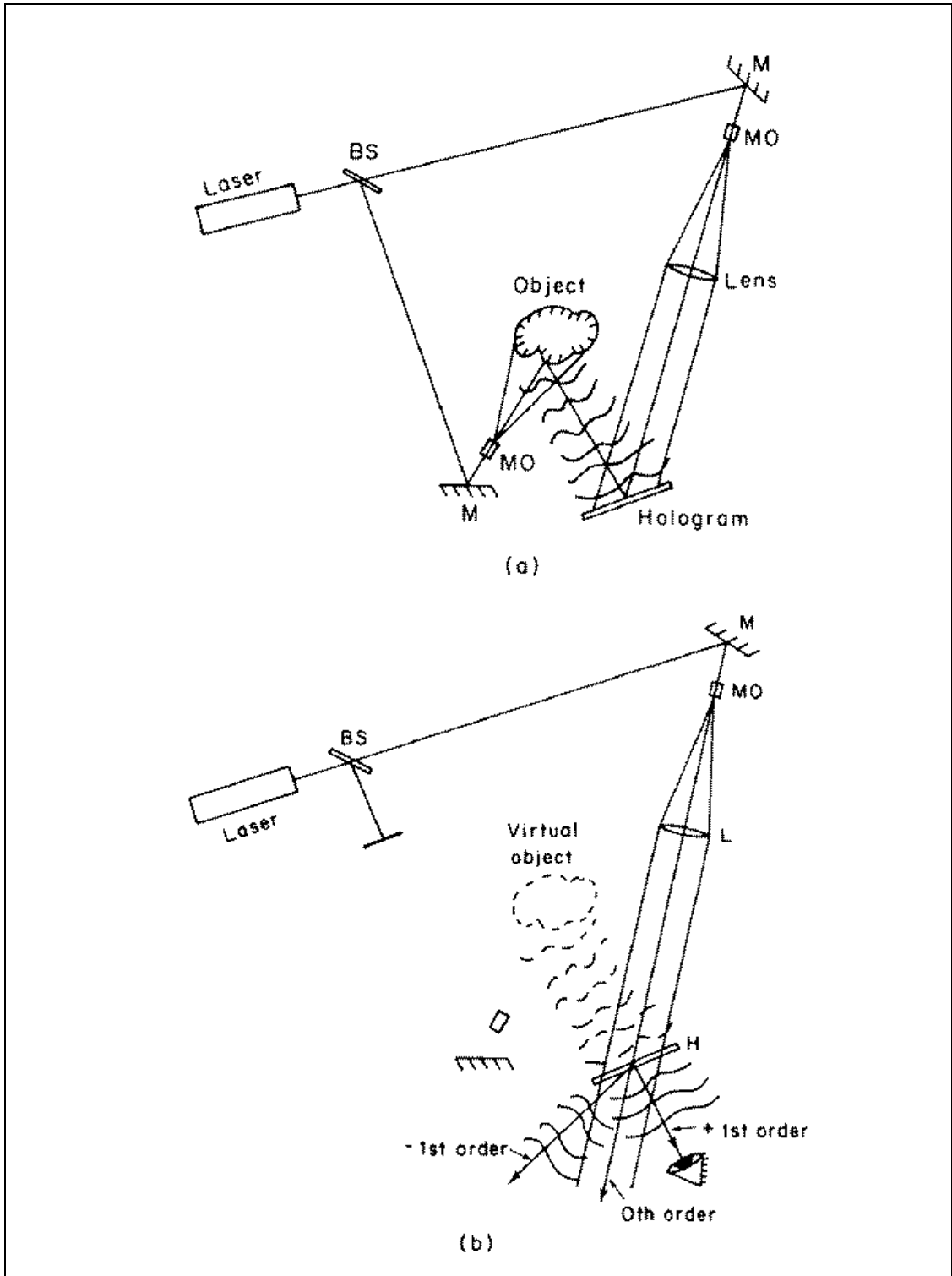


Figure 2.2: Schematic of Holography System (taken from Gasvik)

the imaging surface where the two beams are combined, creating an interference pattern. This reference is then captured on a hologram plate. If this plate is illuminated as shown in Figure 2.2 (b), a virtual image of the original part will be created.

To measure the vibration amplitude, the hologram plate is illuminated by light reflected from the vibrating structure. This creates an interference pattern on the surface of the structure that shows the displacement amplitude of the vibrating part.

While a great deal of work has been done using holographic interferometry for measuring turbine blade vibrations, the most relevant works to be considered here are those related to rotating structures.

In order for holography to work, the reference image and vibrating image must be precisely aligned. Typical measurements of stationary objects are performed on optical tables specifically designed to be immune from vibrations. This ensures that the test structure and hologram plates remain fixed and aligned during the test process. However for rotating structures the condition of fixed alignment of the entire measurement system is violated since the test structure is constantly rotating. To counteract the effects of the structure motion, several approaches have been developed for applying holography to rotating structure.

One of the most comprehensive studies of holographic interferometry for rotating structures is given by Beeck (1988). In this work, Beeck describes three techniques for performing holographic interferometry on rotating structures. In the first, the reference and measurement images are formed during two subsequent rotations of the structure, a technique that was successful at up to 5000 RPM. In the second approach, Beeck rotates both the hologram plate and the reference beam using a toothed-belt arrangement, at speeds up to 1000 RPM.

In the last, and most common, approach, an optical de-rotator is used to create a stationary image of the rotating structure. This is accomplished by combining an image de-rotator with a typical holographic interferometry system for stationary objects. An image de-rotator has

the effect of creating a non-rotating image of a rotating object. When viewed through the de-rotator, the rotating structure will appear stationary. The non-rotating image can then be treated as if it were a stationary object. This technique was used by Lesne et al. (1985) at speeds up to 600 RPM, by Stetson (1978) at speeds up to 9200 RPM, by Beeck at speeds up to 15000 RPM, and at speeds of up to 20000 RPM by Tsuruta and Itoh (1970).

For image de-rotation to work, the image de-rotator, which usually consists of a dove prism, must be rotated at exactly one-half the rotational speed of the test structure. This is typically accomplished by measuring the structure's rotation with a shaft encoder and using a control loop to synchronize the half-speed rotation of the de-rotator with the structure. Loss of synchronization causes the image to oscillate or wobble, introducing errors in the measured displacement field. Additionally, the components of the system must be properly aligned, a problem that is also encountered in laser vibrometry.

2.3 Laser Doppler Vibrometry

Laser Doppler vibrometry is another non-contacting optical technique which relies on the Doppler shift of laser light to measure the velocity of structures. The output consists of voltage signals proportional to the structure velocity. These signals are related to the frequency shift of the reflected light and are therefore accurately calibrated, providing accurate, quantitative measurements.

2.3.1 Stationary Beam Approach

The simplest technique for applying laser vibrometry to rotating structures is to point the laser at a fixed point in space and allow the rotating structure to pass the point. This approach is similar to that taken with blade tip sensors, but has the advantage of not being

limited to the tips of blades. The vibration signal consists of the structure vibration at each structure location as it passes the measurement point.

One of the first published applications of this approach is by Kulczyk and Davis (1973a). This work concentrated on using a fixed measurement location with the laser vibrometer oriented in the plane of rotation of the structure at rotation speeds of up to 13000 RPM. This approach was later adopted by Ewins (1995) for measuring radial vibrations on rotating shafts.

Rothberg (1995) also adopted the approach for torsional measurements. For torsional vibrations this technique has evolved into a commercially available transducer dedicated to torsional vibration measurements Rothberg and Halliwell (1996). The use of two LTV (Laser Torsional Vibrometers) has been applied to measurement of bending in rotating shafts. This technique has been discussed by others including Miles (1995)

Another approach, analogous to the technique used in blade tip sensors, measures the time between passings of the blade relative to the time of another timing signal. In this approach, an independent system is used to measure the shaft speed. A laser beam and photodetector are placed such that the blade to be measured interrupts the laser beam once during its rotation. By comparing the time interval between successive interruptions of the laser beam, the vibration amplitude of the blade can be found.

The more common technique of measuring vibrations with the laser vibrometer oriented perpendicular to the plane of rotation has been investigated by several authors.

Reinhardt et al. (1994) also used the stationary laser approach. Measured velocities, which were inferred from short burst of signals as the blade passed the laser beam, were processed using a least squares approach due to the short record length. Speeds ranging from 80 to 100 RPM were reported. Experiments were run with a non-excited blade and a shaker excited blade. Results showed measured velocities even when the blades were not excited

by the shaker. These signals were attributed to speckle noise and it was noted this noise would be evident even if the measurement beam was normal to the blade surface. The requirement of having two periods of oscillation occurring during the measurement interval was also discussed. Wlezien et al. (1984) applied the stationary laser technique to the vibration measurement on flexible videodisks at 1800 RPM.

The approach of using a measurement point that is fixed in space has two significant disadvantages. First, the vibration of each blade is only measured during a small interval of its rotation. As is the case for blade tip sensors it is not possible to get a continuous measurement of the blade's vibration during its entire rotation. A second difficulty is the introduction of speckle noise. This is caused by relative motion between the cross section of the laser beam and the measurement point on the moving target. While neither of these effects preclude the use of the stationary beam technique, they do introduce significant complications. The most common solution for overcoming these limitations is to move the measurement point with the structure, a solution which has been addressed through several tracking techniques.

2.3.2 Tracking Beam Approach

Laser vibrometry for rotating structures with the measurement point fixed to the target point has centered around mirror based tracking. Although optical de-rotation as used in holography is also applicable to vibrometry, this approach is not commonly discussed in the literature. Though different in their optical configurations, both de-rotation and mirror based tracking rely on electro-mechanical systems to synchronize the location of the measurement point with the rotation of the structure. Although theoretically capable of giving significantly better performance than the stationary beam approach, there is very little published literature on the tracking beam approach.

Tracking with Mirror Based Scanner

In the mirror based tracking technique, a scanning vibrometer is used to point the measurement beam at the moving target. Scanning laser vibrometers consist of a laser vibrometer with a set of scanning mirrors for directing the laser beam. Typically individual mirrors control the horizontal and vertical deflections. In general if the mirrors are driven with two sinusoidal signals 90° out of phase, the laser beam will trace out a circle on a planar surface. If the drive signals are synchronized with the motion of the rotating structure and the laser and structure are properly aligned, the laser beam can be locked onto a single point as the structure rotates. This is the approach most discussed in published literature.

Castellini and Santolini (1996) apply this technique and present results for rotating propellers in water. A shaft encoder and D/A board are used to generate the mirror drive signals. The effects of misalignment of the laser head are noted; the generation of a spurious velocity signal and the laser spot tracing a circle around the desired measurement point. The tests were performed in air and water at speeds up to 600 RPM, stated as the maximum speed for the application. The tendency of the spurious signal to 'hide' the desired signal is also mentioned as is the increase of spurious signal with rotational speed.

Bucher et al. (1994) used this technique and applied it to the vibration of rotating disks. The effect of misalignment on the sensing of in-plane velocities is noted. The need to characterize the dynamic characteristics of the scanning mirrors is also discussed. A shaft encoder based system is used with the drive signals generated by a D/A card. Measurements at rotational speeds of 130 RPM are reported. Later work by Stanbridge uses the same technique, but also alludes to the ability to use a rotating laser to track traveling modes on a stationary disk or rotating disk by scanning the laser at a speed different than the disk's rotational speed.

Two common problems discussed by each of these authors is the crucial issue of proper

alignment of the system, and the presence of signals due to the effects of misalignment. An inherent concern is the limited speed ranges at which the techniques have been used. For some applications, such as naval propellers this is not an issue, while for other applications, such as turbines and compressors in jet engines, this limited speed range renders the technique inadequate. The major limitation to high speed operation is the limited frequency response of the galvanometers used to position the scanning mirrors. These must be driven at the same frequency as the rotational frequency of the rotating structure. At these high frequencies the amplitude and phase response result in significant position and velocity errors.

Tracking with Optical Derotators

One approach for reducing the mechanical bandwidth problems associated with mirror based tracking is to use an optical de-rotator as used in holography. There are two ways to describe the effect of the de-rotator as applied to laser vibrometry. In the first, the de-rotator creates a non-rotating image of the structure. A scanning laser vibrometer can then be used to scan this stationary image. In the second, the de-rotator directs the laser beam to the rotating target and locks it to a single point on the rotating structure.

For the de-rotator to function properly, its axis of rotation must be coincident with the structure's rotation axis and its rotation speed must be exactly one half of the structure's rotation speed. Failure to meet these two requirements causes the non-rotating image of the structure to wander in the case of misalignment or oscillate about its rotation axis in the case of speed fluctuations. The misalignment can be minimized by careful setup of the components. The speed synchronization problem can be addressed through the use of a phase-lock loop to electronically link the structures rotation with the dove prisms rotation. This approach requires a shaft encoder on the structure as well as a servo motor capable of driving the optical de-rotator at one half the structure's speed. This approach presents sev-

eral potential problems. First, in order for the phase-lock loop to track the structure speed, the structure speed must be relatively constant. This precludes the use of the technique during run-up or coast-down of the structure. Second, dove prisms typically have a narrow field of view. Increasing the field of view comes at the cost of increased mass, increasing the performance requirements of the servo-motor.

While this technique has been used extensively for holographic interferometry on rotating structures, it is seldom used with laser vibrometry. Lesne et al. (1985) applied this technique to a bladed disk. In this work the alignment of the de-rotator axis and structure axis was identified as critical. Misalignment was identified to cause a velocity signal at the rotation speed of the structure and related to the angular misalignment. It was proposed that this signal be used to aid in alignment.

2.3.3 Self-Tracking Approach

Both of the current tracking methods are limited by two requirements; the need for proper alignment between the vibrometer and the rotating structure and a system for rotating the optical components synchronously with the rotating structure. The self-tracker simplifies the synchronization scheme by replacing the electromechanical link with a purely mechanical link. This eliminates the need to measure the structure's rotational position, eliminates the errors due to the dynamics of the optical drive components, and removes the speed limitations encountered with the other techniques.

The self-tracking system consists of three major components:

- Laser Vibrometer
- Vertex Mirror
- Fold Mirror

As in the case of the scanner based tracking technique and the de-rotator technique, a laser vibrometer serves as the transducer. However, whereas the other two techniques require a scanning laser vibrometer for moving the measurement point, the self-tracker only requires a single point laser vibrometer.

The vertex mirror is a small mirror attached to the structure. Ideally the size of the mirror needs to be no larger than the diameter of the laser beam. The vertex mirror is tilted relative to the plane of the disk. This tilt angle can either be fixed or variable. It will be shown that the variable arrangement is useful for aligning the system. The intersection of the laser beam with this mirror defines the vertex of a cone. The vertex mirror is mounted so as to be rotatable about the disk's rotation axis. The vertex angle is fixed to the disk and rotates at the same rate as the disk. It is this characteristic that forms the fundamental difference between this and other techniques.

Working in conjunction with the vertex mirror is a fold mirror. The fold mirror is a front surface planar mirror with a circular aperture. This mirror reflects or folds the cone back towards the bladed disk. The aperture need only be as large as the laser beam cross section, but is made larger in order to facilitate alignment. Ideally, the mirror need only be a circular strip with the outside radius approximately one-half the diameter of the bladed disk and inner diameter approximately one half the diameter of the disk. In this study a rectangular mirror is used for convenience.

Following development of the first self-tracker prototype, it was discovered that the self-tracking technique was proposed by Maddux (1997) at Wright Patterson Air Force Base. Correspondence between Mr. Maddux and Dr. Andy Barker indicates that the technique proposed by Maddux was based on a technique used by Dr. Ralph Wuerker at TRW to measure thermal deformations on large space antennae. This technique used a polished metal ball to reflect a laser beam into a spherical reference beam. This served as the basis for the attachment of a mirror to the shaft of the rotating structure. As indicated by

Maddux (1997) , the self-tracker technique was not pursued. Thus the work at Virginia Tech marks the first published implementation of the self-tracker system.

The self-tracker solves some of the problems encountered with other techniques. However it is not immune from the misalignment effects and presents it own unique challenges that can exacerbate these effects. These characteristics manifest themselves as tracking errors and velocity errors.

Two potential sources of tracking error are possible in the self-tracker, static misalignment of the components and dynamic motion of the rotation axis. Static misalignment occurs when the initial set-up of the laser and optical components violates some basic assumptions to be developed later. Dynamic motion occurs when the rotating structure is not rigidly mounted to ground and exhibits some rigid body motion. This work only addresses a subset of the possible static misalignment conditions.

While the primary effect of these two misalignments is a tracking error, a secondary effect is a velocity error. The occurrence of each source of tracking uncertainty will induce a velocity error. There is also an additional source of velocity error caused by laser speckle.

Most of the difficulties with all laser Doppler vibrometry techniques are related primarily to the fact that the transducer is not rigidly mounted to the structure. This means that the orientation of the transducer relative to the structure will have some uncertainty and will change with time due to misalignment or rigid body motion of the rotating structure. This causes errors in the location of the measurement point and induces a measured velocity component not related to the vibration of the desired measurement point.

A second source of difficulty inherent in the self-tracking technique is the effect of speckle noise, an artifact of the relative motion between the laser beam and the measurement point. This results in velocity components correlated with the structure's rotational speed but not related to the structure's vibration. The characteristics of speckle noise have been well

researched by a number of authors, most notably Rothberg and Halliwell. Results from their work will be used to characterize the effects of speckle in the self-tracker.

To a lesser extent laser Doppler vibrometry is hampered by the fact that it is a line-of-sight technique. For some engineering structures the rotating structure will be obscured during a portion of its rotation resulting in a loss of signal. This results in periodic dropouts in the measured time response and increased harmonic content in the frequency response which can be considered as velocity errors. While one approach is to develop signal processing techniques to alleviate the effects of the lost signal, this work will be concerned with cases in which the structure can be seen throughout its entire path.

While this work assumes that the transducer is a laser vibrometer, the self-tracker can also be used with other transducers. The transduction technique most likely to benefit from the self-tracking technique is stress pattern analysis through thermal emission (SPATE). In the case of SPATE, the thermal energy radiated from the structure due to vibration is directed to a thermal detector. The self-tracker can be employed to reflect this thermal energy from the vibrating surface to the detector much as it does the laser beam in the case of vibrometry.

For use with SPATE only the position analysis performed for the laser vibrometer is applicable. Where applicable, design decisions have been made to make the system easily adaptable to SPATE. These decisions are related mainly to the selection of optical components.

2.4 Summary

Current non-contacting techniques for vibration measurements on rotating structures have been reviewed, concentrating on blade tip sensors, holography, and vibrometry. Although the self-tracking vibrometry technique does not match the capabilities of any of the other techniques, it does present a capability not possessed by the other techniques. Because of this

the self-tracking should not be viewed as a replacement for the other techniques, but rather as another tool to complement those already available. It is in this context, as an alternative measurement technique with unique capabilities, that the self-tracker will be evaluated.

Chapter 3

Laser Doppler Vibrometry

Now that an overview of various techniques has been given and the role of the self-tracking technique defined, the operating principle of the laser Doppler vibrometer can be given. This material is well documented in a number of sources. One of the most notable sources, Drain (1980), gives a full description of laser vibrometry. A more specific discussion of the laser Doppler vibrometer as applied in the self-tracker will be presented here.

First a general description of laser vibrometry is given here. Next, a detailed discussion is given of phenomena specific to the self-tracker system that do not appear in most other applications of laser vibrometers.

While any of a number of single point LDV's are commercially available and applicable for use in the proposed system, this discussion focuses on the Ometron VPI, limited to the LDV's characteristics most relevant to the self-tracking technique.

Laser Doppler vibrometers measure the velocity of a structure based on the Doppler shift of light. The velocity information is carried by the frequency modulation of the laser beam. The velocity signal is then extracted from the frequency modulated signal.

To fully describe the use of laser vibrometry in the self-tracker, both the phenomena which produce a Doppler shift of the laser beam and the technique to extract the velocity signal from the frequency modulated laser beam must be discussed. The discussion opens with a simplified overview of laser Doppler vibrometry. Next the phenomena which induce Doppler shifts are described, focusing on the Doppler shifts caused by the motion of diffuse and reflective surfaces. As part of this description, a distinction will be made between velocity and path length changes. These are two similar yet fundamentally different phenomena. This provides an explanation of the circumstances under which velocity and path length changes are analogous, dispelling the commonly held misconception that path length changes cause a velocity response in the vibrometer. Next, the technique for extracting the velocity signal from the frequency modulated laser beam is discussed. This is done to identify a second phenomena not typically encountered in most vibrometry applications, speckle noise. Finally a discussion of laser speckle is given to qualitatively identify the characteristics of speckle noise.

3.1 Laser Doppler Vibrometry for Diffuse Surfaces

Laser Doppler vibrometers measure velocity by detecting the frequency shift of light caused by a moving target. A beam of laser light, typically from a helium-neon (HeNe) laser ($\lambda = 632.8nm, f = 470THz$) is directed to a vibrating structure. The structure's motion shifts the frequency of the light according to the relationship,

$$\Delta f = \frac{2}{\lambda}v_m(t) \tag{3.1}$$

where $\Delta\nu$ is the frequency shift in Hertz, and $v(t)_m$ is the velocity component along the laser beam direction.

In general the structure's velocity is not parallel to the laser beam direction. In this case the velocity component along the laser beam direction is found by taking the dot product

of the velocity vector with the laser beam direction as shown in Figure 3.1. Accounting for

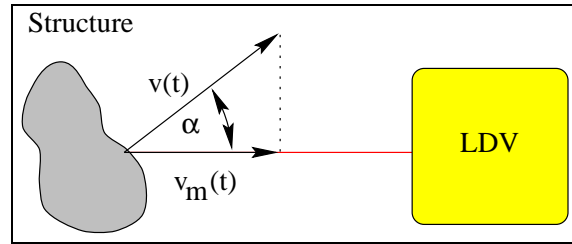


Figure 3.1: Relationship Between True and Measured Velocity

the angle between the structure's velocity and the laser beam direction, the frequency shift can be re-written as

$$\Delta f = \frac{2v(t)}{\lambda} \cos(\alpha) \quad (3.2)$$

The light is then reflected back to the vibrometer where the frequency shift is extracted and converted to a velocity signal.

To extract the velocity signal, a frequency shift of 3160 Hz per mm per second of velocity relative to the 470 THz carrier frequency must be detected. This represents a shift of approximately 1 part in 15 million per each mm/s of velocity. Extracting this small shift at such a high frequency is difficult for most demodulators since it must be performed electronically. The task of demodulating this signal can be simplified by performing part of the processing optically using an interferometer.

The interferometer mixes the modulated measurement beam with a reference beam, shifting the modulating signal from the 4.7 THz carrier frequency down to baseband. This baseband signal can then be frequency demodulated to extract the frequency shift. Once detected, the frequency shift can be converted to the corresponding velocity and provided as an analog voltage at the vibrometer's output.

In its simplest form, the vibrometer produces an analog voltage signal proportional to the velocity component parallel to the laser beam. While this appears a simple concept to

apply, there are several situations that produce counter intuitive results. To further illustrate the relationship between velocity and vibrometer output and to correct some common misconceptions, several experiments were performed. These experiments also motivate the subsequent analysis of the vibrometer's operation.

In each of these experiments, the vibrometer measured the velocity of a small block. The block was fixed to an electrodynamic shaker driven by a 200 Hz sinusoidal signal. Measurements were taken for several different orientations of the velocity and laser beam directions. Figures 3.2 and 3.3 show the configurations and measured velocities.

The first three configurations, shown in Figure 3.2, illustrate the behavior described above. In each case, the block clearly has a velocity component along the laser beam direction. Additionally, it should be noted that the length of the laser beam changes as the block vibrates. The velocity measured in case (a) is the true linear velocity of the block. This serves as a reference case. With the block's velocity oriented at approximately 45° relative to the laser beam direction (cases (b) and (c)), the measured velocity is scaled by a factor of approximately 0.707, the cosine of 45° . As in the reference case, the length of the laser beam changes as the block vibrates. These two cases show that the measured velocity is the component of the true velocity along the laser beam direction. Additionally it shows that the measured velocity is independent of the angle between the measurement surface and the laser beam direction. All of these results agree with the above relationships.

Case (d) is similar to both cases (b) and (c) in that the angle between the velocity vector and laser beam direction is approximately 45° and shows the same measured velocity as the two previous cases. However whereas the motion in cases (b) and (c) are accompanied by a change in the laser beam length, the motion of the block in case (d) does not appear to introduce a change in path length. This dispels a commonly held belief that velocity and path length change are always synonymous. In this particular case the velocity is not accompanied by a path length change, yet the vibrometer is sensitive to the velocity.

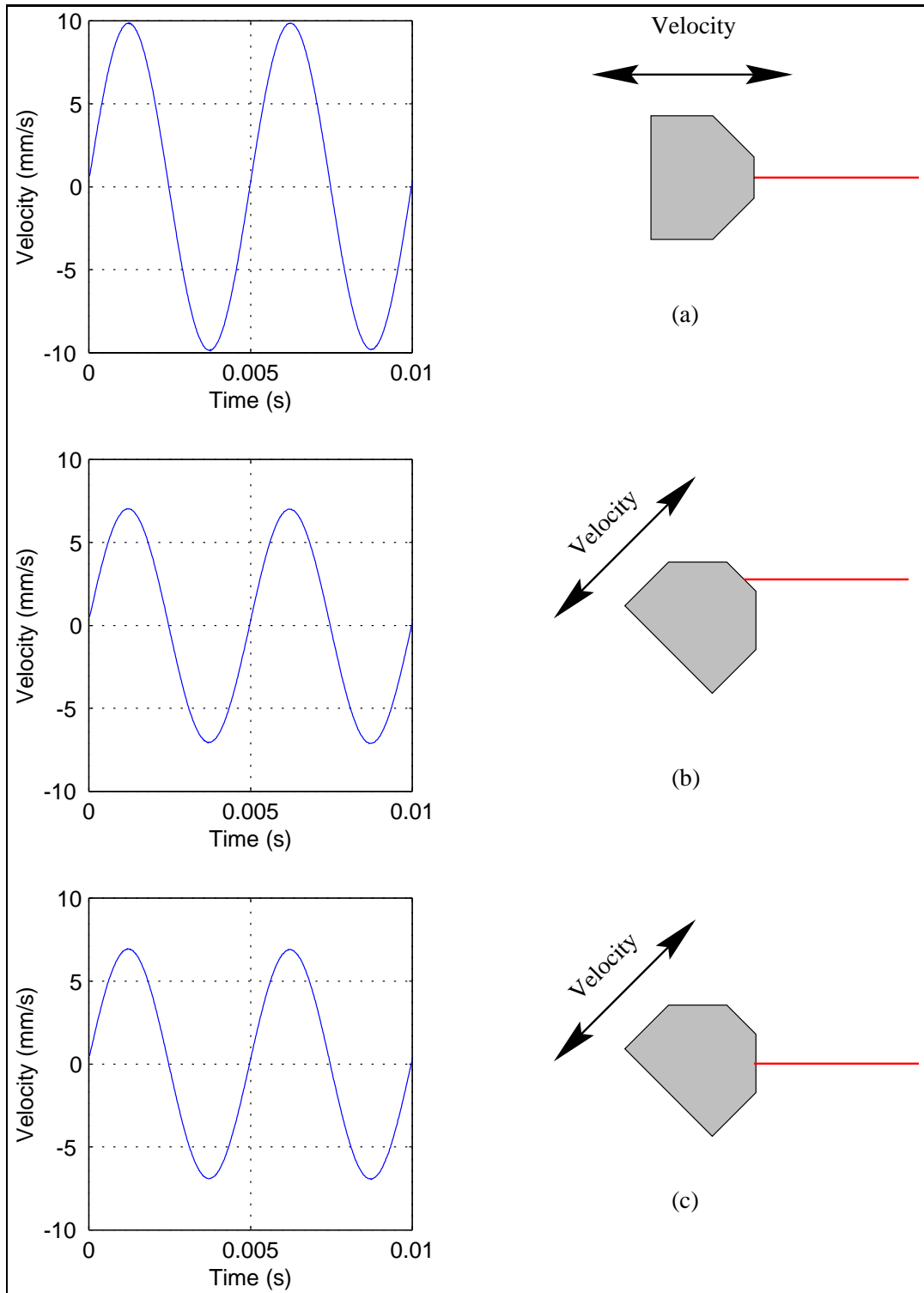


Figure 3.2: Measured Velocity Components, Cases (a)-(c)

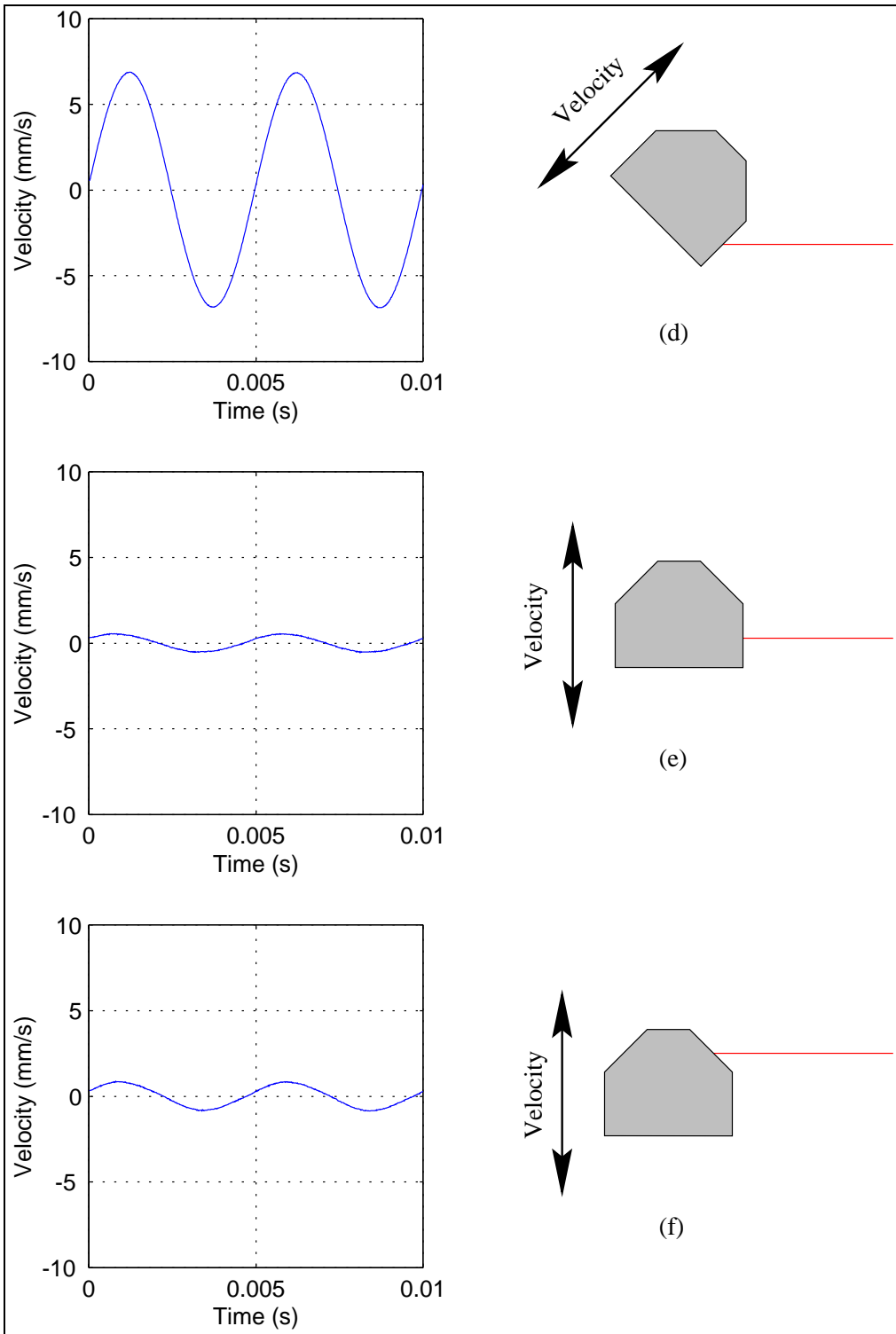


Figure 3.3: Measured Velocity Components, Cases (d)-(f)

In the last two cases the velocity vector is oriented 90° relative to the laser beam direction. Case (e) illustrates the situation where there is no velocity component along the laser beam direction but there is an apparent change in path length. Case (f) shows the situation where there is neither a velocity component nor a change in path length. In each of these cases the expected measured velocity is zero. In both cases the dot product between the velocity and the laser beam direction is zero. However the results show that the velocity does not go to zero as expected. There are two explanations for this. First, it is possible that the angle between the velocity vector and the laser beam direction was not exactly 90° . However repeated attempts to align the shaker to reduce the velocity to zero were not successful. Instead the shaker was oriented to minimize the velocity amplitude. This implies that the block exhibits some motion transverse to its primary vibration direction. This effect is plausible, but not easily verified.

A second explanation is related to the fact that the spot on the block illuminated by the laser beam is time varying due to the block's motion. This causes an effect known as speckle noise which has been widely documented in published literature. This effect will be discussed in much greater detail in a later section.

These experiments illustrate three important concepts about the vibrometer's measurement capability. First, velocity along the laser beam direction causes vibrometer output. Second, path length changes do not cause vibrometer output unless the path length change is accompanied by a velocity component along the laser beam direction. Last, vibration perpendicular to the laser beam induces a vibrometer response due to speckle noise.

These results confirm the assumed performance characteristics of the vibrometer under normal situations, and also identify two situations not addressed by the simple formulation. These two situations are the effects of path length changes which seem to contradict the results predicted by velocity considerations, and the effect of speckle noise which cause a non-zero vibrometer response when no response is predicted. If these two results are tem-

porarily set aside, the output of the vibrometer does indeed give the predicted results for the motion of a diffuse surface.

While this basic explanation is sufficient for most applications of the vibrometer, a more detailed discussion is required to describe the two anomalies. However before addressing these two issues, a situation related to the motion of the diffuse surface will be examined first. This situation, which is present in the self-tracker, is the introduction of a moving mirror along the laser beam path.

3.2 Laser Doppler Vibrometry for Reflective Surfaces

The previous section described the use of the laser Doppler vibrometer to measure the velocity of diffuse surfaces. This discussion is sufficient for explaining the use of the vibrometer in most engineering applications. However there is a special situation occurring in the self-tracker which requires an extension of the previous result. This situation, the introduction of a moving mirror along the laser path between the vibrometer and a diffuse surface, requires a general relationship between velocity and frequency shift. This relationship is based on the frequency shift caused by the motion of a scattering particle.

3.2.1 Frequency Shift Due to a Moving Particle

A model of the general case of Doppler shift caused by scattering of a moving particle is presented in Drain (1980). In this model, shown in Figure 3.4, a laser beam encounters a moving particle.

The particle scatters the incident light in all directions and the scattered light can be observed from any of a number of arbitrary locations. The Doppler shift of the observed light is

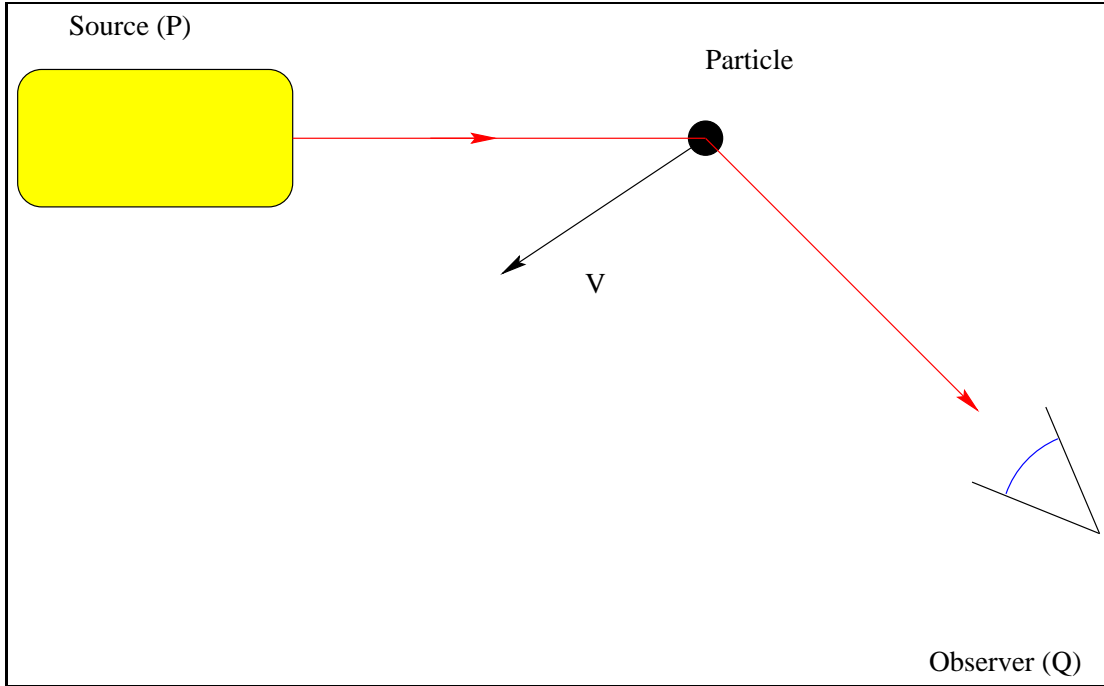


Figure 3.4: Particle Scattering Schematic

dependent on the location of the observer. This general case is not typically encountered in normal use of the vibrometer where the source and observation locations are typically the same point. Thus the relationship used above is a special cases of a more general expression.

Drain derives the Doppler shift caused by a moving particle using a variety of viewpoints, including a relativistic viewpoint, a momentum approach, and a geometric approach. These derivations, whose details are not relevant for this work, result in the following expression for the frequency shift due to a moving particle

$$\Delta\nu = \frac{2v}{\lambda} \cos(\beta) \sin\left(\frac{\alpha}{2}\right) \quad (3.3)$$

where β and α are defined in Figure 3.5.

The two angles of interest are the angle through which the laser beam is deflected (α), referred to as the scattering angle, and the angle between the velocity vector and the bisector of the angle formed between the incident and reflected beam directions (β). The above relationship shows that the laser beam frequency shift is dependent on the velocity component along the

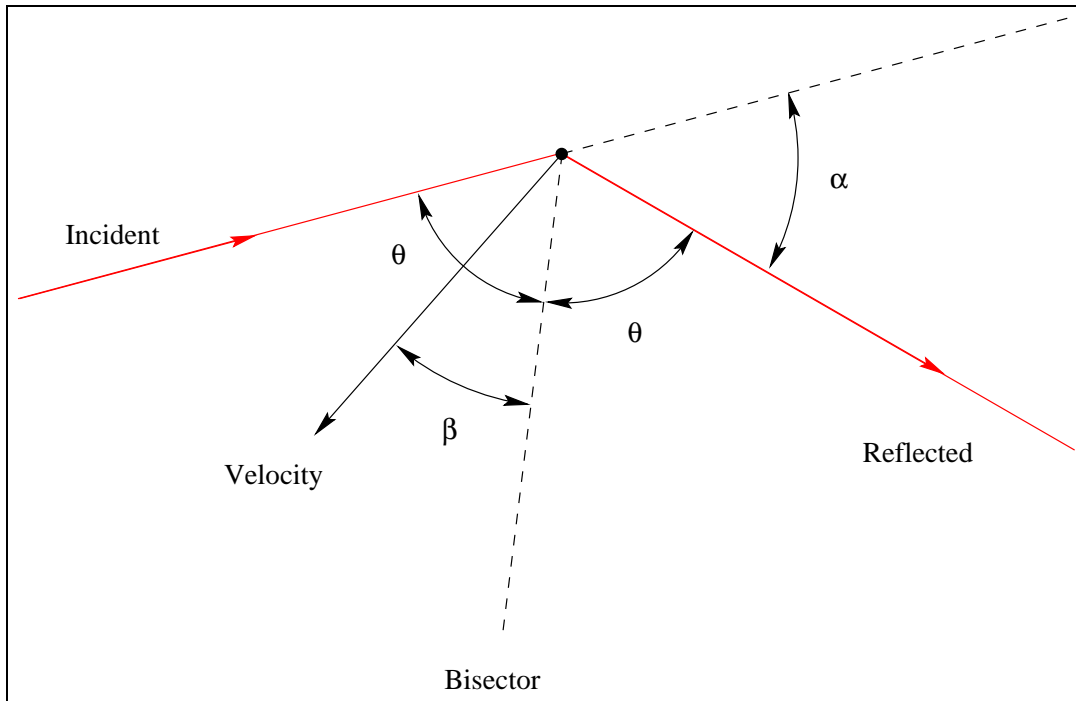


Figure 3.5: Particle Scattering Geometry

bisector and the scattering angle of the laser beam. It is interesting to note here that for the case of the source and observer lying along the same line, the above relationship reduces to the simple relationship used above for the the frequency shift from a diffuse surface. Thus Doppler shift for the LDV, where the laser beam is retro-reflected back upon itself and the source and observer are essentially the same point, is a specific case of the general Doppler shift described here. This relationship can now be applied to the case of a moving mirror.

3.2.2 Frequency Shift for a Moving Mirror

The relationship developed for the Doppler shift caused by a scattering particle serves as the basis for a relationship for Doppler shift caused by a moving mirror. In the case of a mirror, the source and observer generally do not lie along the the same line, thus requiring the general relationship from above. However whereas for the general case the observation

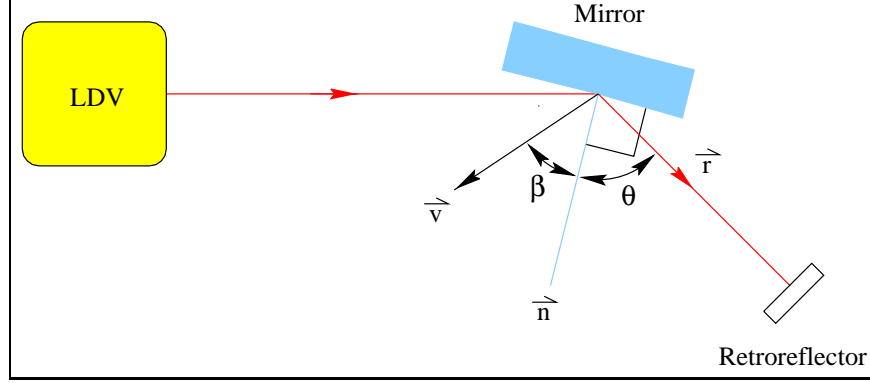


Figure 3.6: Frequency Shift for Moving Mirror

point can be arbitrarily selected since the particle scatters the light in all directions, for the case of a moving mirror the observation direction is fixed since the mirror reflects the light in a single direction. Thus the general result can be further simplified since the deviation angle between the incident and reflected beams is related to the angle between the incoming beam and the mirror normal. The mirror normal and the bisector become collinear, reducing the Equation 3.2.1 to

$$\Delta f = \frac{2v}{\lambda} \cos(\beta) \cos(\theta) \quad (3.4)$$

where both angles are measured relative to the mirror normal.

Before this result can be applied to the self-tracker, two factors must be accounted for. First, the return path must be accounted for. In the self-tracker, the light reflected from the mirror eventually encounters a retroflective surface which returns a portion of the light back to the moving mirror as shown in Figure 3.6. This interaction with the mirror causes a second frequency shift equal to the previous one encountered on the outgoing beam resulting in a total frequency shift of

$$\Delta f = 2 \frac{2v}{\lambda} \cos(\beta) \cos(\theta) \quad (3.5)$$

Next, the two-dimensional relationship must be extended to three dimensions. This is done by replacing the scalar velocity with the velocity vector and replacing the cosine terms with

Table 3.1: Velocity Amplitudes for Vibrating Mirror

Case	Predicted	Measured
a	Not Applicable	$8.30 \frac{mm}{s}$
b	$16.60 \frac{mm}{s}$	$16.62 \frac{mm}{s}$
c	$5.87 \frac{mm}{s}$	$6.00 \frac{mm}{s}$
d	$11.74 \frac{mm}{s}$	$11.46 \frac{mm}{s}$
e	$8.30 \frac{mm}{s}$	$9.05 \frac{mm}{s}$

dot products. Recall that the angles θ and β are both measured relative to the mirror normal from the incoming beam direction, and the velocity vector respectively. This allows the cosine terms to be replaced by dot products. With this modification, the three dimensional relationship can be re-written as

$$\Delta f = \frac{4}{\lambda} (\vec{v} \cdot \vec{n})(\vec{r} \cdot \vec{n}) \quad (3.6)$$

To verify this expression, a series of experiments were performed to measure the velocity signal for a moving mirror. A plane mirror was mounted to an electrodynamic shaker and driven at 200 Hz. The angle between the mirror normal and the velocity and incident laser beam direction was varied. The resulting output for several configurations is shown in Figures 3.7 and 3.8. The predicted and measured velocities are shown in Table 3.2.2.

The predicted and measured velocities is shown in Table 3.2.2

While these results verify the effect of moving mirrors on the Doppler shift and velocity output of the vibrometer, the actual situation encountered in the self-tracker is slightly more complex. In the self-tracker, there are two mirrors, the fixed fold mirror and the rotating vertex mirror. The fixed fold mirror induces no frequency shift in the laser beam, but the rotating vertex mirror does. Extension of the above relationship to the rotating vertex mirror is developed next.

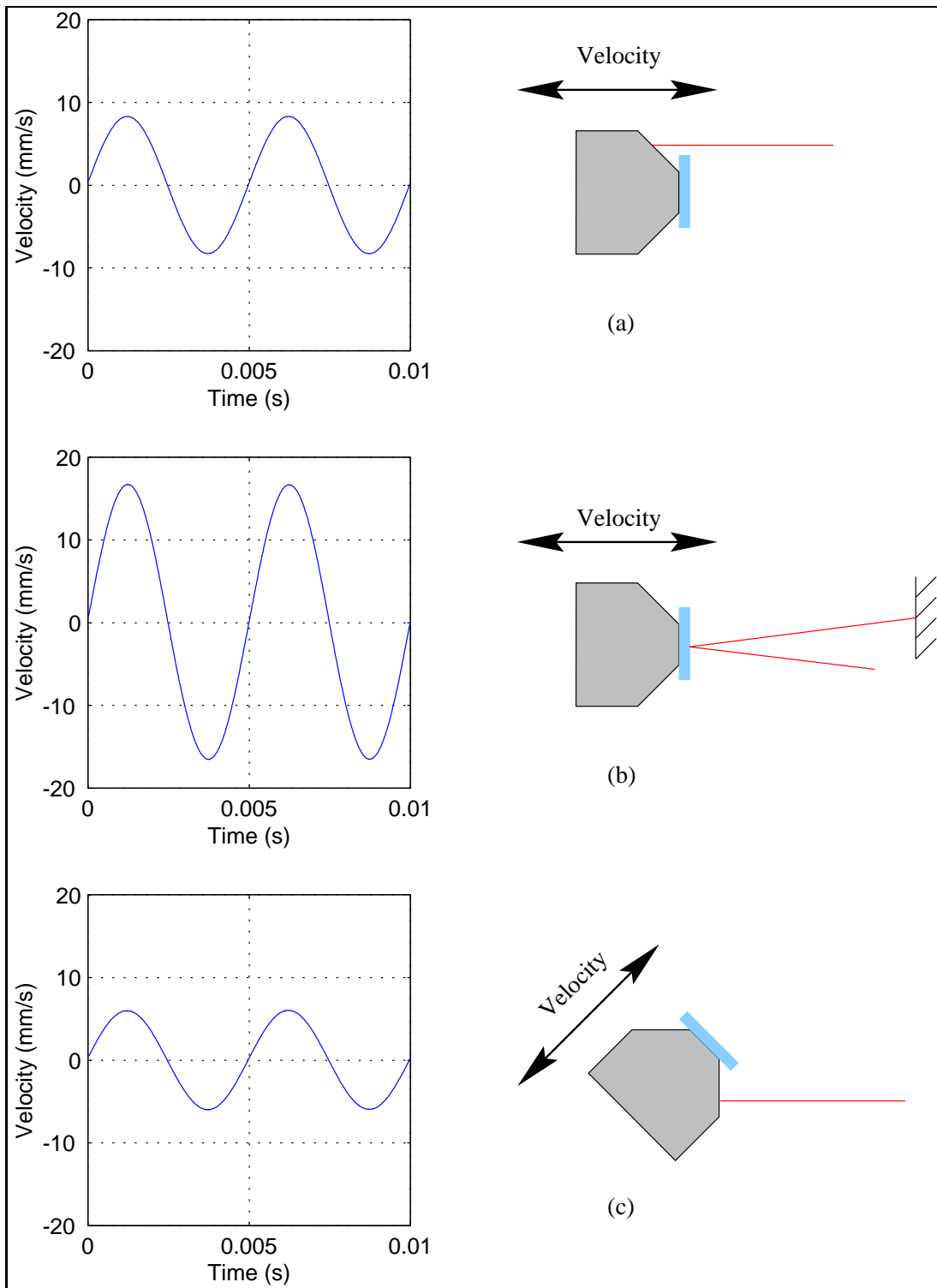


Figure 3.7: Measured Velocity for Moving Mirrors, Cases (a)-(c)

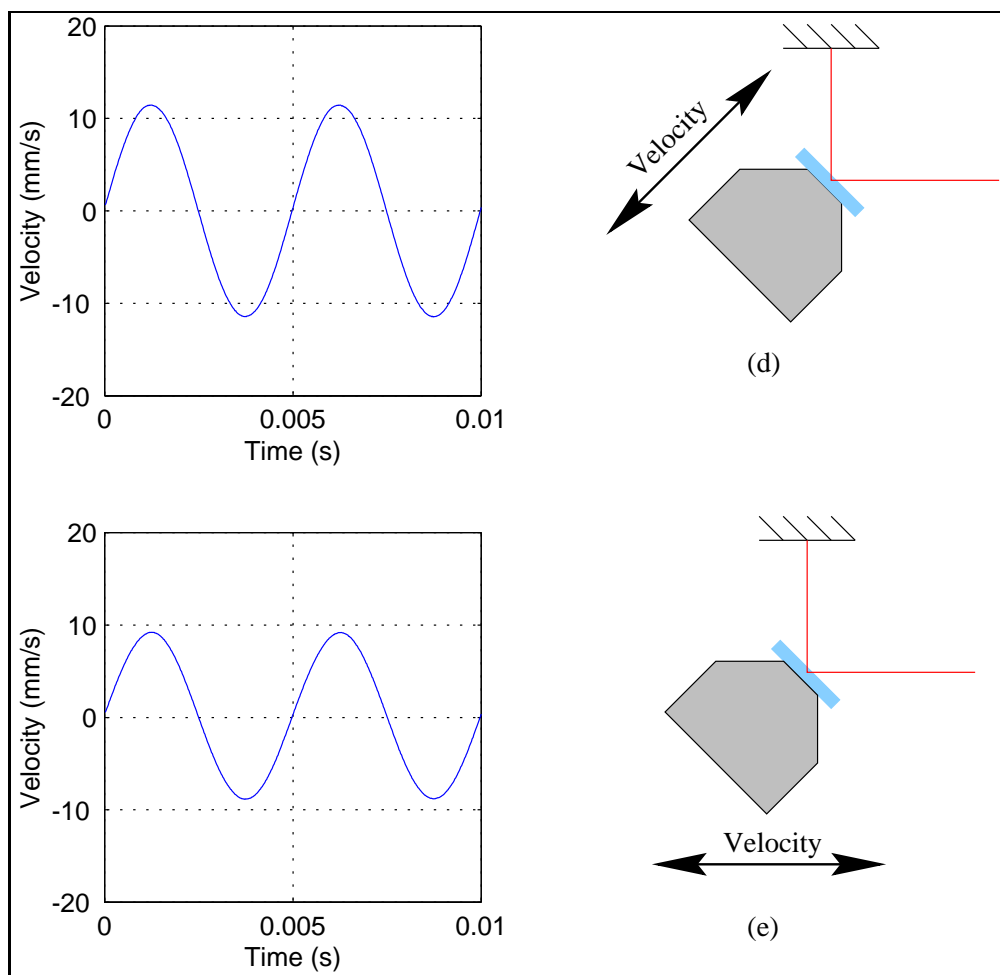


Figure 3.8: Measured Velocity for Moving Mirrors, Cases (d)-(e)

3.2.3 Frequency Shift for a Rotating Mirror

For the rotating vertex mirror, each point on the mirror has the same angular velocity, equal to the rotational speed of the bladed disk. Although the mirror has no rigid body linear velocity, individual points on the mirror do. The velocity vector for these points lies in a plane perpendicular to the rotation axis. The direction of the velocity vector for a single point changes as the point revolves around the rotation axis. However the velocity vector of points fixed to the vertex mirror all have the same direction as they pass the point where the laser beam intersects the vertex mirror.

For a constant rotational speed, this results in a velocity vector at the intersection of the laser beam and vertex mirror that has a fixed magnitude and direction. Similarly, the direction of the incident laser beam is fixed in space. However, the direction of the mirror normal and the reflected beam are time varying, rotating with the same angular speed as the bladed disk. Thus to find the frequency shift induced by the rotating mirror, the time varying vector direction of the mirror normal must be found. Figures 3.9 and 3.10 show the relationship between the velocity vector for a point on the vertex mirror and the plane containing the incoming and reflected laser beam.

Figure 3.9 illustrates the geometry of the laser beam path and the mirror velocity. The mirror is tilted about an axis T-T', that lies in a plane normal to the rotation axis. The incoming and reflected beams define a path that lie in a plane perpendicular to the tilt axis. For the configuration depicted in Figure 3.9, the mirror's linear velocity, V_m is normal to this plane and there is no component of the mirror velocity along the laser beam path. As the mirror rotates, the direction of mirror's velocity vector remains unchanged, but the orientation of the plane containing the laser path changes. This causes the component of mirror velocity projected onto the laser plane to increase. This component, V_l reaches a maximum as the mirror rotates through 90° as shown in Figure 3.10, which corresponds to the angle where the tilt axis, T-T', passes through the intersection point between the laser beam and the

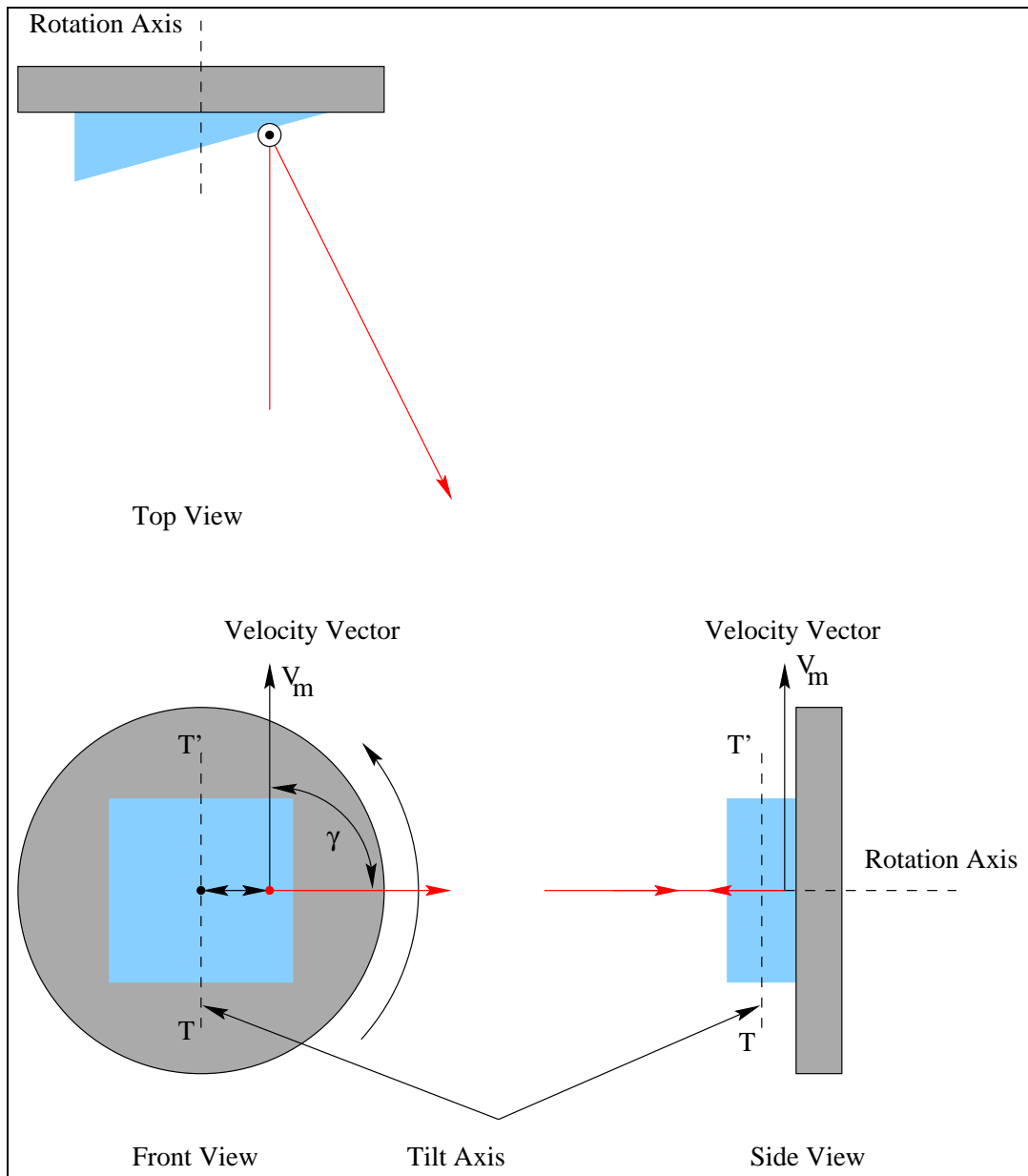


Figure 3.9: Geometry for Rotating Mirror, 0° Rotation Angle

mirror. The component of mirror velocity lying in the plane defined by the laser beam can be shown to be

$$V_l = V_m \cos(\gamma) \quad (3.7)$$

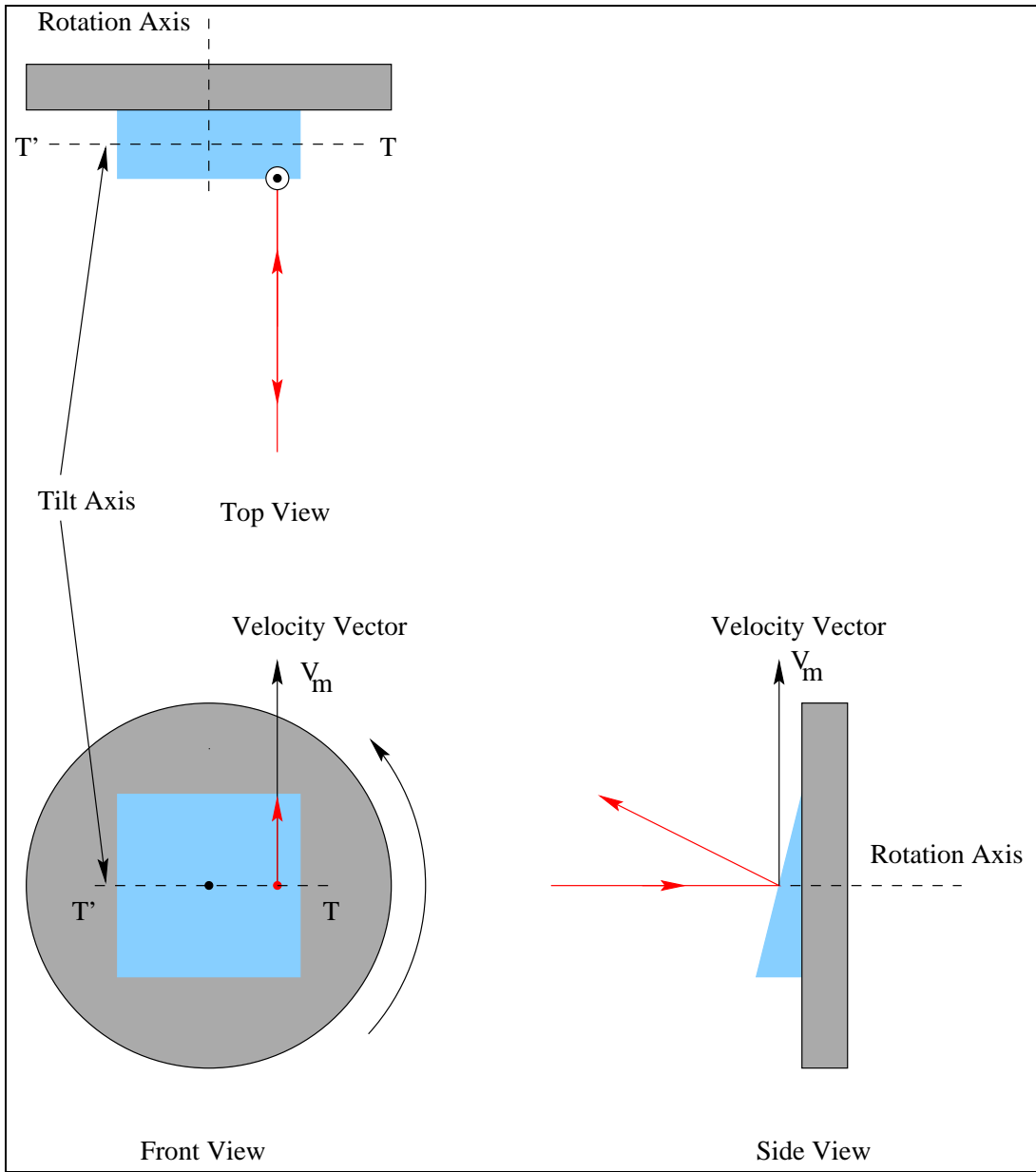


Figure 3.10: Geometry for Rotating Mirror, 90° Rotation Angle

where θ is the angle between the velocity vector and the laser beam plane. Thus as the mirror rotates, the component of mirror velocity in the laser beam plane will have a sinusoidally varying magnitude as shown in Figure 3.11.

Having found the velocity component lying in the laser beam plane, the measured velocity

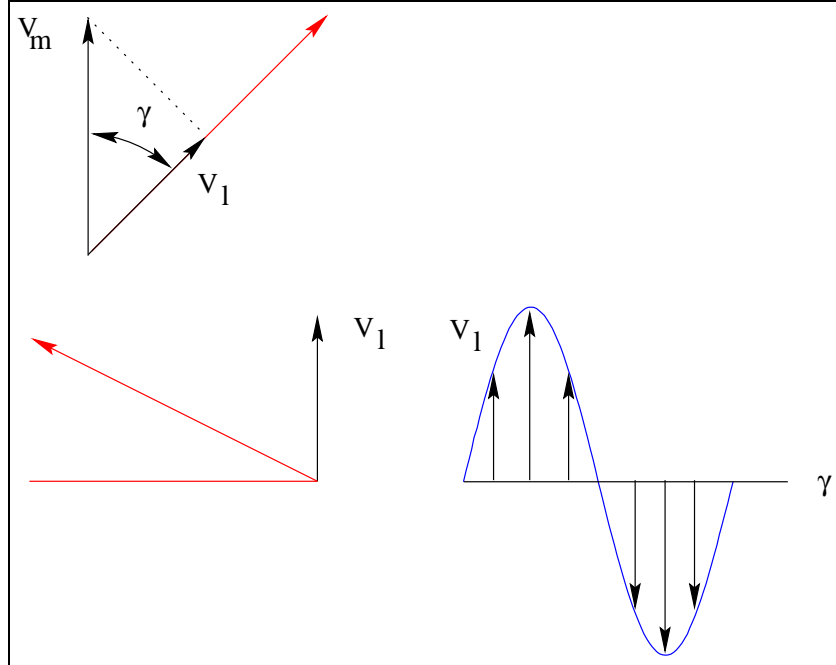


Figure 3.11: Component of Mirror Velocity in Laser Beam Plane

can be found by applying Equation 3.5. Since the geometry of the laser beam path is constant with rotation angle of the mirror, the measured velocity will be scaled relative to V_l .

Several demonstrations were performed to show that the measured velocity of a rotating tilted mirror agreed with the above predictions. The vertex mirror used in the self-tracker was mounted to the end of a shaft with a tilt angle of approximately 2.5° . The laser beam was aimed to the center of the mirror and the shaft was rotated at a speed of 1500 RPM (25 Hz). The laser beam was reflected onto a diffuse surface placed 0.74 m from the vertex mirror. As the shaft rotated, the laser spot traced a circular path with a diameter of approximately 0.13 m.

The velocity output of the vibrometer was recorded for varying radial displacements of the laser beam from the shaft center. The laser beam was displaced horizontally across the face of the vertex mirror in 1mm increments. Figures 3.12 and 3.13 show the frequency spectra for the measured velocity signals.

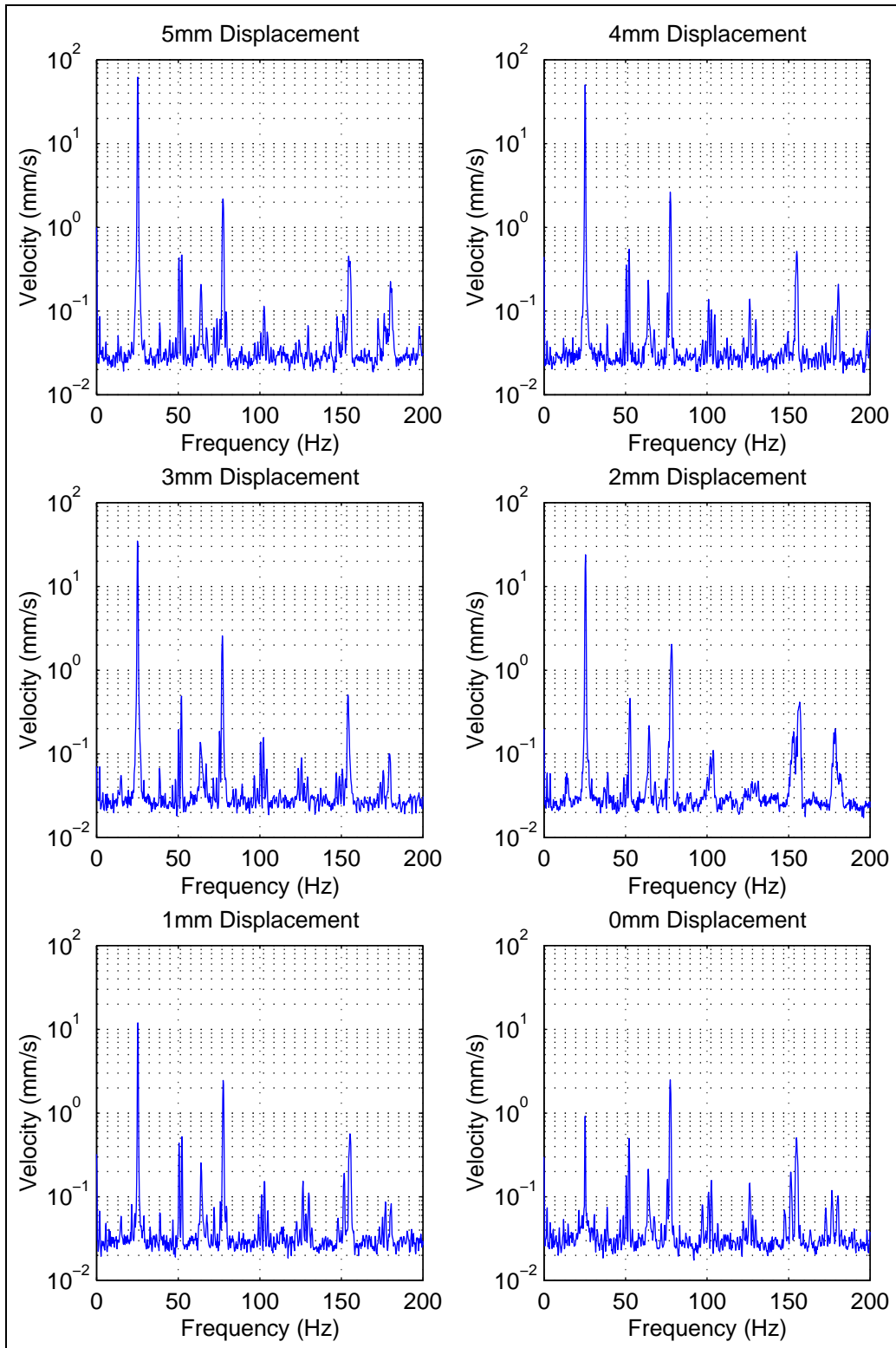


Figure 3.12: Frequency Spectra for Rotating Mirror Velocity, Positive Displacements

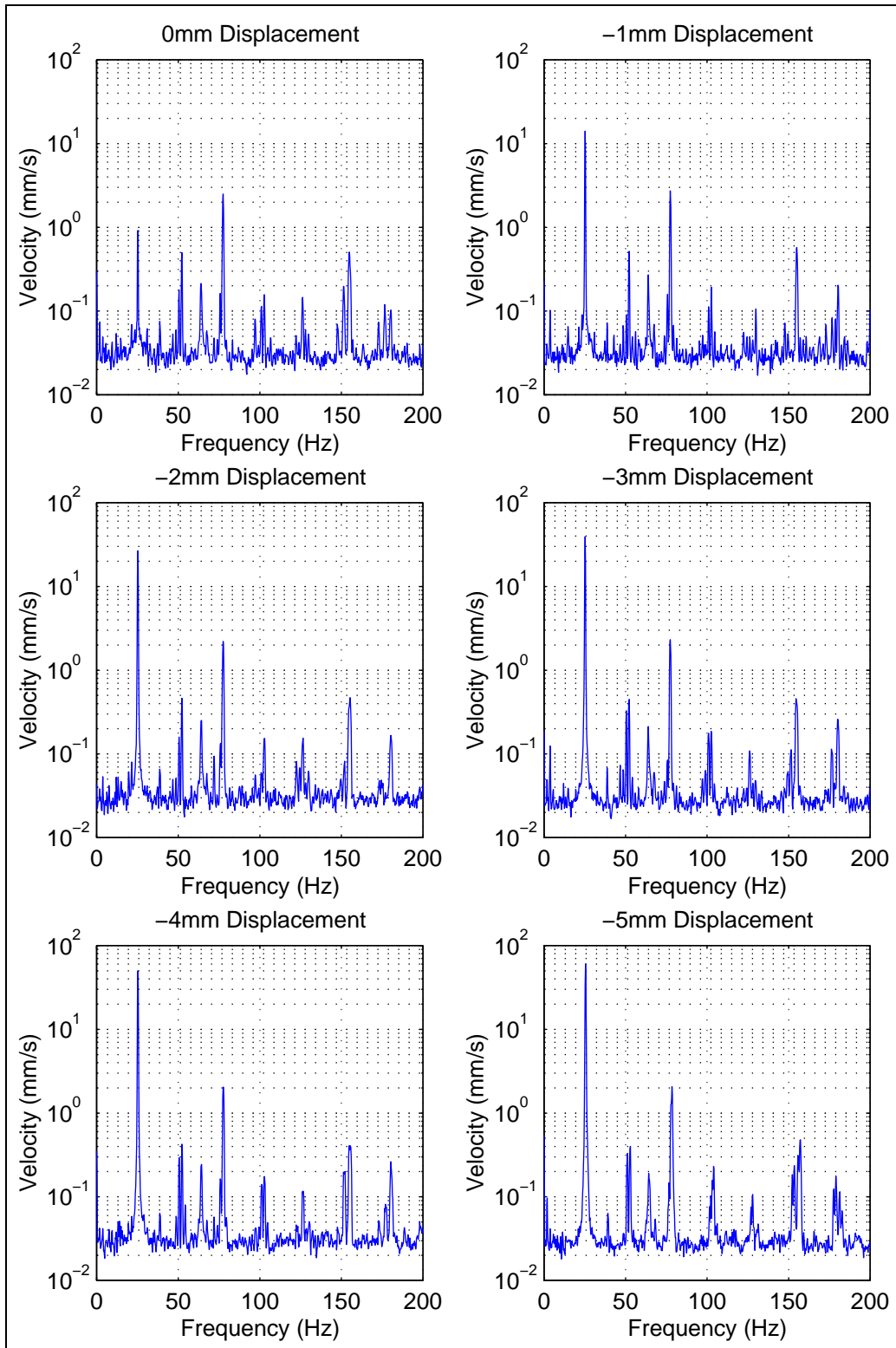


Figure 3.13: Frequency Spectra for Rotating Mirror Velocity, Negative Displacements

The frequency spectra show that as the laser spot is moved radially away from the center of the shaft, the measured velocity at the running frequency increases. Additionally the frequency content at the other frequencies remain relatively constant. This shows that the speckle noise remains constant. The following table compares the actual and predicted velocity amplitude at the running speed as a function of radial distance between the laser beam and the center of the shaft.

Table 3.2: Once Per Rev Velocity Amplitudes for Rotating Mirror

Displacement	Predicted	Measured
-5 mm	62.14 mm/s	67.46 mm/s
-4 mm	50.13 mm/s	53.96 mm/s
-3 mm	34.86 mm/s	40.47 mm/s
-2 mm	23.94 mm/s	26.98 mm/s
-1 mm	11.97 mm/s	13.49 mm/s
0 mm	0.91 mm/s	0 mm/s
1 mm	14.11 mm/s	13.49 mm/s
2 mm	26.53 mm/s	26.98 mm/s
3 mm	39.41 mm/s	40.47 mm/s
4 mm	50.08 mm/s	53.96 mm/s
5 mm	60.53 mm/s	67.46 mm/s

Comparison of these results shows good agreement between the measured and predicted velocity amplitudes.

One important implication of these results is that the vibrometer will measure no velocity when the laser spot is at the vertex mirror's center of rotation, regardless of the angle between the structure's rotation axis and the incoming laser beam. Thus by monitoring the velocity signal, the laser spot can be directed to the center of the rotating vertex mirror.

Additional experiments were performed to show that path length changes had no effect on the velocity signal for the rotating mirror. The diffuse surface, originally aligned parallel to the rotating disk, was tilted through 90° in 15° increments as shown in Figure 3.14.

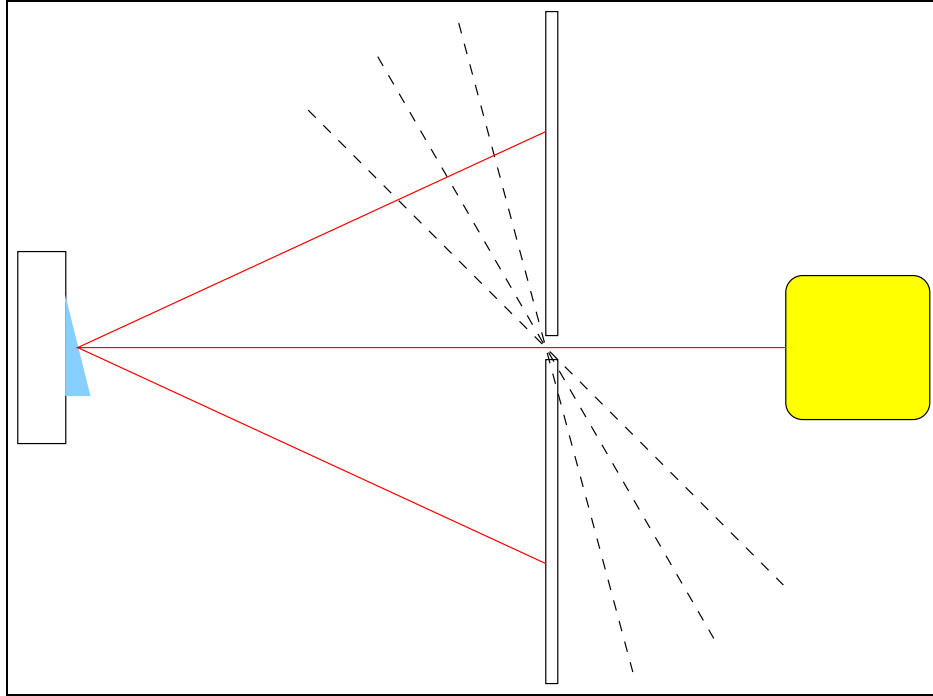


Figure 3.14: Diffuse Surface Tilt

Tilting the surface introduces a time varying path length change between the surface and the vertex mirror. The frequency spectra for the measured velocities shown in Figures 3.15 and 3.16 show minimal changes.

Amplitudes for the frequency component at the rotational speed are shown in Figure 3.17 and Table 3.3.

These results, like the full frequency spectra, show a slight increase in the velocity. However these changes are well below what would be expected if they were caused by the time varying path length. One effect of tilting the diffuse surface is to cause the laser spot to de-focus as it travels around the laser path. This may increase the speckle noise, an effect that would be seen across the entire frequency range.

With the effect of moving surfaces on the frequency shift of the laser beam illustrated, it is now possible to describe the technique used to extract the velocity signal from the frequency

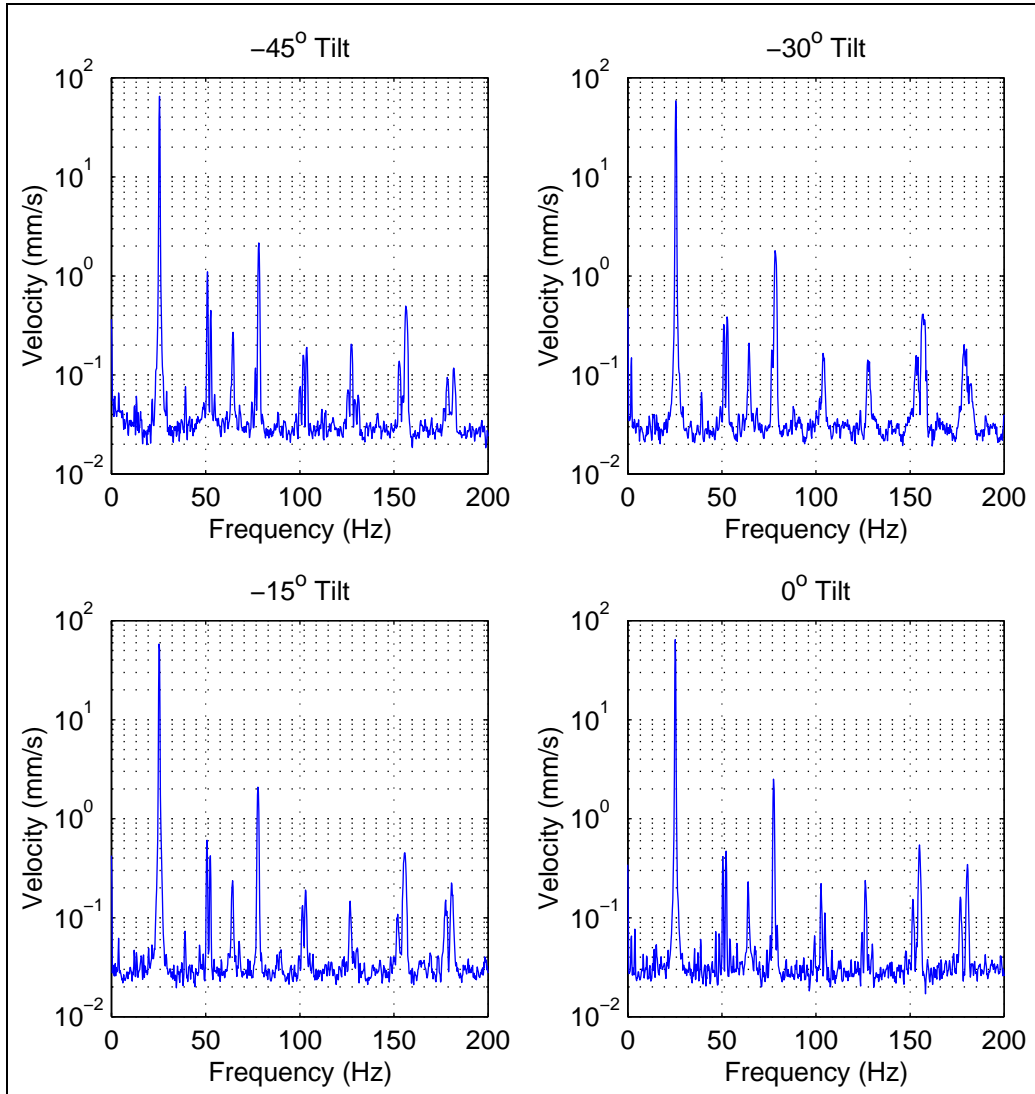


Figure 3.15: Frequency Spectra for Path Length Change, Negative Tilt Angles

Table 3.3: Effect of Diffuse Surface Tilt Angle on Measured Velocity

Tilt Angle	Velocity
-45°	65.03 mm/s
-30°	58.58 mm/s
-15°	58.07 mm/s
0°	64.60 mm/s
15°	60.31 mm/s
30°	62.66 mm/s
45°	62.84 mm/s

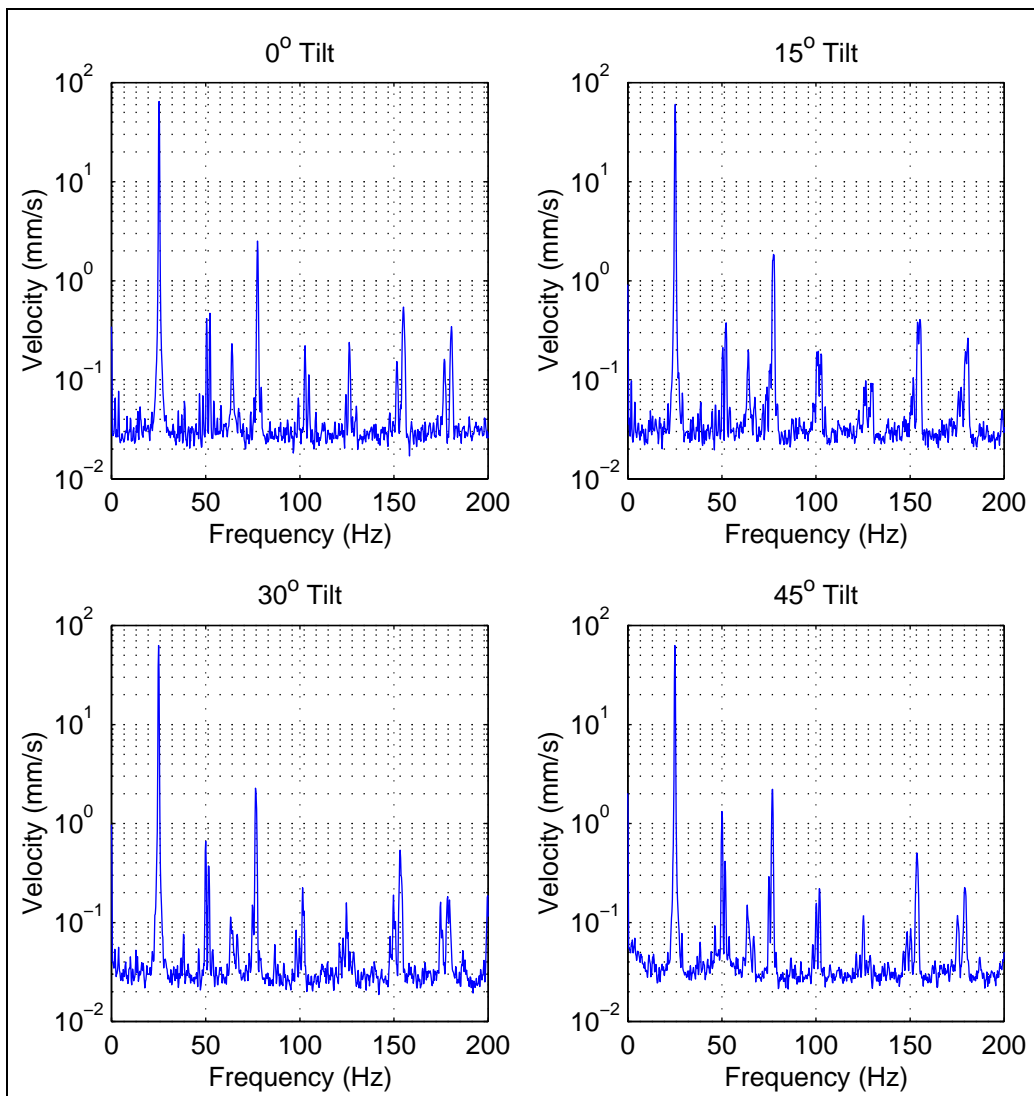


Figure 3.16: Frequency Spectra for Path Length Change, Positive Tilt Angles

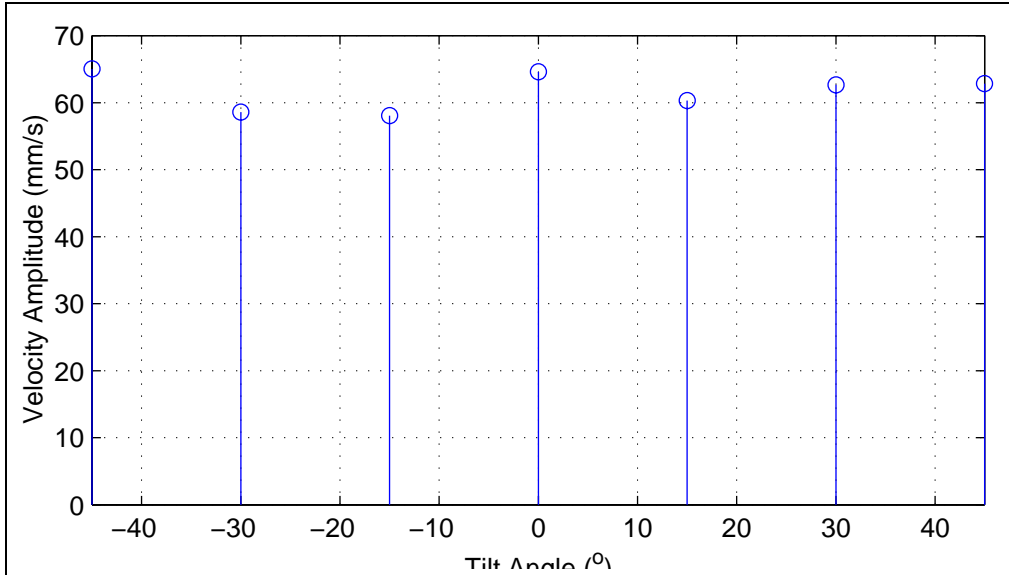


Figure 3.17: Once Per Rev Velocity Amplitudes for Tilted Surface

shifted laser beam.

3.3 Extraction of Velocity Signal from Frequency Shift

The previous section discussed several phenomena encountered in the self-tracker that impart a frequency shift on the laser beam. A general expression was presented and applied to two cases; the frequency shift caused by motion of a diffuse surface and frequency shift caused by the rotation of a mirrored surface. Two other phenomena, path length effects and speckle noise, which resulted in unpredicted results were also identified, yet the mechanisms responsible for these effects were not discussed. To fully understand these phenomena, it is essential to discuss how the vibrometer converts the frequency shift imparted on the laser beam into a velocity signal.

The process of extracting the velocity signal from the frequency shifted laser beam is best explained by tracing the path of the laser beam through the subsystems of the vibrometer.

Figure 3.18 shows a schematic of the laser vibrometer.

The major subsystems and a brief description of their purpose is given below.

- Laser Source-Provides the laser beam which serves as the non-contacting information path and carrier signal
- Interferometer-Mixes the signal and reference beams to isolate the modulating signal
- Photodetector-Captures the optical Doppler signals and converts them into electrical Doppler signals
- Demodulator-Extracts the signed structure velocity from the quadrature Doppler signals

3.3.1 Laser Source

The laser source is a helium-neon (HeNe) laser tube which produces a multi-frequency beam of light. The frequencies produced consists of those with integer multiples of the half wavelength that can fit in the laser tube. In general there are an infinite number of modes that meet this requirement, however only a couple can actually exist due to the lasing power curve. The frequencies of light produced all have a transverse electromagnetic mode that has constant phase across its cross section and a circular Gaussian intensity distribution. The frequencies correspond to longitudinal modes that match the boundary conditions of the laser tube. These boundary conditions require that the field displacement be zero at the tube ends. This condition is met by modes with integer multiples of half wavelength.

The laser tube used in the Ometron VPI system is a Uniphase HeNe laser tube, Model 1122P. It is a Class II, 2 mW laser which produces a polarized laser beam. The laser beam contains several longitudinal modes, with frequency spacing of 730 MHz which gives the laser beam a

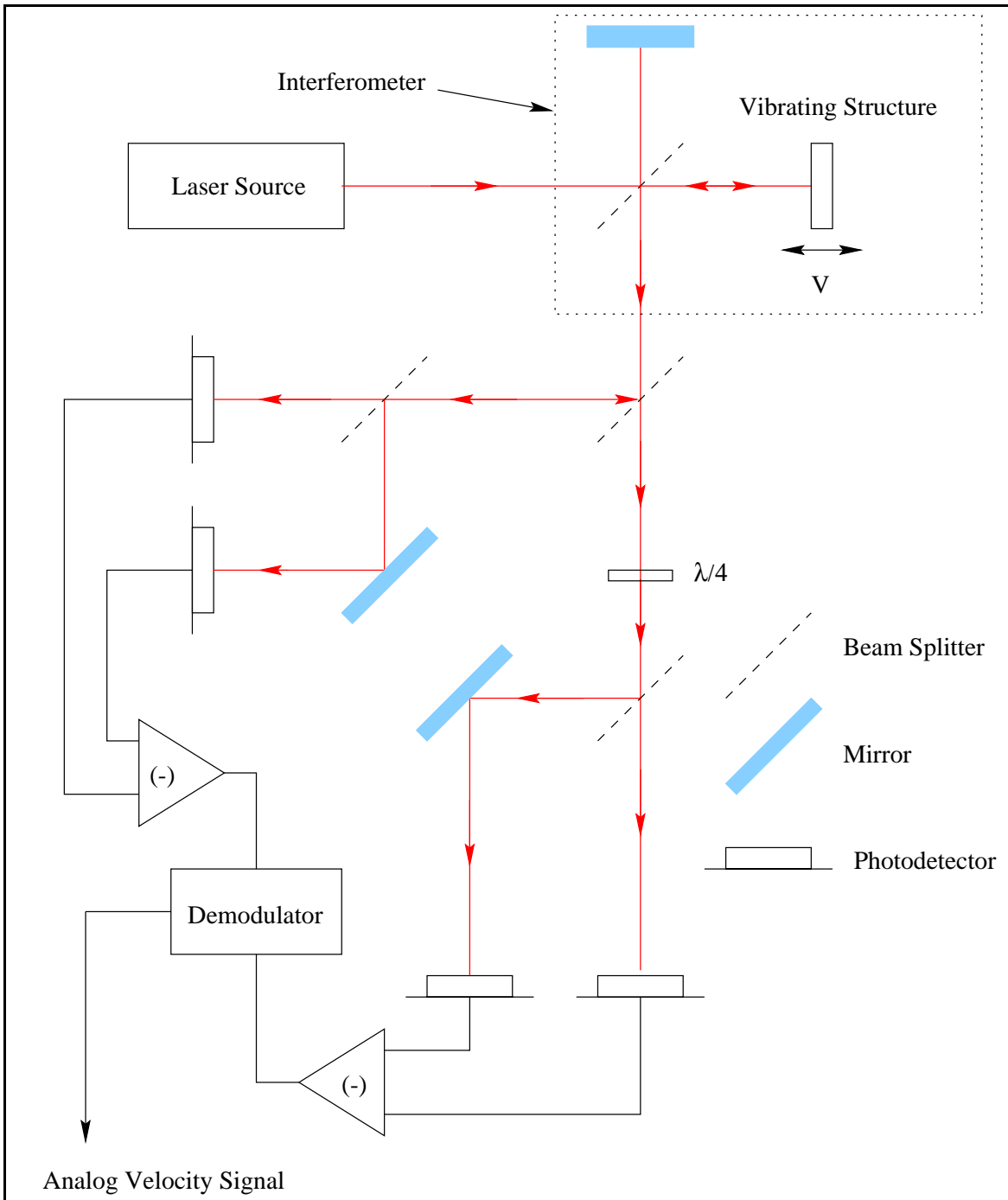


Figure 3.18: Schematic of Laser Vibrometer

coherence length of approximately 0.41 m. The beam leaves the laser tube with a diameter of approximately 0.63 mm.

Drawing from the work of both Drain and Rothberg, an approach which will prove useful in later analysis, the electromagnetic field of the laser beam is described as

$$E(t) = E\cos(\omega t + \phi) \quad (3.8)$$

With the laser beam defined it is now possible to trace its path from the vibrometer to the vibrating structure and back through the interferometer.

3.3.2 Interferometer

The main purpose of the interferometer is to mix the reference and measurement beams. The mixing of the two beams shifts the modulating frequency, which is proportional to the velocity at the measurement point, down to baseband where it can be detected. Recall that the carrier frequency, which is the frequency of the laser light, is $4.7 \times 10^{14} Hz$ and the frequency shift is equal to $\frac{3k Hz}{1 \frac{mm}{s}}$. This coincides to a frequency shift of 1 part in 150 billion for every $1 \frac{mm}{s}$ of structure velocity. By mixing the measurement beam with the reference beam, a signal is created at baseband that contains the modulating signal, a range at which the frequency shift can be more easily sensed.

Once the laser beam leaves the laser tube, it is split by a beam splitter into a reference beam

$$E_R(t) = E_R\cos(2\pi ft + \phi) \quad (3.9)$$

and a measurement beam

$$E_M(t) = E_M\cos(2\pi ft + \phi) \quad (3.10)$$

each with nominally equal amplitudes.

The beam splitter allows light with s-polarization to be passed and light with p-polarization to be reflected. Therefore the measurement beam will have s-polarization and the reference beam will have p-polarization. These two polarization directions are orthogonal and therefore do not interfere. Following the beam splitter, the measurement beam passes through a lens which expands the beam. Two factors motivate this beam expansion.

The first is the requirement for a sufficient amount of light from the measurement beam to be incident on the photodetector. The returning beam, retroreflected from the structure has a divergence angle that produces a cone of light. The amount of light that is incident on the photodetector is equal to the amount of light collected at the lens. Therefore, the lens must capture light over a large diameter spot to focus sufficient light on the photodetector. A second consequence of expanding the beam, not required, but beneficial, is the effect on beam diameter at the lens and the focused spot size. The laser beam, cannot be focused to a point due to diffraction effects. The smallest focus diameter that can be attained is called the waist which has a radius

$$r_0 = \frac{F\lambda}{\pi R_0} \quad (3.11)$$

where r is the focused spot radius, F is the focal length of the lens, λ is the wavelength, and R is the radius of the beam as it enters the lens. This relationship shows that to minimize the spot radius at the measurement point, the spot radius at the lens must be maximized. Therefore before the laser beam, which exits the laser source with a diameter of approximately 0.63 mm, is passed through the focusing lens it is expanded to a diameter of approximately 20 mm. This allows the laser beam to be focused to a diameter of approximately 2 mm at the measurement point.

The primary reason for the beam expander is to collect sufficient light on the return beam. For engineering measurements, a small focused beam sized increases the spatial resolution of the vibrometer. This also motivates the level of pointing accuracy that should be strived

for. The typical rule of thumb is that the error due to inaccurate pointing of the laser beam is only significant if the distance from the desired measurement point is greater than one half the spot size.

The reference beam with p-polarization is first passed through a quarter wave plate which rotates the polarization direction by 45° . It is then reflected back through the quarter wave plate which rotates the polarization by an additional another 45° degrees, before returning to the beam splitter with s-polarization. The introduction of the quarter wave plate ensures that the reference beam will be passed through the beam splitter on its return path.

The measurement beam, with s-polarization is also passed through a quarter wave plate and then a focusing lens and directed towards the vibrating structure. The outgoing beam is retro-reflected from the vibrating surface.

The returned measurement beam, after interacting with the structure is reflected back through the lens and quarter wave plate with p-polarization. As a result of interaction with the moving structure, the returned measurement beam will have undergone a change in amplitude and frequency. For simplicity the amplitude change is assumed constant across the beam's cross section and the phase angle is assumed to remain constant across the beams cross section. These assumptions will be relaxed in subsequent analysis.

Assuming that the structure has constant velocity as implied by Drain, the structure's motion will shift the frequency as described in the previous section. The returned measurement beam, frequency modulated by the structure motion is described by

$$E_{M'}(t) = E_{M'} \cos(2\pi(f + \delta f)t + \phi) \quad (3.12)$$

where

$$\Delta f = \frac{2v}{\lambda} \quad (3.13)$$

If however the approach of Rothberg is adopted, the returned measurement beam will undergo a phase change, described as

$$E_{M''}(t) = E_{M'} \cos(2\pi ft + \phi - 2kd(t)) \quad (3.14)$$

where k is the wave number

$$k = \frac{2\pi}{\lambda} \quad (3.15)$$

In this case the phase shift is a function of the change in path length of the beam. Despite the different in appearance, these two forms can be shown to be mathematically equivalent, a result that proves useful in resolving the previously identified discrepancy between path length changes and velocity.

Rewriting the displacement as

$$d(t) = \int_0^t v(t) dt \quad (3.16)$$

if the velocity is assumed constant as done by Drain, this expression reduces to

$$d(t) = v \cdot t \quad (3.17)$$

Substituting into Equation 3.3.2, yields

$$E_{M''}(t) = E_{M'} \cos(2\pi ft + \phi - 2kv \cdot t) \quad (3.18)$$

Rearranging terms yields

$$E_{M''}(t) = E_{M'} \cos((2\pi f - 2kv \cdot)t + \phi) \quad (3.19)$$

Substituting for k

$$2kv = 2\frac{2\pi}{\lambda}v \quad (3.20)$$

and regrouping

$$2\frac{2\pi}{\lambda}v = 2\pi\frac{2v}{\lambda} \quad (3.21)$$

results in

$$2kv \cdot = 2\pi \Delta f \quad (3.22)$$

which when substituted back into Equation 3.3.2 yields

$$E_{M''}(t) = E_{M'} \cos(2\pi(f + \Delta f)t + \phi) \quad (3.23)$$

which is equal to the result presented by Drain. This shows that Drain's expression, based on constant velocity, is a specific case of Rothberg's general expression based on path length change. At this point the more general path length expression is used. This must be done with some care as will be discussed later.

At the beam splitter the reference and returned measurement beam are directed along a common path, but due to their orthogonal polarization, they do not mix. The reason for this is made clear if we consider the case where they do mix. In this case a mixed beam with the electromagnetic field caused by the addition of the two terms yields

$$E_{mixed} = E_R \cos(2\pi ft + \phi) + E_{M'} \cos(2\pi ft + \phi - 2kd(t)) \quad (3.24)$$

The intensity of this combined electric field, which is equal to the square of the field is

$$I_{mixed} = [E_R \cos(2\pi ft + \phi) + E_{M'} \cos(2\pi ft + \phi - 2kd(t))]^2 \quad (3.25)$$

Carrying out the square of these terms yields

$$\begin{aligned} I_{mixed} = & E_R^2 \cos^2[2\pi ft + \phi] + E_{M'}^2 \cos^2[2\pi ft + \phi - 2kd(t)] \\ & + 2E_R E_{M'} \cos[2\pi ft + \phi] \cos[2\pi ft + \phi - 2kd(t)] \end{aligned} \quad (3.26)$$

After applying suitable trigonometric identities the intensity of the beam is

$$\begin{aligned}
 I_{mixed} = & \frac{E_R^2}{2}[1 + \cos(2[2\pi ft + \phi])] + \frac{E_{M'}^2}{2}[1 + \cos(2[2\pi ft + \phi - 2kd(t)])] \\
 & + E_R E_{M'} \cos[2\pi ft + \phi + 2\pi ft + \phi - 2kd(t)] \\
 & + E_R E_{M'} \cos[2\pi ft + \phi - 2\pi ft - \phi + 2kd(t)]
 \end{aligned} \tag{3.27}$$

The terms at twice the laser beam frequency can be ignored since they are outside the bandwidth of the detectors. Neglecting these terms, the intensity can be rewritten as

$$I_{mixed} = \frac{E_R^2}{2} + \frac{E_{M'}^2}{2} + E_R E_{M'} \cos(2kd(t)) \tag{3.28}$$

This shows that the intensity consists of a DC term and a time varying term dependent on distance. If the distance is fixed, the intensity is also fixed. However if the distance is time varying, the intensity is also time varying. Thus time varying distance, or velocity, changes the intensity of the laser beam.

This presents the complication that positive and negative path length changes produce the same intensity change. Therefore with this arrangement it is not possible to discriminate direction of path length changes. This results in what is referred to in the literature as a directional ambiguity.

This ambiguity can be resolved through a technique called quadrature detection. Recall that in this discussion, the measurement beam was mixed with the reference beam. If instead of directly mixing with a single reference beam, as is done in the LDV, the measurement beam is mixed with two reference beams, one phase shifted 90° relative to the other the directional ambiguity can be resolved.

The resolution of this ambiguity can be illustrated by returning to the orthogonally polarized measurement and reference beams. If the two co-linear beams are split into two components a phase shift can be introduced on one of the reference beams by introducing a quarter wave plate in the optical path. This results in the following two signals, the first consisting of the reference beam and measurement beam

$$E_{mixed_C} = E_R \cos(2\pi ft + \phi) + E_{M'} \cos(2\pi ft + \phi - 2kd(t)) \quad (3.29)$$

and the second consisting of the reference beam shifted by 90° relative to the measurement beam

$$E_{mixed_S} = E_R \sin(2\pi ft + \phi) + E_{M'} \cos(2\pi ft + \phi - 2kd(t)) \quad (3.30)$$

Each of the two beams are now passed through a polarizing beam splitter which causes the orthogonally polarized reference and measurement beams to interfere resulting in the intensities

$$I_{mixed_C} = \frac{E_R^2}{2} + \frac{E_{M'}^2}{2} + E_R E_{M'} \cos(2kd(t)) \quad (3.31)$$

and

$$I_{mixed_S} = \frac{E_R^2}{2} + \frac{E_{M'}^2}{2} + E_R E_{M'} \sin(2kd(t)) \quad (3.32)$$

The intensities have the same DC levels, amplitudes and frequencies, but are phase shifted relative to each other by 90° . For positive path length changes I_{mixed_C} will lead I_{mixed_S} and

for negative path length changes I_{mixed_C} will lag I_{mixed_S} . Figure 3.19 shows the effects of constant positive and negative velocities on the mixed signals.

This effect can be used to resolve the directional ambiguity. At this point, the optical signals contain all the information needed to determine the amplitude and direction of the structure velocity. It is now possible to convert the two quadrature optical signals into electrical signals using a set of photodetectors. These electrical signals can then be processed to extract the structure velocity.

3.3.3 Photodetectors

With the optical processing completed, the optical signals are converted into electrical signals by two sets of photodetectors. Photodetectors are electro-optical transducers that convert light intensity into electrical signals. In the VPI vibrometer, semiconductor photodiodes sense the intensity fluctuations in the Doppler signals and convert these fluctuations to currents. One characteristic of the VPI vibrometer is the use of a balanced detector arrangement for each of the quadrature channels. The balanced detector uses two photodetectors for each of the quadrature channels with the outputs of each detector 180° out of phase. By taking the difference of the two detector outputs, the DC components are removed, and the amplitude of the harmonic components is increased. The output of each balanced detector block is a voltage proportional to the time varying intensity. These two signals, which are called the Doppler signals are

$$v_{Doppler_C}(t) = A\cos(2kd(t)) \tag{3.33}$$

$$v_{Doppler_S}(t) = A\sin(2kd(t))$$

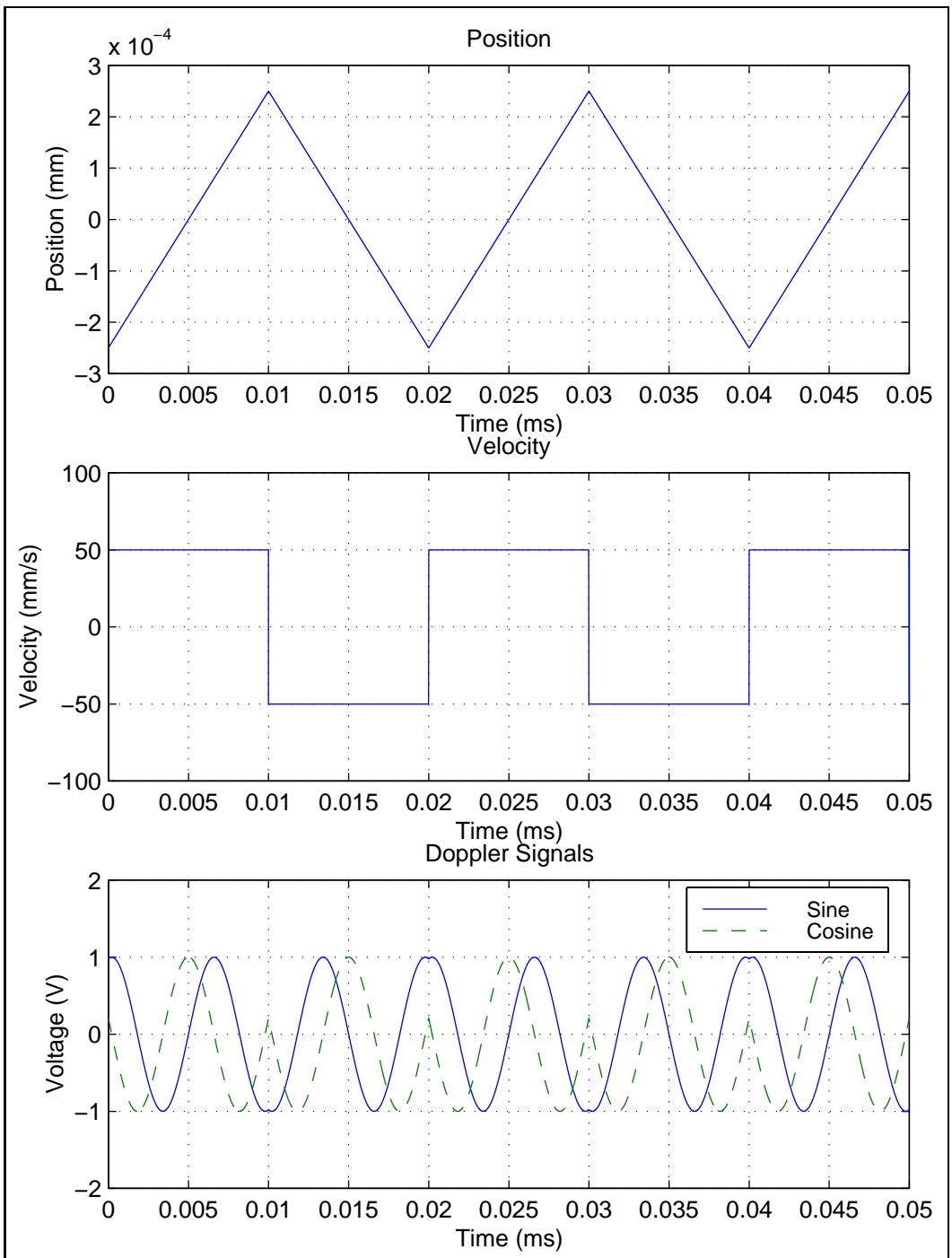


Figure 3.19: Velocity Direction Resolution

Table 3.4: Vibrometer Ranges and Frequency Shifts

Range	Frequency Shift
Low	50 kHz
Medium	500 kHz
High	5 MHz

where A is a constant accounting for the product of the field amplitudes, sensitivity of the photodetector, the conversion from photodetector current to voltage and any gain applied to the voltage signal.

The phase of the time varying signal is linearly related to the path length change. The phase is also time varying and can be related to a velocity with the velocity proportional to the instantaneous frequency of the signal. To extract the measured velocity signal, the Doppler signals must be frequency demodulated.

3.3.4 Demodulator

The demodulators operate on the quadrature Doppler signals to extract the measured velocity. The input signals to the demodulators are quadrature Doppler signals frequency shifted about a 0 Hz carrier signal. The first step in extracting the velocity signal is to frequency shift the Doppler signals up to a range more easily handled by frequency to voltage converters. The frequency shift is dependent on the measurement range as listed in Table 3.4.

This shift is applied to both quadrature signals resulting in a new carrier frequency equivalent to the shift frequency. The frequency shift is performed by multiplying the Doppler signals by a sinusoidal signal,

$$v_{shifted_C}(t) = A\cos(2kd(t)) \cdot \sin(2\pi f_{shift}t) \quad (3.34)$$

$$v_{shifted_S}(t) = A\sin(2kd(t)) \cdot \sin(2\pi f_{shift}t) \quad (3.35)$$

resulting in the two new Doppler signals

$$v_{shifted_C}(t) = A[\cos(2kd(t) - 2\pi f_{shift}t) + \cos(2kd(t) + 2\pi f_{shift}t)] \quad (3.36)$$

$$v_{shifted_S}(t) = A[\cos(2kd(t) - 2\pi f_{shift}t) - \cos(2kd(t) + 2\pi f_{shift}t)] \quad (3.37)$$

This multiplication shifts the Doppler signals from baseband up to a higher frequency where they can be more easily demodulated. The last step before the actual demodulation is performed is to subtract the two signals to create a single side band suppressed carrier

$$v_{shifted}(t) = 2A\cos(2\pi f_{shift}t + 2kd(t)) \quad (3.38)$$

This results in a signal with a carrier frequency equal to the shift frequency and a phase shift related to the structure velocity with the sign of the phase shift agreeing with the sign of the phase shift.

At this point it is useful to replace the displacement with the time integral of velocity. This is done for two reasons. First, it explicitly places the modulating signal, velocity, in the

output equation. Secondly, it eliminates path length changes as sources of velocity output. Replacing the displacement term with

$$d(t) = \int_0^t v(t) dt \quad (3.39)$$

yields

$$v_{shifted}(t) = 2A \cos(2\pi f_{shift} t + 2k \int_0^t v(t) dt) \quad (3.40)$$

which has the same form as the general relationship for frequency modulation of a signal as presented in Schwartz

$$f_c(t) = A \cos[\omega_c t + K \int f(t) dt] \quad (3.41)$$

In this signal $f(t)$ is the modulating signal which is equivalent to $v(t)$ in the expression for the vibrometer signal. This shows that velocity modulates the frequency of the carrier. The velocity is related to the instantaneous frequency of the signal. Therefore in order to extract the velocity information from the signal, the modulating frequency must be extracted.

A more general form of Equation 3.3.4 can be found by replacing the argument of the cosine term with the angle ϕ

$$f_c(t) = A \cos(\phi) \quad (3.42)$$

where for the vibrometer signal

$$\phi = 2\pi f_{shift}t + 2k \int_0^t v(t) dt \quad (3.43)$$

The instantaneous frequency is

$$\frac{d\phi}{dt} = 2\pi f_{shift} + 2kv(t) \quad (3.44)$$

This signal is next processed by a charge balanced frequency-to-voltage converter which extracts the velocity signal.

At this point it worthwhile to resolve the discrepancy between path length changes and velocity.

3.4 Path Length Changes Versus Velocity

Mathematically, velocity is equivalent to the time rate of change of distance. Because of this, it would be expected that path length changes would produce a velocity output. This is only true if the path length change is accompanied by a velocity as shown in previous discussions. Figure 3.20 illustrates the distinctions that must be made between velocity and path length changes in order to properly predict the vibrometers performance.

For each of the three cases depicted in Figure 3.20, a simple experiment was performed to shows the velocity output for each case.

While these results suggest that velocities and not path length changes are responsible for

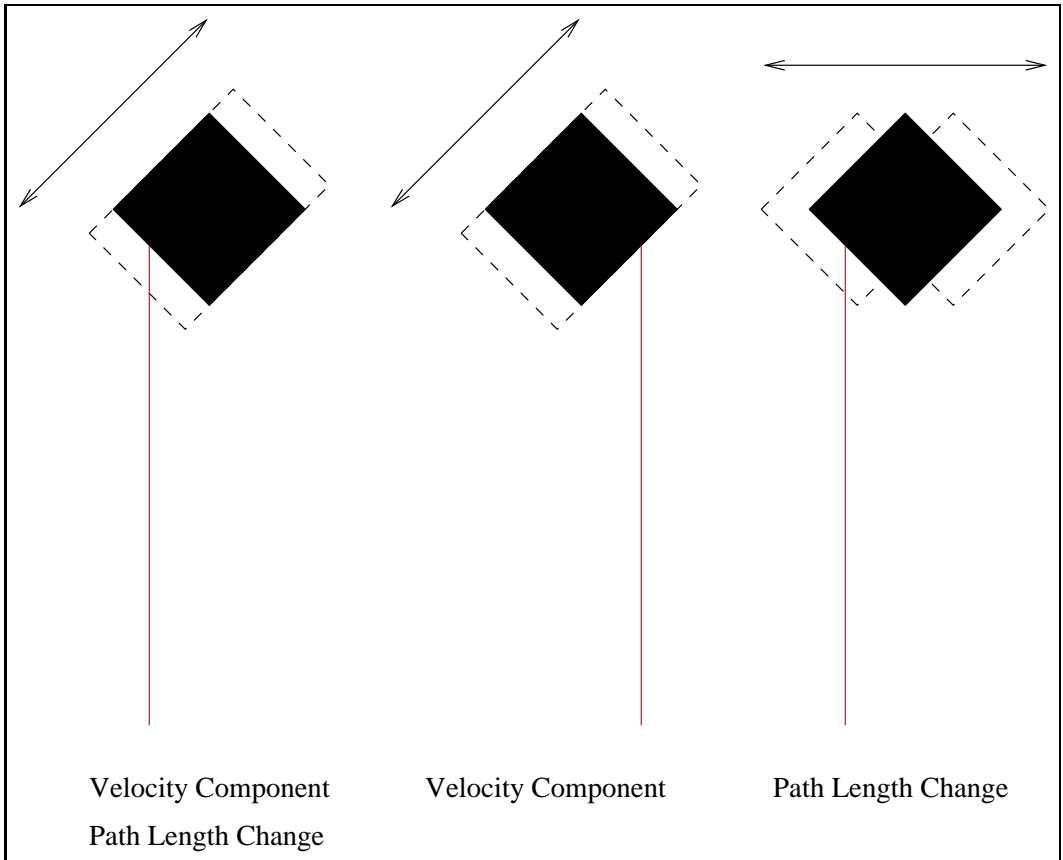


Figure 3.20: Velocity Versus Path Length Change, Macroscopic View

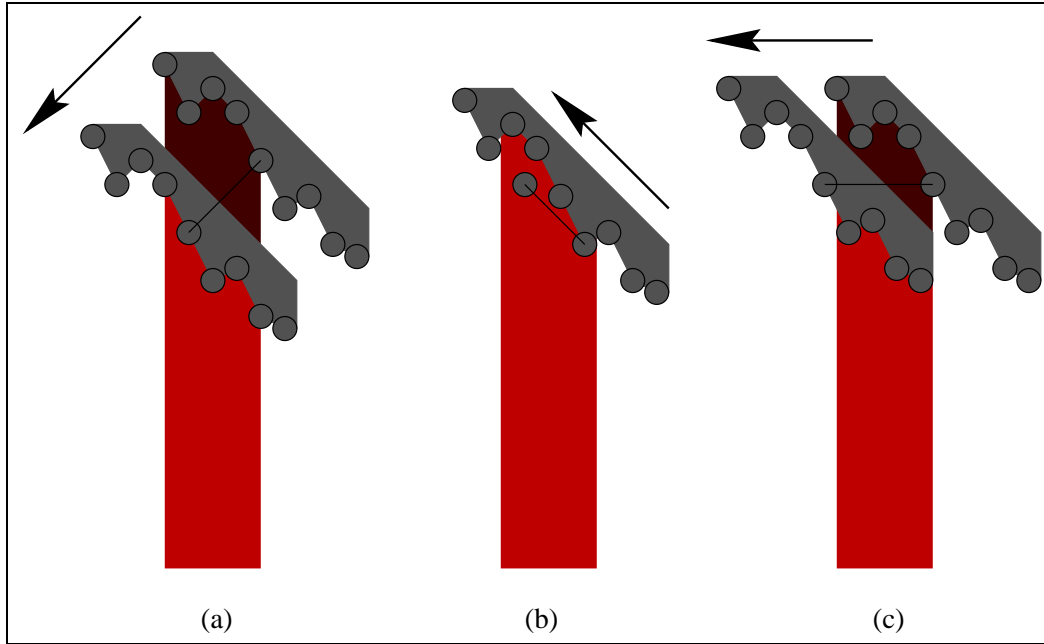


Figure 3.21: Velocity Versus Path Length Change, Microscopic View

producing velocity outputs from the vibrometer, a closer inspection of the physics show that indeed both velocities and path length changes cause velocity outputs if the concept of path length changes are correctly interpreted. To fully understand this distinction, the macroscopic view of the vibrating structure having a smooth surface must be replaced with the microscopic view of the structure having a rough surface.

Figure 3.21 shows an enlarged view of the laser beam-structure interface.

On the scale of the wavelength of the laser light (632 nm) the structure appears rough. Case (a) shows the structure moving towards the laser beam with a component of velocity in the laser beam direction. In this case there is clearly a velocity along the laser beam direction and a path length change to each of the points on the rough surface and the two concepts are equivalent. This coincides with the situation depicted in Figure 3.20 for the macroscopic view of the structure surface.

In case (b) where the structure velocity has velocity components both perpendicular and

parallel to the laser beam direction, the spots on the rough surface have a velocity along the laser beam direction. Additionally as the structure moves, some spots move out of the region illuminated by the laser beam and others move into the illuminated region. While in the illuminating region, the path length from the laser source to each spot is changing. Again there is a velocity along the laser beam direction and path length changes from single spots. This also coincides with the situation depicted in Figure 3.20.

Finally in case (c), the structure has a velocity that is perpendicular to the laser beam direction and no velocity components along the laser beam direction. The spots on the rough surface all move perpendicular to the laser beam and there is no path length change to a single spot on the structure. As the surface moves to the left, points on the structure that are further away from the laser are replaced by points that are closer to the structure, but *there is no path length change to a single point*. Whereas in the macroscopic view it appears that there are path length changes, the microscopic view shows that there are not. The differences being that whereas the macroscopic view treats the moving structure as a smooth surface, the microscopic view shows it as a rough surface with no path length changes.

These results explain the presence of an apparent path length change predicted by the macroscopic view that is not measured by the vibrometer. To accurately predict the velocity output of the vibrometer, the velocity of individual points must be considered. With this approach taken, either the point's velocity or path length can be used to predict the frequency shift. One advantage to adopting the path length point of view is that it can be used to explain another effect, speckle noise.

3.5 Speckle Noise

In the previous section the distinction between path length changes and velocities was made by looking at the microscopic structure of the structure's surface. In this viewpoint it was shown that velocity and path length changes are synonymous if the path length to a single particle is considered. This viewpoint is also useful in explaining laser speckle and speckle noise.

Laser speckle is a phenomenon caused by the the interference of laser light from an optically rough surface. When reflected from a rough surface, the light appears to reflect from a number of small surfaces which constitute the microscopic structure of the diffuse, scattering surface. These irregularities introduce spatially varying phase shifts across the laser beam profile due to the path length differences. The reflected light can be considered as individual sources with random phases and intensities. As the light from these sources combines at a single point on an imaging surface, individual components create a spot of light with a random intensity and phase. The effect of these superposed sources at a single point is illustrated in Figure 3.22 which is adapted from Dainty.

When this concept is extended over the entire area of the image surface, a set of points with random intensities and phases is created, resulting in a distinctive pattern generally referred to as a speckle pattern. Figure 3.23 shows a speckle pattern taken from Dainty.

In this figure the dark sections are locations on the imaging surface where the components interfere destructively. The bright sections are locations of constructive interference. The speckle pattern has randomly distributed intensity and phase. The intensity is exponentially distributed with probability distribution function

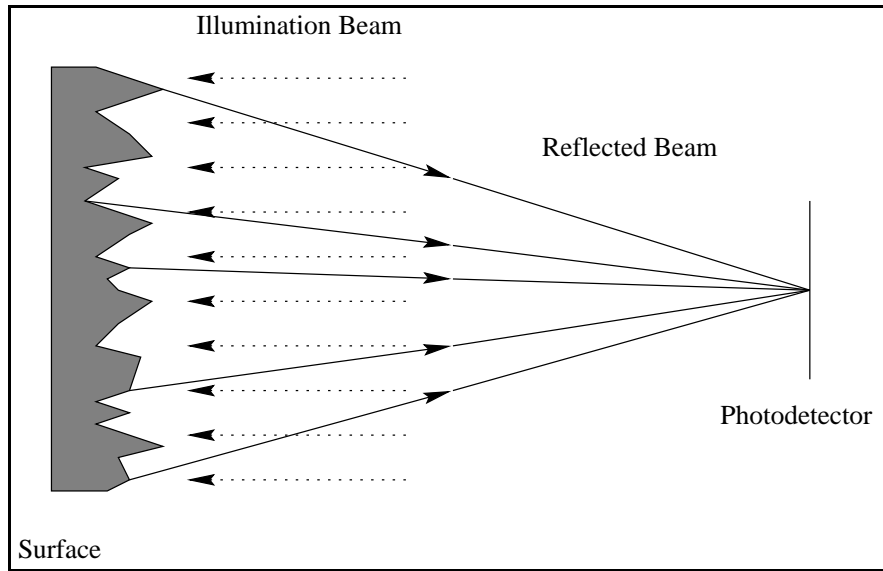


Figure 3.22: Speckle Pattern Formation (adapted from Dainty)

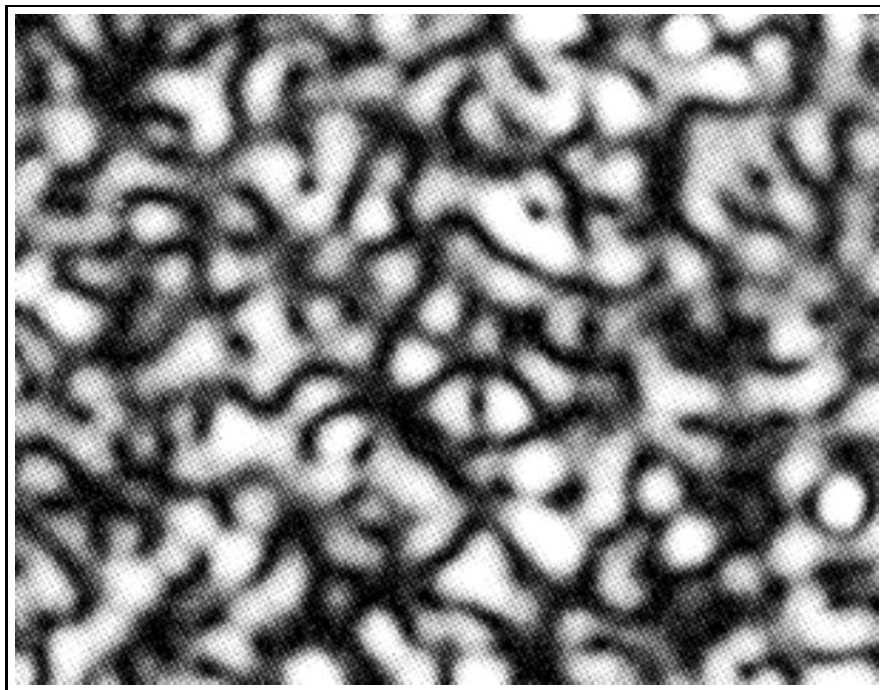


Figure 3.23: Speckle Pattern (taken from Dainty)

$$p_I(I) = \begin{cases} \frac{1}{2\sigma^2} e^{-\frac{I}{2\sigma^2}} & I \geq 0 \\ 0 & \textit{otherwise} \end{cases} \quad (3.45)$$

and the phase is uniformly distributed with probability distribution function

$$p_\phi(\phi) = \begin{cases} \frac{1}{2\pi} & -\pi \leq \phi \leq \pi \\ 0 & \textit{otherwise} \end{cases} \quad (3.46)$$

Although the intensity pattern created due to the constructive and destructive interference of the specular surface has a continuously varying spatial structure, it is common to refer to the pattern as consisting of individual speckles. The bright areas are typically referred to as speckles and considered as discrete entities.

Speckle alone does not cause significant problems in the vibrometer, as long as the integrated intensity over the area of the photo-detector is non-zero. However, speckle is a problem if the speckle pattern changes. This occurs when the spot on the structure reflecting the coherent laser light changes, producing a new speckle pattern on the photodetector and a new photodetector output. This causes time varying intensity and phase changes at the photodetector output which cannot be discriminated from phase changes resulting from structure motion. The vibrometer faithfully converts these phase shifts into velocity signals, when in fact there is no velocity. This erroneous velocity signal is commonly referred to as pseudo-vibrations or speckle noise. To better understand how a changing speckle pattern produces speckle noise, it is useful to revisit the discussion of the vibrometer's operation.

It was assumed in the previous discussion that the reflected measurement beam possessed constant phase and amplitude across its cross section. However due to laser speckle, this is not true. Accounting for the effect of laser speckle, the expression for the reflected beam must be modified, resulting in

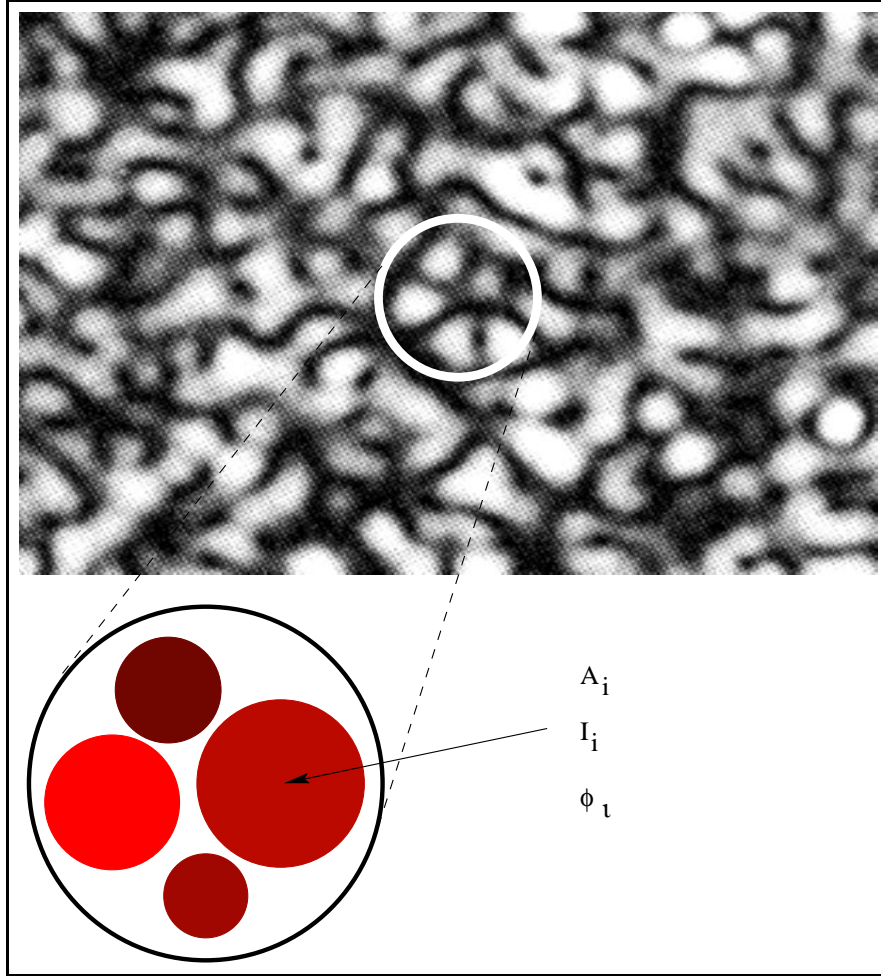


Figure 3.24: Discretization of Continuous Speckle Pattern

$$E_M(t) = E_M(x, y)\cos(2\pi ft + \phi - 2kd(t) + \phi(x, y)) \quad (3.47)$$

which shows spatially varying amplitude and phase across the retro-reflected beam.

When combined with the reference beam, the resulting intensity incident on the photodetector also varies in intensity and phase across the detector surface. Although this variation is continuous, it is modelled as discrete areas of constant phase and intensity as shown in Figure 3.24.

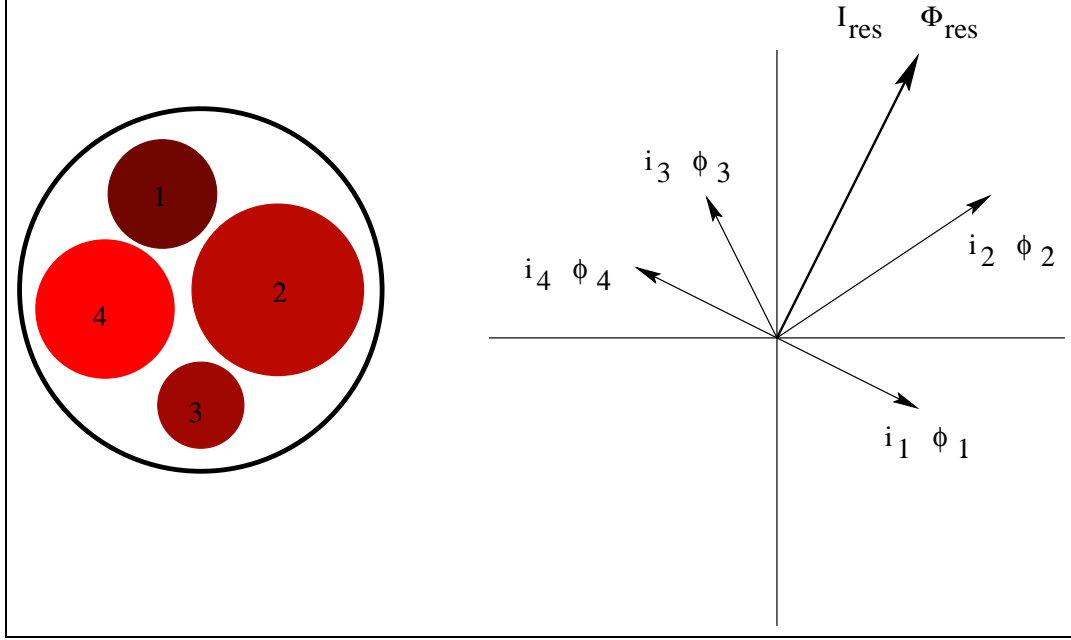


Figure 3.25: Vector Sum of Discrete Speckles

Taking this approach, the current output of the detector to this specular intensity pattern based on Rothberg is

$$i(t) = SI_{res} \cos(2kd(t) + \Phi_{res} + 2\pi ft) \quad (3.48)$$

where S is the sensitivity of the detector. The intensity and phase angle of this signal is found by taking the vector sum of the individual speckle components. This is shown schematically in Figure 3.25.

By propagating this added term through the entire laser vibrometer as was done in the above section, the final frequency shift due to both structure motion and speckle noise is

$$\frac{d\phi}{dt} = 2\pi f_{shift} + 2kv(t) + \frac{d\Phi_{res}}{dt} \quad (3.49)$$

Thus to predict the velocity output due to changing speckle, the parameter $\frac{d\Phi_{res}}{dt}$ must be estimated. The procedure used to estimate this parameter is given below.

3.6 Speckle Noise Prediction

While there is a great deal of published literature on the problem of speckle noise in LDV systems, notably Rothberg et al. (1989), and Asakura, none of the available literature quantitatively predicts the level of speckle noise. While there are several approaches for performing this analysis with varying levels of detail and complexity, a rather simple approach which draws on the work of Rothberg is adopted here.

Since the speckle pattern is random, the exact effect of time varying speckle patterns on the velocity signal cannot be predicted. Rothberg has explored the characteristics of speckle noise, arriving at some qualitative results. His findings indicate that the speckle noise has spectral content at the rotational speed of the structure and harmonics of the rotational speed.

To make this analysis more tractable, several assumptions must be made. The first is related to the characteristics of the time varying nature of the speckle field. Speckle motion can be characterized as either translating or boiling. Translating speckles consists of a fixed speckle pattern that moves across an image plane as the laser spot moves across a diffuse surface. Boiling speckle consists of a time varying speckle pattern which does not move as a whole, but changes in place. While both phenomena are seen in any time varying speckle pattern, Rothberg's assumption that the speckle pattern motion due to movement of the laser beam over a diffuse surface is predominantly translational speckle will be used. Additionally rotation and tilt of the the diffuse surface will introduce time varying speckle. Again to make the analysis more tractable only translation between the laser spot and the diffuse surface will be considered. Under these constraints, the characteristics of speckle

noise under translation will be considered.

In the approach taken, the speckle noise is predicted by mathematically generating a set of speckles and observing the effect that changing these speckles has on the instantaneous phase angle.

Consider a rotating, diffuse disk illuminated at a fixed point in space by a laser beam as shown in Figure 3.26

If the laser is incident at the disk's center of rotation, the speckle pattern remains fixed, meaning the same discrete speckles are produced on the detector, with only the relative orientation of the pattern changing. Since the detector output is the vector sum of the individual speckles, the detector output does not change and there is no speckle noise.

If the laser spot is displaced from the rotation axis, the speckle pattern created on the detector changes with disk rotation. Thus the photodetector output changes. The rate of change of the speckle is based on the linear velocity of the disk at the laser spot. As seen in Figure 3.25, the total photo-detector output is equal to the vector sum of the individual speckles incident on the detector. While this explanation assumes that the laser beam remains fixed in space and the disk rotates, the analysis also applies if the laser beam moves around a fixed disk as shown in Figure 3.26.

Since the path of the laser on the disk is fixed, the random speckle pattern incident on the photodetector is repeated for each revolution of the disk. Thus the time varying intensity and phase angle are random during a single revolution, but repeated on every revolution. This is verified by observing the autocorrelation of the intensity signal.

A rotating target was illuminated by the vibromter and the photodetector output monitored. To confirm that the random intensity pattern is periodic, the autocorrelation of the intensity signal was computed. Figure 3.28 shows the corresponding autocorrelation of the scaled

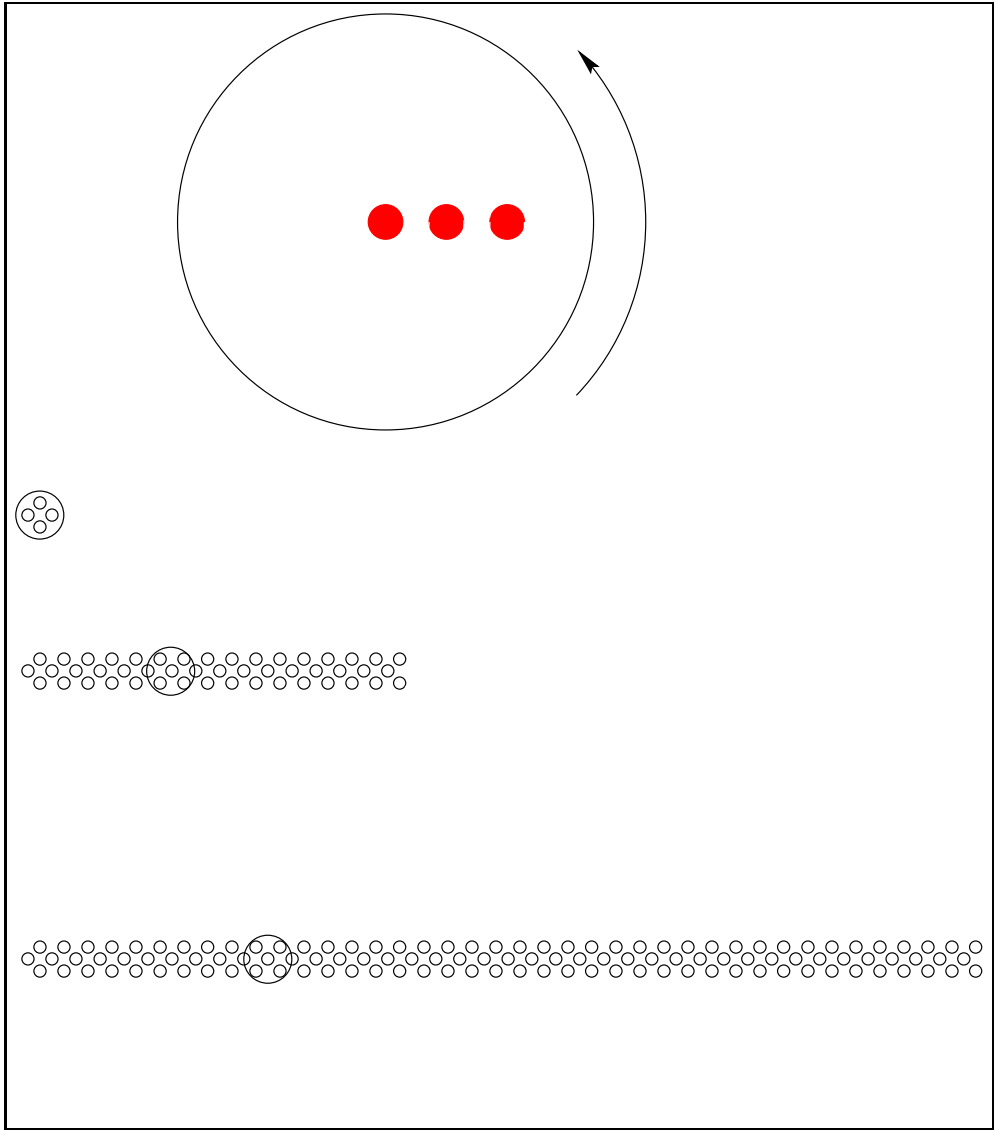


Figure 3.26: Speckle From Rotating Disk

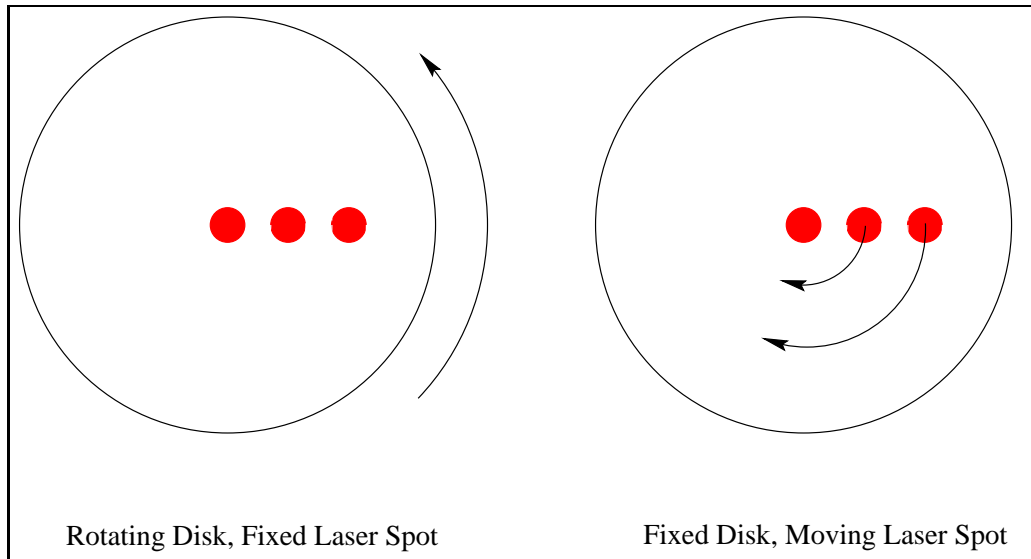


Figure 3.27: Fixed Disk With Moving Laser Spot

intensity for the structure rotating at approximately 23 Hz (1380 RPM).

The structure of the autocorrelation function shows that the intensity signal shows high levels of correlation at time shifts equal to integer multiples of the rotation period. Additionally for all other time shifts, the level of correlation is significantly lower. These results show that the intensity due to the time varying speckle pattern is random, yet repeats itself every revolution of the disk, as predicted above.

This result has an important implication in the use of the self-tracker. Although the speckle noise is random, the usual technique of taking multiple measurements and averaging the results to remove the random content is not applicable here. This is because the random speckle pattern does not change during subsequent revolutions of the structure. Therefore, if classical order analysis is performed, where the data collection is referenced to a once per rev signal, the speckle noise will not average to zero. This makes it difficult to experimentally verify the simulation results, but more importantly it precludes the use of averaging to remove the speckle noise from actual measurements.

Characterization of the speckle requires a relationship between the number of speckles on

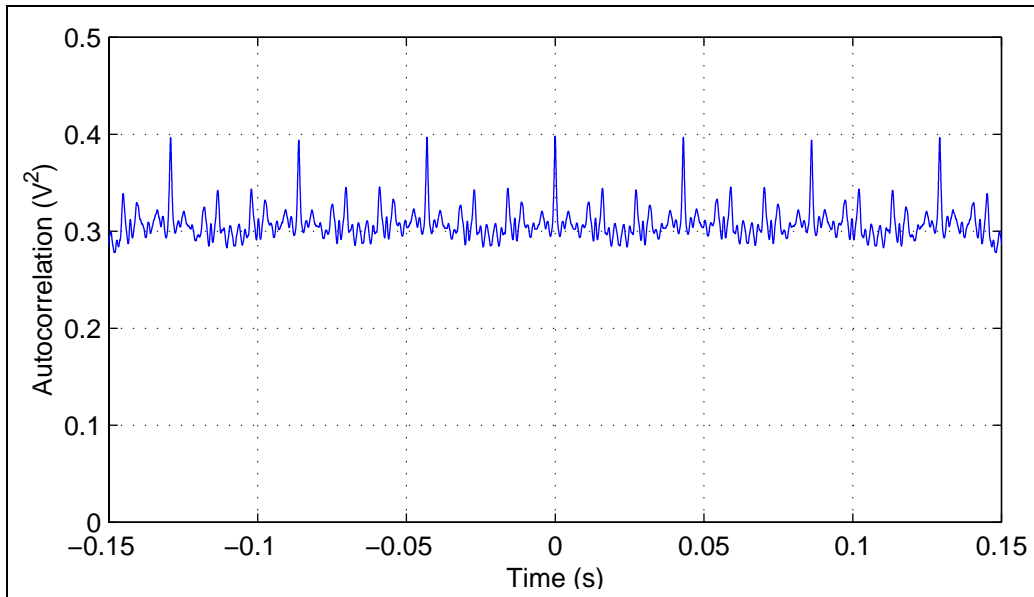


Figure 3.28: Autocorrelation of Intensity Signal

the detector, the rate at which the speckle pattern moves across the detector, and the actual spectral content of the produced speckle noise.

A mathematical simulation was performed to determine an expression for predicting the speckle noise based on the following parameters:

- Number of speckles created on the photo-detector surface
- Number of non-overlapping laser spots around laser path

First, the number of speckles incident on the detector was estimated based on the configuration of the vibrometer and rotating disk. Next the number of non-overlapping spots around the path of the laser beam on the disk was found. The product of these indicates the number of individual speckles encountered during one disk rotation. Next a set of random speckles was created, based on a uniform phase distribution and a negative exponential intensity distribution. Next the output of the photodetector was determined by summing the speckles incident on the detector as the speckle pattern moved across the detector. This results in a

set of complex valued variables. Since the speckle noise is only dependent on the phase angle of this complex variable, the angle was found.

$$\frac{d\Phi}{dt} = \frac{d\Phi}{d\theta} \frac{d\theta}{dt} \quad (3.50)$$

This approach was used since it provides a general relationship regardless of rotational speed. Next, the derivative

$$\frac{d\Phi}{d\theta} \quad (3.51)$$

was found by taking the difference between subsequent output values and dividing by the rotational displacement. This gives a signal which represents the variation of phase angle with rotation angle. After dividing by $2k$ to convert from frequency shift to velocity, a Fourier transform was performed on to identify the frequency content. This entire procedure was then repeated for a new, random set of speckles.

Once this procedure was applied to a sufficient number of the speckle sets, the mean frequency spectrum was found. The following figures shown the resulting speckle noise frequency spectra for varying path circumferences in terms of the number of laser spots around the circumference.

These results predict that as the circumference of the laser path increases, so does the level of the speckle noise. The level of noise due to speckle is relatively low. Even for high-speed rotational speeds (20,000 RPM) the level of speckle noise for significant amounts of position error is approximately 15 mm/s. While this precludes the use of the vibrometer's low range (0-10 mm/s) it provides a 40 dB signal to noise ratio on the vibrometers high range.

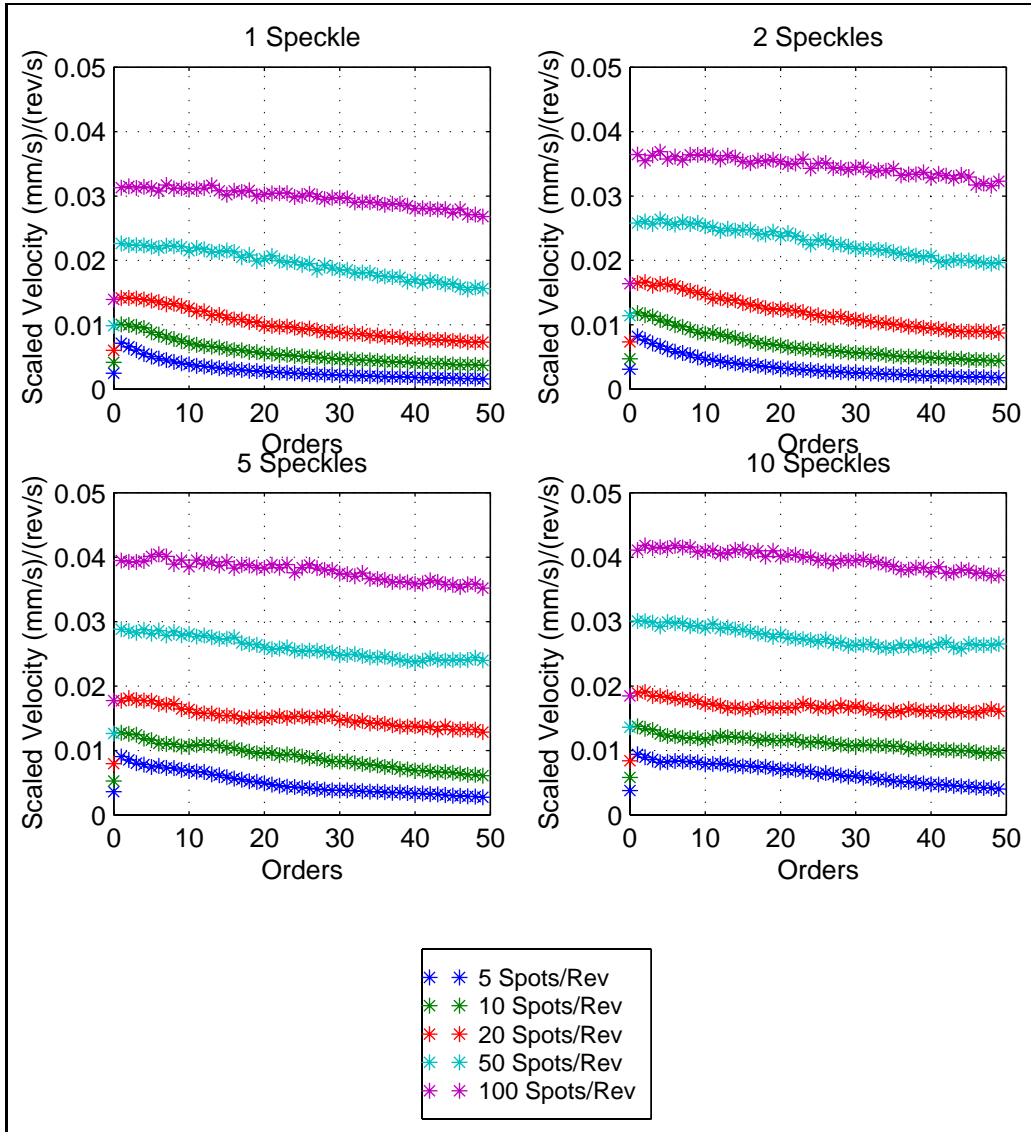


Figure 3.29: Simulated Effect of Laser Path on Speckle Noise Spectrum

Because the prediction of speckle noise was based on a simplified model, several experiments were performed to verify the results. The vibrometer was used to measure the velocity of a rotating disk. The laser beam was focused to the center of the disk and moved radially across the disk surface in 1mm increments. At each location the frequency spectrum of the vibrometer was recorded. The results, shown in Figure 3.30 show that increasing the rate of speckle pattern change does not significantly increase the level of speckle noise as predicted by the simulation results.

Based on these results, it was determined that a more rigorous model of speckle noise is required for accurately predicting the speckle noise in the self-tracker system. Since further development is beyond the scope of this work, the effects of speckle noise will be noted throughout the remaining study, yet no attempt will be made to quantitatively predict the amount of speckle noise present. Thus the only contributors to velocity noise that will be considered are those due to the rotation of the self-tracker's vertex mirror and the rotation of the bladed disk.

3.7 Summary

The operating principle of the laser vibrometer has been discussed to illustrate the phenomena which create a velocity signal at the vibrometer output. Three separate phenomena have been identified as causing vibrometer response:

- Diffuse surface velocity
- Reflective surface velocity
- Speckle pattern motion

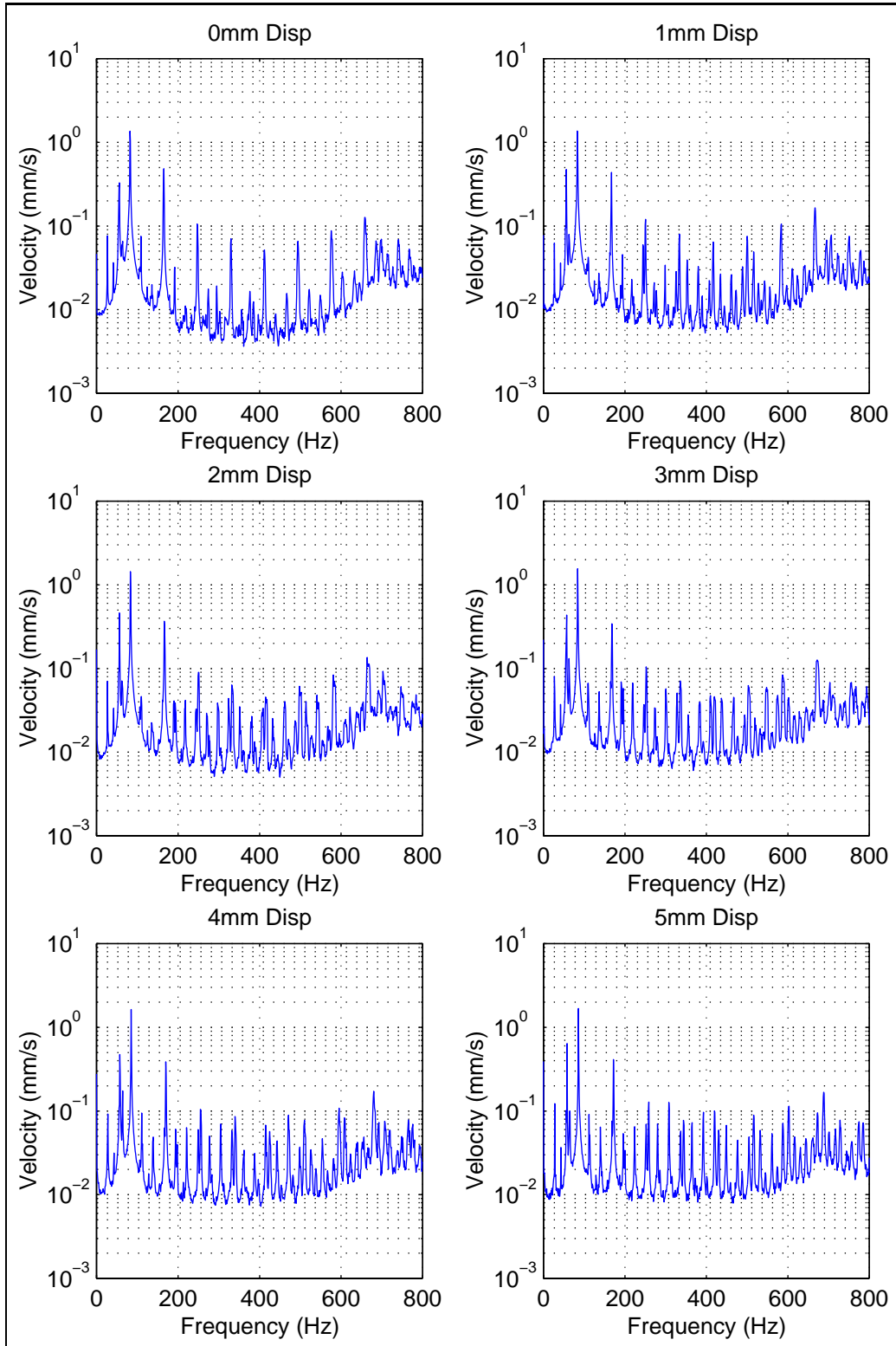


Figure 3.30: Actual Effect of Laser Path on Speckle Noise Spectrum

The effect of surface velocities can be quantitatively predicted based on the general expression for frequency shift due to a scattering particle. This general equation was simplified for each of the two cases of surface velocity. The effect of speckle pattern motion has been discussed and shown to be only qualitatively predictable due to the random nature of the speckle pattern variation. Therefore only the velocities due to the velocity of diffuse and reflective surfaces will be considered. With these contributors identified, it is now possible to examine the self-tracker and determine the extent to which each of these two phenomena impact the measured velocity.

Chapter 4

Component Models and Analysis Techniques

To characterize the performance of the self-tracker system, mathematical models of the system components must be developed. Two separate systems, the rotating structure and the self-tracker system, must be modeled.

A model of each component is developed to be used to predict the position and velocity errors. First, descriptions of the mathematical models of the rotating bladed disk and the self-tracker are given. These models are based on simplified representations of the physical components. Next the analysis procedures used to predict the position and velocity errors are given.

4.1 Bladed Disk Model

The bladed disk model represents the rotating structure being tested. To make the problem more tractable without losing generality, several simplifying assumptions are made about the bladed disk.

The primary purpose for modeling the bladed disk is to predict the rigid body velocity at the measurement point. Additionally, the velocity of the vertex mirror must be found as well as the location and orientation of the vertex mirror since this effects the tracking error.

The self-tracker requires the vertex mirror being fixed to the rotation axis of the bladed disk and that the line of sight to the vertex mirror is not obstructed. The ideal arrangement for these two conditions to be met is for the bladed disk to be fixed to the end of an overhung shaft. Therefore the bladed disk will be modeled as an overhung shaft.

Overhung shafts exhibit complicated motions due to rotating imbalances, centrifugal forces, and gyroscopic forces. In general the bladed disk may possess six degrees of motion, three translational and three rotational. Accounting for all combinations of these motions becomes extremely cumbersome. Therefore for this study, only rotation of the bladed disk about its rotation axis will be considered. Thus the disk motion can be fully characterized by the instantaneous rotation angle and rotational speed of the bladed disk. Under these assumptions the velocity of any point on the bladed disk can be found using simple rigid body relationships for rotational and linear velocity. This also constrains the vertex mirror to pure rotation about a point fixed in space, a conditions which greatly simplifies the subsequent self-tracker analysis.

With this simplified motion of the disk assumed, the actual blade vibration can be considered. The vibratory motion is assumed to be dominated by out of plane vibration, with the vibration perpendicular to the blade surface. This assumption can be supported by the

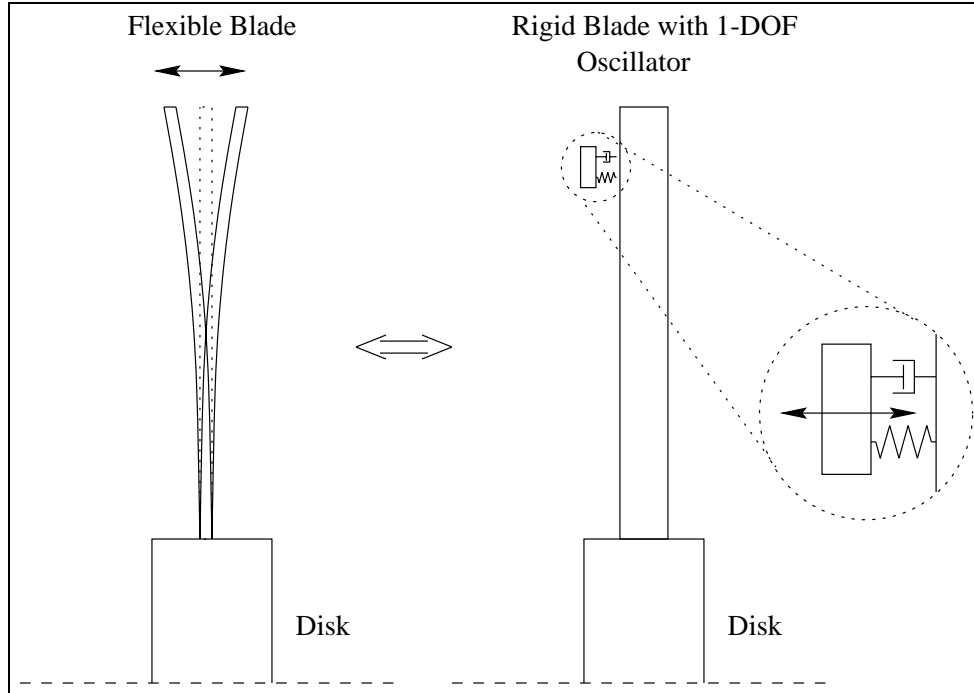


Figure 4.1: Simplified Model of Bladed Disk

fact that most blades have a relatively thin cross section, with the bending stiffness orders of magnitude lower in one direction than the other. It is also assumed that the desired vibration to be measured is the local blade vibration, not the rigid body motion of the entire bladed disk. Furthermore, the area in the region of the target point is assumed to be planar. In general the blade may have high curvature, but if the region is made small enough it can be assumed to be planar. With these assumptions the bladed disk can be modeled as shown in Figure 4.1.

It is also assumed that the vibration of the bladed disk does not contribute to the position error of the measurement point. This allows the measurement point to be found assuming the structure is not vibrating and the position analysis to be performed using a rigid model of the blade. Finally, since the goal of the velocity analysis is to predict the velocity error, which consists of all components other than the local oscillatory motion of the blade, in all models of the blade, the oscillatory motion is assumed to be zero. Therefore all measured velocities will consist of only the noise components.

4.2 Self-Tracker Model

The self-tracker system requires less assumptions for modeling than the bladed disk due to the simplicity of the self-trackers optical components. The self-tracker's components are modeled as simple geometric elements. The laser beam is modeled as a ray emanating from a fixed point in a fixed direction. The vertex and fold mirrors are modeled as planes with the vertex mirror experiencing pure rotation about a fixed axis and the fold mirror rigidly mounted to ground.

With the above assumptions, the measurement location can be found by solving for the intersection and reflection of the the ray from the planar surfaces. This reduces the problem to solving three sets of equations, each consisting of finding the intersection of a ray with a plane.

Once the measurement position has been found, the velocity can be determined. In the previous section three contributors to the vibrometer response were identified. The first, velocity of a diffuse surface, occurs at the interface between the measurement beam and the blade. The second, velocity of a reflective surface occurs at the vertex mirror. The last speckle noise, occurs at the blade surface. Thus to predict the contribution of each contributor, the velocity of the blade and vertex mirror must be found as well as the path of the measurement point on the blade. Once these parameters have been found, the total velocity error can be predicted.

With the above modeling approach, the position and velocity error can be found for any orientation of the structure and optical components. Although there are a multitude of possible orientations, only static misalignments will be studied based on the orientations most likely to be found in actual use. The first configuration is the ideal alignment case. In this case, the optical components and structure are aligned to eliminate tracking and velocity errors. The second set consists of three kinds of static misalignment. These consists

of static displacements and rotation of the structure from the ideal alignment cases. This is representative of improper set-up of the self-tracker system.

Having identified the LDV theory of operation and limitations, the development of the analytical models of the self-tracker will be presented. These models will be used to predict the contributors to tracking error and velocity error. Several models are developed, ranging from a general, three-dimensional model capable of describing the full system performance, to several two-dimensional models describing specific nuances of the system.

The general model developed for the self-tracker is based entirely in the realm of linear algebra, relying on the simple concepts of rays, planes, and coordinate transformations in three dimensions. This approach allows for a full description of the systems performance within a mathematically manageable framework. Other models which describe individual performance characteristics are based on two-dimensional geometric models to help develop a greater depth of understanding than is capable with the full three-dimensional models. Together, these models will form the basis for evaluating the effects of static misalignments of the self-tracker.

4.3 Analysis Procedure

With a general description of the bladed disk and the self-tracker given, it is now possible to describe the analysis procedure used to predict the position and velocity errors.

To evaluate the theoretical performance of the self-tracker system, a three dimensional model of the system is developed. The model predicts the position and velocity errors of the self-tracker in an ideal alignment configuration and in several misaligned configurations. Although the model is capable of handling any misalignment configuration, including misalignment of the fold mirror and the vibrometer, only misalignment of the rotating structure

relative to the combined fold mirror/vibrometer structure will be studied.

The general approach for predicting the system performance consists of two steps. First, a position analysis is performed with the primary purpose of identifying the location of the measurement point on the bladed disk. A secondary purpose of this analysis is to find the location and directions of several vectors that are used in the velocity analysis.

Once the position analysis is completed, the velocity analysis is performed. The velocity analysis examines the interaction of the laser beam with each surface it encounters along its path from the vibrometer to the measurement point. In the self-tracker there are two moving surfaces that influence the velocity signal, the rotating vertex mirror and the rotating and vibrating disk blade.

Though somewhat complicated, the analysis of the self-tracker system consists of several steps that are individually quite simple. The overall approach is to first locate the intersection points between the laser beam and the planar surfaces of the self-tracker. Once these points are found, the velocity of the surfaces at these points can be found. These two steps are referred to as the position and velocity analysis respectively. The detailed steps required to do this are listed below.

1. Define the location and orientation of the component coordinate frames
2. Calculate the origin and normal directions for the rays and planes
3. Solve the simultaneous linear equations for the intersection point and reflection directions
4. Solve for the measurement point location
5. Calculate the surface velocities at the vertex mirror and the blade surface
6. Calculate the velocity components parallel to laser beam direction

7. Calculate the rate of speckle pattern change

Two approaches can be taken to perform this analysis. For simple cases, closed form solutions can be found, resulting in an analytical expression that can be evaluated for any rotation angle. This approach is used to analyze the ideal alignment case. For more complex cases, such as the misaligned cases, the results can be evaluated for each step at a single rotational angle of the structure and used in the following step. To determine the results for a full rotation of the structure, the procedure is repeated for a new rotation angle. This gives results for discrete angular positions of the structure, but these are still exact solutions, within the computational precision of the computer.

4.3.1 Position Analysis

The purpose of the position analysis is to determine the location and directions of the segments of the laser beam path in the self-tracker system. The analysis is based on a three dimensional model of the system components. The laser beam is modeled by the algebraic equations for a ray in a three dimensional coordinate system. The planar components are modeled by the algebraic equations for planes in a three-dimensional coordinate system. Once the individual components have been modeled, the intersection points and direction vectors can be found by solving sets of algebraic equations. The solutions of these equations give the source and directions for the individual segments of the laser beam path as shown in Figure 4.2

Thus the first step in solving for these parameters is to define the equations that define rays representing the three laser beam segments.

The laser beam is represented mathematically by a ray. The equations for a ray originating from a source at (x_S, y_S, z_S) pointing in the direction defined by the unit vector (a_S, b_S, c_S)

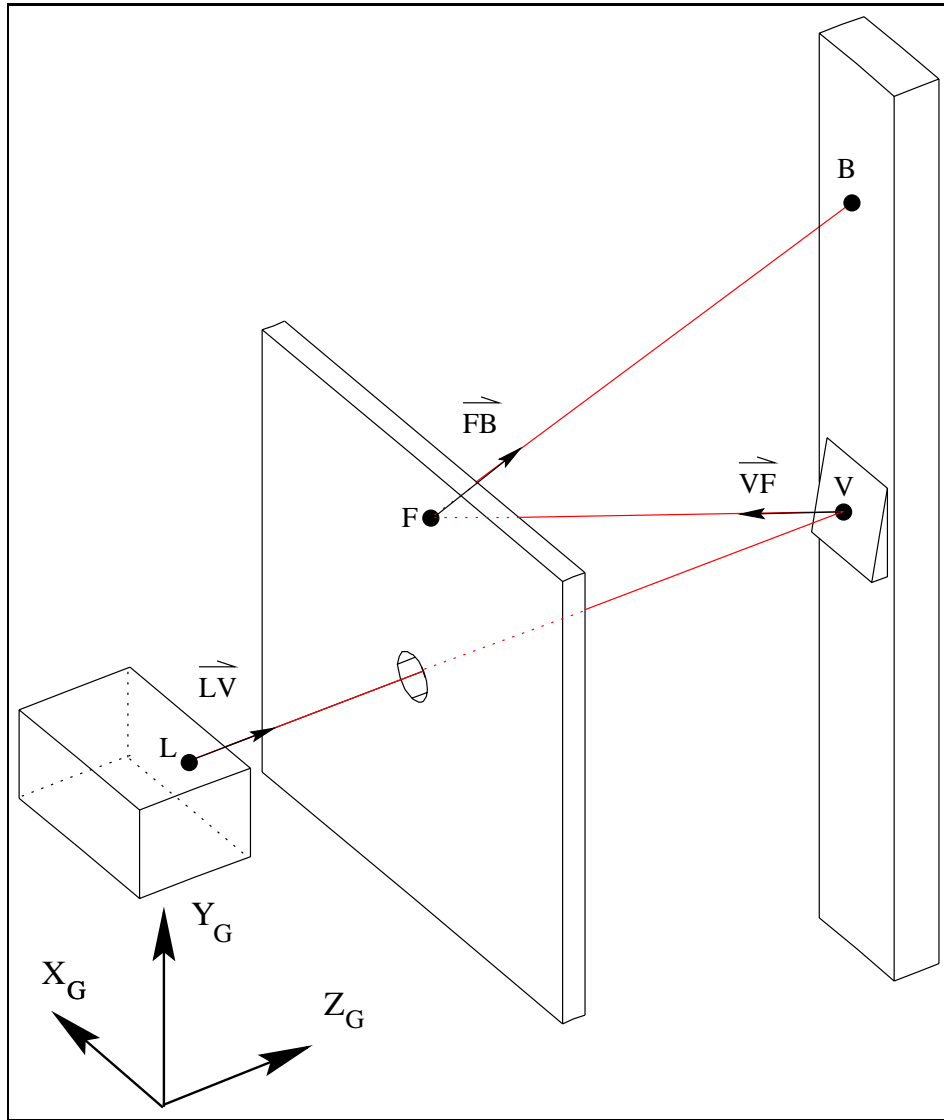


Figure 4.2: Origins and Directions of Laser Beam Segments

are

$$\begin{aligned}x &= a_S l + x_S \\y &= b_S l + y_S \\z &= c_S l + z_S\end{aligned}\tag{4.1}$$

where l is the length of the ray.

To find the intersection point between the incident rays and the planar surfaces, equations for the surfaces must be developed. The vertex mirror, fold mirror, and the blade are modeled as planes. Each surface is described in the global coordinate system by a point on the plane (x_i, y_i, z_i) and the unit vector normal to the plane (a_i, b_i, c_i) . The normal vector's directional ambiguity is resolved by always placing the origin of the normal on the side of the plane facing the incident laser beam.

Each plane can be described by the equation

$$a_i(x - x_i) + b_i(y - y_i) + c_i(z - z_i) = 0\tag{4.2}$$

To fully describe the self-tracker, a total of four position and direction vectors must be specified. One set of position and normal vectors is required for each of the two mirrors, one set is required for the blade, and a fourth set for the vibrometer.

With these definitions it is possible to determine the points of intersection between the laser beam and the surfaces as well as the direction of reflection from the mirrored surfaces.

First the intersection point between the laser beam and the planar surface is found by solving the set of equations

$$a_i(x - x_i) + a_i(y - y_i) + a_i(z - z_i) = 0\tag{4.3}$$

and

$$\begin{aligned}x &= a_i l + x_i \\y &= b_i l + y_i \\z &= c_i l + z_i\end{aligned}\tag{4.4}$$

A general solution for the intersection point between the ray can be found by first solving the equations for l and then substituting this value into the equations for the ray. If the equations are rewritten for convenience as

$$\begin{aligned}x &= A + D \times l \\y &= B + E \times l \\z &= C + F \times l\end{aligned}\tag{4.5}$$

and

$$J(x - G) + K(y - H) + L(z - I) = 0\tag{4.6}$$

a closed form solution for l is

$$l = \frac{J(G - A) + K(H - B) + L(I - C)}{JD + KE + LF}\tag{4.7}$$

which can then be substituted into 4.5 find the intersection point on the plane.

The solution gives the intersection of the incoming ray with the plane, a point which also serves as the source for the outgoing ray reflected from the mirror. The direction for the outgoing ray can be determined by applying the rules of reflection from a planar mirror. The angle between the reflected ray and the mirror normal is equal to the angle between the incident ray and the mirror normal. Furthermore, the incident ray, reflected ray, and mirror normal lie in a single plane.

This can easily be seen in the following two dimensional example.

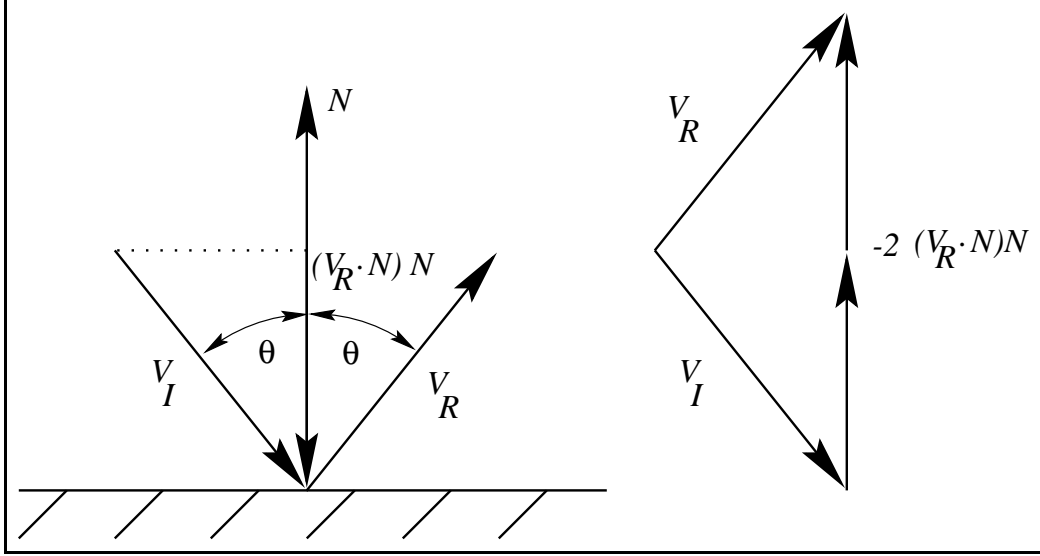


Figure 4.3: Reflection From Plane Mirror

From this a general vector expression for the direction of the reflected ray can be found to be

$$\vec{V}_R = \vec{V}_I - 2(\vec{V}_I \cdot \vec{n})\vec{n} \quad (4.8)$$

Using the definitions in 4.5 and 4.6 the reflection direction is

$$\begin{bmatrix} D \\ E \\ F \end{bmatrix} - 2(JD + KE + LF) \begin{bmatrix} J \\ K \\ L \end{bmatrix} \quad (4.9)$$

With the source of the outgoing ray and its direction known, the procedure is repeated to find the intersection with the next plane. This procedure can then be used to find the intersection of the ray with the structure.

Although it is possible to find a closed form solution for the intersection point of the laser with the bladed disk for arbitrary locations and orientations of the individual components, the difficulty of the process and the complexity of the results motivates a solution based on

evaluation of the intermediate results. However for special cases of component locations and orientations, closed form solutions will be found. It needs to be noted that although closed form solutions will not generally be found, these solutions are exact in that they are based on evaluation of the individual relationships. There is no approximation performed at any step of the analysis.

Before this method can be used, the mirror locations and surface normal must be known. These are easily found for the laser source and the fold mirror since these are assumed to be fixed and static. However, the locations and normal directions of the vertex mirror and structure are time varying due to rotation of the structure. The major task now becomes determining the locations and normals defining the vertex mirror plane and the blade plane.

4.3.2 Determining Location and Orientation of Planes

To determine the location and orientation of the moving planes, a series of coordinate systems will be specified. The relationships between the coordinate systems can be defined using fixed angle rotation matrices, a well developed technique used in kinematic analysis of rigid body structure. Once defined, these frames can be used to define coordinate transformation matrices that relate vectors in one frame to vectors in another frame.

These coordinate transformations serve several purposes. First, they will be used to define the locations and directions of the structure and vertex mirror in the global frame. Secondly, they will be used to define the structure's velocity in the global frame. Thirdly, they will be used to transform the measurement point on the structure into the global frame and the intersection of the laser beam with the structure into the structure frame in order to find the tracking error and velocity error. The field of kinematics provides a structured system for defining coordinate systems and transforming points between different coordinate systems. A detailed discussion of the various methods for defining coordinate systems and performing

transformations can be found in most kinematics texts. A brief discussions of the method applied to the self-tracker, based on the presentation given in Craig (1989), is given in the next section.

4.3.3 Coordinate Frame Transformations

In general, the location and orientation of one coordinate frame relative to another can be described by a 4-by-4 transformation matrix. This is illustrated in Figure 4.4.

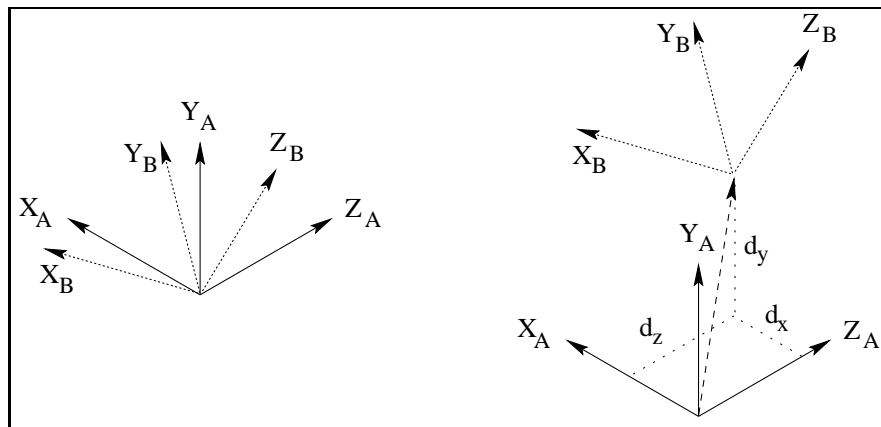


Figure 4.4: Fixed Angle Transformations

Coordinate frame $\{B\}$ is rotated and translated relative to coordinate frame $\{A\}$. First $\{A\}$ is rotated using the fixed angle convention. With fixed angle conventions, the $\{B\}$ frame is rotated about the X_A , Y_A , and Z_A axes of the $\{A\}$ coordinate system. The rotations must be performed in the following order:

1. Rotation of $\{B\}$ about X_A by γ
2. Rotation of $\{B\}$ about Y_A by β
3. Rotation of $\{B\}$ about Z_A by α

Next the rotated {B} system is translated relative to {A} along X_A , Y_A , and Z_A by the distances d_x , d_y , and d_z respectively. Adopting the convention of replacing \cos with c and \sin with s , the transformation matrix relating a point in {B} to a point in {A} is

$${}^A_B T = \begin{bmatrix} cac\beta & cas\beta s\gamma - sac\gamma & cas\beta c\gamma + sas\gamma & d_x \\ sac\beta & sas\beta s\gamma + cac\gamma & sas\beta c\gamma - cas\gamma & d_y \\ -s\beta & c\beta s\gamma & c\beta c\gamma & d_z \\ 0 & 0 & 0 & 1 \end{bmatrix} \quad (4.10)$$

This transformation allows a point or vector in one coordinate frame to be defined in terms of parameters of another coordinate frame. This approach will be used to transform the points and vectors representing the surface origins and normals into a common coordinate system. Before this can be done, coordinate frames must be attached to the laser source and the three surfaces. Next, the relationship between the coordinate frames must be determined. This will require the introduction of several intermediate coordinate frames. Transformations matrices can then be defined and used to defined the relevant parameters into a single coordinate frame.

Next a series of coordinate frame will be defined to develop the transformations to relate points and vectors in each frame to corresponding points and vectors in the global frame.

4.3.4 Definition of Coordinate Frames

Figure 4.5 shows the individual coordinate frames of the self-tracking, with the preferred relative location and orientation.

Each frame is described by the location of its origin and the fixed angle rotations as described above. Detailed descriptions of these frames and their relation to each other are given below.

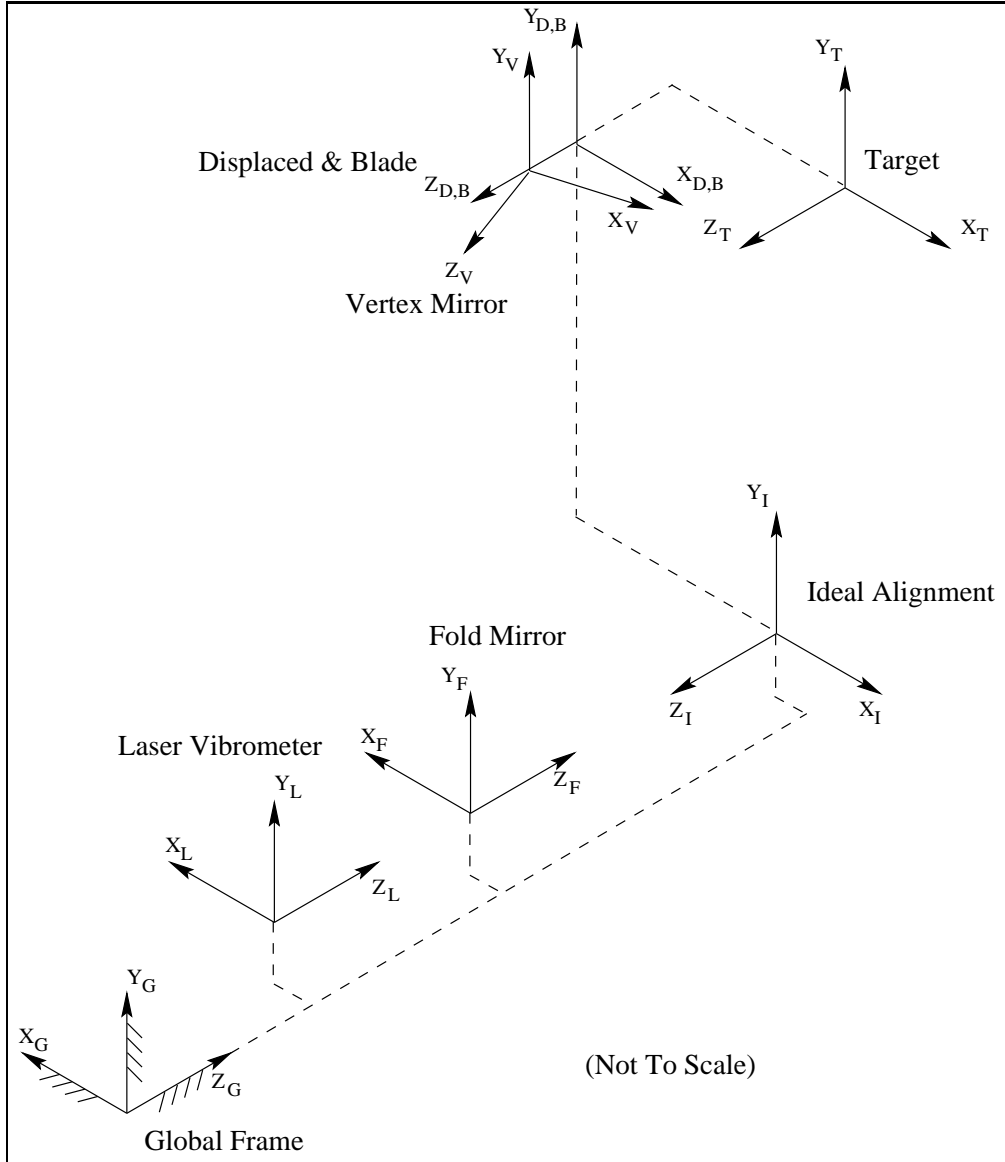


Figure 4.5: Preferred Locations and Orientations of Coordinate Frames

Global Frame

The global coordinate frame $\{G\}$ is fixed in space. All other frames and the laser source and fold mirror locations and directions are defined in this frame.

Laser Frame

The laser coordinate frame $\{L\}$ is attached to the laser vibrometer with the Z_L axis aligned with the laser beam and the $X_L - Y_L$ plane fixed to the front of the vibrometer. It is translated and rotated relative to the global frame $\{G\}$. The transformation from the laser frame $\{L\}$ to the global frame $\{G\}$ is ${}^G_L T$.

Fold Mirror Frame

The fold mirror coordinate frame $\{F\}$ is fixed in space. It is translated and rotated relative to the global frame $\{G\}$. The Z_F axis defines the surface normal on the reflecting surface, with the $X_F - Y_F$ plane fixed to the mirror reflecting surface. The transformation from the fold mirror frame $\{F\}$ to the global frame $\{G\}$ is ${}^G_F T$.

Ideal Alignment Frame

The ideal alignment frame $\{I\}$ is a hypothetical frame attached to the bladed disk that remains fixed in space. It is translated and rotated relative to the global frame $\{G\}$. It represents the home location of the structure when the rotating structure is perfectly aligned with the tracking system. The transformation from the ideal alignment frame $\{I\}$ to the global frame $\{G\}$ is ${}^G_I T$.

Displaced Frame

The displaced frame $\{D\}$ orients and locates the bladed disk's instantaneous rotation axis relative to the static frame accounting for any misalignment from the ideal alignment location and orientation. The Z_D axis is aligned with the rotation axis of the structure. The frame is translated and rotated relative to the ideal alignment frame $\{I\}$. This frame accounts for static and dynamic translation and rotation of the instantaneous axis of rotation. It is used to introduce the static and dynamic misalignments into the system to characterize the sensitivity of the system to misalignments. The transformation from the displaced frame $\{D\}$ to the ideal frame $\{I\}$ is ${}^I_D T$.

Bladed Disk Frame

The bladed disk frame $\{B\}$ is fixed to the structure. The Z_B axis is aligned with the bladed disk's axis of rotation, and rotates with the bladed disk. It is translated relative to the displaced frame $\{D\}$ a distance d_{z_B} along Z_D . The $\{B\}$ frame rotates about the Z_D axis. The X_D and Y_D axes are arbitrarily aligned with the bladed disk, with the preferred alignment being with the Z_B axis lying along the blade to measure. The transformation from the bladed disk frame $\{B\}$ to the displaced frame $\{D\}$ is ${}^D_B T$.

Target Point Frame

The target point frame $\{T\}$ is fixed to the desired measurement point on a blade. It is translated and rotated relative to the bladed disk frame $\{B\}$. The $X_T - Y_T$ plane is tangent to the structure at the measurement point. Although the blade is generally considered to be non-planar, the $\{T\}$ frame defines a planar region around the target point. The origin is attached to the target point with the Z_T axis normal to the blade surface. Since the preferred

orientation of the bladed disk frame $\{B\}$ aligns the Z_B axis along the radial line from the center of rotation to the target point, d_{Y_D} is typically equal to zero. The transformation from the target point frame $\{T\}$ to the bladed disk frame $\{B\}$ is ${}^B_T T$.

Vertex Mirror Frame

The vertex mirror frame $\{V\}$ is attached to the tilted vertex mirror. It is translated and rotated relative to the bladed disk frame $\{B\}$. The $X_V - Y_V$ plane coincides with the mirror reflecting surface and the Z_V axis coincides with the mirror normal. This axis Z_V maintains a fixed angle with respect to the Z_B axis of the structure frame. The vector direction of the Z_V , transformed in the global coordinate frame, determines the time varying vertex mirror normal required for the ray tracing analysis. The transformation from the vertex mirror frame $\{V\}$ to the bladed disk frame $\{B\}$ is ${}^B_V T$.

4.3.5 Definition of Transformations

In general, each transformation will take the form of Equation 4.10. In this case the transformation matrix will be unnecessarily complicated. The transformation can be simplified by recalling that the purpose for defining the transformations is to define the location and direction of the laser beam, and the location and surface normals of the fold mirror, vertex mirror, and bladed disk in the global coordinate frame. Also recall that the laser beam lies along the z-axis of the laser frame. Similarly the surface normals for the fold mirror, vertex mirror, and bladed disk all lie along the z-axis of their respective coordinate frames. It can be shown that the direction of the z-axis of each of these coordinate frames can be positioned in an arbitrary direction with only two rotations. This fact can be used to reduce the complexity of the coordinate transformations, a simplification which will be exploited later.

With these coordinate frames and transformation matrices defined, it is now possible to determine the origin and surface normal of the fold mirror, vertex mirror, and target plane in the global frame. This is done by first defining the transformation from the desired frame to the global frame. The complete transformations from $\{L\}$, $\{V\}$, $\{F\}$, and $\{T\}$ to the global frame $\{G\}$ are,

$$\begin{aligned}
{}^G_L T &= {}^G_L T \\
{}^G_F T &= {}^G_F T \\
{}^G_B T &= {}^G_I T {}^I_D T {}^D_B T \\
{}^G_V T &= {}^G_I T {}^I_D T {}^D_B T {}^B_V T \\
{}^G_T T &= {}^G_I T {}^I_D T {}^D_B T {}^B_T T
\end{aligned} \tag{4.11}$$

These transformation transform a point from the laser, fold mirror, bladed disk, vertex mirror, and target frames into the global frame. The inverse transformation which take points in the global frame and transform them into the other frames are easily found by inverting these transformations. For instance, the transformation for taking a point in the global frame and transforming it into the target point frame can be found by inverting the transformation from target point frame to the global frame

$${}^T_G T = {}^G_T T^{-1} \tag{4.12}$$

The origin and normal direction of each frame can now be transformed into the global frame. The origins are transformed into the global frame by applying the transformation to the location vector

$$\begin{bmatrix} 0 \\ 0 \\ 0 \\ 1 \end{bmatrix} \quad (4.13)$$

Recalling that the normal directions of each plane is aligned with the z-axis of that frame, the normal directions of each plane can be transformed into the global frame by applying the transformation to the direction vector

$$\begin{bmatrix} 0 \\ 0 \\ 1 \\ 0 \end{bmatrix} \quad (4.14)$$

It is now possible, by solving equations 4.5 and 4.6 for each segment of the laser beam, from laser to vertex mirror, vertex mirror to fold mirror, and fold mirror to blade, to find the location of the measurement beam on the target plane.

Once the location of the measurement point is found, it can be compared to the target point location to define for the position error. The position error can be viewed from two viewpoints, either from the global frame or from the target frame. When viewed from the global frame, the position error will be superimposed on the rigid body motion of the rotating bladed disk. This viewpoint is most useful during system alignment. When viewed from the target frame viewpoint, the path traced out by the laser beam on the target plane can be easily seen. This viewpoint is most useful for identifying the error between the target and measurement points and also provides the information needed to predict the speckle noise in the velocity analysis. Once the position analysis is completed, the velocity analysis can be performed.

4.3.6 Velocity Analysis

The velocity analysis is somewhat complicated by the fact that there several phenomena which cause variations in the intensity signals that are sensed by the photodetectors. These phenomena, discussed in detail in Chapter 3 are

- Velocity of a diffuse surface
- Velocity of a reflective surface
- Speckle change from a diffuse surface

In the self-tracker there are four instances where these phenomena occur

- Vibratory motion of the blade
- Rigid body motion of the blade
- Rotational motion of the vertex mirror
- Translational variation of the speckle pattern

represented as $v_{vb}(t)$, $v_{rb}(t)$, $v_m(t)$, and $v_s(t)$ respectively. The total sensed velocity will be equal to the vector sum of theses individual components. To predict each of these velocity components, several parameters must be computed as part of the position analysis.

The first two contributors to velocity are the ones most normally associated with the vibrometer, velocity along the laser beam direction. In the self-tracker there are two mechanisms that cause velocities along the laser beam direction. The velocity componenet along the laser beam direction is found by first identifying the velocity at the measurement point due to the rigid body rotation of the structure and the local vibratory motion. The rigid body

component is equal to the cross product between the vectors describing the measurement point location and the structures rotation. The vibratory motion is the velocity of the planar region in the vicinity of the measurement point. The total velocity at the measurement point is equal to the vector sum of these components. The component along the laser beam direction is found by taking the dot product of the laser beam direction with the velocity vector. Since the actual vibratory motion of the blade is unknown, it is assumed to be zero. Since this is the velocity component of interest, all other velocity components are considered noise. Therefore, the results of the velocity analysis are the noise components of the velocity signal.

The third contributor to velocity requires a more simplified version of a more general relationship for the frequency shift from a scattering particle. Application of this relationship requires that the direction of the mirror normal, reflection angle, and mirror velocity be known.

The fourth contributor is also somewhat complicated because it is based on random fluctuations of the speckle pattern. Furthermore predicted values of speckle noise did not agree with the measured values. Despite the lack of verification of these results, the one parameter that effects speckle noise that can be predicted is the motion of the laser path. The position analysis provides this information as a series of discrete points. This can be used to determine the rate at which the speckle pattern changes and therefore the level of speckle noise.

To present the results of the velocity analysis, several parameters will be presented, all as functions of the rotation angle of the bladed disk. First, the velocity components due to the vertex mirror motion and rigid body velocity of the bladed disk along the laser direction will be shown. Next, the frequency spectrum of the speckle noise, based on the path of the laser beam on the target plane as predicted in the position analysis will be presented. Lastly the value of the dot product of the laser beam direction with the target plane normal vector

will be shown. The dot product is shown since it is the scaling factor that is applied to the actual oscillatory motion of the blade, a motion that is assumed to be zero in the velocity analysis.

4.4 Summary

A description of the modeling approach and analysis techniques for predicting the position and velocity errors for the self-tracker has been given. While this can be done for arbitrary locations and orientations of the laser, fold mirror, and vertex mirror, there are preferred orientations and locations that can be selected to better illustrate the contributors to tracking and velocity uncertainties. The application of these models and techniques for specific alignment configurations are described in the following chapters.

Chapter 5

Experimental Apparatus and Setup

The analytical models provide a means for determining the theoretical performance of the self-tracker system. To fully assess the system's capability, the models must be compared to the actual system performance. A series of experiments are performed to verify the model predictions. These experiments are centered around measuring the effects of static misalignments on tracking error and velocity errors.

To verify the self-tracker's predicted performance, a self-tracker and a sample structure were built and instrumented. A photograph of the test rig used to characterize the self-tracker is shown in Figure 5.1.

The test rig consists of two separate parts; the rotating structure and the traverse mounted fold mirror and vibrometer. Along with the above components, a shaft encoder, position sensitive photo-detector, and various data acquisition systems are used to collect the position and velocity data. The following sections give detailed descriptions of the hardware components as well as their set-up and use.

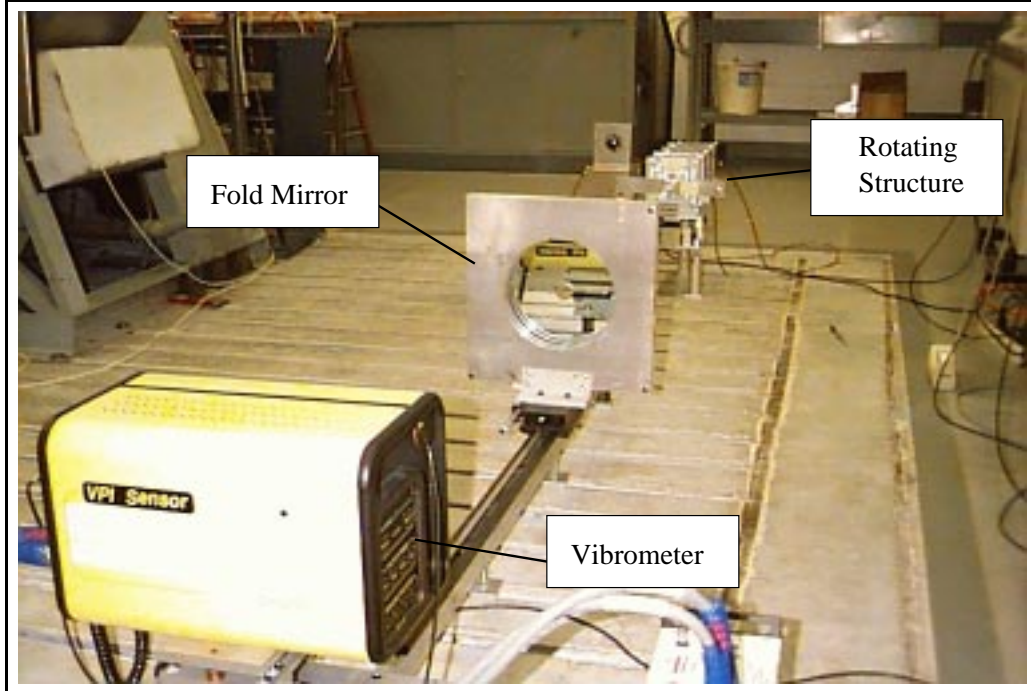


Figure 5.1: Self-Tracker Test Rig

5.1 Tracking System

The tracking system consists of two individual components; a vertex mirror mounted to the rotating structure, and a traverse system mounted to the isolation pad. The vertex mirror mount, shown in Figure 5.2 consists of two steel disks held together with three sets of screws and springs.

The vertex mirror is glued to the front mount plate and the shaft collar is attached to the rotating shaft with two set screws. Three springs are sandwiched between the mount plate and shaft collar. Three screws threaded into the shaft collar compress the springs between the two disks. This arrangement allows the mirror mount to be tilted relative to the shaft collar through differential adjustment of the three screws.

The traverse system, shown in Figure 5.3, consists of a 'T' shaped mounting bar to which the fold mirror and vibrometer are attached.

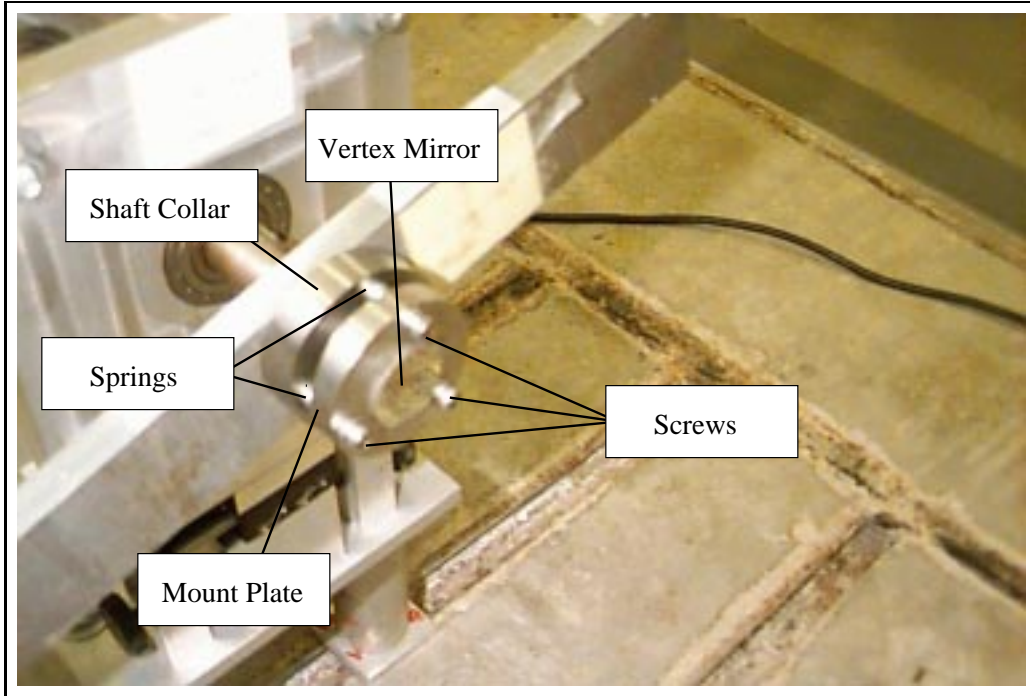


Figure 5.2: Vertex Mirror Mount

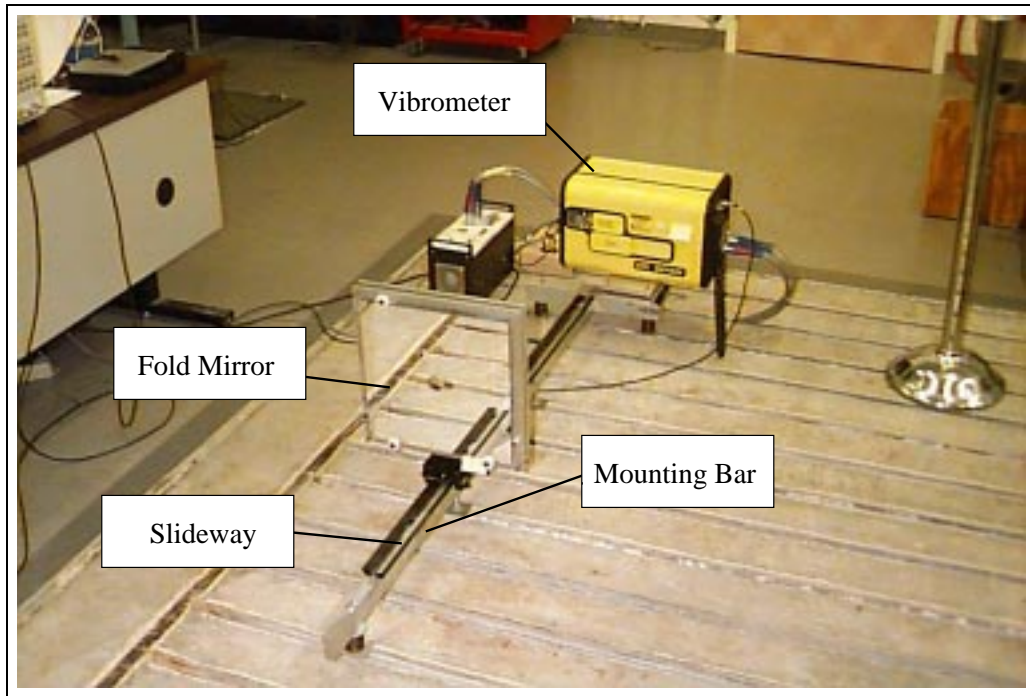


Figure 5.3: Self-Tracker Traverse System

The mounting bar is bolted to the isolation pad at three points. At each attachment point, a spring is placed between the mounting bar and isolation pad. As in the vertex mirror mount, this allows for adjustment of the mounting bar. This mounting bar serves as the base for the fold mirror and vibrometer.

The vibrometer is attached to the mounting bar by way of an adjustable platform. The platform, shown in Figure 5.4, allows for pitch, yaw, and horizontal adjustment of the vibrometer.

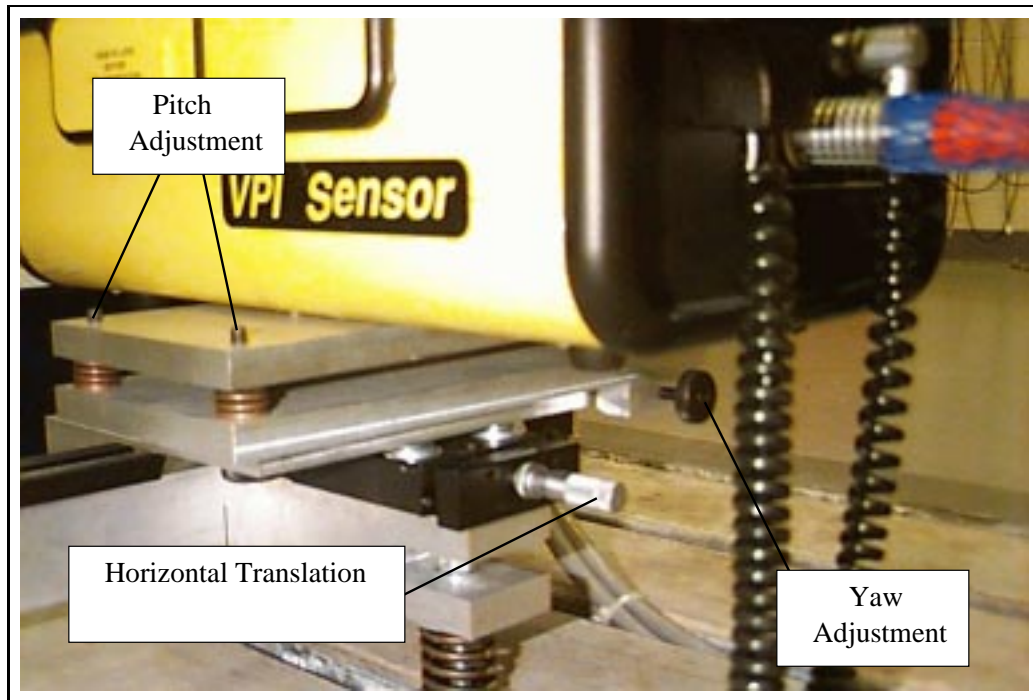


Figure 5.4: Vibrometer Adjustment Platform

The fold mirror, shown in Figure 5.5 is attached to plates in a similar arrangement as used on the vertex mirror.

This again allows for pitch and yaw adjustment. The adjustable plates are fixed to a dove-tail block which rides on a linear slideway attached to the mounting bar. The dove-tail block can be positioned along the slideway for coarse adjustment of the distance between the fold mirror and the rotating structure. A linear translational stage is positioned between the

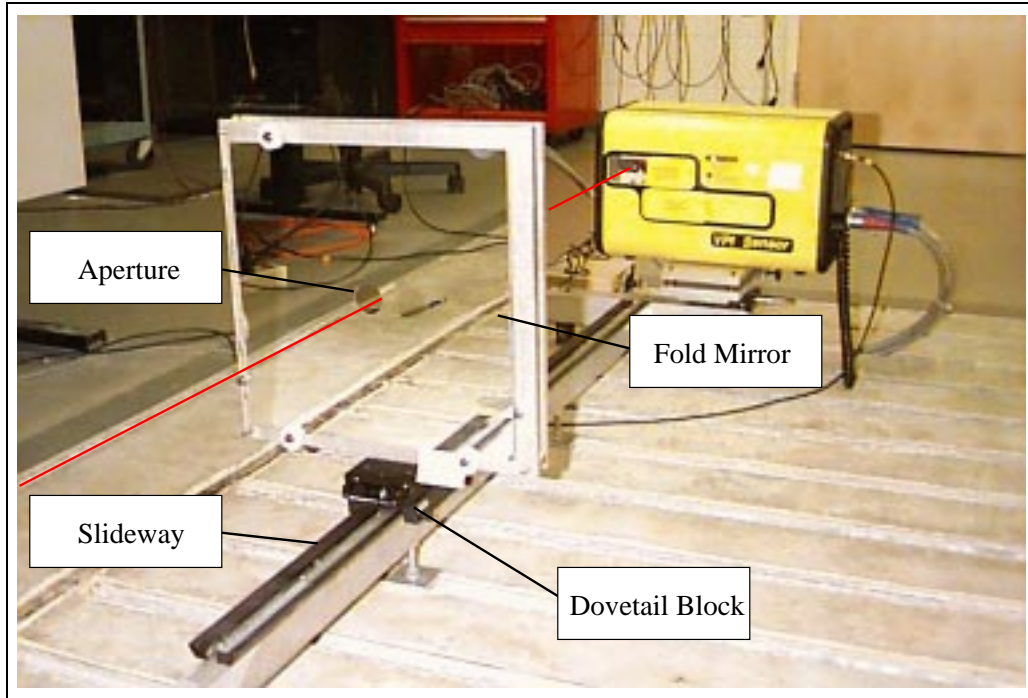


Figure 5.5: Fold Mirror Mount

dove-tail block and the support plate to provide fine adjustment of the fold mirror location.

5.2 Rotating Structure Description

The second hardware component used to characterize the self-tracker system is the rotating structure. This rotating structure is designed to simulate a rotating bladed disk with the added benefit of adjustable and measurable alignment capabilities. Figure 5.6 shows a photograph of the rotating structure.

The rotating test rig consists of an aluminum blade driven by a double-ended DC motor. A shaft encoder is connected with a flexible coupling to one of the motor shafts. The other motor shaft is connected with a second flexible coupling to a steel shaft to which the blade and vertex mirror are mounted. The shaft is supported at each end with a radial bearing,

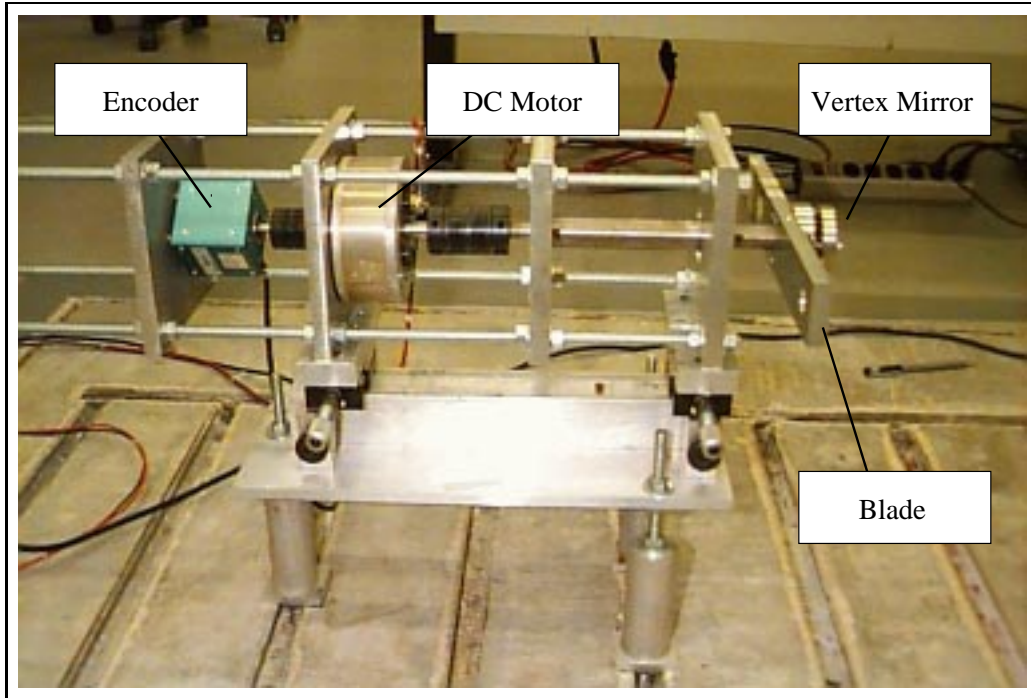


Figure 5.6: Rotating Structure Test Rig

each pressed into a support plate. The encoder and motor are each bolted to support plates. The four support plates are connected with four threaded rods which pass through the corners of each plate. Each plate is fixed to the rods by a nut on each side of the plate. This arrangement allows the plates to be adjusted parallel to each other.

The entire rotating rig rest on an adjustable support structure designed to align the structure to the laser beam. This support structure is designed to allow the rotating structure to be adjusted in the vertically and horizontal. The main components of the support structure are a base plate and a shuffle block. The base plate is used to adjust the rotation and displacement of the structure in the vertical plane. The base plate is secured to the isolation pad by three threaded rods. The plate is sandwiched between two nuts on each threaded rod. This allows the vertical position as well as the pitch angle of the base plate and the rotating test rig to be adjusted and locked into place.

A shuffle block, placed on top of the base plate, allows for adjustment of the rotating structure

in the horizontal plane. Four posts, one at each corner of the base plate, with thumb screws oriented parallel to the top of the base plate are used to adjust the yaw angle and horizontal translation of the block relative to the base plate.

Additionally, a translation stage is mounted on each end of the shuffle block. These allow for measurable adjustment of the horizontal displacement and yaw angle of the rotating structure. Two support plates of the rotating structure rest on the block. Each plate is fitted with a dowel pin that fixes the positions of the rotating structure relative to the shuffle bar. The pin in the forward plate fits into a hole in the front block while the pin in the rear plate rides in a slot in the rear block.

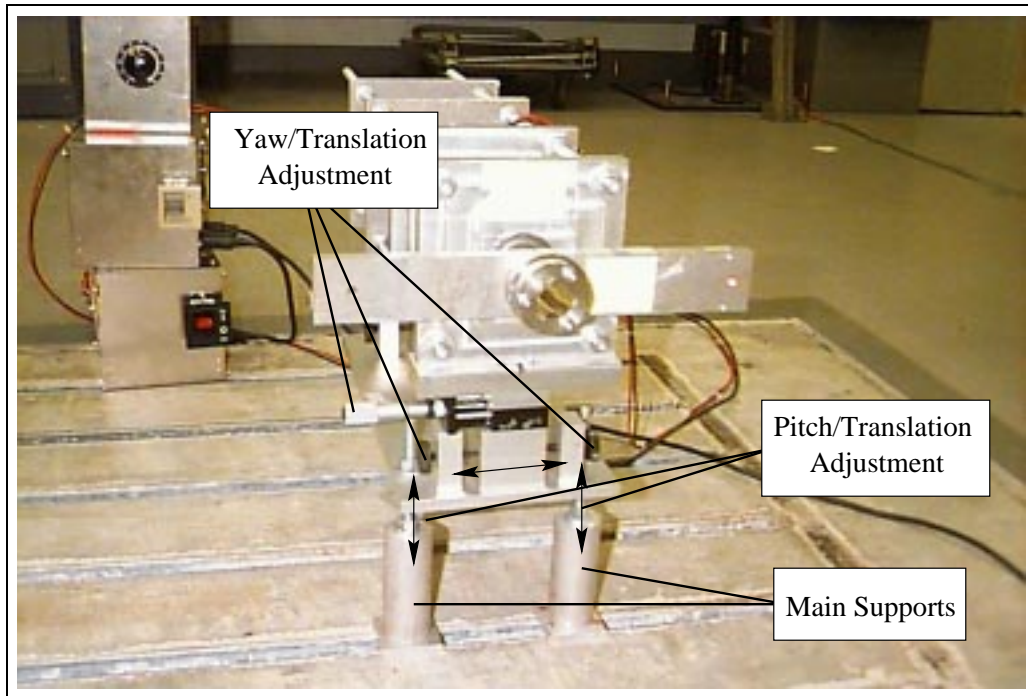


Figure 5.7: Rotating Structure Adjustments

With this support structure, the rotating rig possess all the adjustment capabilities to be properly aligned with the laser beam. Additionally, the support structure has the capability for introducing known, measurable misalignments in the horizontal plane. This capability is used introduce known misalignment into the system.

5.3 Shaft Encoder

The rotational position and speed of the rotating structure are measured using a shaft encoder. The encoder (Dynapar CUBE 22) produces two 512 pulses per revolution quadrature signals and a once per rev index signal. The encoder is aligned with the structure so that the leading edge of the once per rev index signal corresponded to the blade's horizontal orientation. The absolute angular position of the blade can be found by counting the number of pulses that occur after the passage of the once per rev pulse. Using this approach eliminates the need for an absolute position encoder.

5.4 Position Sensitive Photodetector

The position sensitive photodetector is used to align the system and to measure the position error caused by static misalignments. The detector measures the location of an incident laser spot on its surface relative to the detector's center. The photodetector, which is a semi-conductor device, produces currents proportional to the distance between the incident spot and the four edges of the detector. The amount of current is also proportional to the total spot power. These current signals are converted to voltages and amplified using current-to-voltage circuits. The voltage signals are converted to position according to the relationships

$$\begin{aligned}x_{calc} &= \frac{A - B L}{A + B 2} \\y_{calc} &= \frac{C - D L}{C + D 2}\end{aligned}\tag{5.1}$$

where L is the detector length. While the position can be obtained from a single current along each of the x and y axis, measurement of both currents along each cancels the effect of power fluctuations in the incident light. This provides more accurate measurements in instance where the power of the laser beam fluctuates or the background lighting in the room changes.

The detector used in this study (Spot 10D, UDT) is a two-dimensional, tetra-lateral type. The active area of the detector is approximately 10mm by 10mm. It has a nominal sensitivity to incident light power of 0.7 A/W and responds linearly to light level fluctuations at power densities up to approximately 20 mW/cm^2 . The power of the laser spot generated by the vibrometer is 0.5 mW. When focused to a 1mm diameter spot, this gives a power density of approximately 64 mW/cm^2 , well above the linear range of the detector. Although the linearity of this parameter is not important in this work since we are not interested in the intensity measurements, a neutral density filter (density 1.0) was attached to the detector to reduce the power density to approximately 6.4 mW/cm^2 . This results in a nominal current output of 3.5 μA per channel. These current signals are converted to voltages using four current-to-voltage converters, one for each signal. A schematic of the current-to-voltage circuit is shown in Figure 5.8.

The current to voltage gain (230,000 V/A) and low pass filter cutoff frequency (120 Hz) were selected based on the observed noise levels of the voltage output. Additionally a cylindrical hood was placed over the detector to reduce the amount of ambient light incident on the detector. This makes the laser beam the significant contributor to photo current.

The four photodetector signals were collected using a four-channel, simultaneous sampling A/D board (National Instruments NB-A2000) and processed according to Equation 5.4. To verify the detector's performance, measurements of the actual and calculated spot position were made. First, the detector was covered and each amplifier was zeroed using the input offset null adjustments. Next the detector was mounted on a two axis translation stage.

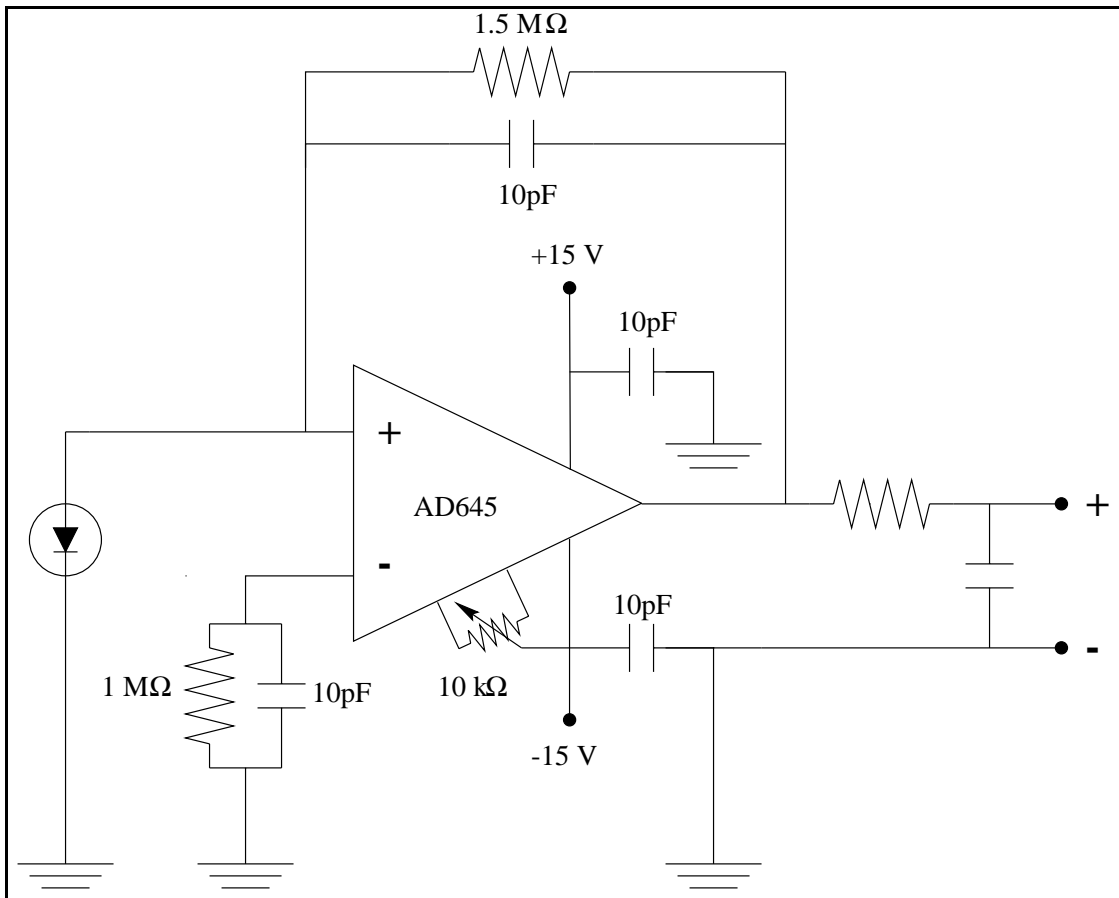


Figure 5.8: PSD Op-Amp Circuit

With the laser beam focused on the detector surface, the detector was translated in 1mm increments over a 4mm by 4mm grid. At each grid location the actual location read from the translational stage and the calculated locations, x_{calc} and y_{calc} , were recorded. A comparison of the actual and calculated positions are shown in Figure 5.9.

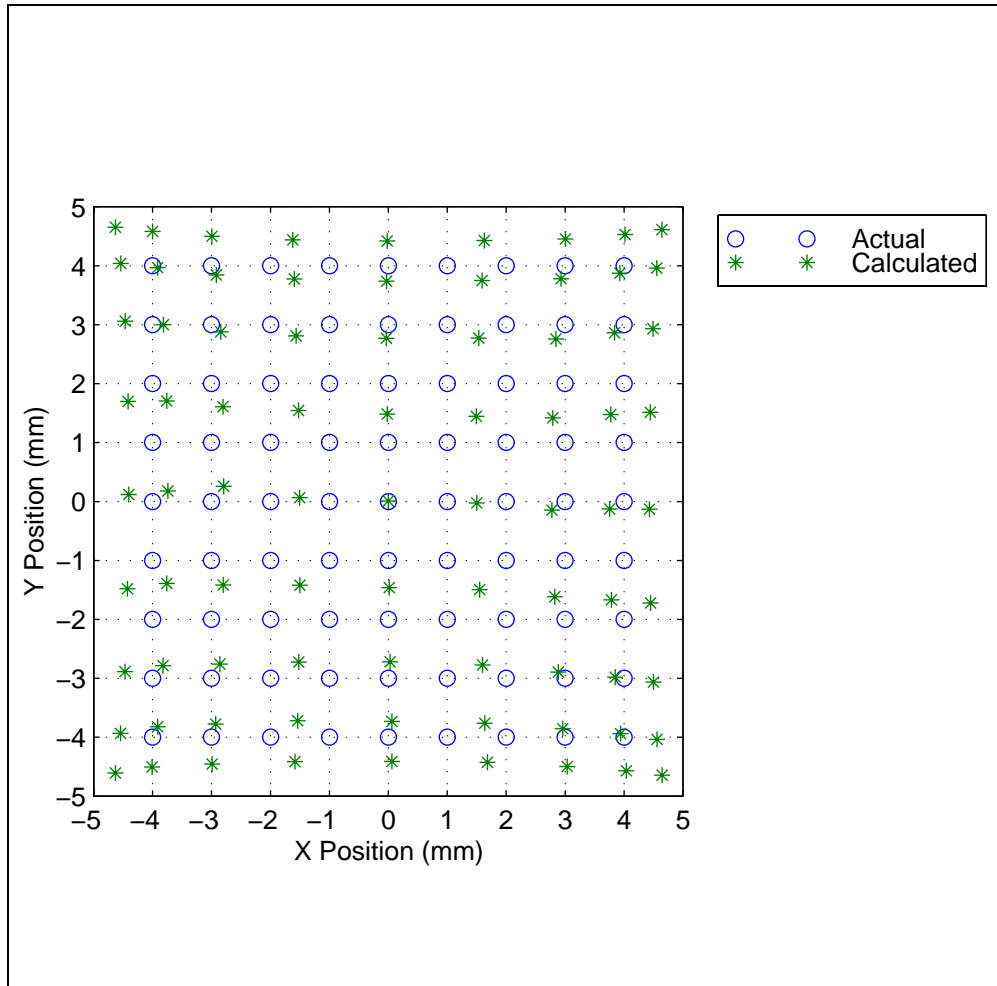


Figure 5.9: Actual Versus Calculated Positions for Linear Relationship

This plot clearly shows unacceptable levels of non-linearity. This level of non-linearity is typical of tetra-lateral detectors. Additionally there appears to be a cross dependence of the x and y output. To compensate for these effects, two polynomial expressions, one for the x location and one for the y location were developed. The expressions, found using a least squares fit, relate the measured outputs to the actual spot position, based on two 36

term polynomials of order five in both x and y . Based on these relationships, the actual and calculated locations show much greater agreement as shown in Figure 5.10.

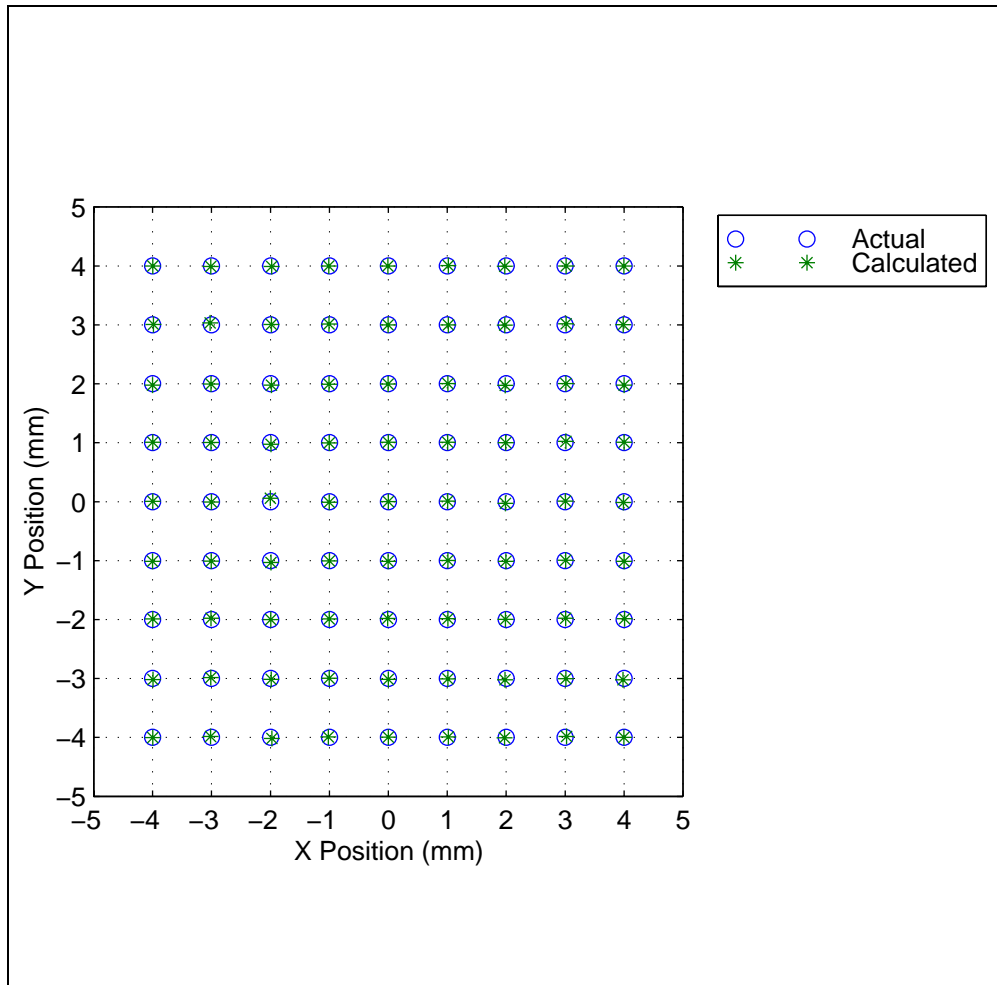


Figure 5.10: Actual Versus Calculated Positions for Polynomial Relationship

Use of the polynomial expression greatly increases the accuracy of the position measurement over a greater area of the detector. With the detector properly calibrated its use in aligning the system components and in measuring the position error can be discussed.

For use in system alignment, the detector was mounted to a two axis translation stage placed on the optical rail. This allowed the alignment of the laser beam and the optical rail to be measured and adjusted, a procedure discussed later.

For use in determining position errors on the bladed disk, the detector is mounted on the rotating structure with the signal leads connected to the preamplifiers through a length of shielded cable. With this arrangement the position of the laser beam on the detector can be measured by rotating the structure by hand for one revolution. The use of the cable prevents measurements of the beam location during continuous rotation of the structure.

One approach for overcoming this limitation is to install a multi-channel slip ring on the structure and attach the preamplifiers to the structure. The power for the circuits can be provided through the slip ring and the amplified outputs sent back to the data acquisition system through the slip rings. Placing the amplifiers on the structure reduces the noise that would otherwise be introduced by the sliprings if the unamplified signals were sent through the slip rings.

Ideally the location of the measurement beam on the rotating structure would be monitored using the position sensitive photodetector. This would give a quantitative measurement of the laser spots instantaneous location as the structure rotates. Since a slipring was not available, position data was only collected for rotation of the structure by hand.

5.5 Data Acquisition Systems

To collect the data several different systems were used. A four channel digital storage oscilloscope (Tektronix xxxxx) was used for general monitoring of the various vibrometer and encoder signals. Data collection and processing of the detector and vibrometer signals was performed using a four channel simultaneous sampling analog-to-digital (A/D) converter board (National Instruments NB-A2000) installed in a PC (Apple Macintosh Quadra 950) and a dynamic signal analyzer(DSA) (Hewlett Packard). The specific application of the A/D board and the DSA with each transducer is described below.

5.5.1 Photodetector Data

All photodetector data collection and processing was performed using the A/D board and PC. For detector calibration and system alignment the A/D board's internal sample clock was used. The photodetector signals were sampled using a four channel A/D board (NB-A2000) which performs simultaneous sampling of each channel at up to 250 kHz. This board was used to collect the four channels of photodetector output. For performing the initial system alignment, a data acquisition code which samples the signals and calculates the position 10 times per second was used.

For the tracking error analysis a shaft encoder providing a 512 pulses per revolution and a single pulse per revolution was used. The 512 pulse signal was used as the sample clock signal on the A/D board. This ensures that the data is collected at equal angular intervals of the structure's rotation. To fix the absolute angular location of the samples, the encoder's one per revolution signal was used to trigger the data acquisition. This ensures that the pulse train starts at a fixed rotational angle of the shaft and data is collected at 512 equally spaced angular positions around the target points path (one point every $360/512 = 0.703125$ degrees) This eliminates the need for an absolute encoder to measure the shaft's angular position.

5.5.2 Velocity Data

The velocity signals were collected using several devices depending upon the analysis to be performed. For verification of the alignment of the system, the velocity signal was displayed on a digital storage oscilloscope, triggered by the shaft encoder's one per rev signal. A second NB-A2000 board was used to collect large blocks of velocity data. Order tracking and frequency analysis of the velocity was performed on an HP Dynamic Signal Analyzer.

5.6 Set-Up Procedure

One of the first steps required before using the self-tracker is to properly align the system components. First, the components that make up the actual radial traverse system, the LDV, linear slideway, and fold mirror must be aligned. Once completed, this entire traverse structure must be aligned to the rotating structure.

System alignment is performed for two reasons. First it serves as a reference case for the misalignment study. For this purpose it is ideal for the system to be perfectly aligned. However in practice it is not possible to achieve this perfect alignment. This points out a second reason for performing the alignment and that is to determine the level of alignment that can be achieved with relatively simple alignment tools.

Before the alignment procedure was implemented, the individual components were assembled and attached to the isolation pad. The relative locations of the components are shown in Figure 5.11.

Once the components were mounted to the isolation pad, the components were aligned, starting with the traverse system.

5.6.1 Traverse System Alignment

For the traverse to operate properly, the laser beam must be aligned parallel to the slideway and the fold mirror must be perpendicular to the laser. This ensures that motion of the fold mirror along the slideway produces linear motion of the measurement point along a radial line on the rotating structure. To perform this alignment, the vibrometer is first be aligned to the slideway and then the fold mirror is aligned to the laser beam.

Before the alignment procedure can begin, the laser must be allowed to reach equilibrium

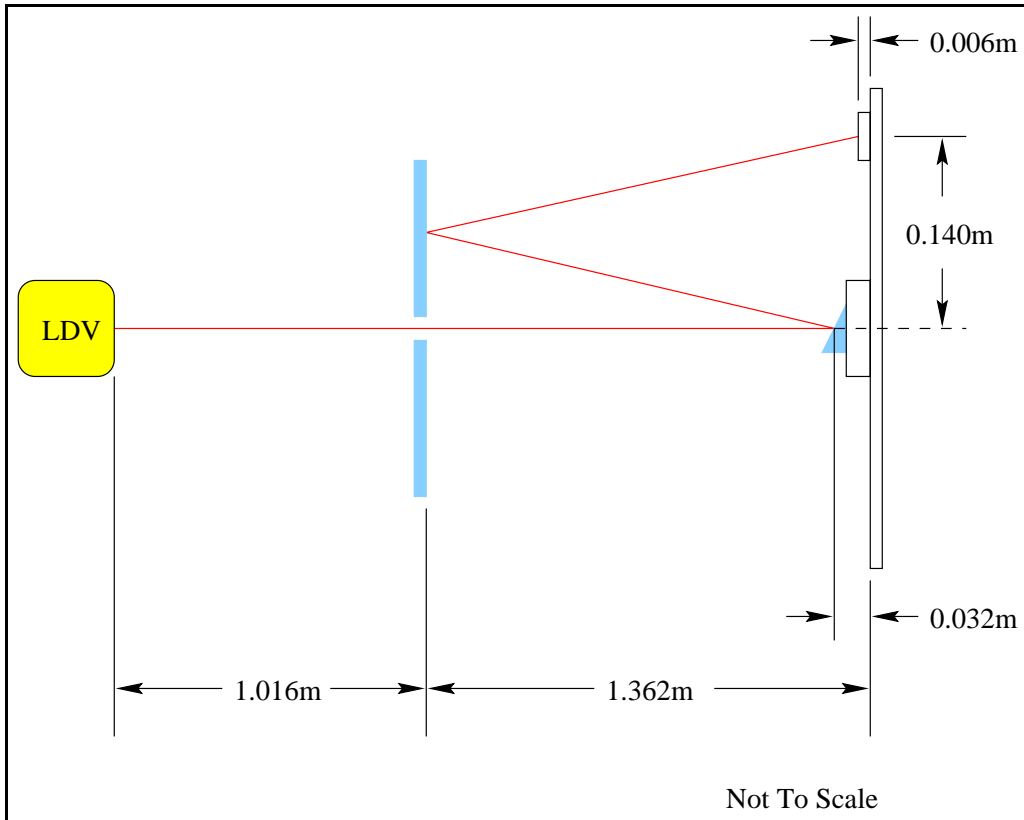


Figure 5.11: Self-Tracker Component Locations

temperature. In this work a scanning laser vibrometer is used. The scanning capability is provided by a set of scan mirrors driven by galvanometers. These scan mirrors are prone to thermal drift when first activated. Therefore before the alignment procedure is begun, the vibrometer is turned on and allowed to warm up for approximately one hour. Once this was done, the alignment procedure was carried out.

Laser to Slideway Alignment

The first step for aligning the traverse system is to align the laser beam parallel to the linear slideway. The goal of this step is align the laser beam parallel to the slideway in the vertical plane that contains the slideway centerline. The vertical distance between the laser beam and slideway is of secondary concern as long as the entire traverse system can be brought into alignment with the rotating structure.

To achieve this alignment, the position sensitive photodetector is used as a target. The target is placed at the far end of the slideway and adjusted on the two axis positioning stage to position the laser spot in the detector's center. The detector is next moved towards the laser and the spot position at increments along the slideway is recorded. Any variation of the spot from the detector's center is considered an error. This information can be used to adjust the horizontal location and pitch and yaw angles of the LDV relative to the slideway until the error along a length of the slideway is minimized.

Although conceptually simple, there are several practical considerations which limit the accuracy of the procedure. First the linear slideway has inherent waviness in both the vertical and horizontal planes. This translates into displacements of the detector as it is positioned at various points along the slideway. Secondly, the adjustments available on the laser plate do not allow for decoupled adjustment of the laser yaw and pitch angles. Furthermore, screws which fix the vibrometer once it is aligned introduce small angular changes as they

are tightened. Therefore an iterative approach of adjustment, locking, and checking must be used. Using this approach the laser beam was aligned to the slideway over a .4m segment of the slideway.

Fold Mirror to Laser Alignment

Once the laser is aligned with the slideway, the fold mirror can be aligned perpendicular to the laser beam. The goal of this procedure is to make the fold mirror perpendicular to the laser beam at all locations along the linear slideway. This alignment technique relies on reflecting the laser beam from the back of the fold mirror back onto the outgoing beam. If the fold mirror is perpendicular to the laser beam, the reflected beam will be colinear with the outgoing beam.

To check for this colinearity, the laser vibrometer, aligned parallel to the slideway, is displaced horizontally so that the laser beam intersects the fold mirror instead of passing through the circular aperture. A target is placed in the path of the outgoing between the vibrometer and fold mirror. The target consists of a cross hair with the center portion removed and a small target suspend in the hole as shown in Figure 5.12.

Perpendicularity is achieved when the reflected beam intersects the center of the suspended target. Unfortunately it is not possible to quantitatively characterize the error in this alignment. An estimate of the alignment error was made by visually noting that the laser spot fell on the target at a location that was approximately at the center within 1mm in both the horizontal and vertical direction. Since this alignment technique is somewhat suspect, the angle of the fold mirror is a parameter that will be adjusted as part of a later alignment procedure.

With these two alignment procedures completed, the alignment of the traverse system and rotating structure can be performed.

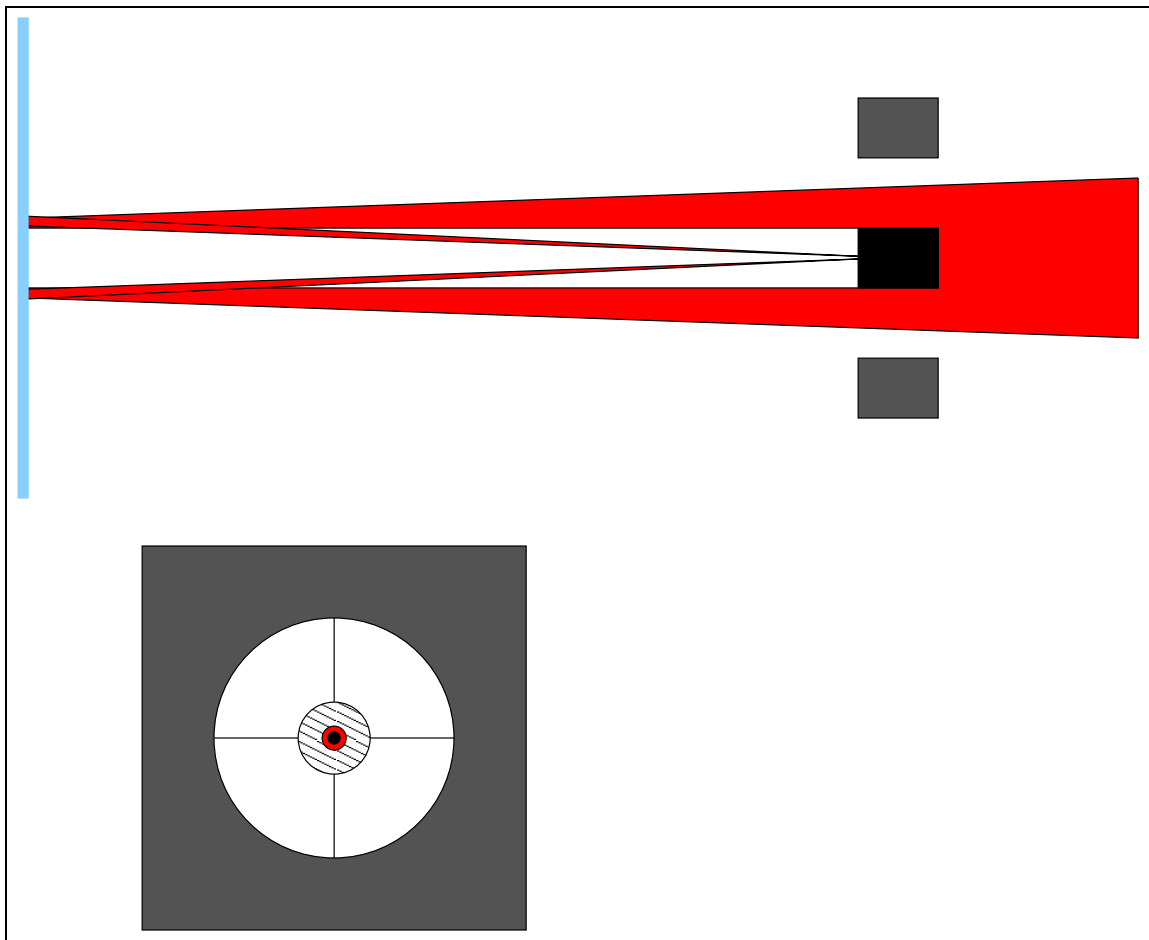


Figure 5.12: Cross Hair Target for Fold Mirror Alignment

5.6.2 Laser to Structure Alignment

With the internal alignment of the traverse components completed, the structure-traverse alignment can be performed. The first step is to perform a coarse alignment using a level and a plumb line.

This initial coarse horizontal and pitch and yaw alignments of the structure and traverse components is performed using a plumb line. A plumb line is strung across the isolation pad and each component is visually aligned with the plumb line.

The ideal alignment conditions consists of the laser beam being colinear with the structure's rotation axis. The following iterative procedure is used:

- Attach position sensitive photodetector to shaft
- Translate structure assembly so laser beam strikes single point on detector as structure is rotated by hand
- Attach vertex mirror to structure and introduce small vertex mirror tilt angle
- Rotate structure assembly so laser beam intersects center of cross-hair target mounted on slideway

This procedure is repeated until a minimal amount of misalignment remains. For the perfect alignment condition the reflected circle will be centered on the slideway mounted cross-hair target. The vertex mirror tilt angle determines the circle radius. This angle can be adjusted throughout the alignment procedure to aid in locating the circle's center.

The translational alignment of the structure was characterized based on the diameter of the circle traced out on the photodetector as the structure rotates. The circle diameter was found to be less than 0.1mm. For perfect alignment the detector would measure the laser

beam at a single point. As in the case of the fold mirror alignment, the rotational alignment of the structure was based on the location of the laser beam on the cross-hair target. This spot was estimated to be at the center of the target to within 1mm.

5.6.3 Characterization of Ideal Alignment Case

In theory the above alignment procedure should cause the laser beam to remain fixed to a single point on the structure as it rotates. To verify this, the position of the laser spot was measured for one full rotation of the blade. If the laser spot did not remain fixed to a single point, indicative of the system not being properly aligned, the system alignment was adjusted. This presents a problem since there is no indication from the laser spot on the photodetector as to which component should be adjusted. The fold mirror was selected as the component to adjust for two reasons. First, the procedure used to verify its alignment with the laser beam was considered the most unreliable since it is based on the local normal of a single point on the fold mirror. Secondly, the fold mirror is the most easily adjusted component. An iterative procedure was used to adjust the fold mirror to minimize the size of the path traced out on the photodetector by the laser spot. Figure 5.13 shows the path of the laser spot on the detector under the best alignment condition achieved.

Under ideal alignment conditions, the laser spot should remain at a single point on the detector throughout a full revolution of the structure. While the above results show only .5mm of position error, the shape of the path raises several issues.

During one full revolution of the structure, the measurement point makes two revolutions around the target point. There are several possible causes for this. First it is possible that the shaft which the vertex mirror is mounted to wobbles as it rotates. This would cause the angle between the incoming laser beam and the reflected beam direction to change slightly. This slight change is magnified by the distance over which the laser beam travels from the

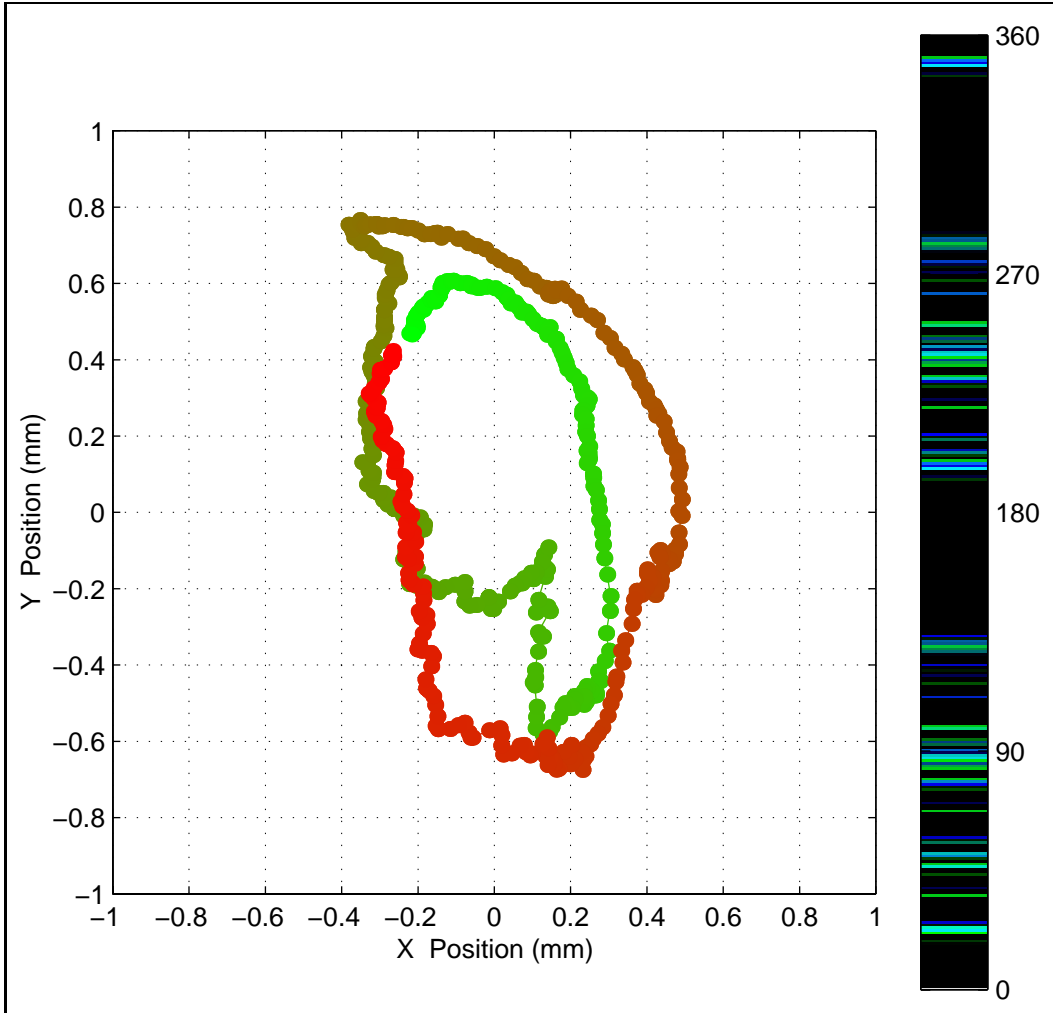


Figure 5.13: Laser Path for Ideal Alignment

vertex mirror to the fold mirror and back to the detector. While it is not possible to directly determine if the shaft wobbles, and indication of shaft motion can be determined.

To measure the amount of shaft motion, the photodetector was mounted to the shaft. With the laser beam focused on the detector, the structure was rotated through a full revolution and the location of the laser spot measure. If the shaft does not wobble, the path should be a perfect circle. As seen in Figure 5.14, the path is nearly circular, but indicates that there may be some level of wobble in the shaft.

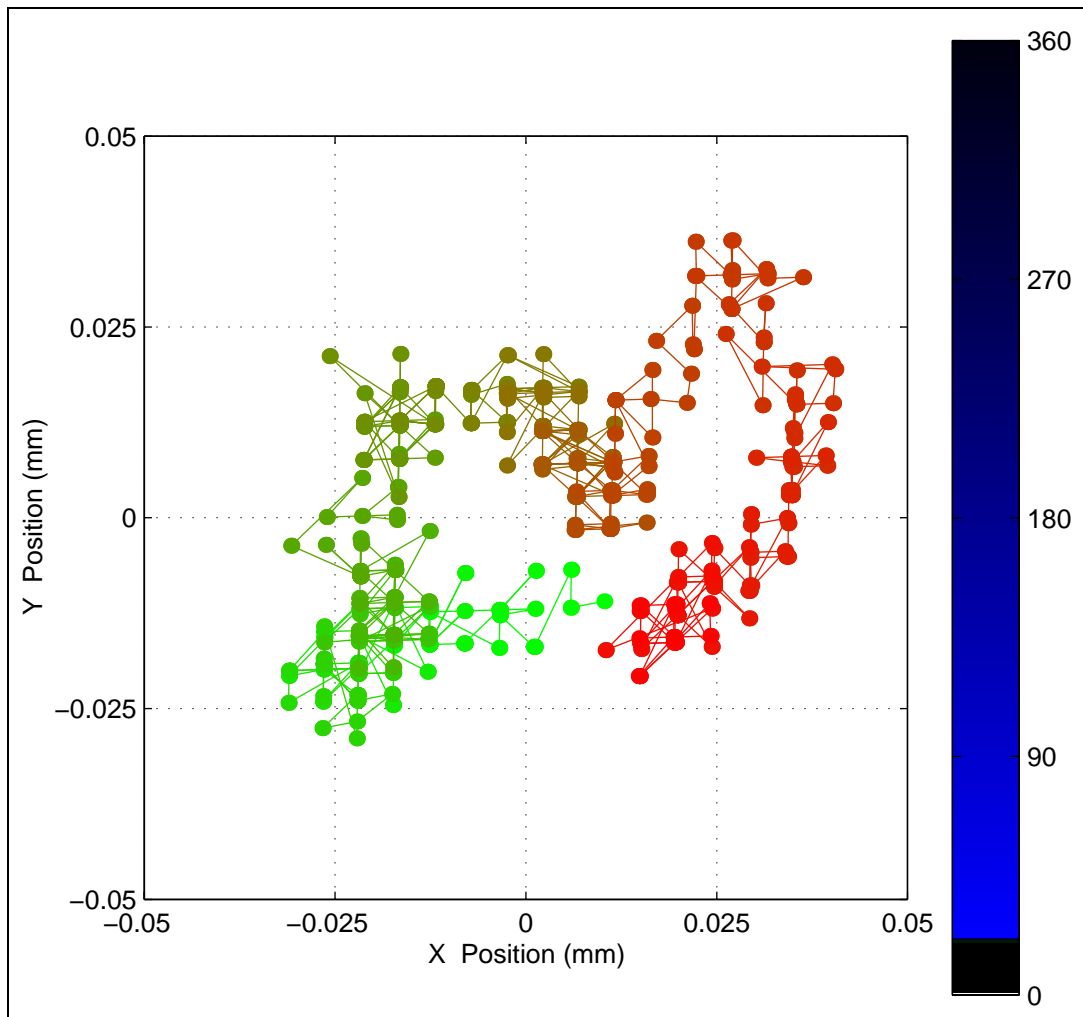


Figure 5.14: Laser Path on Shaft End

While this is not conclusive evidence of the cause of the position error, it does indicate that

the shaft wobble cannot be eliminated as a possible contributor. The amount of wobble that would be required to give the observed level of position error seen on the detector can be estimated.

Assuming that the position error is due solely to vertex mirror wobble, the maximum angular wobble can be estimated based on a simple geometric model. The largest measured error is approximately 0.5mm. This occurs over a run of approximately 2.6m. This represents an angular rotation of the vertex mirror from its ideal orientation of approximately $200\mu rad$, which is a reasonable amount of angular rotation.

A second possible cause of the position error in the measurement point location is waviness of the fold mirror. Slight changes in the local mirror normal direction will also change the reflection direction of the laser beam from the fold mirror to the blade. Again, there is no easy way to measure the amount of waviness in the mirror, and therefore this possible source of error cannot be eliminated. Using the same approach as for the vertex mirror, the error of 0.5mm occurs over a run of approximately 1.3m. This represents an angular variation of the local fold mirror normal of approximately $100\mu rad$, again a reasonable amount considering the possibility of distortion of the mirror as a result of drilling the aperture hole..

There are several steps that could be taken to reduce the chances of these errors occurring. First, high precision bearings could be used to support the shaft carrying the vertex mirror and blade. This would reduce the amount of shaft wobble. Secondly, a higher grade mirror, with increased thickness, would reduce the amount of variation in the mirror's normal direction. Both of these improvements should be incorporated into any upgrade of the present system.

5.7 Summary

The experimental apparatus used to verify the self-tracker's predicted performance has been described. The data acquisition hardware has been described as has its use. A procedure for aligning the self-tracker components and the level of alignment that can be achieved has also been illustrated. With the hardware and experimental procedures described, the theoretical performance of the self-tracker will be presented next.

Chapter 6

Ideal Alignment Case

Having developed a full three-dimensional model of the self-tracker it is now possible to predict the position and velocity errors. This can be done for any location and orientation of the individual system components. The first case to be studied is the ideal alignment case.

6.1 Ideal Alignment Model

The ideal alignment case describes the orientations and locations of the system components that will provide the self-tracker's best performance. This case serves as a benchmark for comparison of the static misalignment cases to be studied later. To help identify the individual contributors to position and velocity errors, a simplified two-dimensional model of the ideal alignment case is also developed. The first step in developing these models is to describe the alignment conditions for the ideal alignment case.

The ideal alignment case is defined by the following conditions:

- The displaced frame $\{D\}$ is coincident with and rigidly fixed to the ideal alignment frame $\{I\}$
- The fold mirror normal, structure rotation axis, and laser beam direction are collinear.
- The blade is planar and parallel to the fold mirror.

With these constraints, the general form of the transformation matrices are significantly simplified, allowing for a closed form solution to be found. Though not necessary for this analysis, several more constraints can be applied to further reduce the complexity of the equations and better illustrate the characteristics of the ideal alignment case. These constraints require that the z -axes of the laser frame, fold mirror frame, and ideal alignment frame are co-linear with the global z -axes. This eliminates the need to carry through terms for the x and y displacements without a loss of generality. The application of these two sets of constraints results in the following transformation matrices.

The laser frame $\{L\}$ is translated a distance d_{z_L} along the z_G axis.

$${}^G T_L = \begin{bmatrix} 1 & 0 & 0 & 0 \\ 0 & 1 & 0 & 0 \\ 0 & 0 & 1 & d_{z_L} \\ 0 & 0 & 0 & 1 \end{bmatrix} \quad (6.1)$$

The fold mirror frame $\{F\}$ is translated a distance d_{z_F} along the z_G axis.

$${}^G T_F = \begin{bmatrix} 1 & 0 & 0 & 0 \\ 0 & 1 & 0 & 0 \\ 0 & 0 & 1 & d_{z_F} \\ 0 & 0 & 0 & 1 \end{bmatrix} \quad (6.2)$$

The ideal alignment frame $\{I\}$ is rotated about the y_G axis by 180° and is translated a

distance d_{z_I} along the z_G axis.

$${}^G_I T = \begin{bmatrix} -1 & 0 & 0 & 0 \\ 0 & 1 & 0 & 0 \\ 0 & 0 & -1 & d_{z_I} \\ 0 & 0 & 0 & 1 \end{bmatrix} \quad (6.3)$$

The displaced frame {D} is coincident with the ideal alignment frame {I}.

$${}^I_D T = \begin{bmatrix} 1 & 0 & 0 & 0 \\ 0 & 1 & 0 & 0 \\ 0 & 0 & 1 & 0 \\ 0 & 0 & 0 & 1 \end{bmatrix} \quad (6.4)$$

The bladed disk frame {B} is translated a distance d_{z_B} along the z_D axis and is allowed to rotate about the z_D axis. This angle α_B represents the rotation of the bladed disk in operation.

$${}^D_B T = \begin{bmatrix} c\alpha_B & -s\alpha_B & 0 & 0 \\ s\alpha_B & c\alpha_B & 0 & 0 \\ 0 & 0 & 1 & d_{z_B} \\ 0 & 0 & 0 & 1 \end{bmatrix} \quad (6.5)$$

The vertex frame {V} is translated a distance d_{z_V} along the z_B axis. This frame is by angles β_V and α_V about the y_B and z_B axes respectively.

$${}^B_V T = \begin{bmatrix} c\alpha_V c\beta_V & -s\alpha_V & c\alpha_V s\beta_V & 0 \\ s\alpha_V c\beta_V & c\alpha_V & s\alpha_V s\beta_V & 0 \\ -s\beta_V & 0 & c\beta_V & d_{z_V} \\ 0 & 0 & 0 & 1 \end{bmatrix} \quad (6.6)$$

The target frame $\{T\}$ is translated by the distance d_{z_T} along the z_B axis. The target frame is not displaced in the x_B and y_B so that it will be easier to determine the absolute location of the measurement point on the blade.

$${}^B_T T = \begin{bmatrix} 1 & 0 & 0 & 0 \\ 0 & 1 & 0 & 0 \\ 0 & 0 & 1 & d_{z_T} \\ 0 & 0 & 0 & 1 \end{bmatrix} \quad (6.7)$$

With these transformations defined it is now possible to determine the locations and directions of the rays and planes that describe the self-tracker's components.

Recall that the basis for using a full three-dimensional model is to define the location and direction of the laser beam, vertex mirror, fold mirror, and target plane. Applying the above transformations, the locations and directions for the laser source, vertex mirror, fold mirror, and target point are:

$$\begin{aligned} \vec{N}_L &= [0, 0, 1] \\ \vec{N}_V &= [-s\beta_V c(\alpha_b + \alpha_V), s\beta_V s(\alpha_b + \alpha_V), -c\beta_V] \\ \vec{N}_F &= [0, 0, 1] \\ \vec{N}_T &= [0, 0, -1] \end{aligned} \quad (6.8)$$

and

$$\begin{aligned} {}^G O_L &= [0, 0, d_{z_L}] \\ {}^G O_V &= [0, 0, -d_{z_V} - d_{z_B} + d_{z_I}] \\ {}^G O_F &= [0, 0, d_{z_F}] \\ {}^G O_T &= [0, 0, -d_{z_B} - d_{z_T} + d_{z_I}] \end{aligned} \quad (6.9)$$

With the origin and normals defined, the laser path can be traced from the laser origin to the measurement point using the procedure described in Chapter 5.

6.1.1 Ideal Alignment Position Analysis

Once the location and directions of the laser, vertex and fold mirror, and the bladed disk are known, it is possible to determine the location of the laser beam intersection with the blade. By applying the procedure described in Section 6.1, the intersection point between the laser beam and the target point frame in global coordinates is found to be:

$${}^G P_M = \begin{bmatrix} -c(\alpha_B + \alpha_V)t2\beta_V(2d_{z_I} - 2d_{z_F} - 2d_{z_B} - d_{z_V} - d_{z_T}) \\ s(\alpha_B + \alpha_V)t2\beta_V(2d_{z_I} - 2d_{z_F} - 2d_{z_B} - d_{z_V} - d_{z_T}) \\ d_{z_I} - d_{z_B} - d_{z_T} \end{bmatrix} \quad (6.10)$$

Transforming this point into the target point frame {T} using the transformation

$${}^T_G T = {}^G_T T^{-1} = \begin{bmatrix} c\alpha_B & -s\alpha_B & 0 & 0 \\ s\alpha_B & c\alpha_B & 0 & 0 \\ 0 & 0 & -1 & d_{z_I} - d_{z_B} - d_{z_T} \\ 0 & 0 & 0 & 1 \end{bmatrix} \quad (6.11)$$

yields

$${}^T P_M = \begin{bmatrix} -c\alpha_V \cdot t2\beta_V \cdot (2d_{z_I} - 2d_{z_F} - 2d_{z_B} - d_{z_V} - d_{z_T}) \\ s\alpha_V \cdot t2\beta_V \cdot (2d_{z_I} - 2d_{z_F} - 2d_{z_B} - d_{z_V} - d_{z_T}) \\ 0 \end{bmatrix} \quad (6.12)$$

Careful examination of these results show the significance of the ideal alignment case.

The first result that can be directly seen is that the point intersected by the laser beam on the structure is constant with rotation angle of the bladed disk, α_B . As the structure rotates, the measurement point remains fixed to a single point on the blade.

A second important result can be seen following closer examination and manipulation of the results. First, the path of the laser beam can be shown to lie in a single plane by considering the individual segments of the laser beam path. The laser beam path, as shown in Figure 6.1 consists of three segments, \overrightarrow{LV} , \overrightarrow{VF} , and \overrightarrow{FB} .

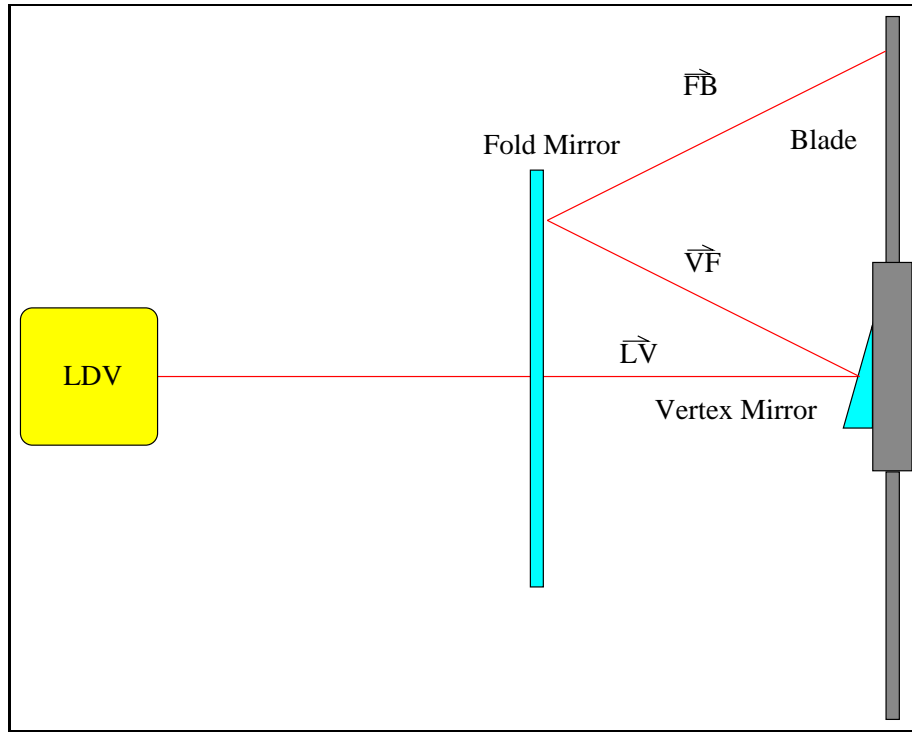


Figure 6.1: Two-dimensional Laser Path

The first segment starts at the laser source and ends at the surface of the vertex mirror. This segment, \overrightarrow{LV} originates at the point

$${}^G P_L = \begin{bmatrix} 0 \\ 0 \\ d_{z_L} \end{bmatrix} \quad (6.13)$$

and travels in the direction

$$\vec{N}_L = \begin{bmatrix} 0 \\ 0 \\ 1 \end{bmatrix} \quad (6.14)$$

This ray intersects the vertex mirror at the point

$${}^G P_V = \begin{bmatrix} 0 \\ 0 \\ d_{Z_I} - d_{Z_V} - d_{Z_B} \end{bmatrix} \quad (6.15)$$

which is the starting point for the next segment. The second segment, \overrightarrow{VF} , is reflected from the vertex mirror in the direction

$$\vec{N}_{VF} = \begin{bmatrix} -2c\beta_V s\beta_V c(\alpha_B + \alpha_V) \\ 2c\beta_V s\beta_V s(\alpha_B + \alpha_V) \\ -c(2\beta_V) \end{bmatrix} \quad (6.16)$$

and intersects the fold mirror at the point.

$${}^G P_F = \begin{bmatrix} c(\alpha_B + \alpha_V) \cdot t2\beta_V \cdot (d_{Z_F} - d_{Z_I} - d_{Z_V} + d_{Z_B}) \\ -s(\alpha_B + \alpha_V) \cdot t2\beta_V \cdot (d_{Z_F} - d_{Z_I} - d_{Z_V} + d_{Z_B}) \\ d_{Z_F} \end{bmatrix} \quad (6.17)$$

This intersection point forms the origin of the third segment \overrightarrow{FT} which is reflected to the blade in the direction

$$\vec{N}_{FT} = \begin{bmatrix} -2c\beta_V s\beta_V c(\alpha_B + \alpha_V) \\ 2c\beta_V s\beta_V s(\alpha_B + \alpha_V) \\ c(2\beta_V) \end{bmatrix} \quad (6.18)$$

The effect of the fold mirror is to retain the x and y directions of the laser beam but reverses the z direction. This effect proves useful in a simplification of the model to be developed later.

With the directions of the three segments defined, two planes can be defined, the first defined by \overrightarrow{LV} and \overrightarrow{VF} and the second defined by \overrightarrow{LV} and \overrightarrow{FT} . The normals to these two planes can be found by taking the cross products between the two defining vectors of each plane. The normal for the plane containing the first vector pair \overrightarrow{LV} and \overrightarrow{VF} is

$$\overrightarrow{LV} \times \overrightarrow{VF} = \begin{bmatrix} -2c\beta_V s\beta_V s(\alpha_B + \alpha_V) \\ -2c\beta_V s\beta_V c(\alpha_B + \alpha_V) \\ 0 \end{bmatrix} \quad (6.19)$$

The normal for the plane containing the second vector pair \overrightarrow{LV} and \overrightarrow{FT} is

$$\overrightarrow{LV} \times \overrightarrow{FT} = \begin{bmatrix} -2c\beta_V s\beta_V s(\alpha_B + \alpha_V) \\ -2c\beta_V s\beta_V c(\alpha_B + \alpha_V) \\ 0 \end{bmatrix} \quad (6.20)$$

Since the normal directions for the two planes are equal, the planes are parallel, regardless of the values of β_V , α_B , and α_V . Furthermore, since the two planes share a common vector,

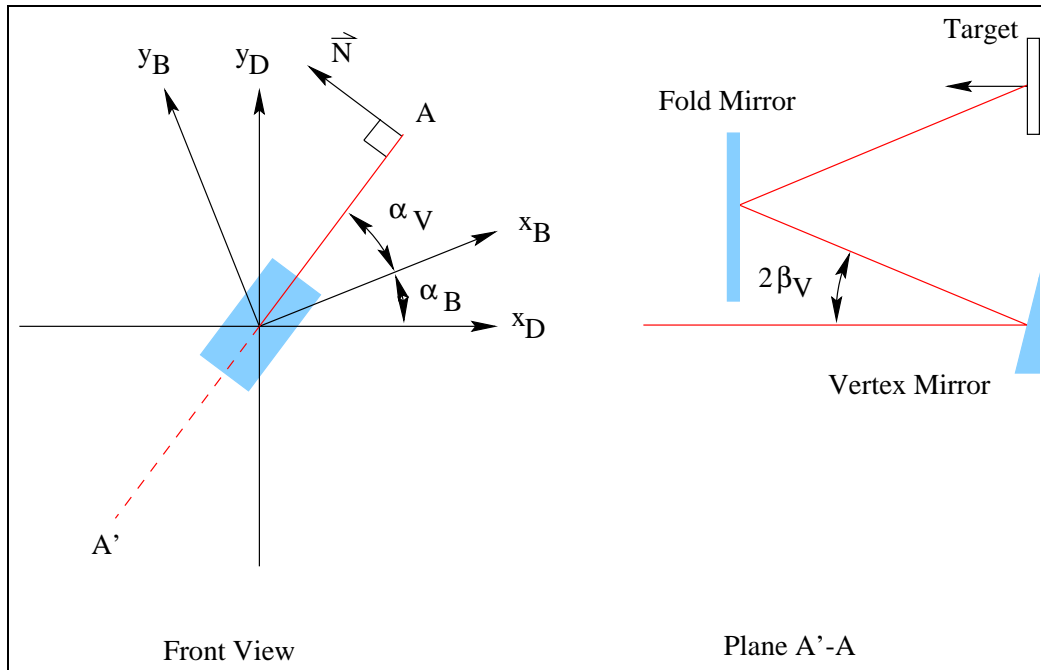


Figure 6.2: Laser Beam Path

namely \overline{LV} the parallel planes are coplanar. Therefore all three laser segments lie in a single plane, and the path can be described in that plane by a two-dimensional model. This allows a two dimensional model, as shown in Figure 6.2, to be used to describe the operation of the self-tracker for ideal alignment.

The plane that contains the laser beam path, A-A', rotates about a hypothetical line which is the reflection of the incoming laser beam segment if the vertex mirror had zero tilt angle. For the ideal alignment case, this line coincides with the incoming laser beam axes. The plane rotates at the same angular rate as the structure.

This two-dimensional model can now be used to identify the significance of the terms in Equations 6.10 and 6.11. Referring to Figure 6.2, the *sine* and *cosine* terms in both position vectors orient the plane that contains the laser beam path. The *tangent* term defines the slope of the laser path from vertex mirror to fold mirror and fold mirror to target plane.

Considering just the path of the beam in the plane A-A', the location of the measurement

point can be found based on Figure 6.3

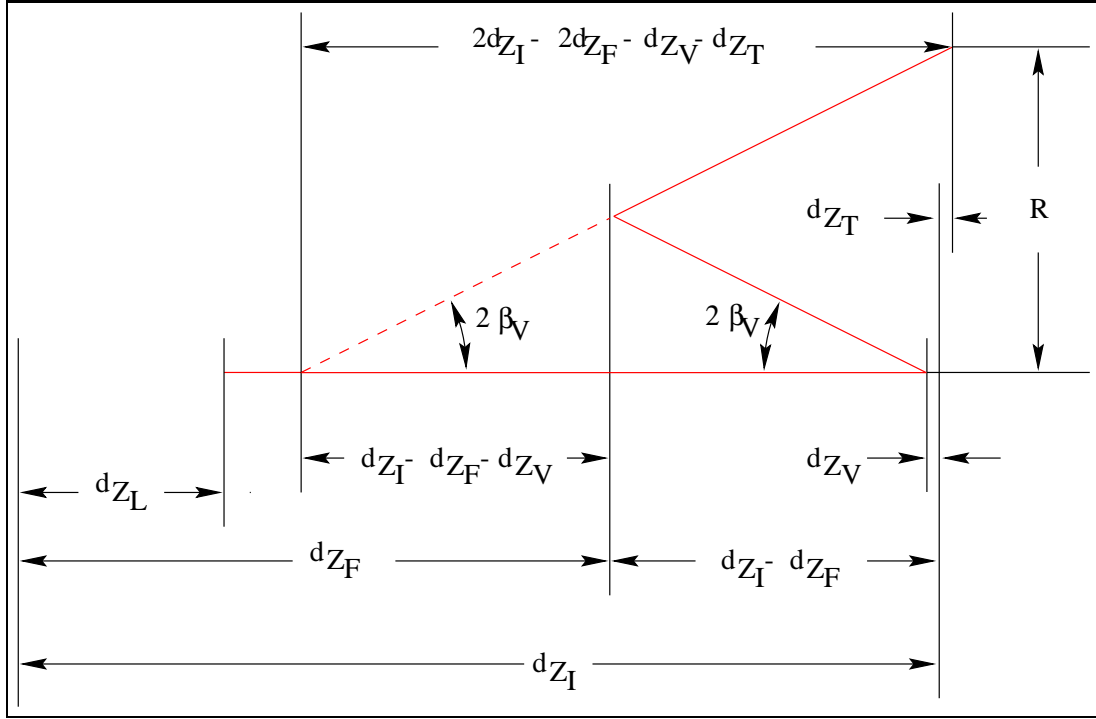


Figure 6.3: Laser Beam Path

Letting

$$d_I = 2d_{Z_I} - 2d_{Z_F} - 2d_{Z_B} - 2d_{Z_V} - d_{Z_T} \quad (6.21)$$

where d_I is the total distance parallel to the rotation axis over which the laser beam path, the measurement point coordinates in the target frame can be re-written as

$$\begin{bmatrix} -c\alpha_V \cdot t2\beta_V \cdot d_I \\ s\alpha_V \cdot t2\beta_V \cdot d_I \\ 0 \end{bmatrix} \quad (6.22)$$

This result motivates a simplification arrived at by unfolding the laser beam path about the fold mirror. Once unfolded, an alternative position analysis can be performed.

6.1.2 Alternative Position Analysis

The above analysis is based on tracing the laser path from the vibrometer to the target frame, via the vertex mirror and fold mirror. For the ideal alignment case this is relatively simple, but for other alignment conditions the above procedure can become cumbersome when solving for a closed form solution. One simplification is to use the virtual images of the vertex mirror and vibrometer formed by the fold mirror and remove the fold mirror from the analysis. This reduces the number of simultaneous equations to solve from three sets of four to two sets of four since the intersection point on the fold mirror and reflection direction from the fold mirror have been eliminated. While this is not overly important for the ideal alignment case, it is developed here to show the agreement between the two methods. The resulting model found based on this alternative viewpoint will serve as the simplified model used to describe the effects of static misalignments.

The analysis based on this unfolded arrangement begins by defining the origins and directions based on the orientations of the coordinate frames as defined in Equations 6.9 and 6.8.

Next, the origins and directions are modified to account for unfolding the system and eliminating the fold mirror as shown in Figure 6.4.

Unfolding changes the origin and directions of the laser, vertex mirror, and target plane. Since it is equally valid to consider either the real object or its virtual image, the images of the laser and vertex mirror will be used and the real target plane will be used. This has the effect of unfolding the system. As a result of unfolding the system, the locations of the vibrometer and vertex mirror origins change. The direction vectors maintain their x and y components, but the z component changes sign. The resulting virtual origins and directions

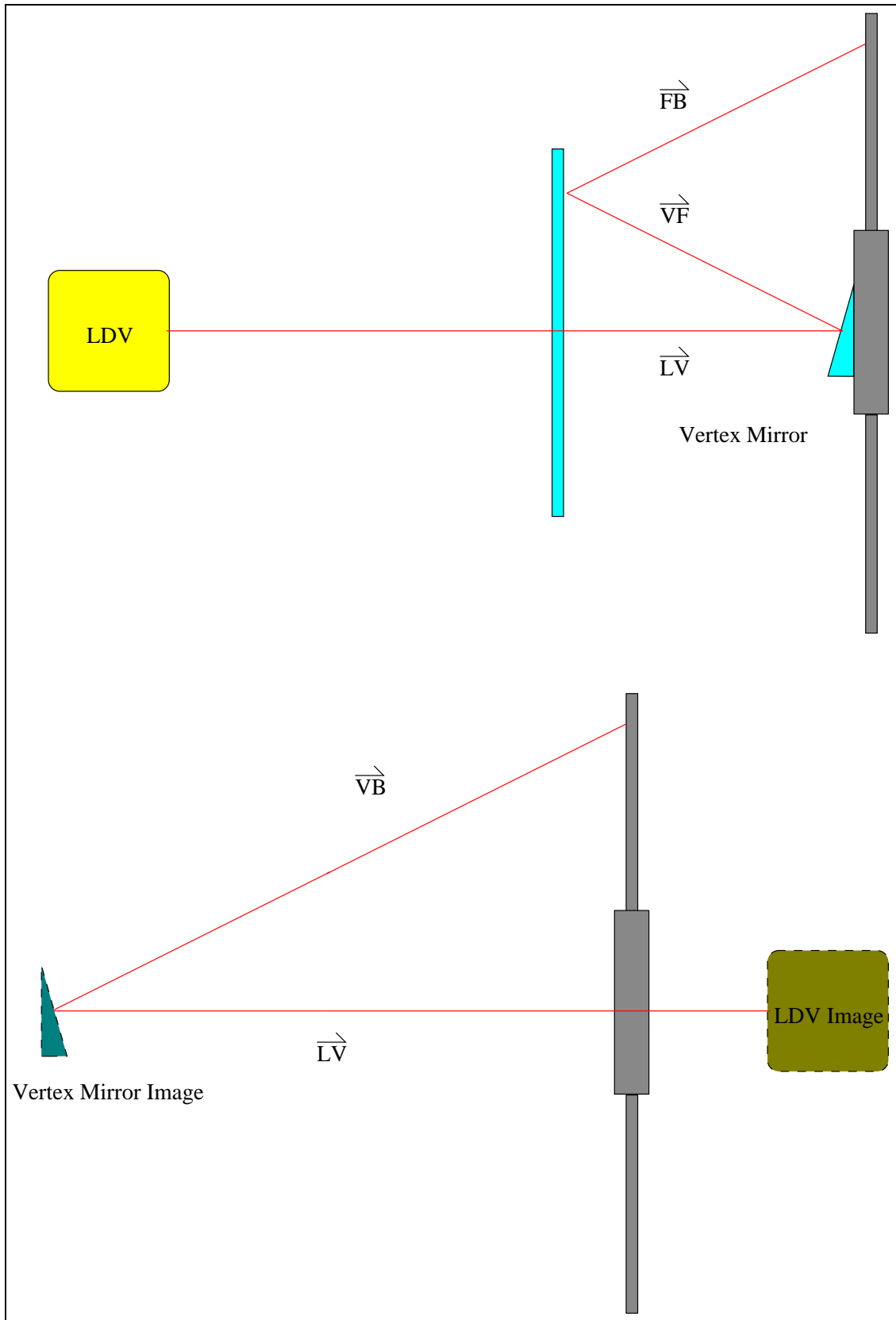


Figure 6.4: Unfolding of Laser Path

are

$$\begin{aligned}
{}^G O_{L'} &= [0, 0, 2d_{z_F} - d_{z_L}] \\
{}^G O_{V'} &= [0, 0, -d_{z_V} - d_{z_B} + d_{z_I}] \\
{}^G O_T &= [0, 0, -d_{z_B} - d_{z_T} + d_{z_I}]
\end{aligned} \tag{6.23}$$

and

$$\begin{aligned}
\vec{N}_{L'} &= [0, 0, -1] \\
\vec{N}_{V'} &= [-s\beta_V c(\alpha_b + \alpha_V), s\beta_V s(\alpha_b + \alpha_V), c\beta_V] \\
\vec{N}_F &= [0, 0, -1]
\end{aligned} \tag{6.24}$$

With these changes the measurement point can be found and the position and velocity analysis can be performed as previously described without any other changes. There are two benefits to adopting this approach. First, it reduces the number of sets equations that need to be solved. More importantly, it provides a simplified model of the system in which the cone traced out by the laser path is more easily seen.

6.1.3 Ideal Alignment Case Velocity Analysis

With the position analysis complete for the ideal-alignment case, the velocity analysis can be performed. Recall from Chapter 4 the phenomena interpreted by the vibrometer as velocity signals:

- Motion of diffuse surfaces
- Motion of reflective surfaces

- Variation of speckle patterns

Two of these contributors can be eliminated in the ideal alignment case due to findings from the position analysis.

First, it was shown that the laser beam intersects the vertex mirror at the vertex mirror's center of rotation. Therefore there is no linear velocity of the vertex mirror at this point and subsequently no induced velocity signal at the vibrometer output due to the mirror motion.

Second, since the measurement point remains fixed to a single point on the structure, there is no relative linear motion between the beam and the blade and therefore no speckle noise. One subtlety worth mentioning here is that even though there is relative rotational motion between the bladed and the laser beam, the same segment of the structure is viewed from a fixed angle, as defined by the vector direction of segment \overrightarrow{FT} . The effect of this relative rotational motion is for the speckle pattern at the photodetectors to rotate but not vary in total intensity or phase due to the rotation. With these two contributors to velocity eliminated, the remaining contributor, the velocity component along the laser beam direction can be studied.

To determine the remaining velocity component, it is useful to recall the assumed model of the bladed disk. The bladed disk, which consists of a rigid hub and flexible blades, is modeled as a rigid disk and blade, with a one degree-of-freedom oscillator at the measurement point. The oscillator is assumed to vibrate in a direction normal to the blade. With these assumptions, the velocity at the measurement point can be separated into two contributors, that arising from local vibratory motion of the structure and that due to rigid body motion of the structure.

The velocity at the measurement point in the global coordinate frame can be written as the vector sum of the individual velocity components. The local vibratory motion in the target

frame can be described by the velocity vector

$${}^T\vec{V}_{m_{vib}} = \begin{bmatrix} 0 \\ 0 \\ V_Z \cdot \sin(\omega t + \phi) \end{bmatrix} \quad (6.25)$$

This velocity vector can be transformed into the global frame by multiplying by the transformation matrix ${}^G_T T$, which for the ideal alignment cases is

$${}^G_T T = {}^G_T T^{-1} = \begin{bmatrix} c\alpha_B & -s\alpha_B & 0 & 0 \\ s\alpha_B & c\alpha_B & 0 & 0 \\ 0 & 0 & -1 & d_{z_I} - d_{z_B} - d_{z_T} \\ 0 & 0 & 0 & 1 \end{bmatrix} \quad (6.26)$$

to yield

$${}^G\vec{V}_{m_{vib}} = \begin{bmatrix} 0 \\ 0 \\ -V_Z \cdot \sin(\omega t + \phi) \end{bmatrix} \quad (6.27)$$

The linear velocity due to rigid body rotation of the structure in the global frame is equal to the cross product of the rotational velocity vector with the measurement point position vector.

$${}^G\vec{V}_{m_{rig}} = \vec{\omega} \times {}^G\vec{P}_m \quad (6.28)$$

For the ideal alignment case, using results from the previous section

$${}^G\vec{V}_{m_{rig}} = \begin{bmatrix} 0 \\ 0 \\ \frac{\partial \alpha_B}{\partial t} \end{bmatrix} \times \begin{bmatrix} -c(\alpha_B + \alpha_V)t2\beta_V d_I \\ s(\alpha_B + \alpha_V)t2\beta_V d_I \\ d_{z_I} - d_{z_B} - d_{z_T} \end{bmatrix} \quad (6.29)$$

yields

$${}^G\vec{V}_{m_{rig}} = \frac{\partial\alpha_B}{\partial t} \cdot \begin{bmatrix} -s(\alpha_B + \alpha_V)t2\beta_V d_I \\ -c(\alpha_B + \alpha_V)t2\beta_V d_I \\ 0 \end{bmatrix} \quad (6.30)$$

The total linear velocity at the measurement point is equal to the sum of these two components. The component along the measurement beam direction is equal to the dot product of the total velocity and the laser beam direction. Handling each component separately and noting that the laser beam measurement direction is equal to the negative of the laser beam's incoming direction at the measurement point, the velocity component due to the rigid body rotation of the bladed disk is

$${}^G\vec{V}_{m_{rig}} \cdot (-\vec{N}_{FT}) \quad (6.31)$$

which is equal to zero. This shows that the rigid body rotation of the bladed disk will have no contribution to the measured velocity.

The remaining velocity component is due to the blade vibration along the laser beam direction. With the the vibratory motion defined as

$${}^G\vec{V}_{m_{vib}} = \begin{bmatrix} 0 \\ 0 \\ -V_Z \cdot \sin(\omega t + \phi) \end{bmatrix} \quad (6.32)$$

and the laser beam direction equal to the negative of its incoming direction defined as

$$-\vec{N}_{FT} = \begin{bmatrix} 2c\beta_V s\beta_V c(\alpha_B + \alpha_V) \\ -2c\beta_V s\beta_V s(\alpha_B + \alpha_V) \\ 1 - 2c^2\beta_V \end{bmatrix} \quad (6.33)$$

the velocity component along the laser beam direction is equal to the dot product between the two which is

$$V_{m_{vib}} = c(2\beta_V) \cdot V_Z \cdot \sin(\omega t + \phi) \quad (6.34)$$

This analysis shows that the measured velocity for the ideal alignment case is equal to a constant times the true vibratory velocity, with no other errors. Thus knowing the the normal direction of the blade and the direction of the incoming laser beam the scaling factor can be found and the true blade velocity found from the measured velocity.

6.1.4 Characteristics of Ideal Alignment Case

The ideal alignment case is important for three reasons. First, it is a unique solution for tracking a circular path with constant system parameters. Second, it described the only case for which there will be no tracking error and no velocity error. Because of this it also serves as the condition under which the scan parameters are defined.

The laser path always lies in a single plane defined by the laser source location, the intersection of the vertex mirror and rotation axis, and the vertex mirror normal. The laser path for an arbitrary rotation angle of the structure can be described by the following 2-D figure based on the unfolded laser path.

Based on this figure and previous results, the relationship between the measurement point location, fold mirror location, and vertex mirror angle is

$$R_T = d_I \cdot \tan(2 * \beta_V) \quad (6.35)$$

where R is the distance from the structure's rotation axis to the target point and d_I is defined

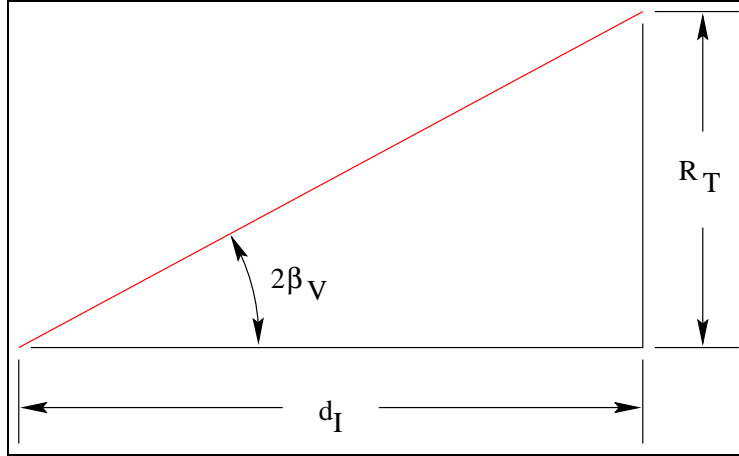


Figure 6.5: Unfolding of Laser Path

in Equation 6.21.

6.2 Single Point Capability

The previous section described several models for determining the measurement point on the bladed disk. From this analysis it is clear that the self-tracking system is capable of tracking a single point on the structure. Given the location of the point in the structure coordinate system and a vertex mirror tilt angle, it is possible to find the fold mirror location that will lock the laser beam to the measurement point.

Using the results for the ideal alignment it is possible to generate scan parameters which will point the measurement point to a point on the bladed disk. Although the three parameters α_V , β_V , and Z_F can be found to track any point on the structure, generally β_V is assumed to be fixed. The procedure for finding these parameters are as follows:

1. Select the target point, P_T on the structure, defined by the coordinates (x_T, y_T, z_T) .
2. Solve for the radial distance, R_T , of the target point from the rotation axis.

3. Solve for the fold mirror location to define a circle at the bladed disk frame with radius R .
4. Find the angle between the line to the target point and the x-axis of the bladed disk frame.
5. Set the vertex mirror rotation angle equal to the above angle

By applying this procedure, the laser beam can be aimed to a single point on the structure and will remain locked to that point as the structure rotates, independent of rotational speed.

While there are a number of combinations of vertex mirror angle and fold mirror location that can be chosen to track a single point, there are several practical considerations that suggest certain combinations.

The first of these is the minimal allowable distance between the bladed disk and the fold mirror. This restriction is most likely to be imposed to allow for adequate air flow into the bladed disk system and to keep the airflow from upsetting the fold mirror. This constraint suggests that the fold mirror be placed as far as possible from the bladed disk. This requirement then requires a shallow vertex mirror angle β_V to be used, which presents no problems to the vertex mirror. The only limitation to the maximum distance between the fold mirror and bladed disk is the maximum working distance of the vibrometer, which for the Ometron VPI should be kept below 30 meters.

The second constraint is imposed by the allowable tilt angle on the vertex mirror and the size of the vertex mirror.

6.2.1 Radial Scan Capability

Although the ability to remain fixed to a single point is useful, the added ability to relocate that fixed point on the structure is advantageous. To change the radial location of the measurement point on the bladed disk, two parameters can be adjusted. The first is the distance between the fold mirror and the bladed disk which is controlled by changing d_I . The second is the tilt angle on the vertex mirror which is controlled by β_V . The preferred technique is to move the fold mirror since it can be performed while the structure is rotating.

6.2.2 Azimuthal Scan Capability

To provide full scanning capability, not only must the radial location be changed as described above, but also the circumferential location. With the proposed system, adjustment for changing the circumferential location of the measurement point is accomplished by rotating the vertex mirror about its x-axis relative to the structure frame. Unfortunately this cannot be done while the bladed disk is rotating.

One solution is to design an electro-mechanical mechanism to mount on the structure for rotating the vertex mirror. The control power, control, and monitoring signals can be fed through a slip ring. This approach greatly increases the complexity of the system and has been dismissed as a possible solution.

A second approach is to develop an optical system that can change the azimuthal measurement location without disturbing the structure. This approach has been studied in outline by Dr. Andy Barker. An optical arrangement has been devised that will allow for azimuthal adjustment, but this technique has not been verified experimentally. The proposed system uses a pair of perpendicularly mounted mirrors in place of the fold mirror and a dove prism along the laser path from the vertex mirror to the now fold mirror. The one limitation to

this technique is the limited field of view through the dove prism which can be overcome by placing it close to the vertex mirror. While both approaches are technically feasible, they are not addressed here due to the added complexity to the basic self-tracking system. Instead this work will concentrate on single point tracking only.

6.2.3 Experimental Verification of Ideal Alignment Performance

With the theoretical performance of the self-tracker under the ideal alignment condition described, it is now possible to determine how well these conditions can be met in practice. As discussed in Chapter 5, as part of the initial test-rig setup the self-tracker system was aligned.

6.2.4 Summary

The analysis of the self-tracker under ideal alignment conditions has been performed. The general three-dimension model was solved in closed to predict the position and velocity errors. An alternative viewpoint of the system which removes the fold mirror was developed, resulting in a simplified model of the self-tracker. A quasi-two dimensional model was developed from the full three-dimensional model.

Results show that for the ideal alignment case, the measurement point is fixed to a single point on the structure regardless of rotational speed. The measured velocity will contain no components due to the structures rotation. The measured velocity is equal to a scaled version of the actual velocity with a constant scaling factor related to the vertex mirror tilt angle. The capability of the system to perform radial scans has also been shown. The only limitation is that the self-tracker, in its present configuration, is not able to easily perform complete scans of the structure due to the lack of circumferential scanning capability.

With the performance of the ideal alignment case defined, the effects of violation of the ideal alignment case can now be studied.

Chapter 7

Misalignment Cases

The previous chapter described the performance of the self-tracker when the system is perfectly aligned. Two significant results were shown for the ideal alignment case. First, the measurement beam remains fixed to a single point on the rotating structure, tracking the target point with no position error. Secondly, the vibrometer measures a scaled version of the target point's vibratory velocity with no velocity error. In practice, the ideal alignment condition can only be nominally achieved as was demonstrated in the experimental results for the ideal alignment case. Since some residual misalignments will always be present, it is useful to determine their effect.

Misalignments introduce two types of error; position errors and velocity errors. Position errors can be attributed solely to the alignment of the self-tracker's components and are independent of the laser vibrometer's operating principle. However the velocity errors are related to both the position errors and the vibrometer's operating principle. Therefore, the position errors discussed here will be the same for any transduction technique used with the self-tracker. However, the velocity errors are directly related to the vibrometer, and are not applicable to other transduction techniques.

In general, two classes of misalignment are possible; static misalignments which remain constant with time and dynamic misalignment which vary with time. Static misalignments typically result from improper set-up of the self-tracking system and are somewhat within the control of the experimenter. Once identified they can usually be minimized. Dynamic misalignments are generally caused by the dynamics of the rotating structure, motions which are beyond the control of the experimenter, unless the structure is adequately balanced and supported. If this is not done, the dynamic motions may be quite complex and highly dependent on the specific application. For this reason, only static misalignments are studied here. Although it may appear that this limits the usefulness of this study, the results from the static misalignment cases can be used to define allowable envelopes on the dynamic motion of the structure. While this does not provide all the information as would be found for dynamic misalignments, it does provide a starting point for a more extensive study. Additionally, only static misalignment between the bladed disk and the combined vibrometer-fold mirror structure are considered here.

Static misalignments are studied for two reasons. First, by determining the size of the position and velocity errors resulting from misalignments, the level of alignment needed to achieve a required level of position and velocity error can be found. Secondly, when the effects of misalignments are seen in practice, an understanding of the mechanisms that cause the misalignments will prove valuable in identifying the necessary adjustments for reducing these effects.

Using the analytical model of the self-tracker, it is possible to examine the effects of static misalignments on the position and velocity errors. The approach consists of first introducing each misalignment into the general three-dimensional model and noting the corresponding effects. While it is possible to solve for the position and velocity errors analytically to find closed form solutions as in the ideal alignment case, the complexity of the results for the non-ideal alignment cases motivate using an alternative approach. Here the simulation model, which is based on the same analytical model used for the ideal alignment case is

used. The misalignment conditions are entered into the simulation and the resulting errors are calculated for discrete angular rotation positions of the bladed disk. This is performed for a full revolution of the bladed disk for each of the static misalignment cases considered.

7.1 Definition of Misalignment Cases

To reduce the misalignment cases to examine to a small set, the actual configuration of the self-tracker needs to be recalled. It was shown in Chapter 5 that to track a single point, several constraints defining the ideal alignment case had to be met. One of these constraints, the alignment between the fold mirror and vibrometer, requires the fold mirror to be perpendicular to the laser beam. This constraint can be met in hardware by attaching the vibrometer and a linear slideway to the mounting bar and attaching the fold mirror to the slideway. Once these components are aligned to each other, the entire traverse can be moved as a unit and aligned to the rotating structure. With this configuration, only three misalignments are possible:

1. Laser beam parallel to the bladed disk's rotation axis but not collinear with rotation axis
2. Laser beam not parallel to the bladed disk's rotation axis but intersects vertex mirror at rotation axis
3. Laser beam not parallel to the bladed disk's rotation axis and does not intersect vertex mirror at rotation axis

These misalignment cases, along with the ideal alignment case, are shown schematically in Figure 7.1. Each of these misalignments can be introduced into the analytical model by moving the displaced frame relative to the ideal alignment frame. The first misalignment

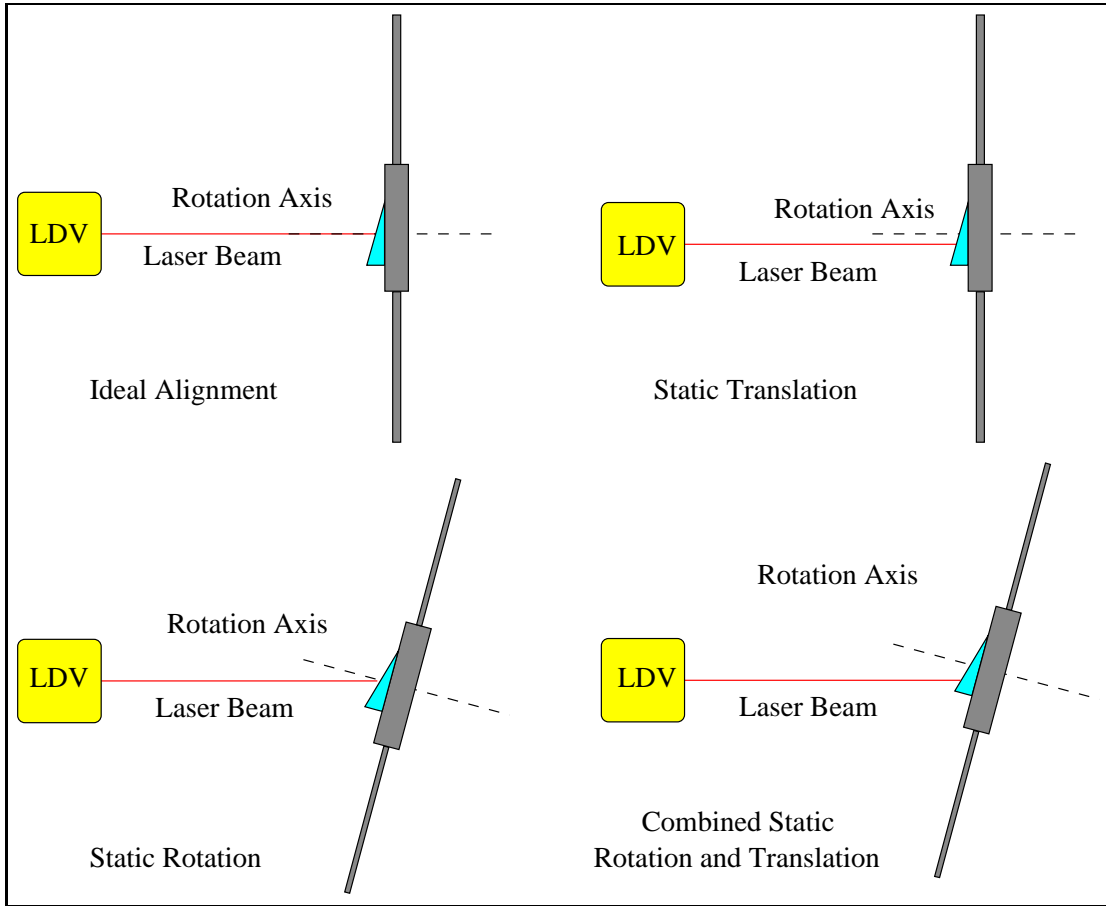


Figure 7.1: Static Misalignments

results when there is a non-zero translation of the static frame relative to the ideal alignment condition. The second results when there is a non-zero rotation of the displaced frame relative to the ideal alignment frame. The third conditions exists when there are both non-zero translation and non-zero rotation of the displaced frame relative to the ideal alignment frame. While each misalignment can be classified as based on the orientations of the structure's rotation axis and the incoming laser beam direction, an alternative classification can be considered.

Recalling the simplified model for the ideal alignment case, only two parameters were needed to predict the radial location of the measurement spot on the target plane. These two parameters are the distance from the cone vertex to the target plane and the vertex angle. It was shown that for the ideal alignment case that these two parameters remain constant with rotation angle. Each of the three misalignment cases can also be described in terms of these parameters as listed below:

- Ideal Alignment
 - Fixed vertex angle
 - Fixed vertex location
- Translational Misalignment
 - Fixed vertex angle
 - Time varying vertex location
- Rotational Misalignment
 - Time varying vertex angle
 - Fixed vertex location
- Translational and Rotational Misalignments

- Time varying vertex angle
- Time varying vertex location

All three of these classifications, based on the orientation of the laser beam and rotation axis, the relationship of the displaced and ideal alignment frames, and the time varying nature of the vertex location and angle, are used to describe the effects of misalignments on the position and velocity errors.

7.2 Contributors to Position and Velocity Errors

The results from Chapter 6 showed that for the ideal alignment case, the self-tracker can track a single point with no position error. This characteristic is directly related to the fact that the vertex location and angle remained fixed throughout a revolution of the bladed disk. Thus it is expected that the time varying nature of the vertex location and angle will introduce position errors in the misalignemnt cases as a direct result of these parameters changing.

The same conditions that eliminated tracking error in the ideal alignment case also contribute to the lack of velocity error. In the case of the vertex mirror there is no linear velocity at the intersection between the laser beam and the vertex mirror. Additionally it was shown that the plane containing the laser beam path remained perpendicular to the bladed disk's rigid body velocity vector. Therefore there was no component of the rigid body velocity along the laser beam direction and hence no noise contributor due to the blade's rotation. Lastly, since the measurement point remained fixed to a single point, there was no speckle noise. Another condition, which is not exactly a noise source, was the fixed angle between the laser beam direction and the target planes normal. The combination of these conditions resulted in a noise free velocity signal whose magnitude was a scaled version of the traget

Table 7.1: Model Parameters

Frame	Rotations Radians			Displacements Meters		
	α	β	γ	d_x	d_y	d_z
Laser	0	0	0	0	0	0
Fold Mirror	0	0	0	0	0	1.016
Ideal Aligned	0	π	0	0	0	2.347
Displaced	0	β_D	β_D	d_{x_D}	d_{y_D}	0
Bladed Disk	α_B	0	0	0	0	-0.032
Vertex Mirror	0	0.026	0	0	0	0.032
Target Plane	0	0	0	0.140	0	0.006

planes velocity. Since these conditions are violated in the misalignment cases, it is expected that there will be a corresponding velocity error.

The first step in performing the sensitivity analysis for static misalignments is to introduce known misalignments into the model and note the effects on the position and velocity errors. These misalignments are introduced into the ideal alignment case and are described by the parameters listed in Table 7.2.

Once the qualitative effects of the misalignments have been identified, the full three-dimensional model can be simplified to isolate the identified effects. These results can then be experimentally verified within the constraints of the test rig. This approach will be used for the first two misalignment cases to confirm the model prediction. The third misalignment case, with combined translational and rotational misalignments, is investigated using the simulation model only due to limitations in the test rig.

To illustrate the effects of misalignment, several plots are created. The first set of plots characterize the position errors. The first plot shows the path of the measurement point paths on the target plane. A second shows the variation of the position error as the difference from the mean value of position error.

The second set of plots characterize the velocity error. In the first plot shows the velocity induced by the rotation of the vertex mirror and and the rigid body motion of the blade. The second plot shows the scaling factor that must be applied to the measured component of the vibratory velocity to find the true velocity.

7.3 Translational Misalignments

Translational misalignemnts are introduced into the model by displacing the displaced frame relative to the ideal alignment frame as shown in Figure 7.2.

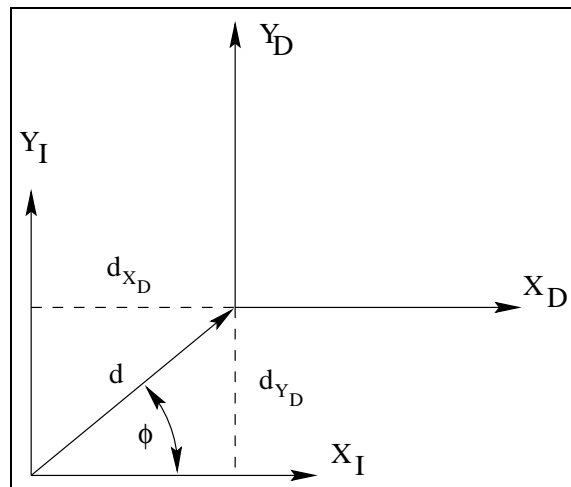


Figure 7.2: Introduction of Translational Misalignments

This shift is equal to $d = \sqrt{d_{X_D}^2 + d_{Y_D}^2}$ in the direction $\arctan d_{Y_D}/d_{X_D}$. There are two effects due to translational misalignment that contribute to the tracking error. The first, and most dominant effect, is to change the location of the target point in the global coordinate frame as shown in Figure 7.3.

The difference between the target and measurement points due to this shift is equal in magnitude and direction to the translational misalignment.

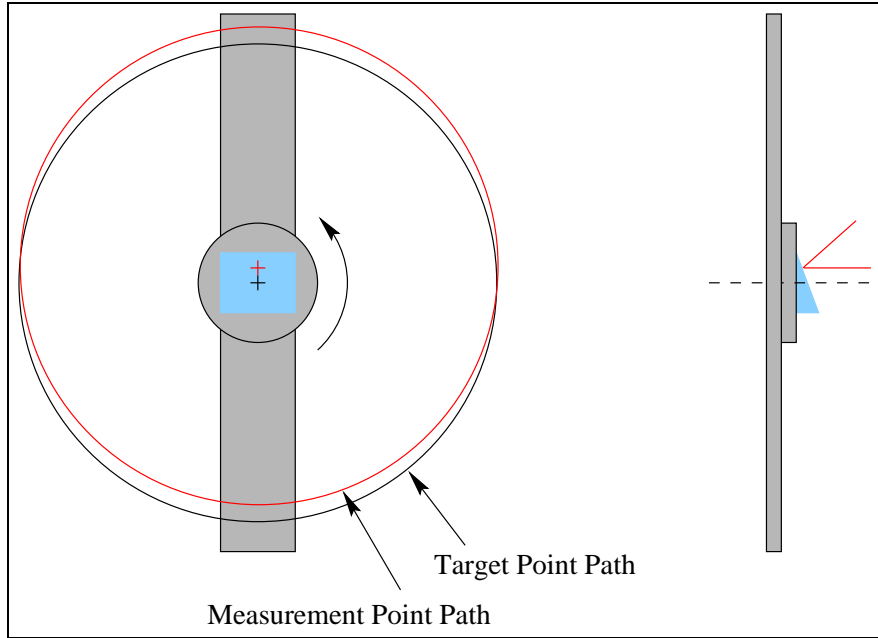


Figure 7.3: Shift in Target Point Path due to Translational Misalignment

The effect of this translation can also be viewed based on the path of the measurement point on the target plane. As shown in Figure 7.4, as the blade rotates through an angle of α_B , the target point rotates through the same angle.

The measurement point remains a fixed distance away from the target point and moves around a circular path in a direction opposite to the blade's rotation. As the blade and target plane make a full counter-clockwise rotation, the target plane also rotates relative to the measurement point, resulting in the measurement point tracing a clockwise circular path on the target plane.

The second effect due to the translation misalignment is the change in the distance between the fold mirror and intersection point of the laser and vertex mirror as the structure rotates. This effects is shown in Figure 7.5 for the two extreme positions of the vertex location.

Since the translational misalignment move the locations of the vertex and measurement point relative to the ideal alignment case, the position errors are expected to be accompanied by

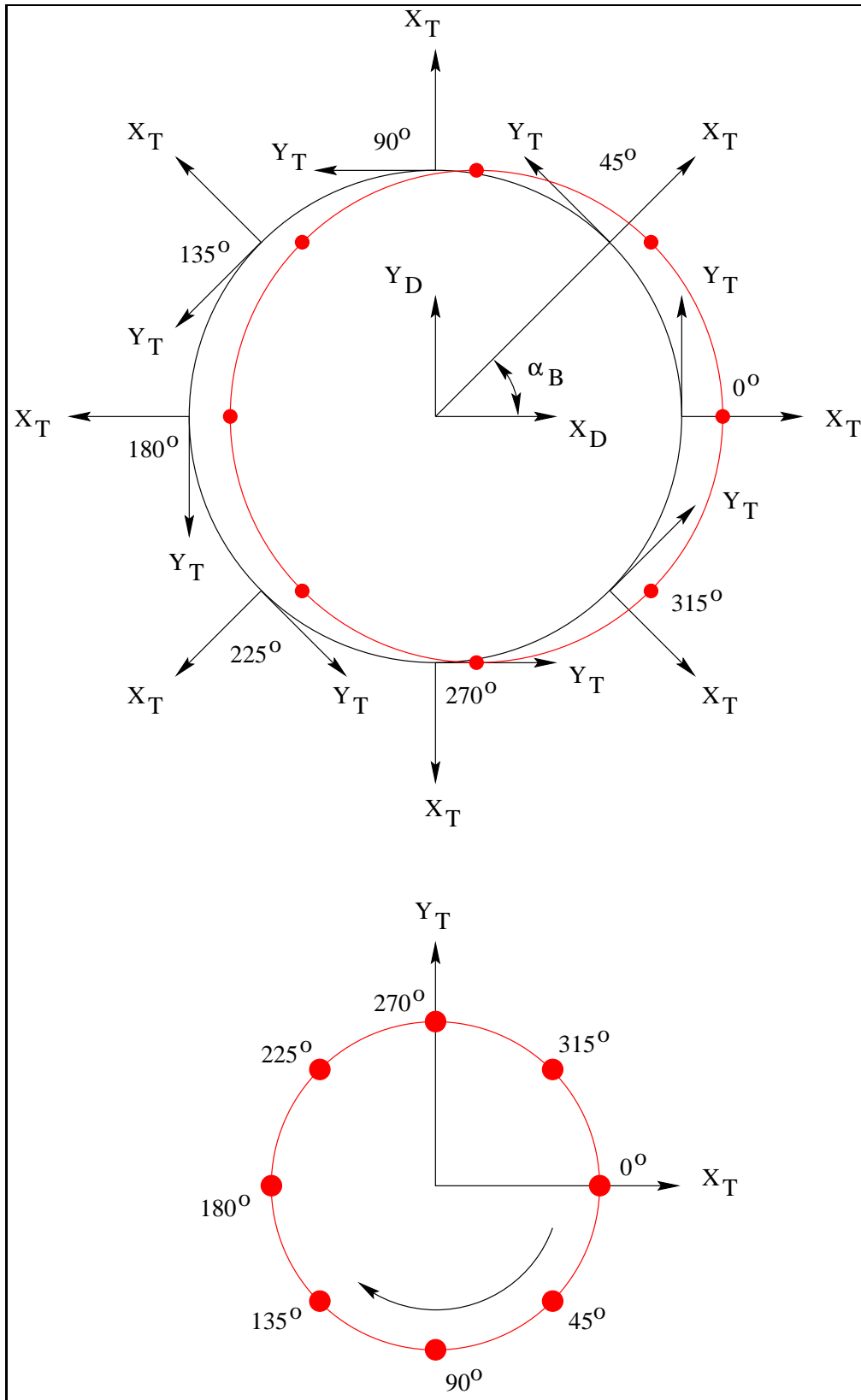


Figure 7.4: Measurement Point Path on Target Plane

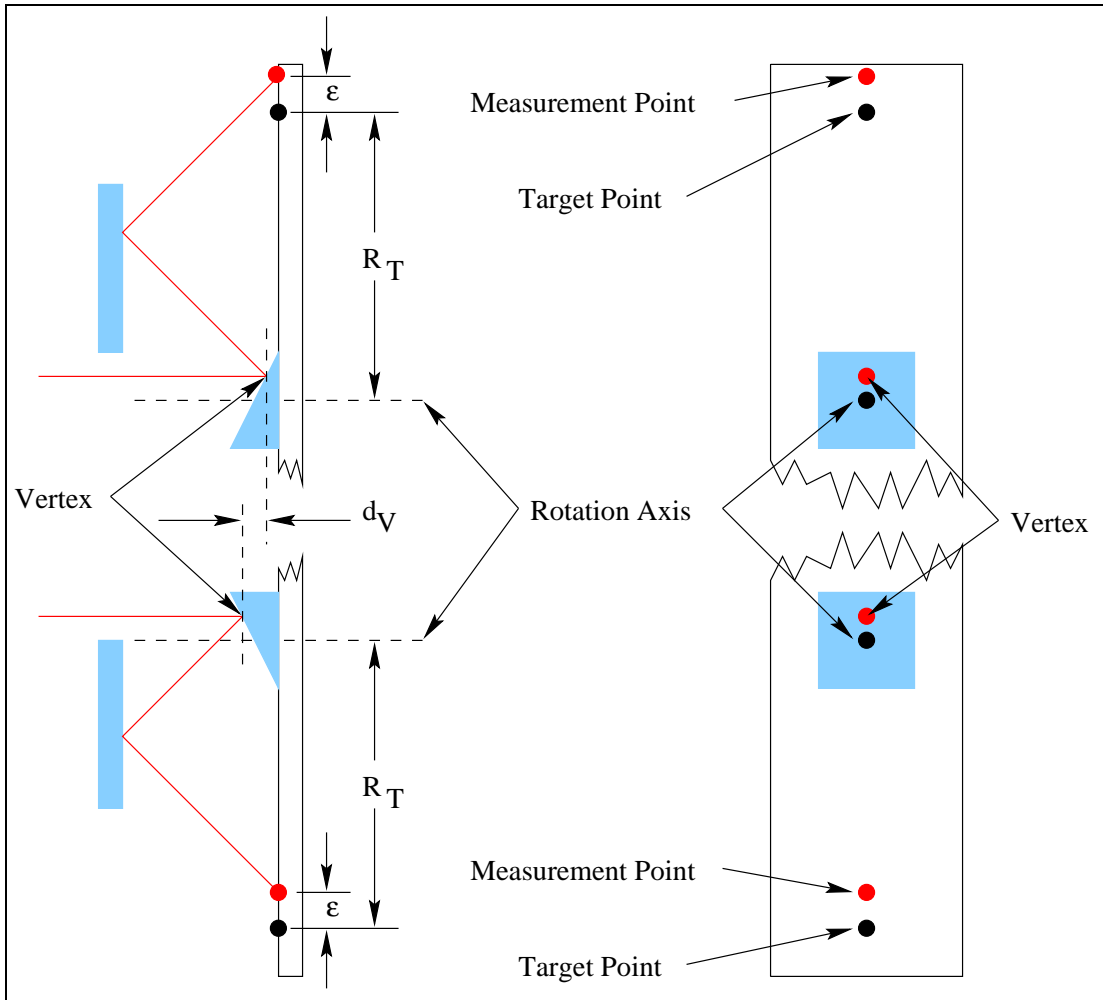


Figure 7.5: Vertex Motion for Translational Misalignment

velocity errors. This is caused by two effects, a linear velocity component caused by the rotation of the vertex mirror, and a component of the blade rotation. A detailed explanation of these two velocity components is given following discussion of the simulation results.

7.3.1 Simulation Results

To determine the effects of the translational misalignments, several simulation were performed with different amounts of translation in different directions. In the first set of simulations, all displacements were performed in the d_{X_I} direction to study the effect between the magnitude of the translational misalignment and the position and velocity errors. Translations ranging from -5mm to 5mm in 1mm increments where introduced between the displaced and ideal alignment frames.

In the second set of simulations, a fixed amount of displacement was introduced in several directions to study the directional effects of the translational misalignments. The origin of the displaced frame was moved in 45° increments around a 2mm radius circle.

Figures 7.6 through 7.24 show the position and velocity errors predicted by the simulations, with the results summarized in Tables 7.3.1 and 7.3.1.

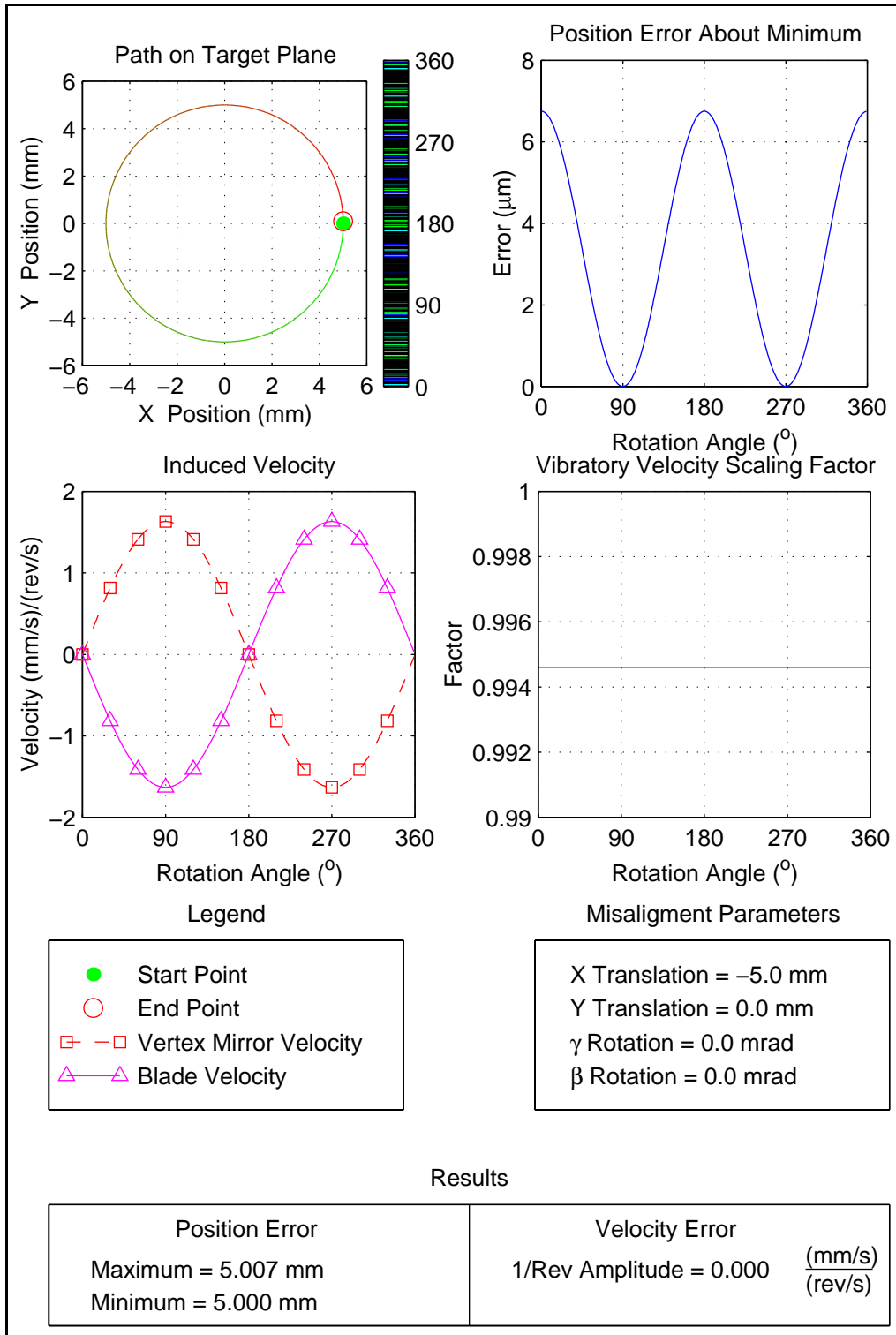


Figure 7.6: Translational Misalignment, Magnitude Effects, $d_X=-5$ mm

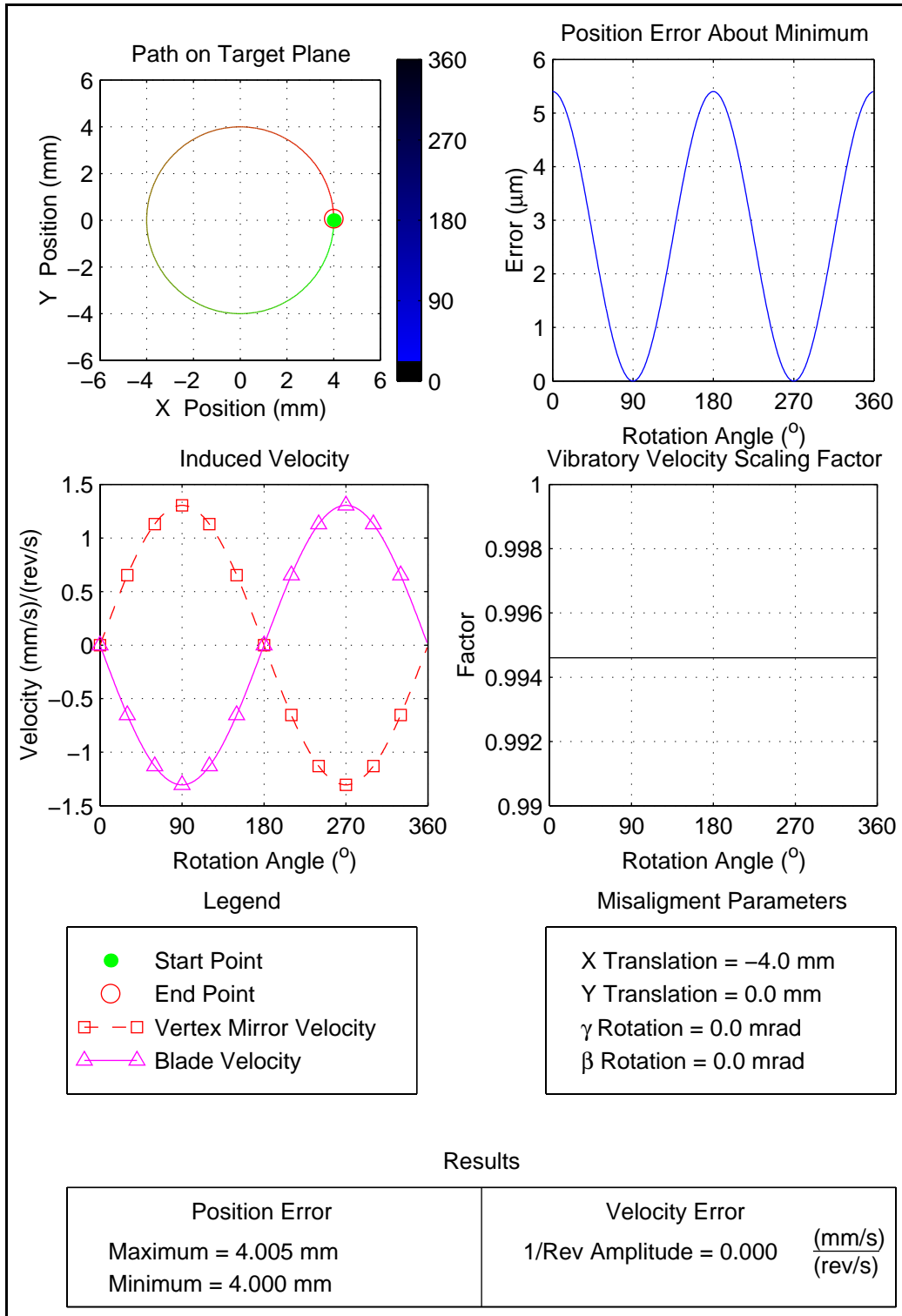


Figure 7.7: Translational Misalignment, Magnitude Effects, $d_X=-4$ mm

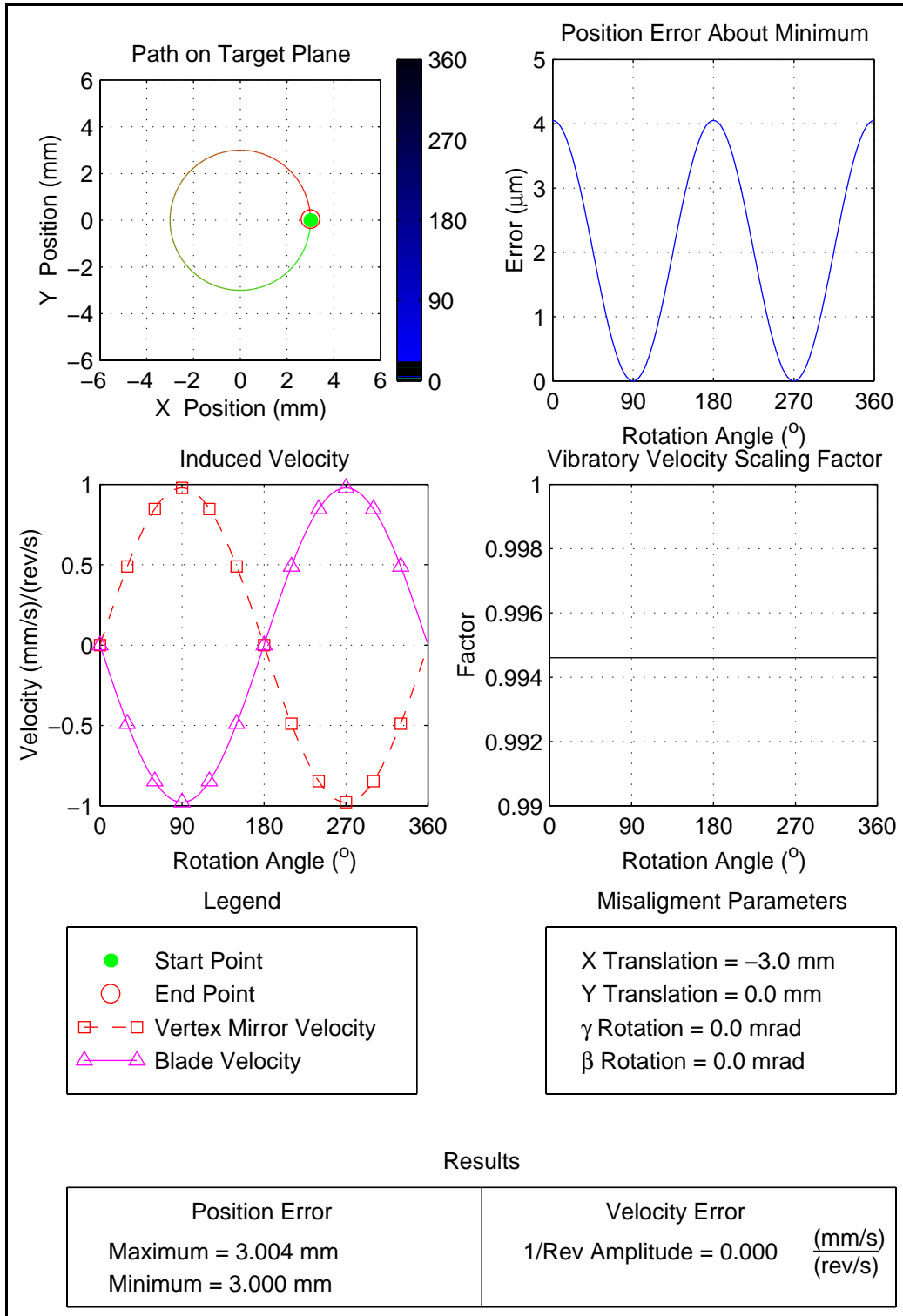


Figure 7.8: Translational Misalignment, Magnitude Effects, $d_X = -3$ mm

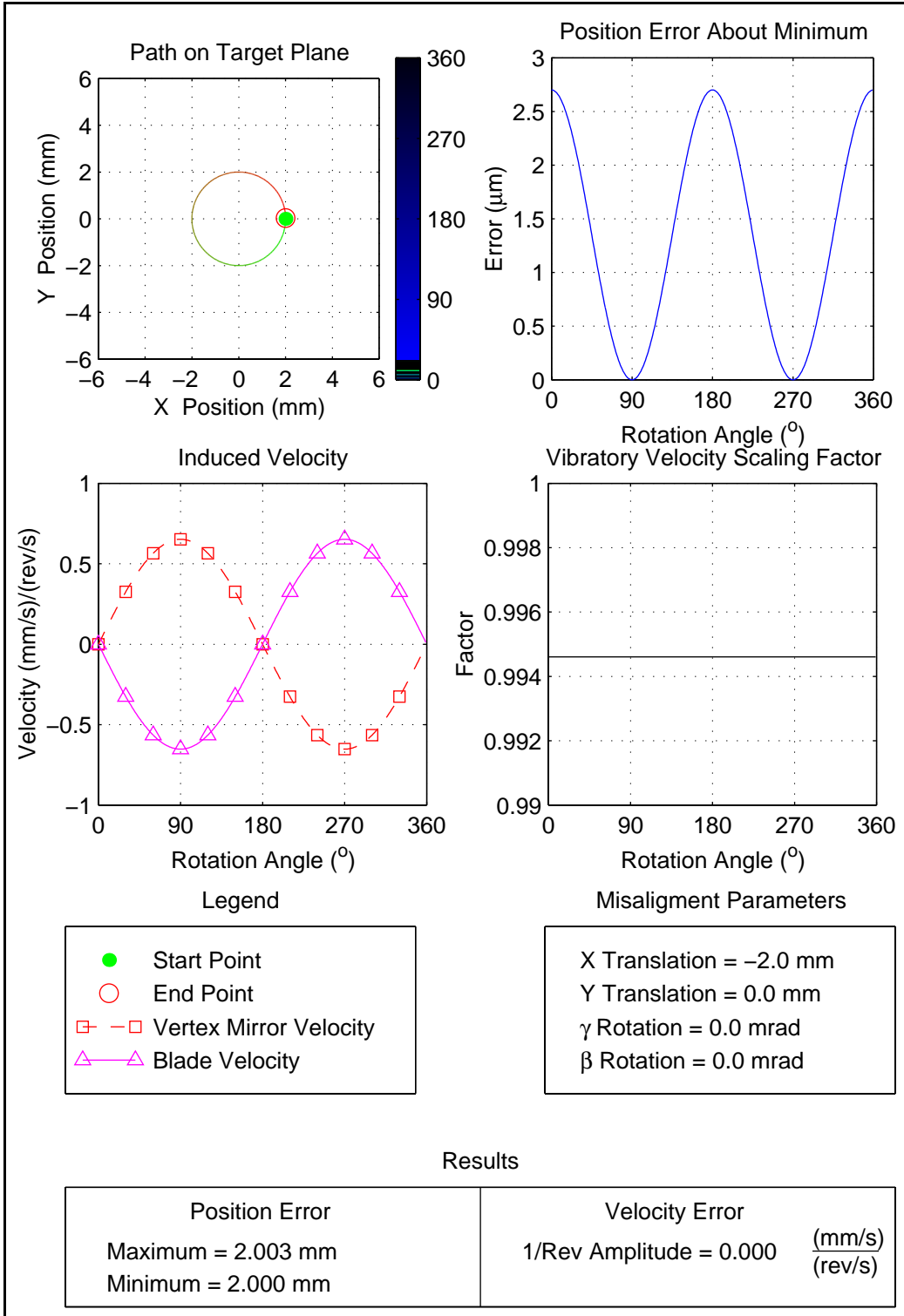


Figure 7.9: Translational Misalignment, Magnitude Effects, $d_X = -2$ mm

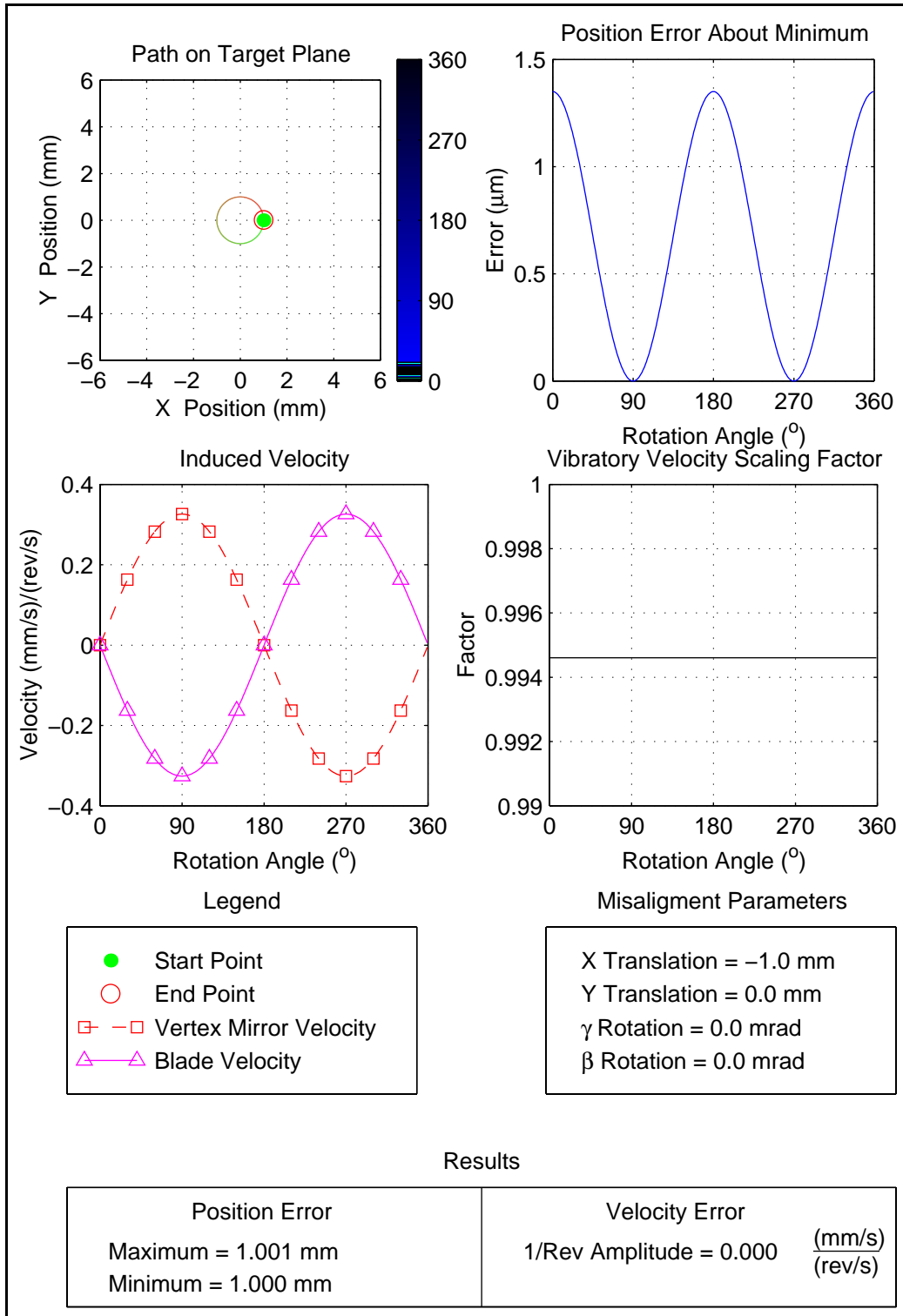


Figure 7.10: Translational Misalignment, Magnitude Effects, $d_X = -1$ mm

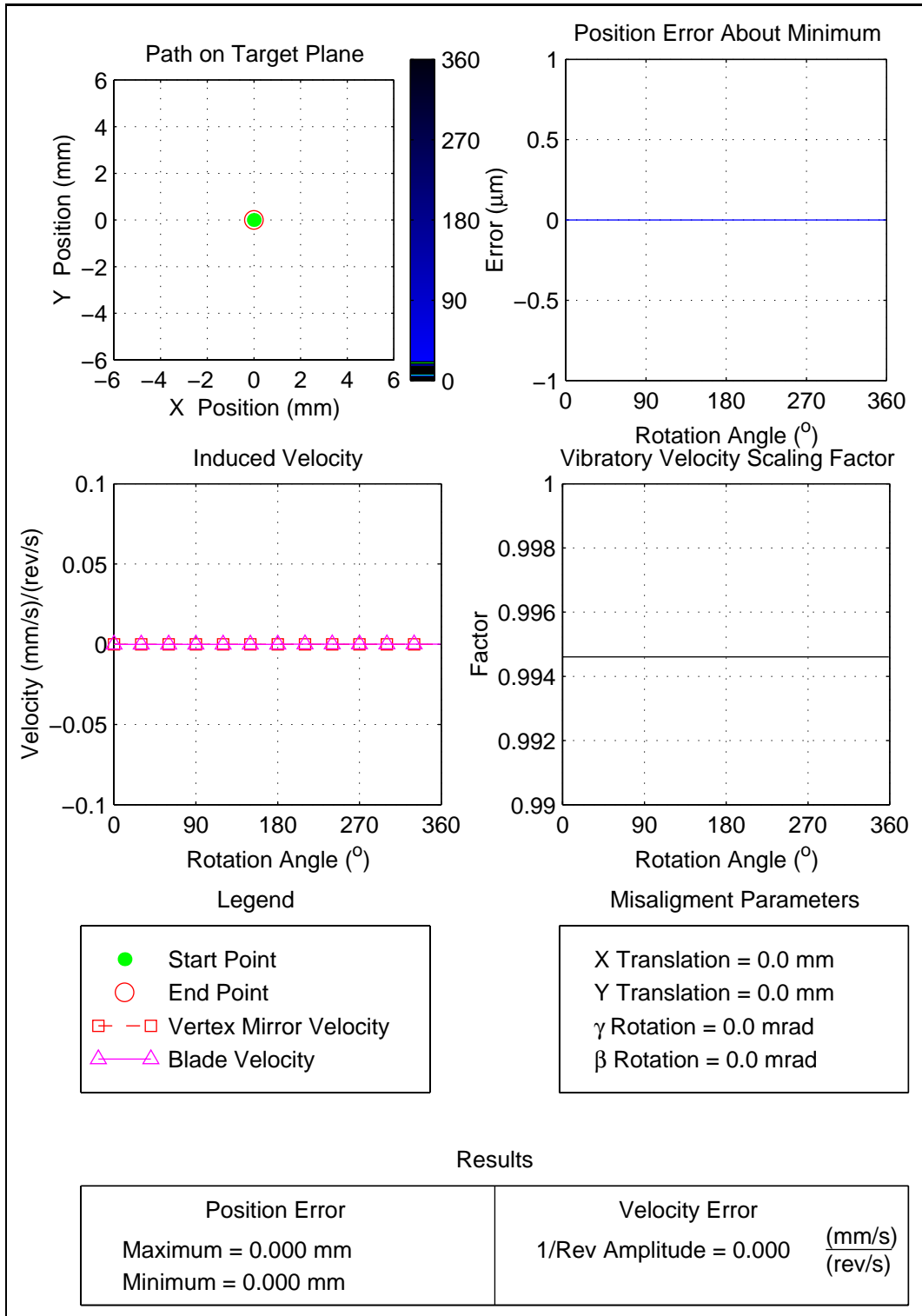


Figure 7.11: Translational Misalignment, Magnitude Effects, $d_X=0$ mm

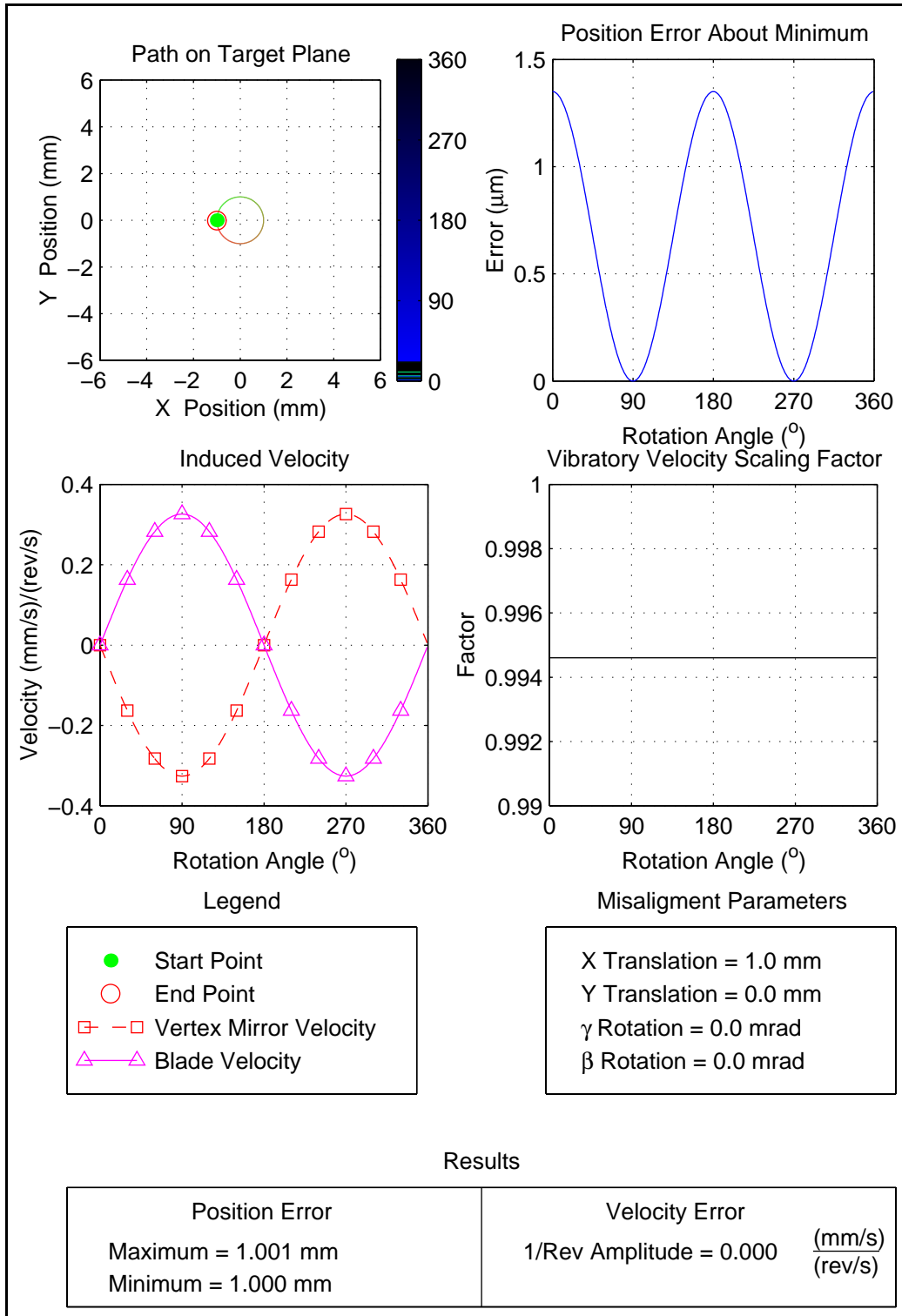


Figure 7.12: Translational Misalignment, Magnitude Effects, $d_X=1$ mm

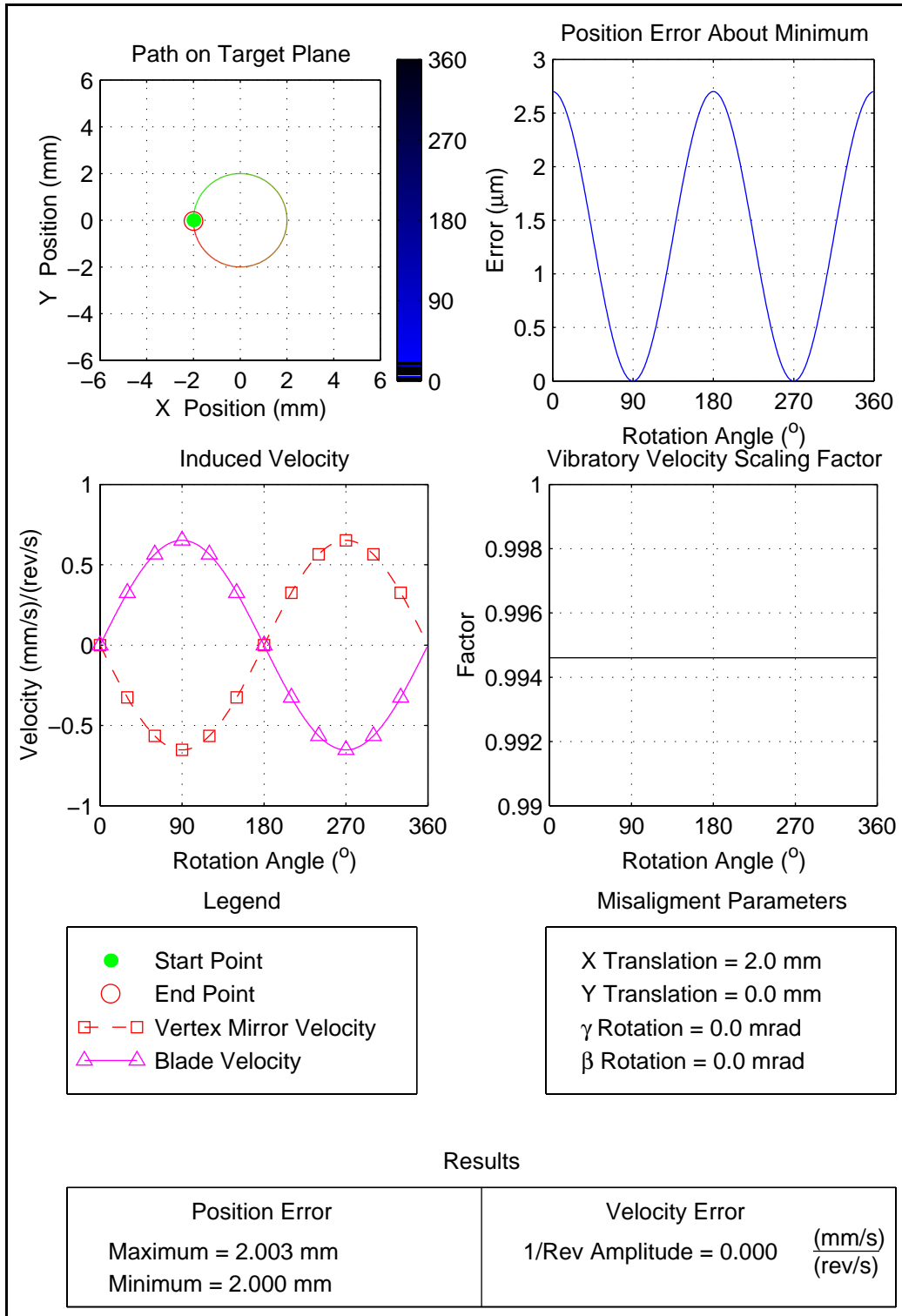


Figure 7.13: Translational Misalignment, Magnitude Effects, $d_X=2$ mm

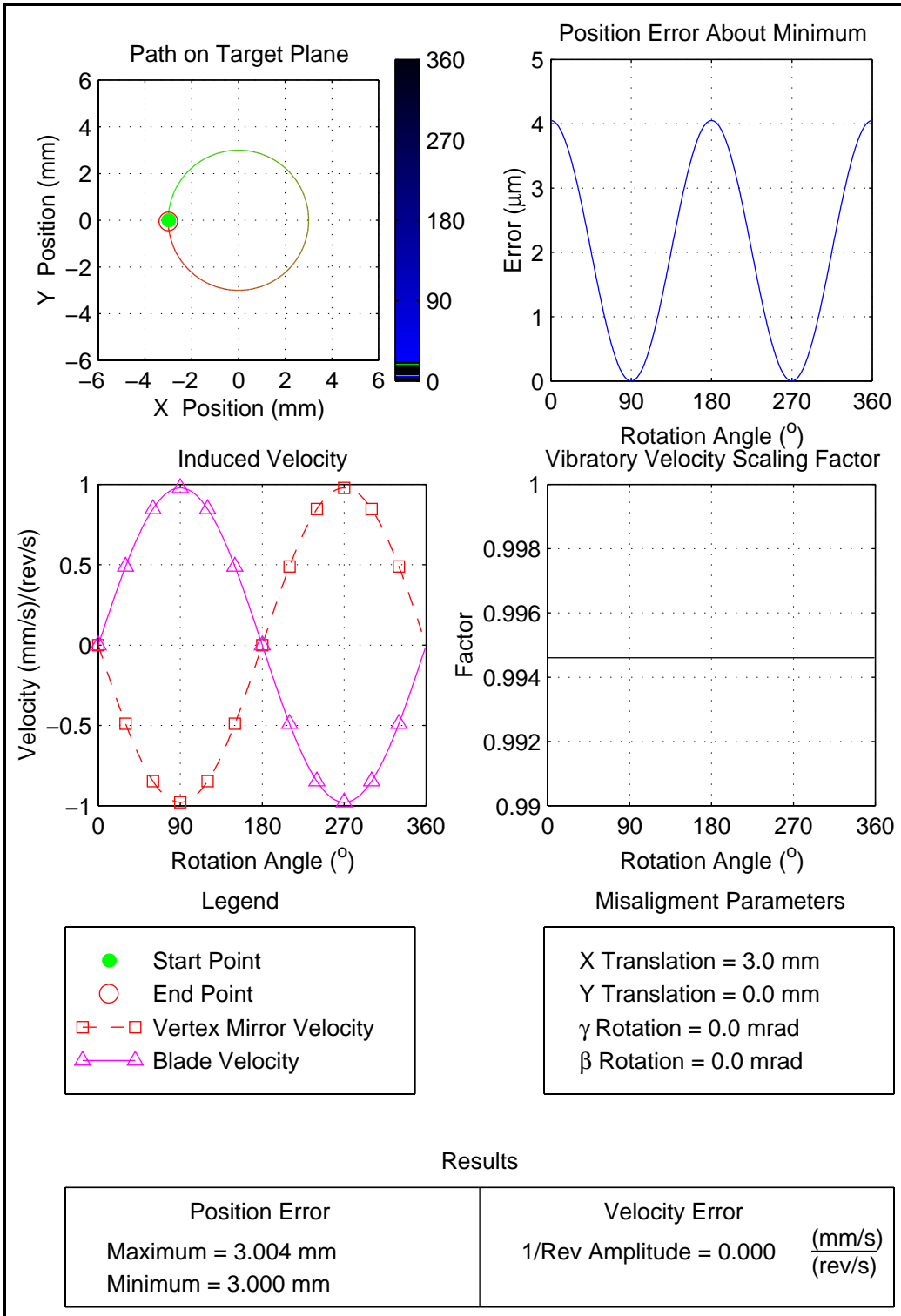


Figure 7.14: Translational Misalignment, Magnitude Effects, $d_X=3$ mm

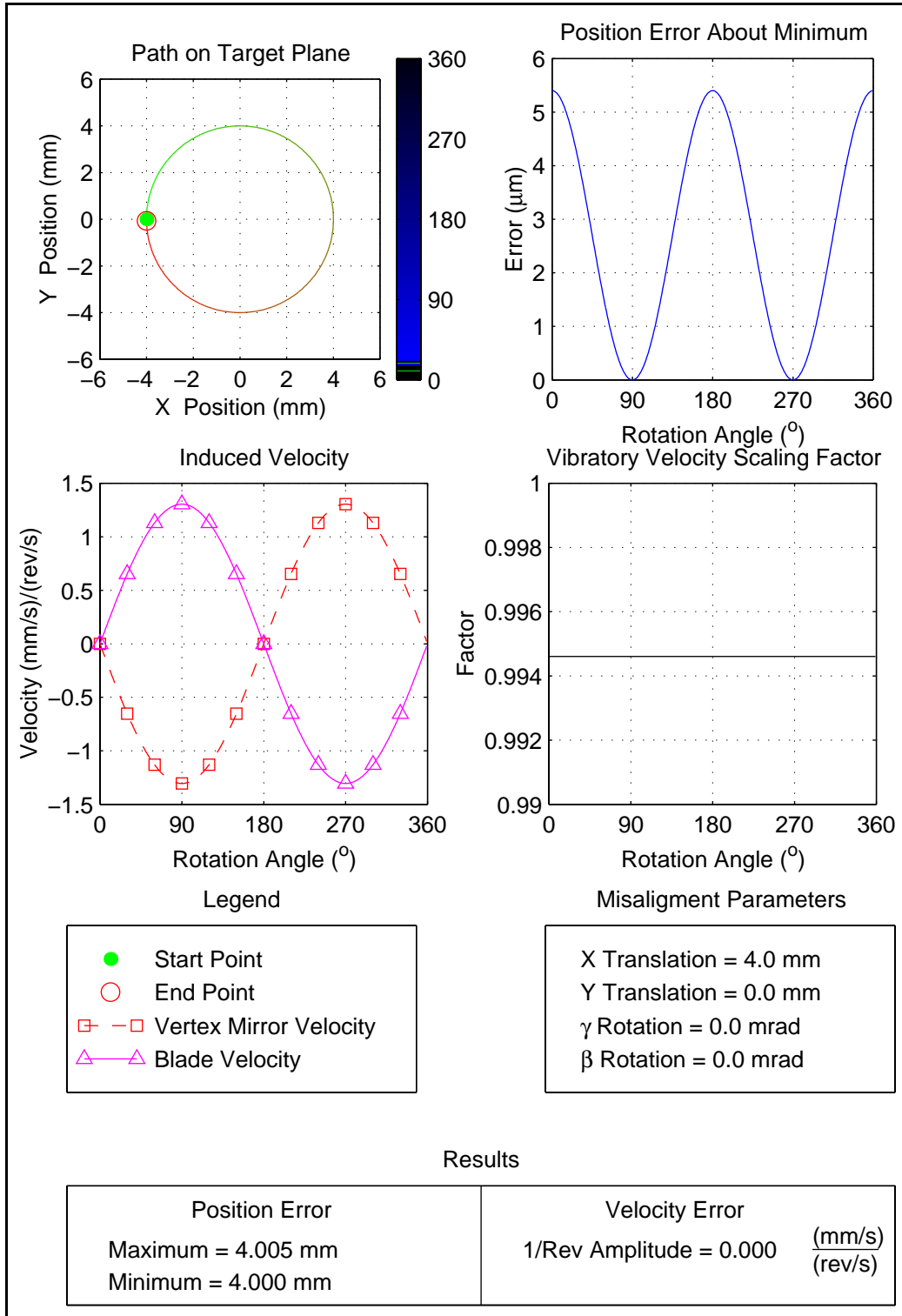


Figure 7.15: Translational Misalignment, Magnitude Effects, $d_X=4$ mm

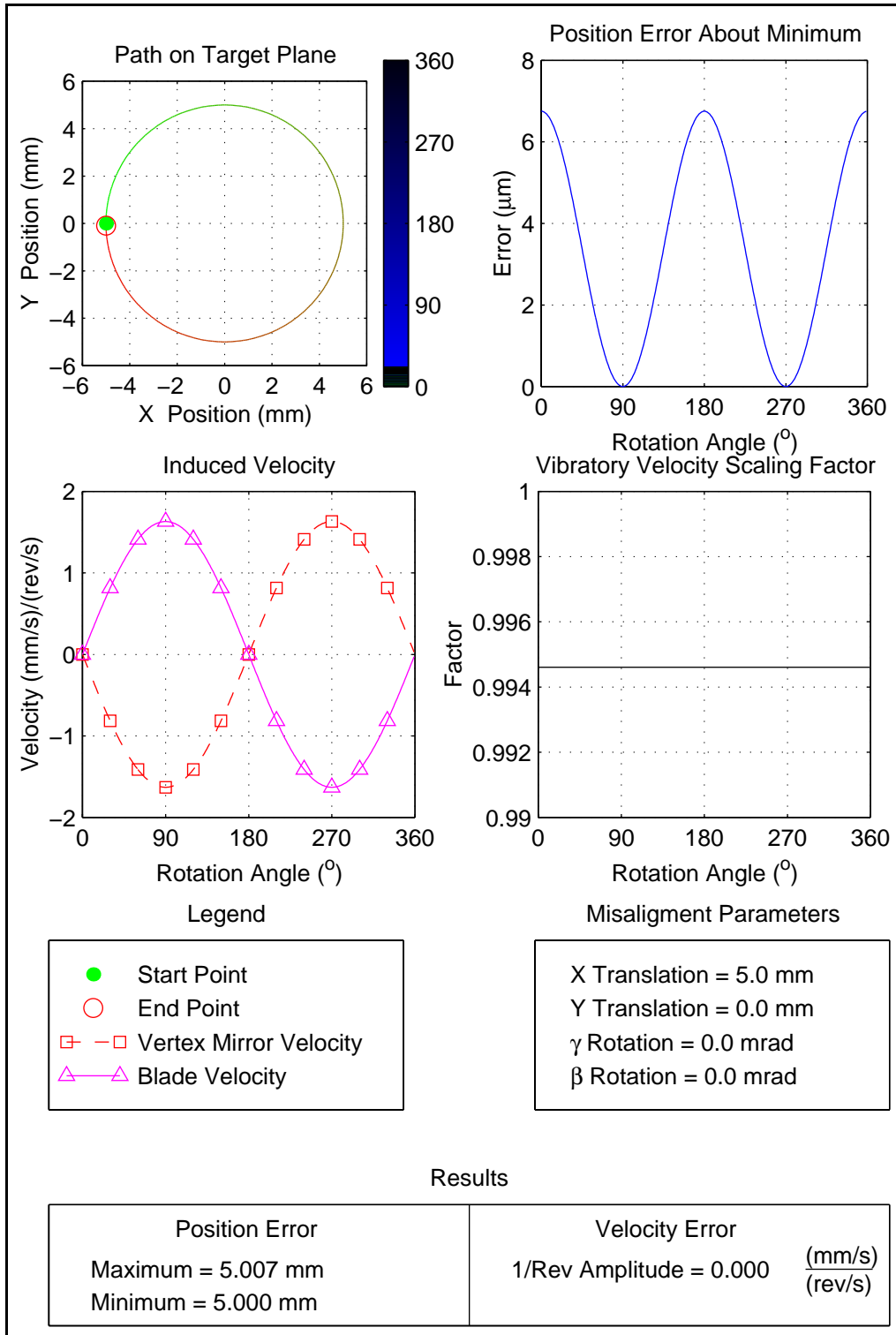


Figure 7.16: Translational Misalignment, Magnitude Effects, $d_X=5$ mm

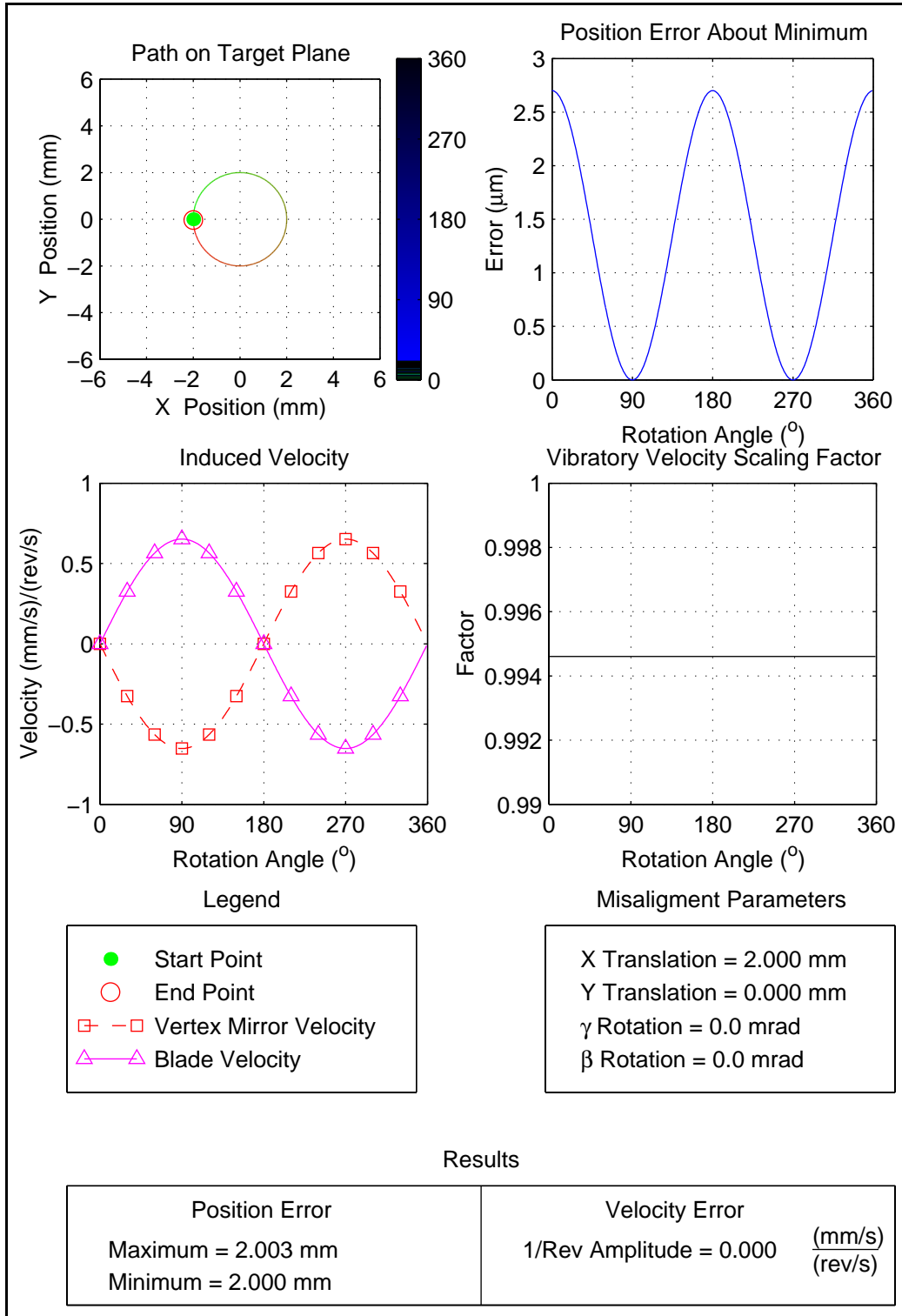


Figure 7.17: Translational Misalignments, Directional Effects, $d_X=2$ mm, $d_Y=0$ mm

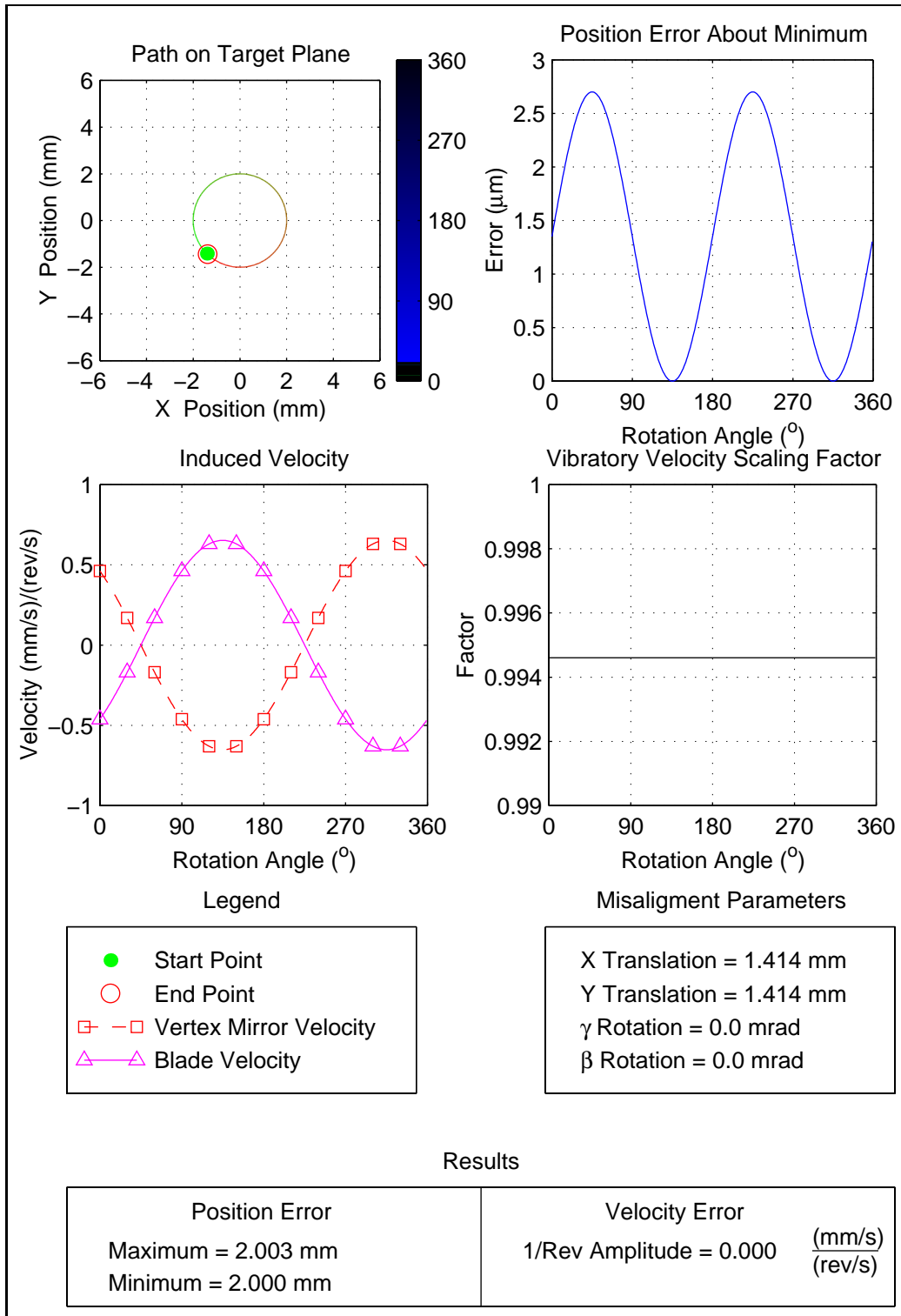


Figure 7.18: Translational Misalignments, Directional Effects, $d_x=1.414$ mm, $d_y=1.414$ mm

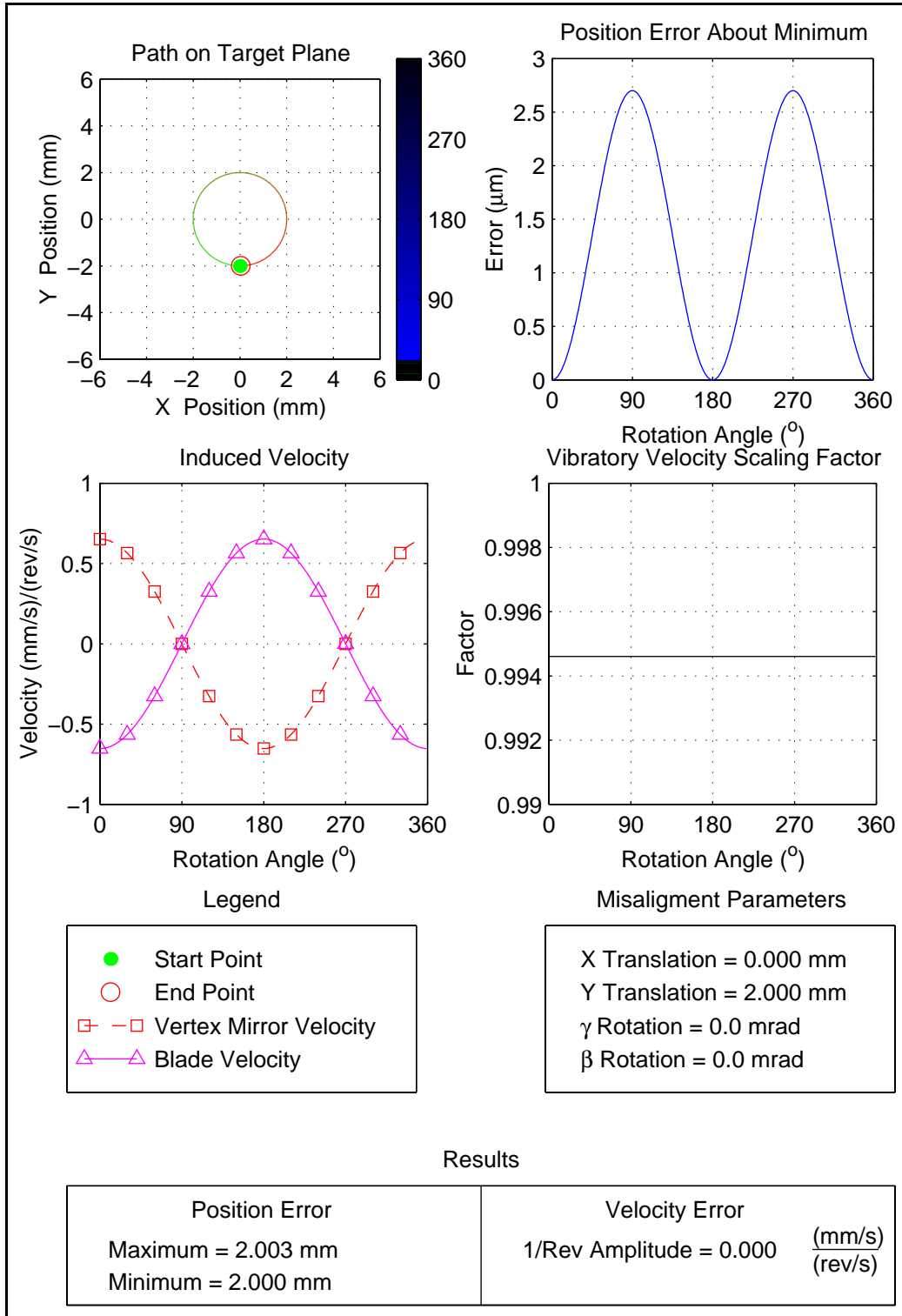


Figure 7.19: Translational Misalignments, Directional Effects, $d_X=0$ mm, $d_Y=2$ mm

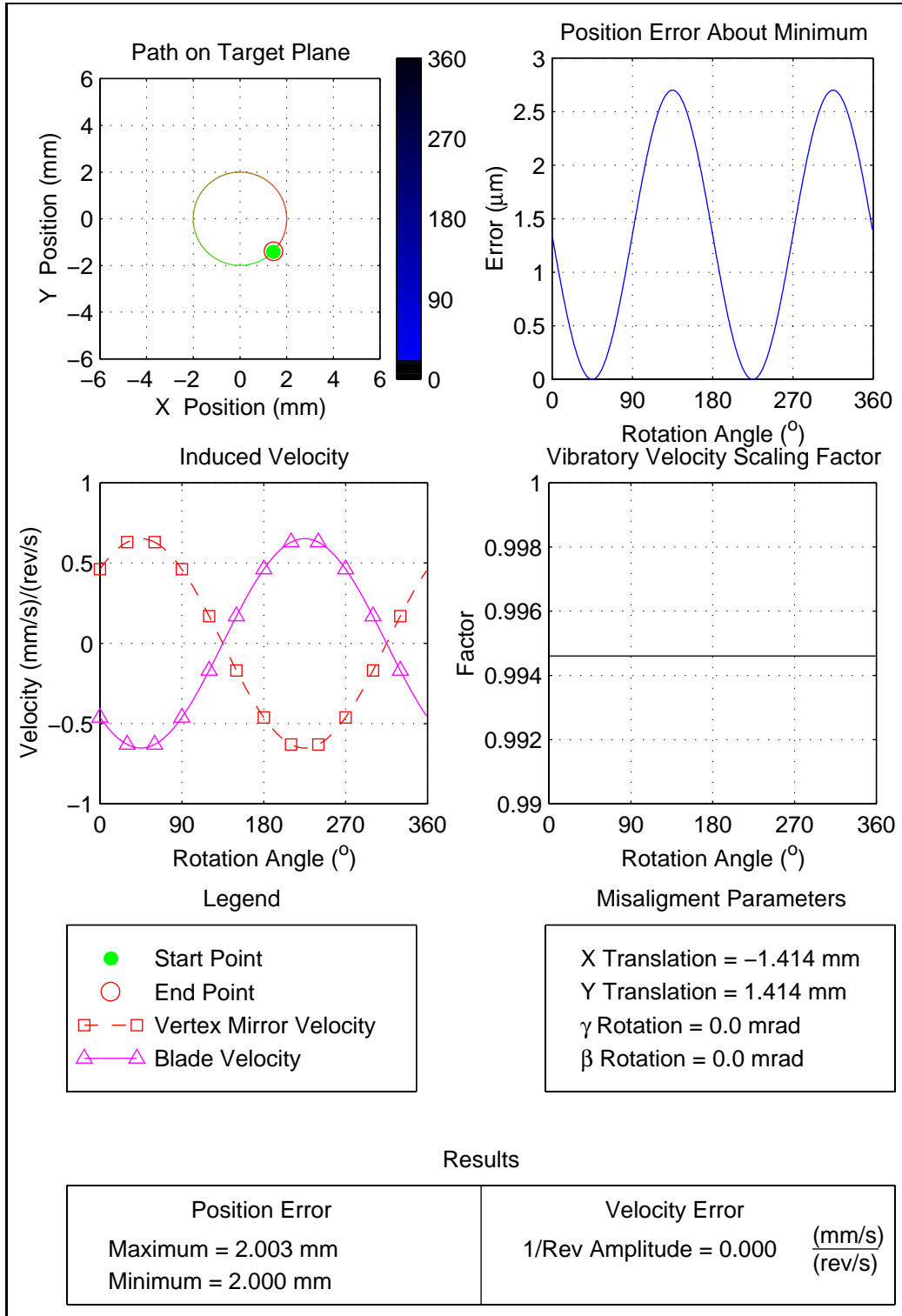


Figure 7.20: Translational Misalignments, Directional Effects, $d_X = -1.414$ mm, $d_Y = 1.414$ mm

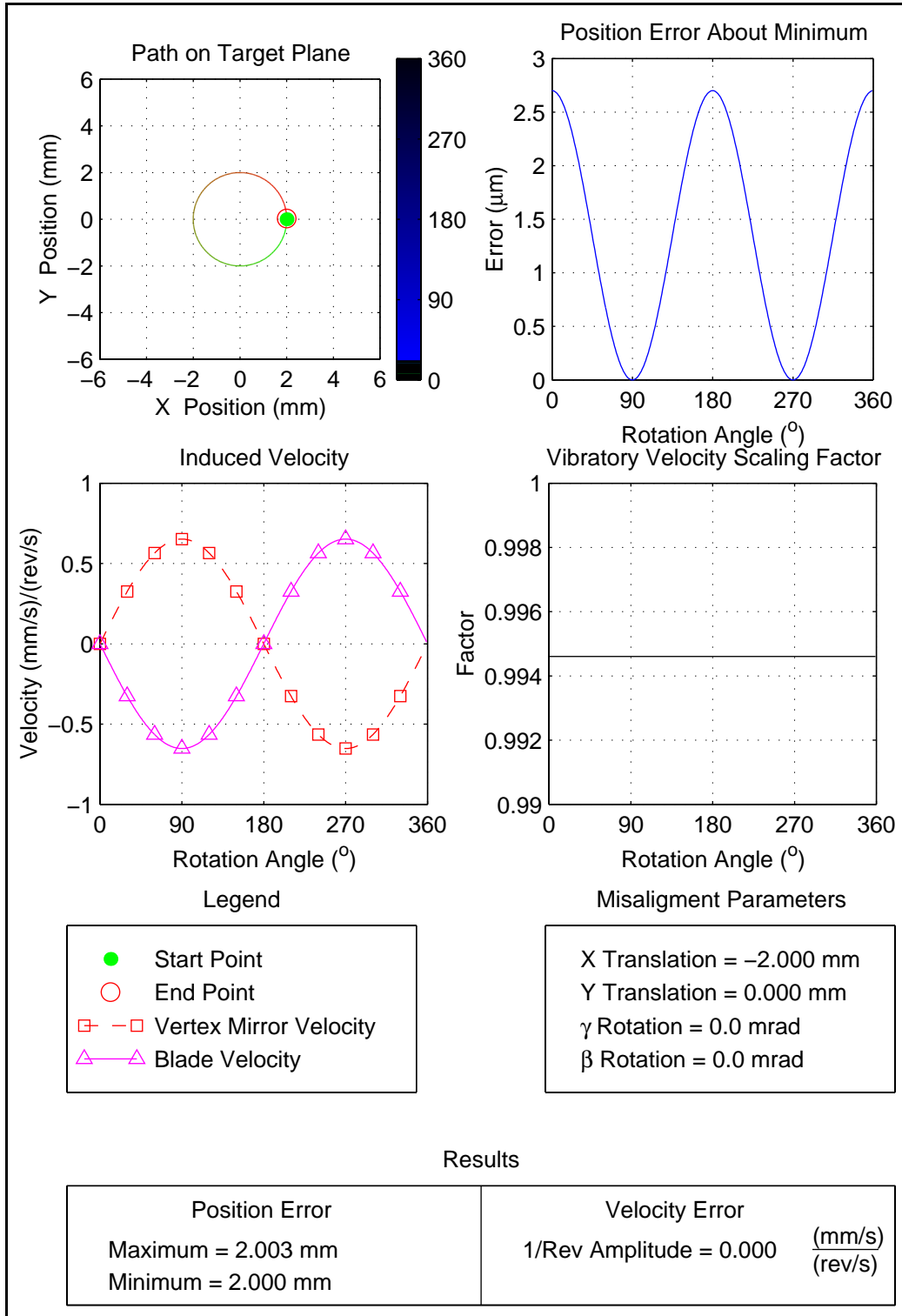


Figure 7.21: Translational Misalignments, Directional Effects, $d_X = -2$ mm, $d_Y = 0$ mm

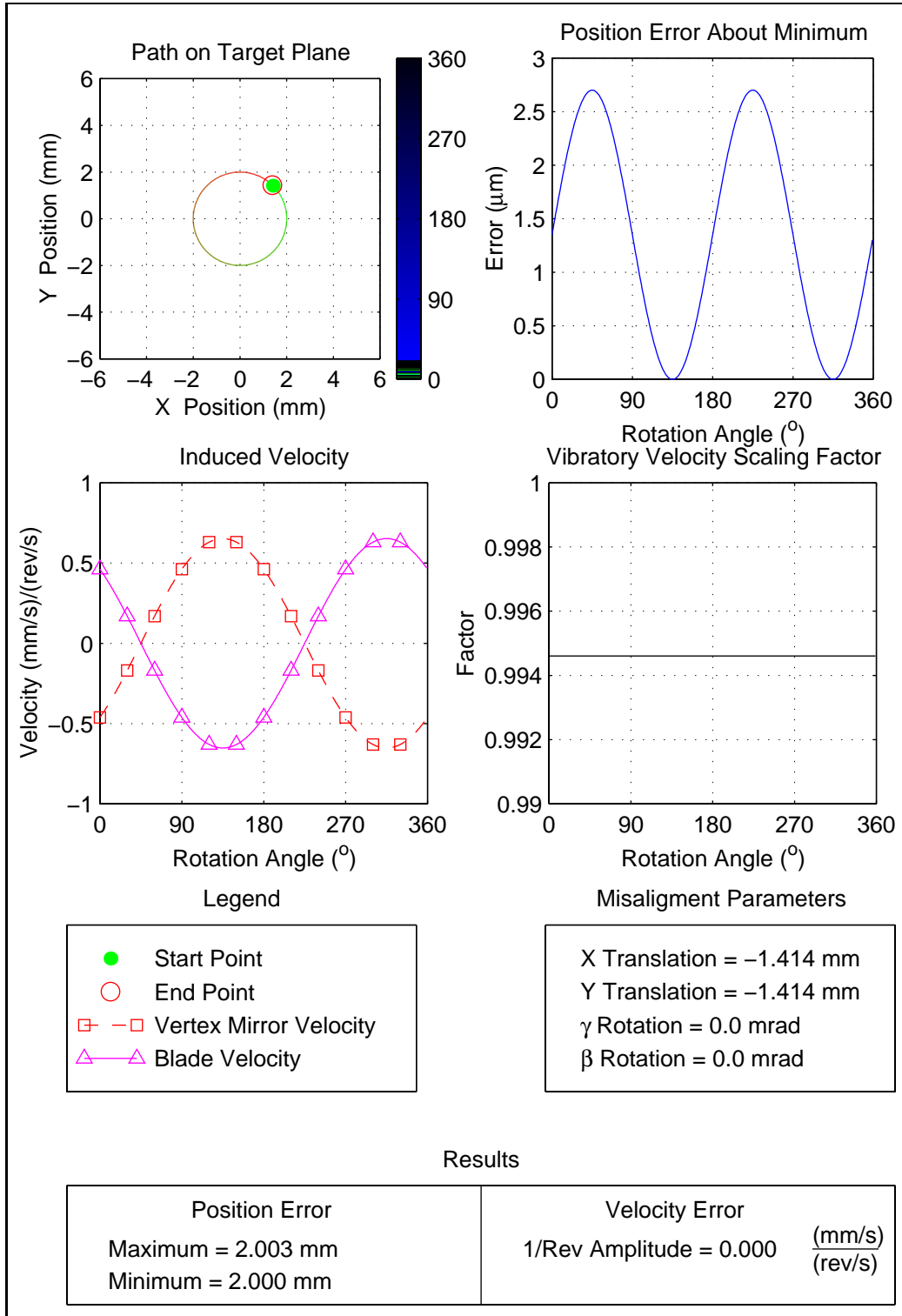


Figure 7.22: Translational Misalignments, Directional Effects, $d_x = -1.414$ mm, $d_y = -1.414$ mm

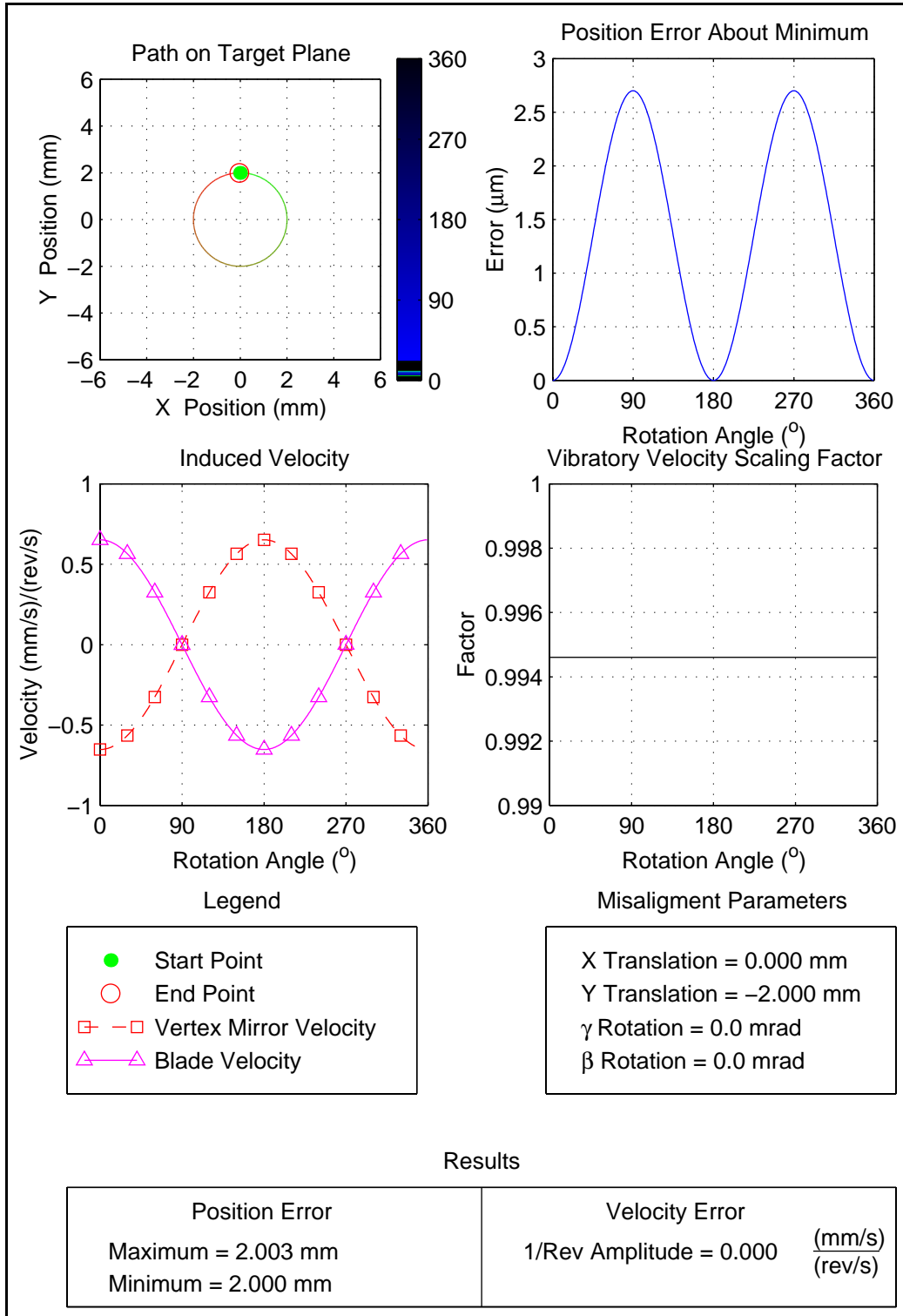


Figure 7.23: Translational Misalignments, Directional Effects, $d_X=0$ mm, $d_Y=-2$ mm

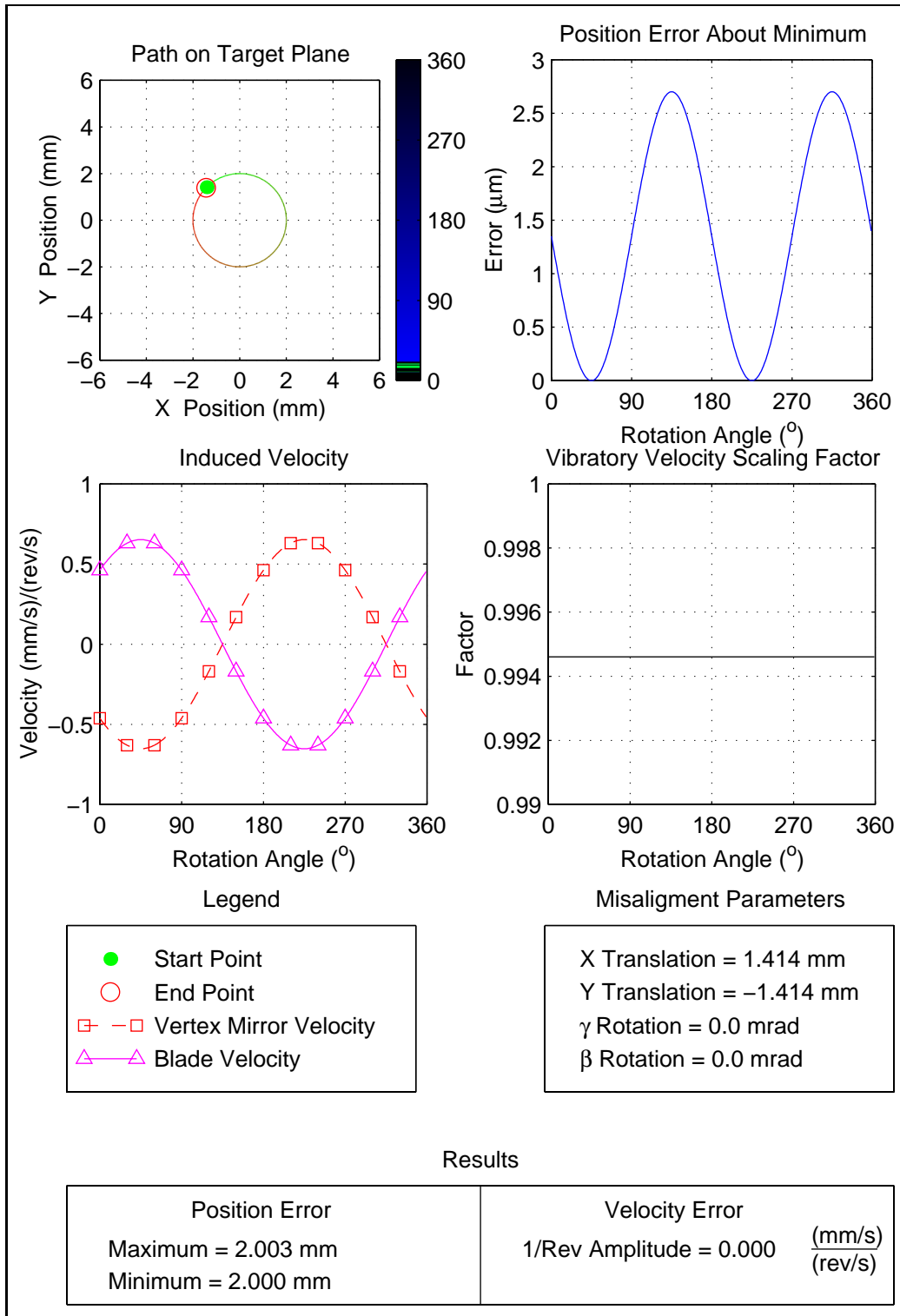


Figure 7.24: Translational Misalignments, Directional Effects, $d_x=1.414$ mm, $d_y=-1.414$ mm

Table 7.2: Translational Misalignment Magnitude Effects

Case	Translations		Position Errors		Velocity Errors	
	d_x (mm)	d_y (mm)	Minimum (mm)	Variation (μm)	Induced (mm/s)/(rev/s)	Vibratory Scaling Factor
1	-5	0	5	7	0	0.994
2	-4	0	4	5	0	0.994
3	-3	0	3	4	0	0.994
4	-2	0	2	3	0	0.994
5	-1	0	1	1	0	0.994
6	0	0	0	0	0	0.994
7	1	0	1	1	0	0.994
8	2	0	2	3	0	0.994
9	3	0	3	4	0	0.994
10	4	0	4	5	0	0.994
11	5	0	5	7	0	0.994

There are three important results to point out. First, the minimum error is equal to the translational misalignment. An additional amount of position error is also present, however this is several orders of magnitude lower than the minimum error. Thus a fair approximation of the position error can be found based on the translation distance.

Second, the velocity error remains zero for all translations. This is due to the fact that the velocity induced by the rigid body motion of the blade is equal and opposite in sign to the velocity induced by the rotating vertex mirror. This result is somewhat unexpected and requires a further explanation.

Third, the scaling factor between the measured velocity and the blade's true vibratory velocity remains constant with rotation angle.

These results show that the level of translational misalignment that can be tolerated depends solely on the amount of allowable position error. Additionally the amount of position error is approximately equal to the translational misalignment.

Table 7.3: Translational Misalignment Direction Effects

Case	Translations		Position Errors		Velocity Errors	
	d_x (mm)	d_y (mm)	Minimum (mm)	Variation (μm)	Induced (mm/s)/(rev/s)	Vibratory Scaling Factor
1	2	0	2	3	0	0.994
2	1.414	1.414	2	3	0	0.994
3	0	2	2	3	0	0.994
4	-1.414	1.414	2	3	0	0.994
5	-2	0	2	3	0	0.994
6	-1.414	-1.414	2	3	0	0.994
7	0	-2	2	3	0	0.994
8	1.414	-1.414	2	3	0	0.994

7.3.2 Analytical Verification

The simulation results show that static displacements introduce two effects that contribute to tracking error. The most dominant effect is a constant shift of the measurement point relative to the target point equal in magnitude and direction to the displacement error. A secondary effect is a varying shift in the measurement point caused by the changing distance between the intersection of the laser beam and vertex mirror and the fold mirror. The simulations also show that the shift in the measurement point is in the same direction as the displacement due to the axisymmetric nature of the system.

As expected, the simulation results show that translational misalignments introduce velocity errors due to the vertex mirror motion and the blade's rigid body motion. One unexpected result is that these two components are equal in amplitude but opposite in sign. While it can be clearly seen in the simulation results that the velocities are always have opposite sign, it is not readily obvious that the amplitudes are equal. This can be shown by considering the situation depicted in Figure 7.26

This figure shows the orientation of the vertex mirror and blade velocity vectors for a trans-

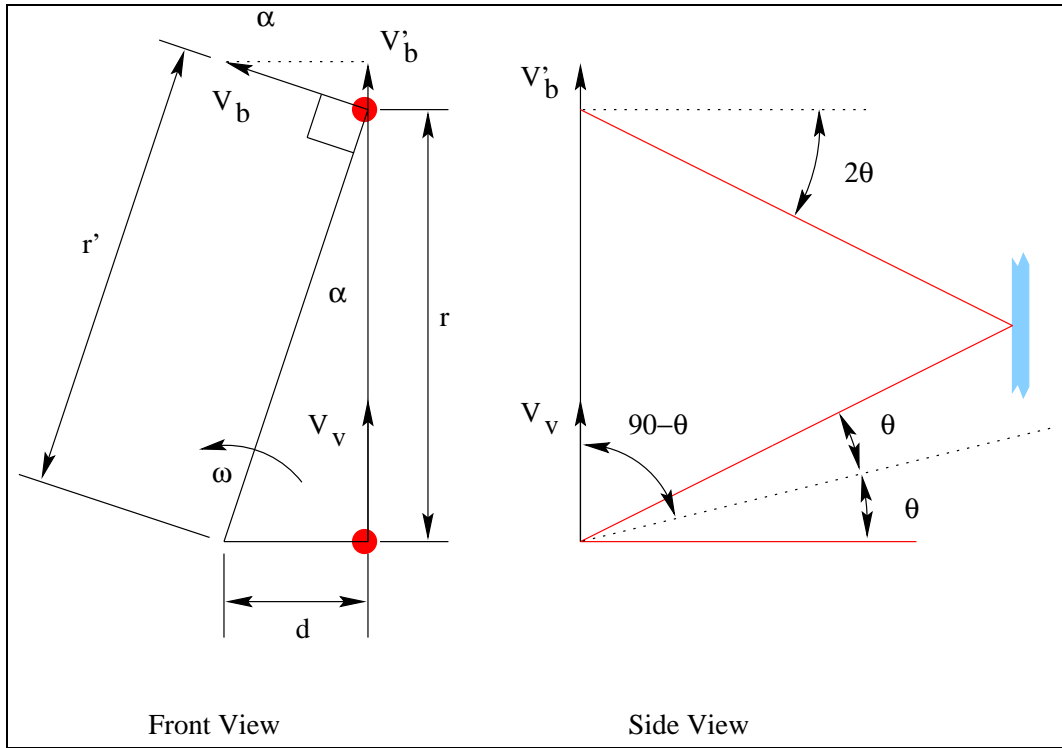


Figure 7.25: Velocity Resolution for Translational Misalignment

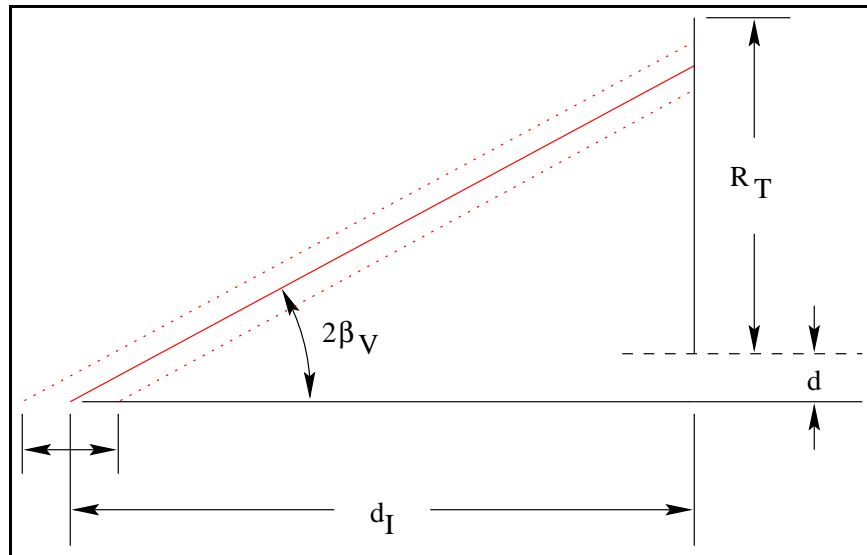


Figure 7.26: Simplified Model for Translational Misalignment Position Errors

lational misalignment of d_x in the negative x direction and blade rotation angle of 90° , a position which corresponds to the maximum induced vertex mirror velocity.

First, the velocity components that lie in the plane of the laser beam path are found. The linear velocity of the vertex mirror is considered first. This velocity component, V_v is

$$V_v = \omega \cdot d \tag{7.1}$$

which is also velocity component that lies in the plane of the laser beam path.

Similarly, the linear velocity of the blade at the measurement point, V_b , is

$$V_b = \omega \cdot \sqrt{r^2 + d^2} \tag{7.2}$$

Its component in the plane of the laser beam path is

$$V'_b = \omega \cdot \sqrt{r^2 + d^2} \cdot \sin(\alpha) \tag{7.3}$$

Rewriting the sine term in terms of the distances r and d yields

$$V'_b = \omega \cdot \sqrt{r^2 + d^2} \cdot \frac{d}{\sqrt{r^2 + d^2}} \tag{7.4}$$

which reduces to

$$V'_b = \omega \cdot d \quad (7.5)$$

This shows the the velocity components that lie in the plane of the laser beam path are equal. Next the velocities along the laser beam path can be found.

First, the component of V'_b is found to be

$$V''_b = \omega \cdot d \cdot \cos(90^\circ + 2\theta) \quad (7.6)$$

which after applying the trigonometric identity

$$\cos(90^\circ + \phi) = -\sin(\phi) \quad (7.7)$$

can be rewritten as

$$V''_b = -\omega \cdot d \cdot \sin(2\theta) \quad (7.8)$$

The velocity induced by the rotating vertex mirror, found using the previous results for velocity induced by a rotating mirror is

$$V'_v = 2 * \omega \cdot d \cdot \cos(\theta) \cdot \cos(90^\circ - \theta) \quad (7.9)$$

Again after applying the trigonometric identity

$$\cos(90^\circ - \phi) = \sin(\phi) \quad (7.10)$$

can be rewritten as

$$V'_v = 2 * \omega \cdot d \cdot \cos(\theta) \cdot \sin(\theta) \quad (7.11)$$

Finally, by applying the trigonometric identity

$$\cos(\phi) \cdot \sin(\phi) = \frac{1}{2} \sin(2\phi) \quad (7.12)$$

it can be shown that

$$V'_v = \omega \cdot d \cdot \sin(2\theta) \quad (7.13)$$

and therefore

$$V''_b = -V'_v \quad (7.14)$$

This shows that the velocity components due to the blade's rigid body motion and the vertex mirror's motion cancel each other, resulting in no net velocity, confirming the result predicted by the simulation.

7.3.3 Experimental Verification

To verify the simulation results, a series of experiments were performed. Because of the limited adjustment capability of the rotating structure test rig, only horizontal translations, corresponding to the translations introduced to study the magnitude effects of translational misalignments, were performed. As in the simulations, translations of the displaced frame relative to the ideal alignment frame were introduced. This misalignments consisted of translation from -5mm to 5mm in 1mm increments. For each increment of translation, the position and velocity errors were recorded. Position data was collected by rotating the blade by hand. Velocity data was collected with the motor driving the blade at approximately 10 revolutions per second. Figures 7.27 and 7.28 show the measured position errors for negative and positive translations.

As predicted by the simulation, the measured position error increases with the amount of translational misalignment. The magnitude of the position error is approximately equal to the amount of translational misalignment in each case and the direction of the position error agrees with the direction of the translational misalignment.

Next the velocity errors are considered, with the experimental results shown in Figures 7.29 and 7.30.

Checking the velocity error, misalignment appears to have very little effect on the measured velocity. Although the simulation predicted no velocity error, it is expected that the measured velocity will be non-zero for several reasons.

Since the system was not precisely aligned, as shown by the position error for the ideal alignment case, it is reasonable to expect the same level of velocity for translational misalignments as is measured for the ideal alignment case. Inspection of the velocity spectra for the translational misalignment shows slight changes in the velocity across the frequency range for changing levels of translation. This is due to the increase in the speckle noise

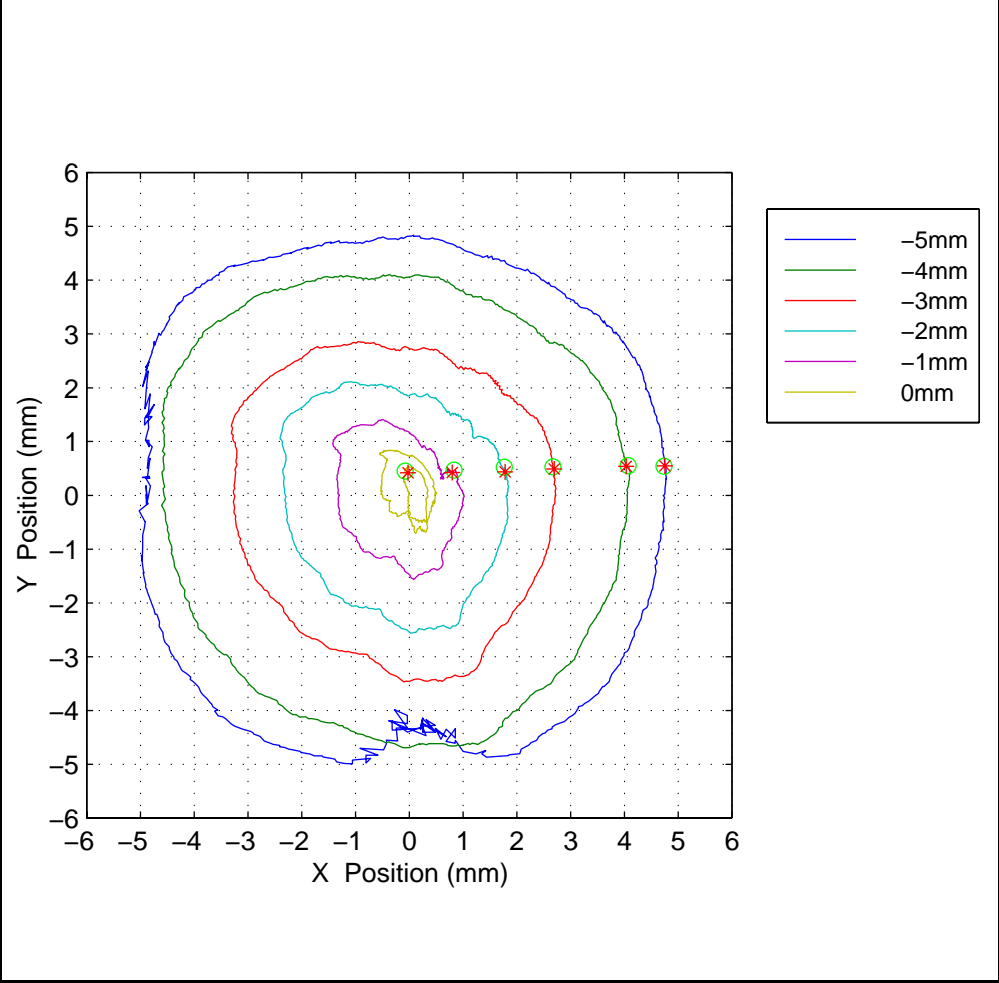


Figure 7.27: Measured Position Errors for Negative Translational Misalignments

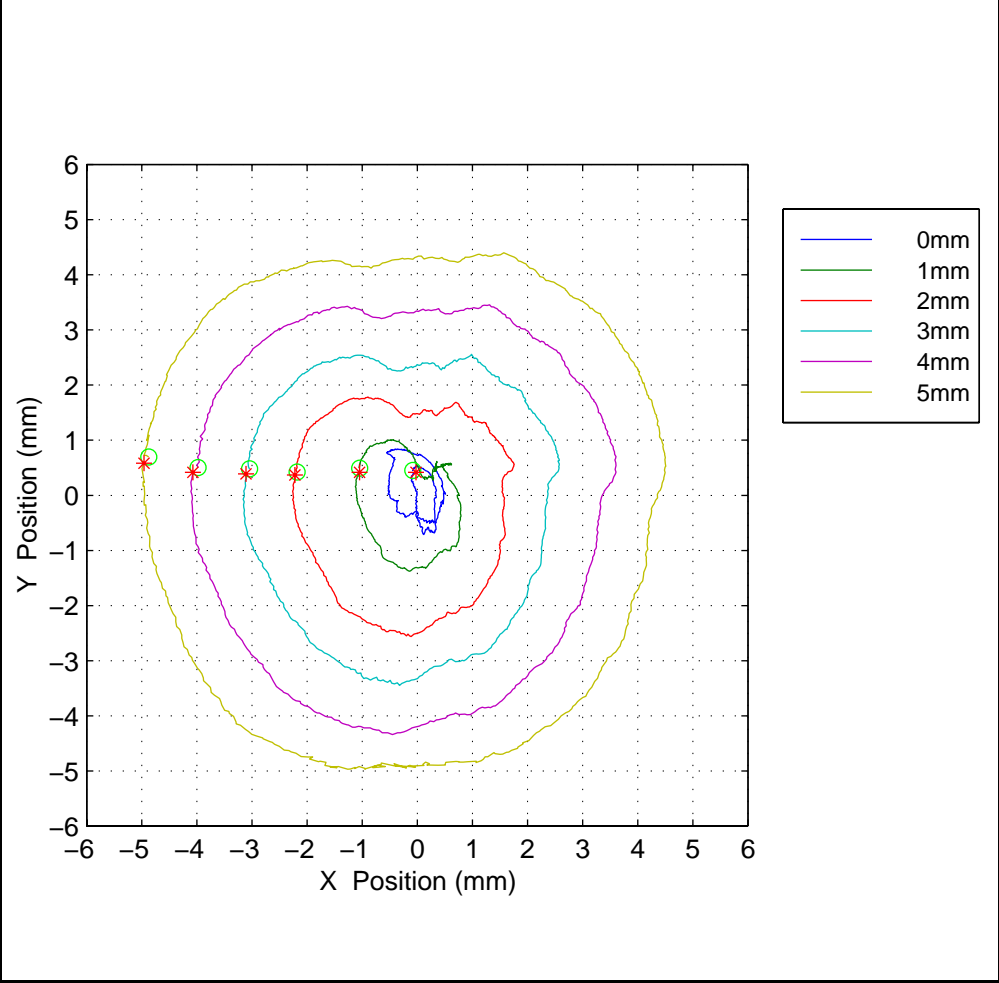


Figure 7.28: Measured Position Errors for Positive Translational Misalignments

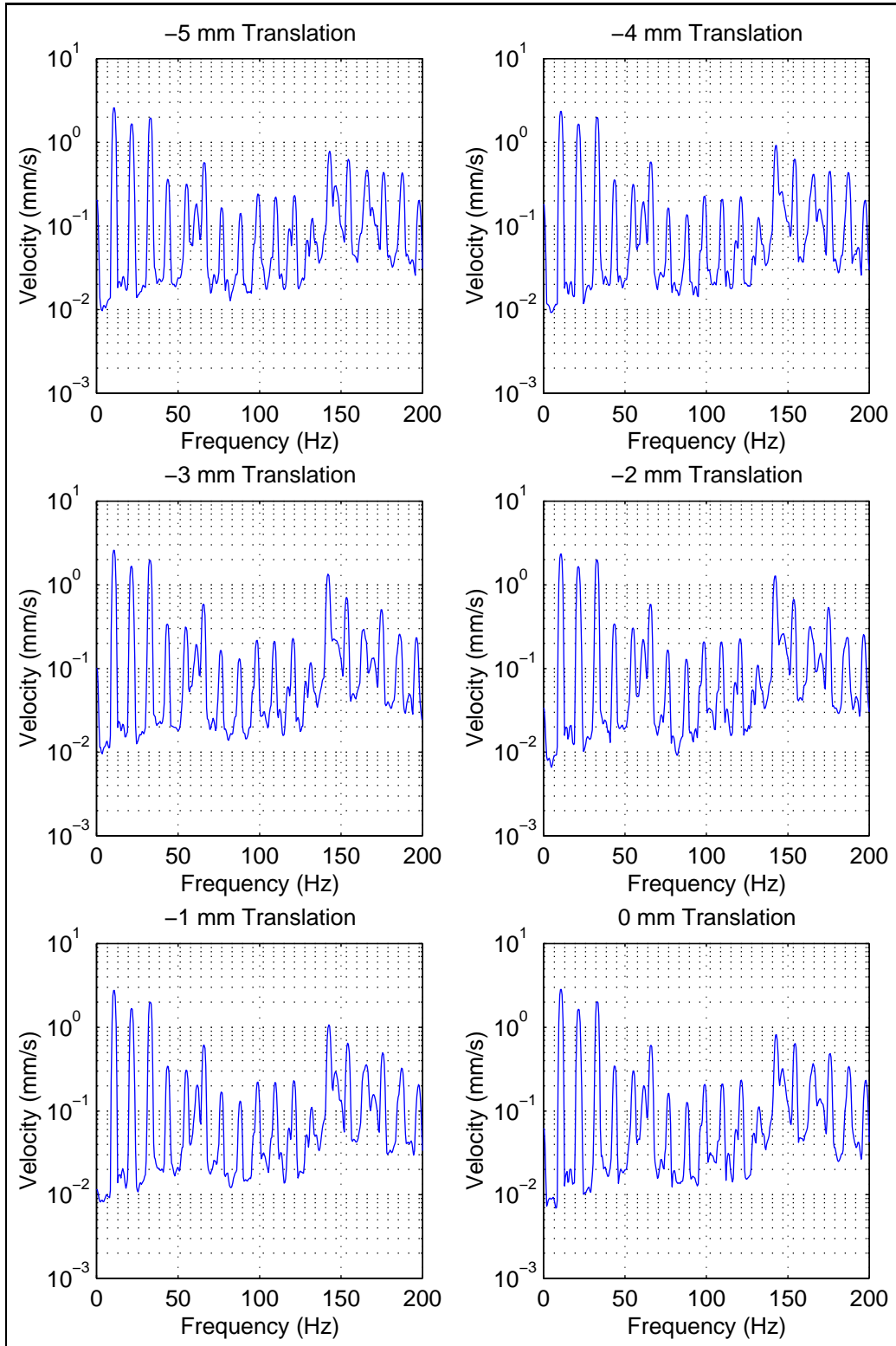


Figure 7.29: Measured Velocity Errors for Negative Translational Misalignments

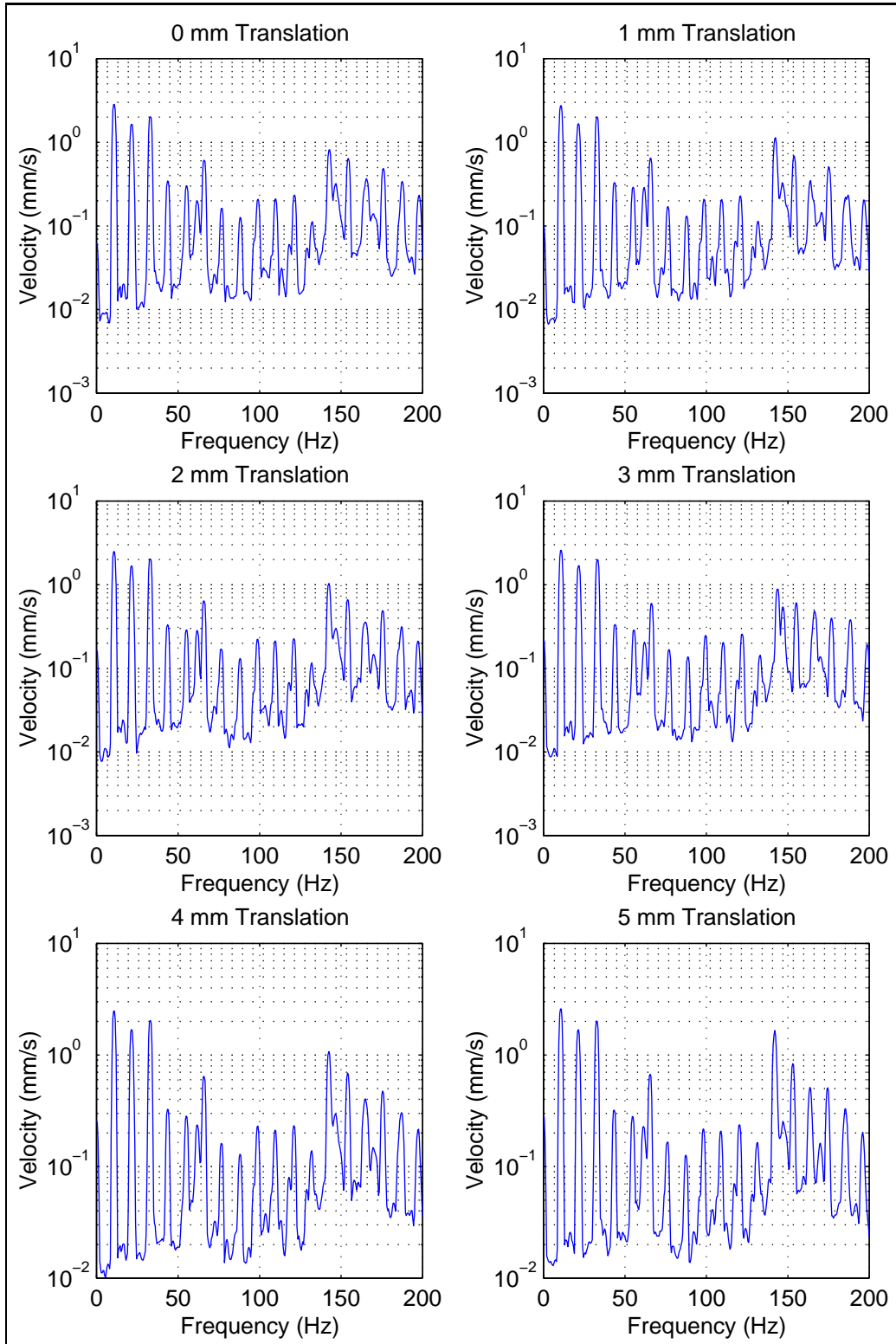


Figure 7.30: Measured Velocity Errors for Positive Translational Misalignments

resulting from the increase in the circumference of the path traced out by the measurement point on the target plane. Recall that the simulation does not account for speckle noise.

Closer inspection of the once per rev signal as a function of translation distance, as shown in Figure 7.31 shows that this velocity component remains relatively constant.

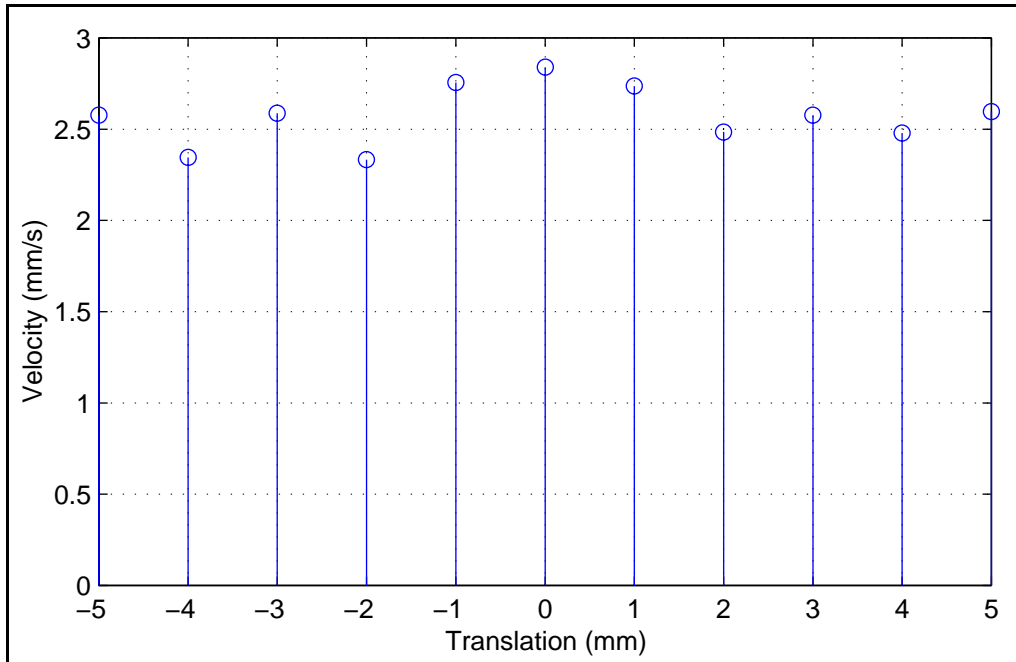


Figure 7.31: Once Per Rev Measured Velocity for Translational Misalignments

Thus while the experimental results do not duplicate the results predicted by the simulations, the experimental results do support the trends seen in the simulation. The level of agreement is reasonable considering the non-idealities experienced in the test rig. Therefore based on these results, the model is capable of predicting the effects of translational misalignments on both position and velocity errors.

7.4 Rotational Misalignments

With the effects of translational misalignments on the position and velocity errors characterized, the effects of rotational misalignments can be considered. As in the case of translational misalignments, rotational misalignments are introduced into the model by rotating the displaced frame relative to the ideal alignment frame as shown in Figure 7.32.

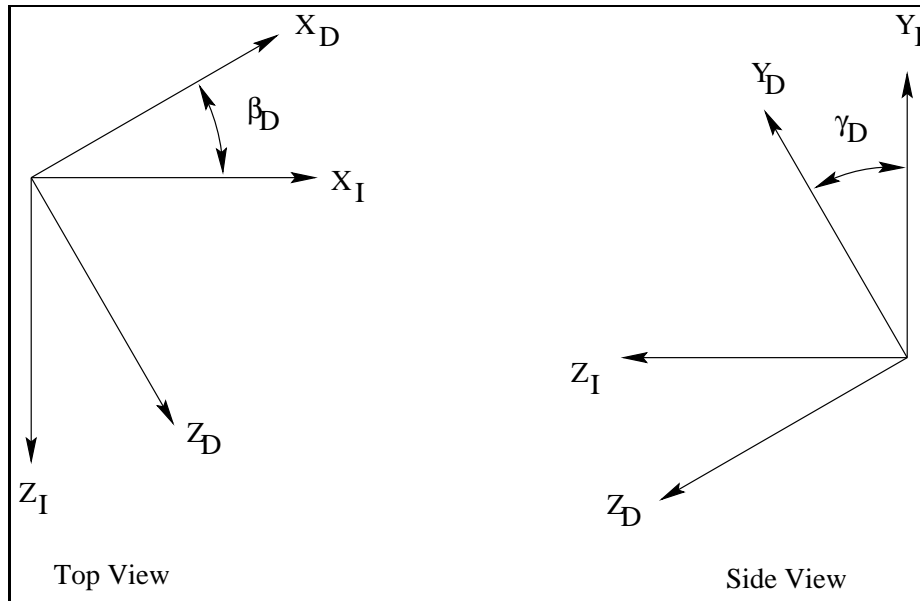


Figure 7.32: Introduction of Rotational Misalignments

The primary effect of this rotational misalignment is to change the angle between the incoming laser beam direction and the vertex mirror normal as shown in Figure 7.33.

The effect of this misalignment is similar to that as seen in the translational misalignment case, with the measurement point path becoming displaced from the target point path. Thus, as in the previous case, the measurement point traces a near circular path on the target plane.

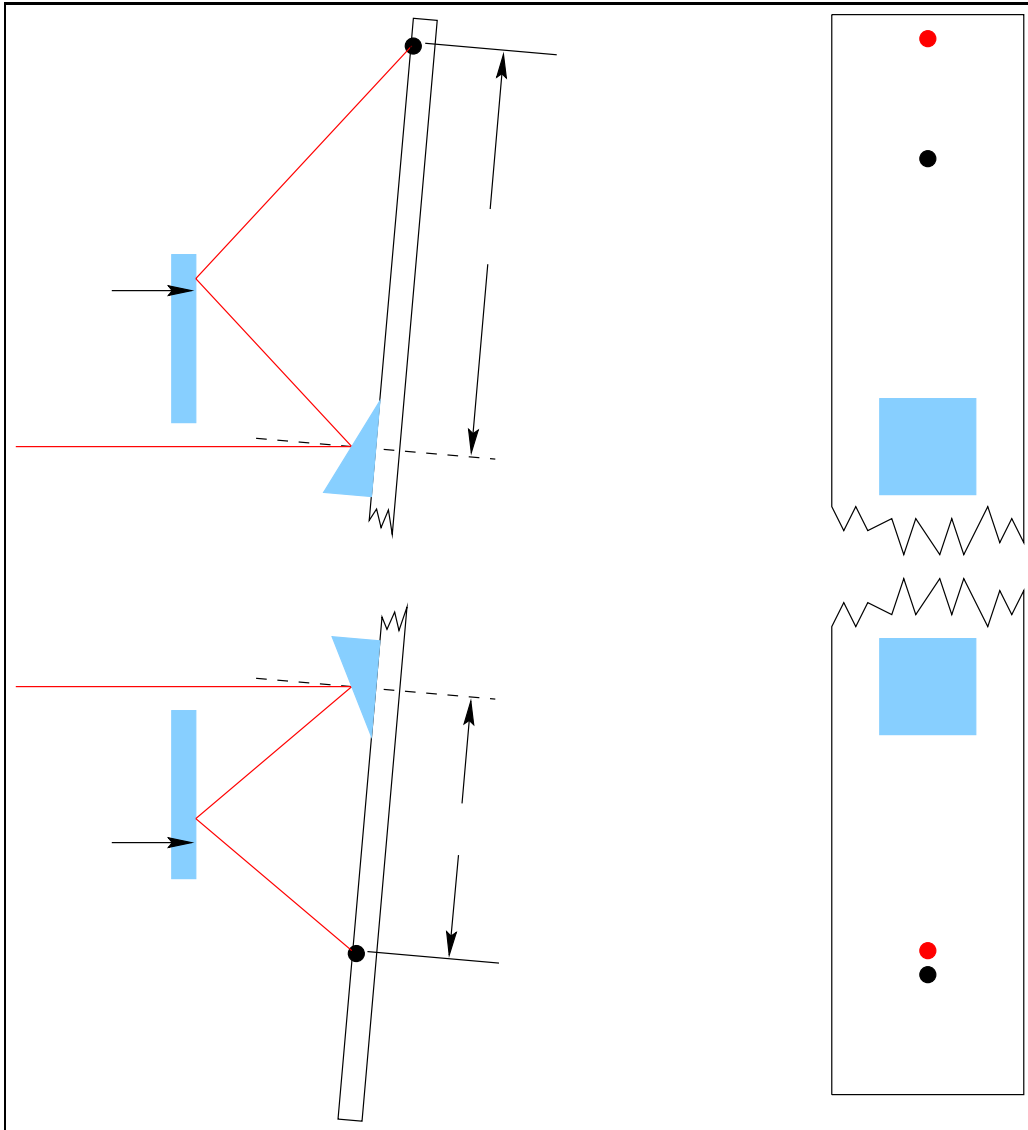


Figure 7.33: Effect of Rotational Misalignment

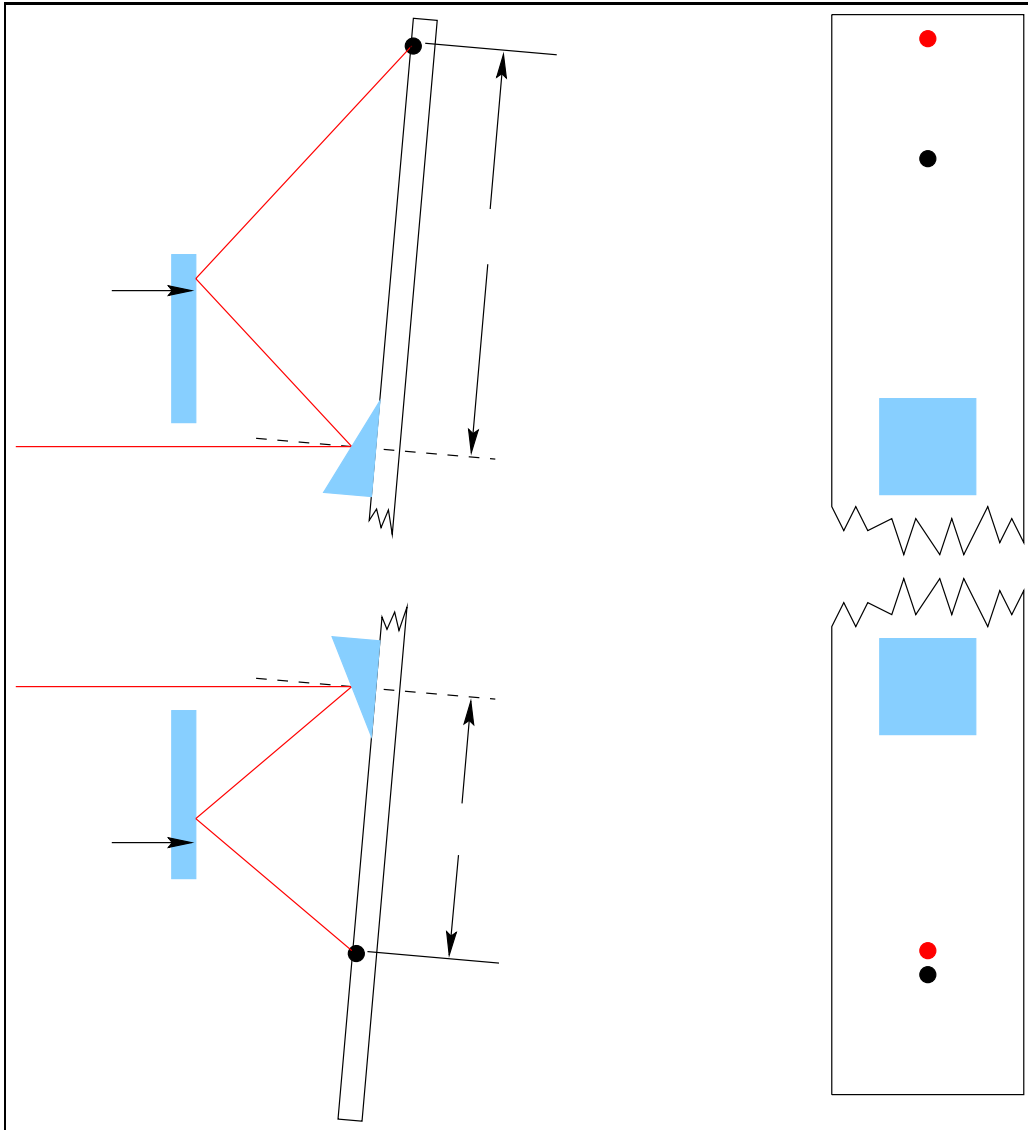


Figure 7.33: Effect of Rotational Misalignment

7.4.1 Simulation Results

To characterize the effects of rotational misalignments, rotational misalignments were introduced into the simulation model. As in the case of translational misalignments, the effects of the magnitude and the direction of the rotational misalignment were studied separately.

To study the effect of the magnitude of the rotational misalignments, the displaced frame was rotated relative to the ideal alignment frame in 0.2 mrad increments from -1 mrad to 1 mrad about the y axes of the ideal alignment frame. To study the directional effects, a fixed rotation of 0.2 mrad was introduced, directing the blade's rotation axis to trace a path along a circular path in 45° increments.

Figures 7.34 through 7.52 show the position and velocity errors predicted by the simulations, with the results summarized in Tables 7.4.1 and 7.4.1.

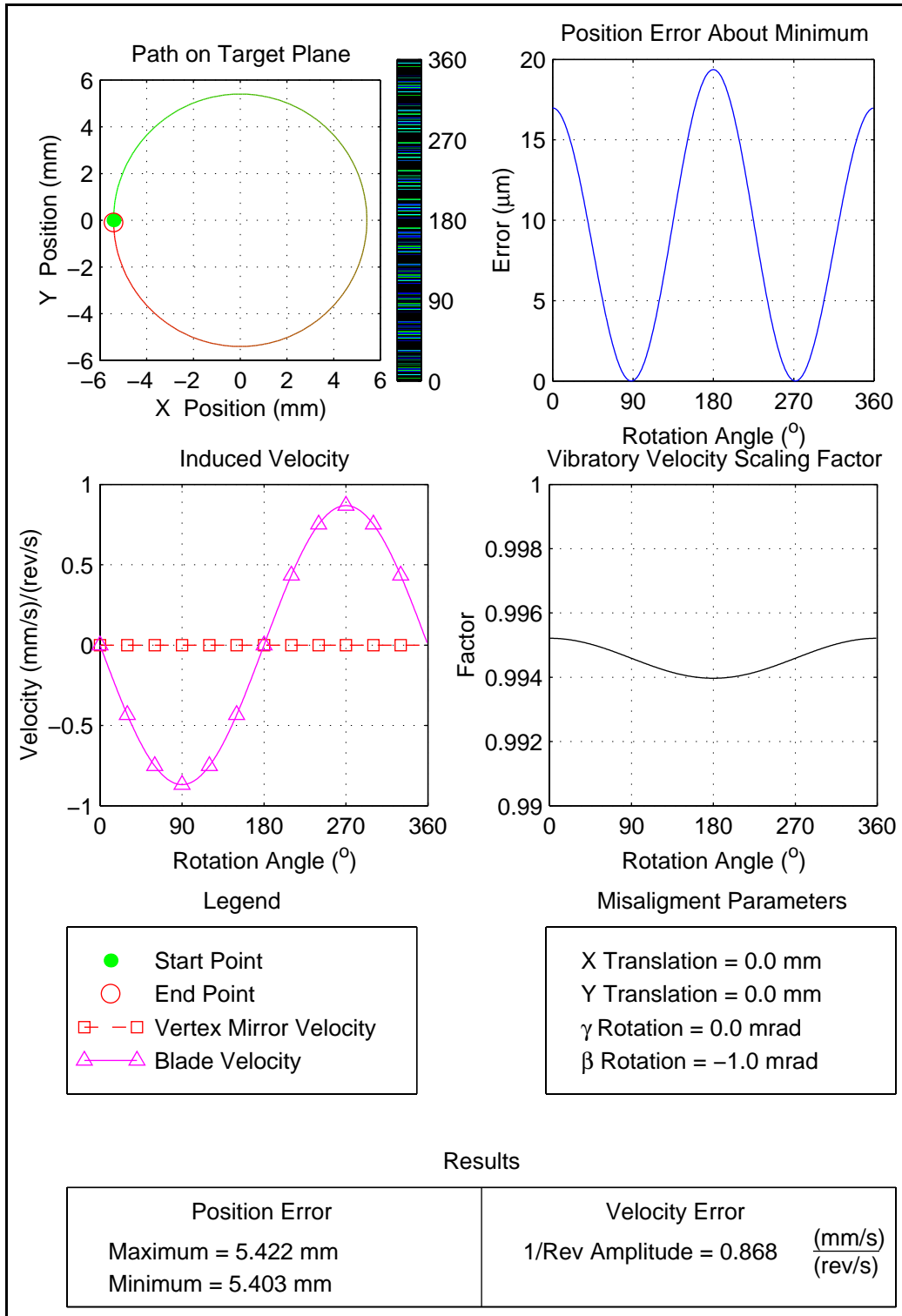


Figure 7.34: Rotational Misalignments, Magnitude Effects, $\beta=-1.0$ mrad

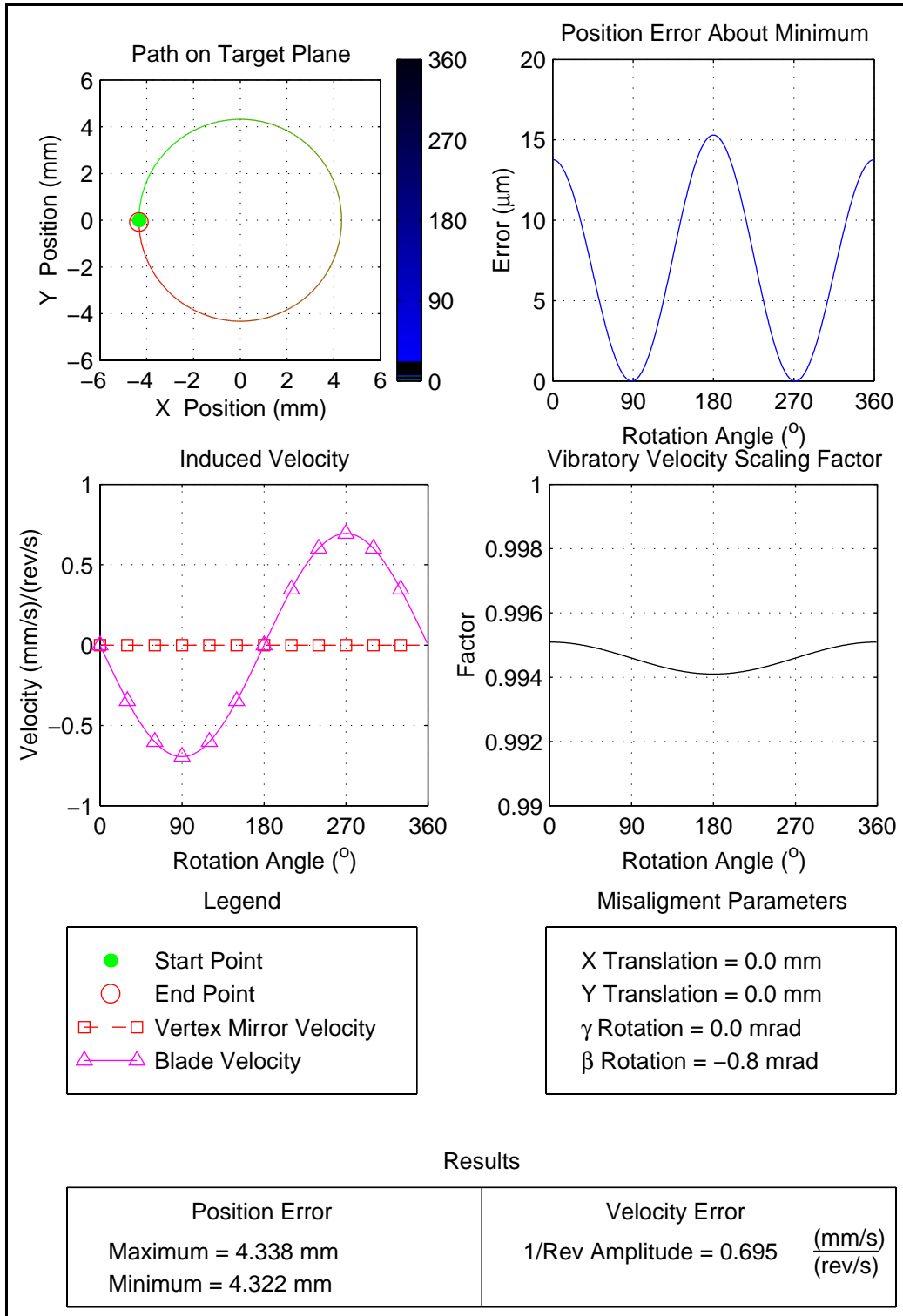


Figure 7.35: Rotational Misalignments, Magnitude Effects, $\beta=-0.8$ mrad

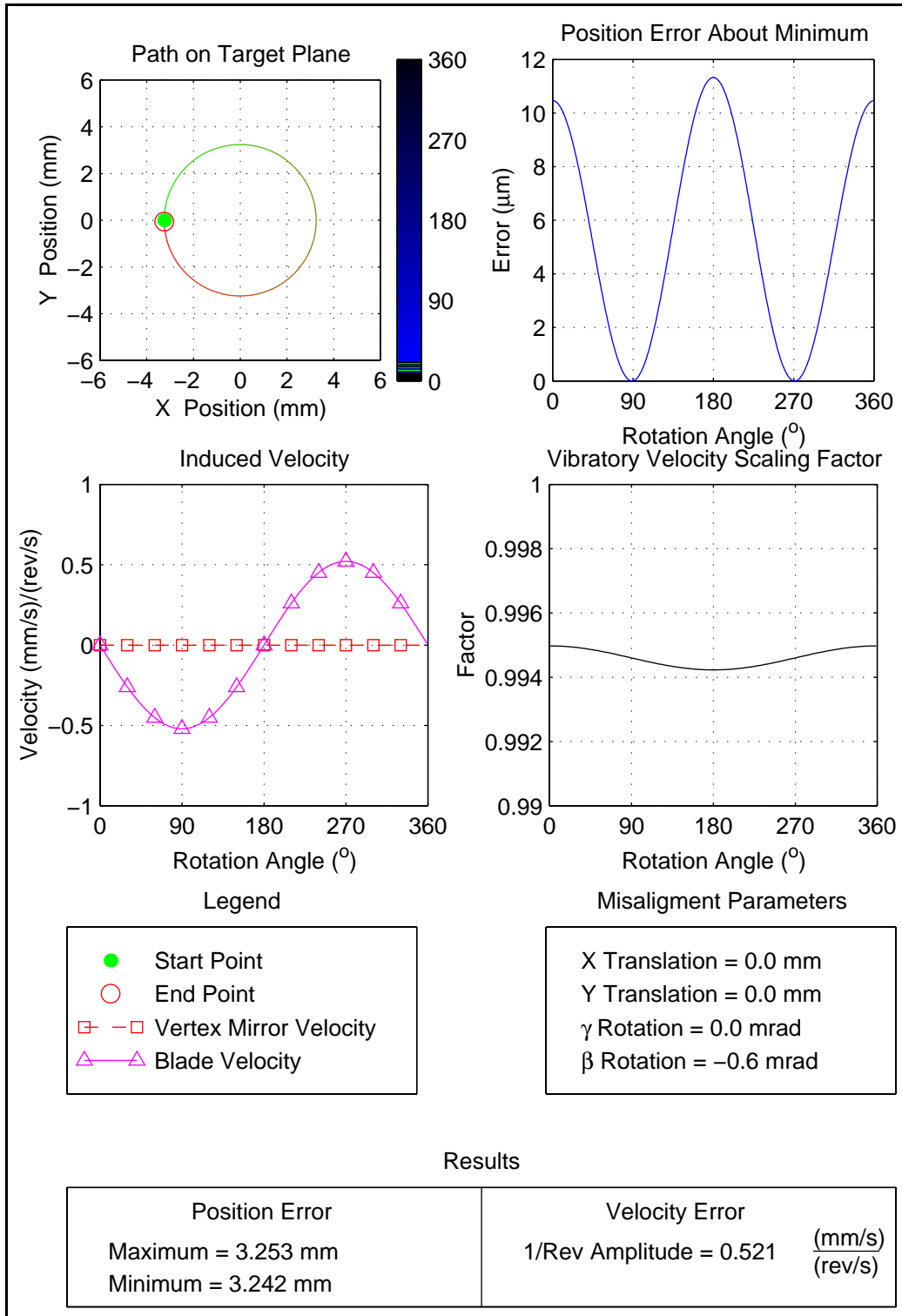


Figure 7.36: Rotational Misalignments, Magnitude Effects, $\beta=-0.6$ mrad

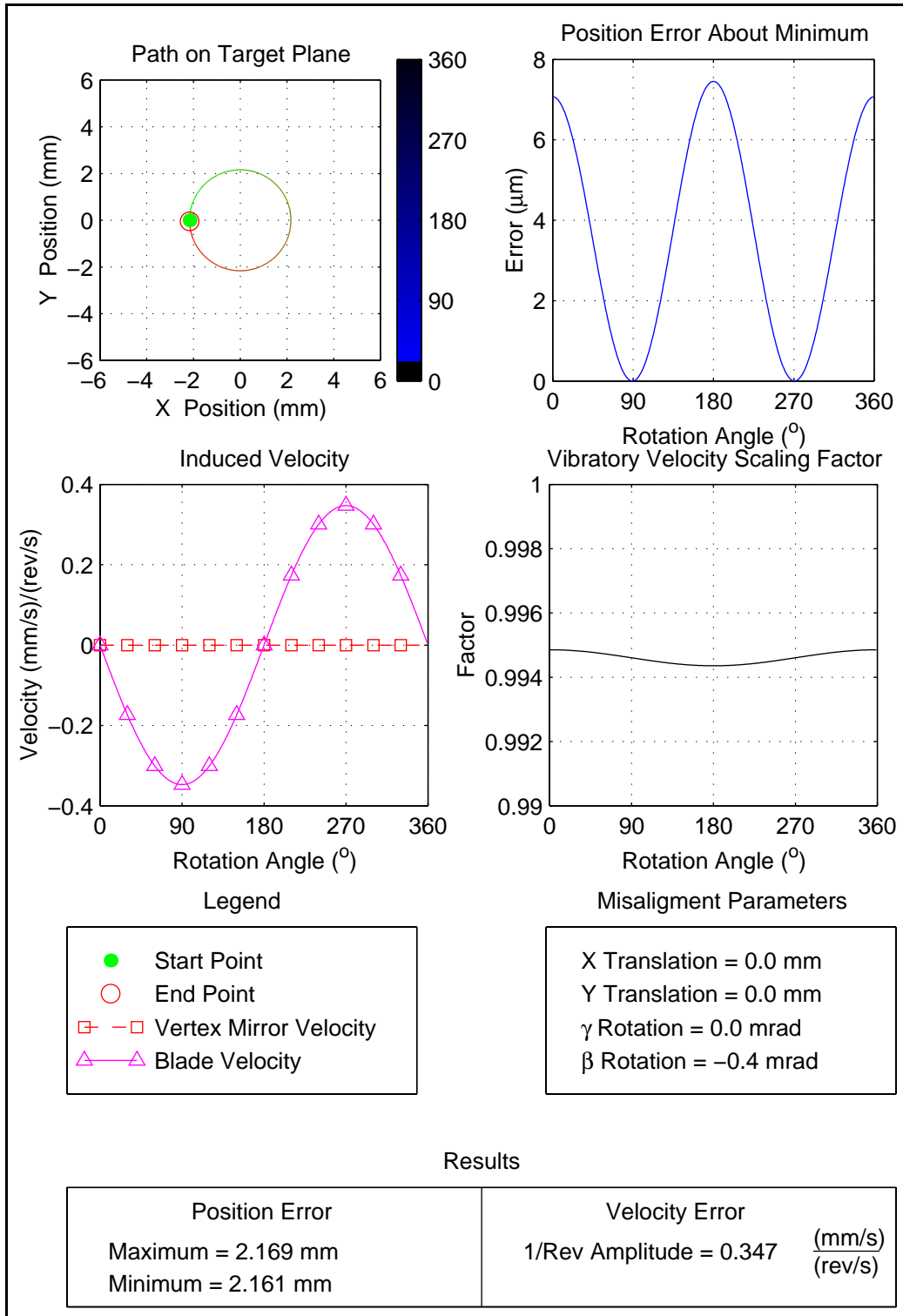


Figure 7.37: Rotational Misalignments, Magnitude Effects, $\beta=-0.4$ mrad

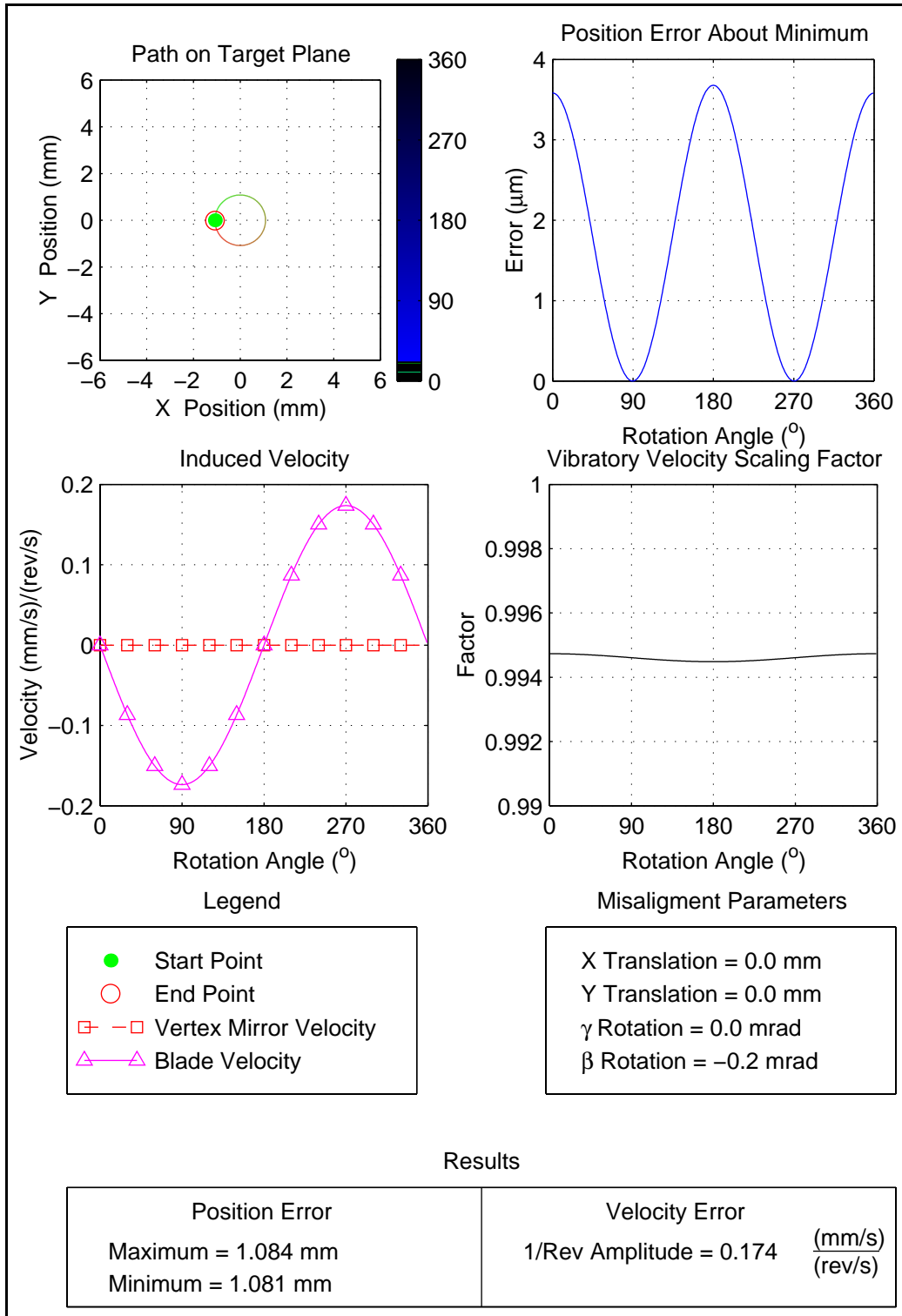


Figure 7.38: Rotational Misalignments, Magnitude Effects, $\beta=-0.2$ mrad

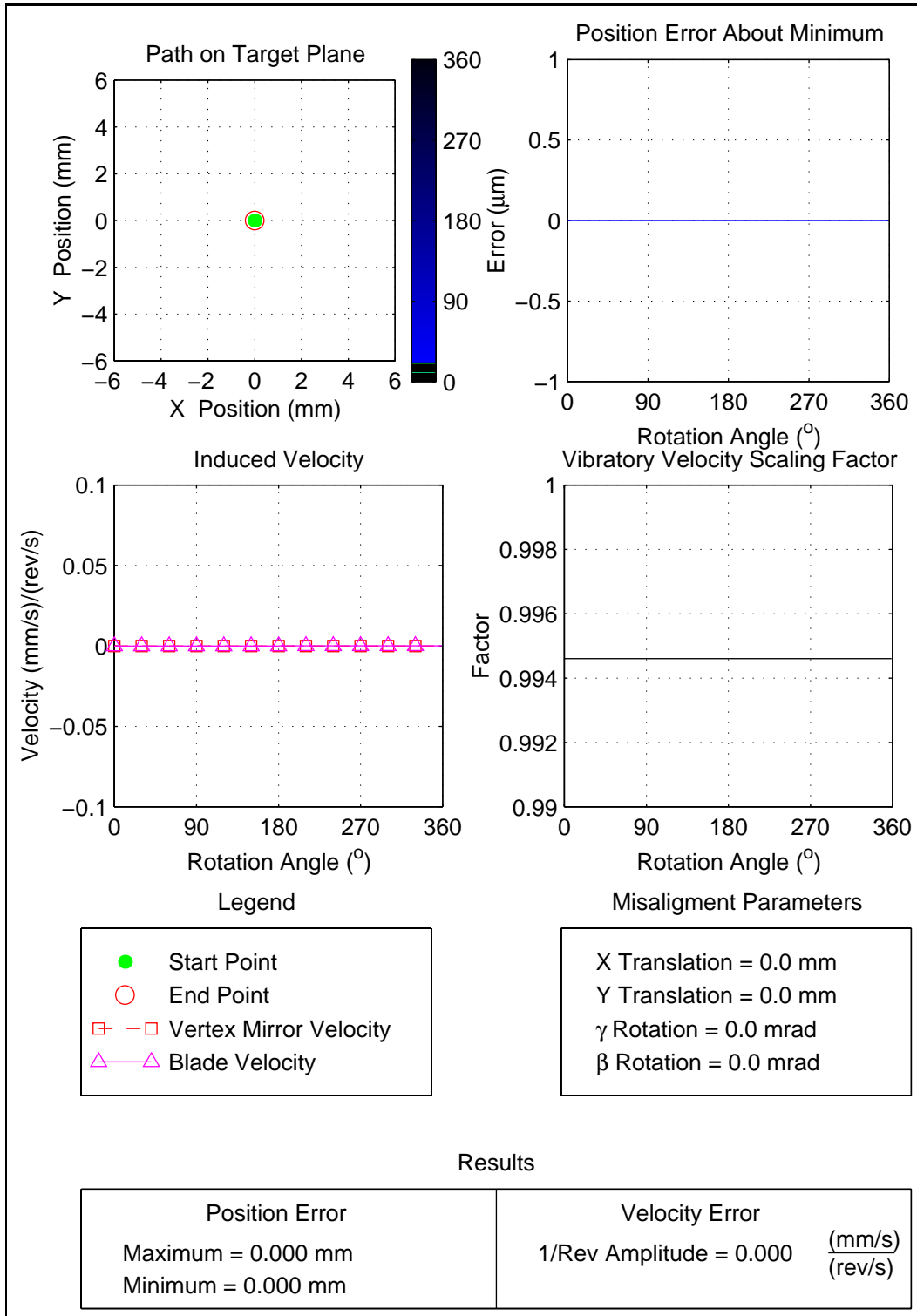


Figure 7.39: Rotational Misalignments, Magnitude Effects, $\beta=0$ mrad

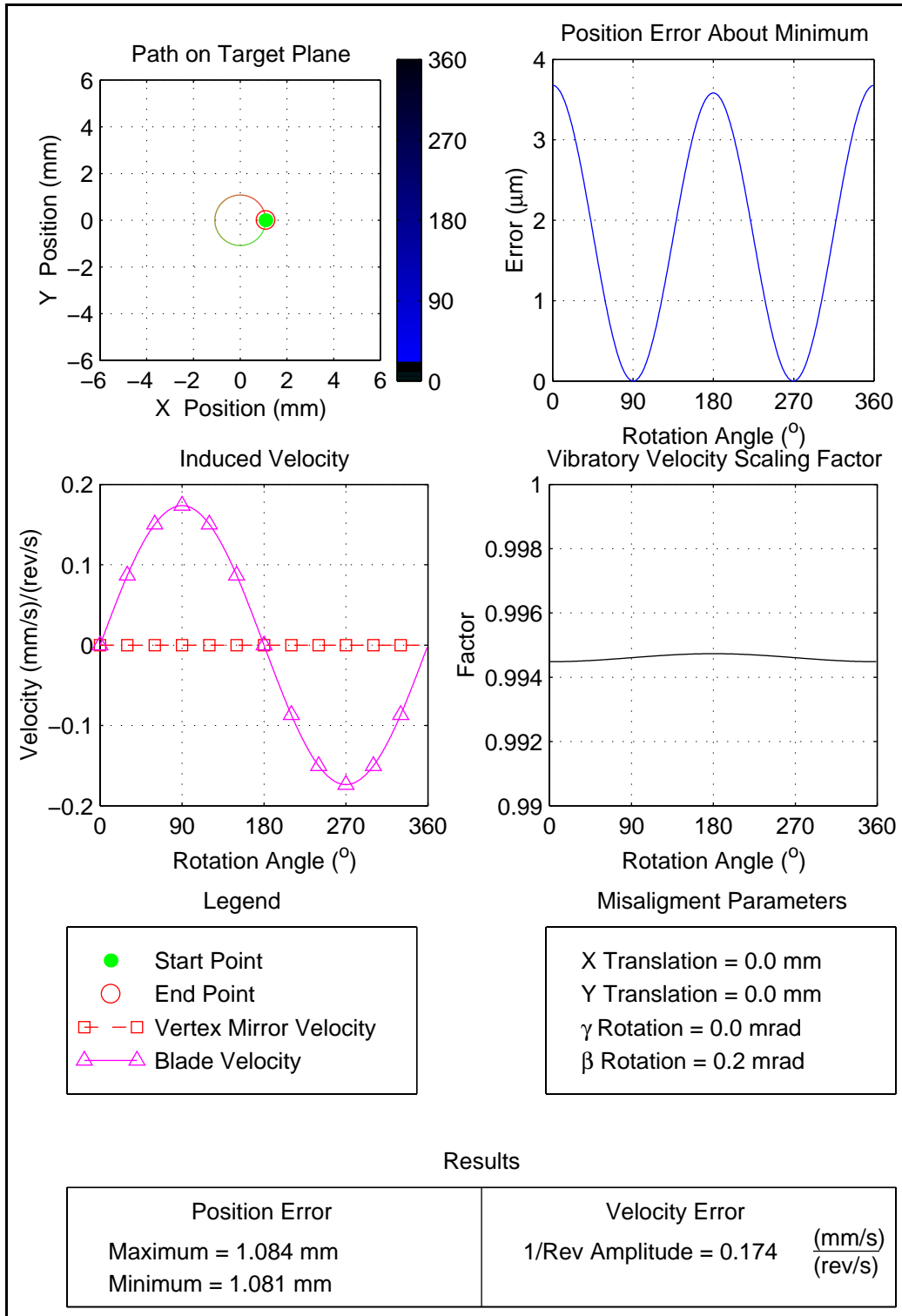


Figure 7.40: Rotational Misalignments, Magnitude Effects, $\beta=0.2$ mrad

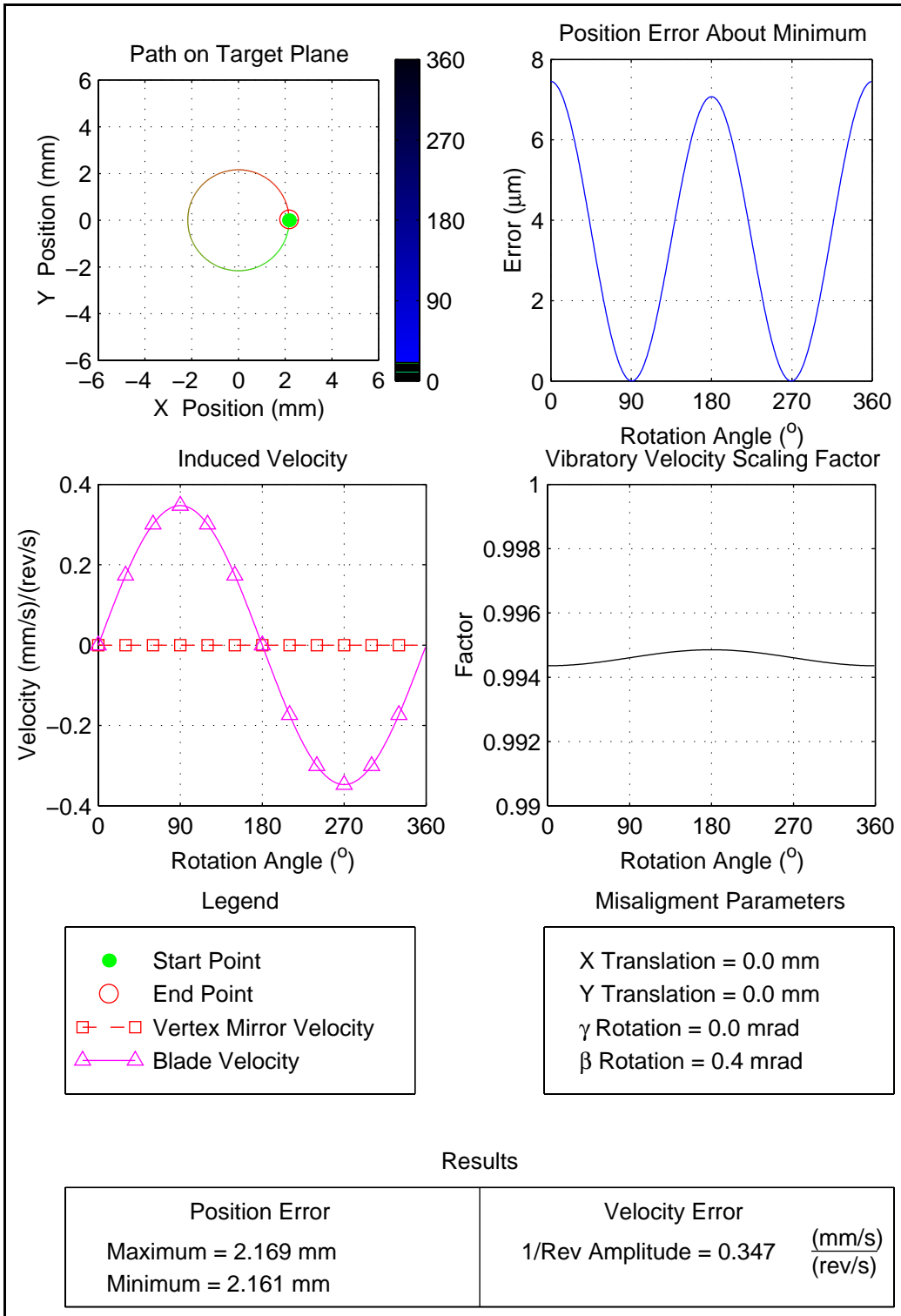


Figure 7.41: Rotational Misalignments, Magnitude Effects, $\beta=0.4$ mrad

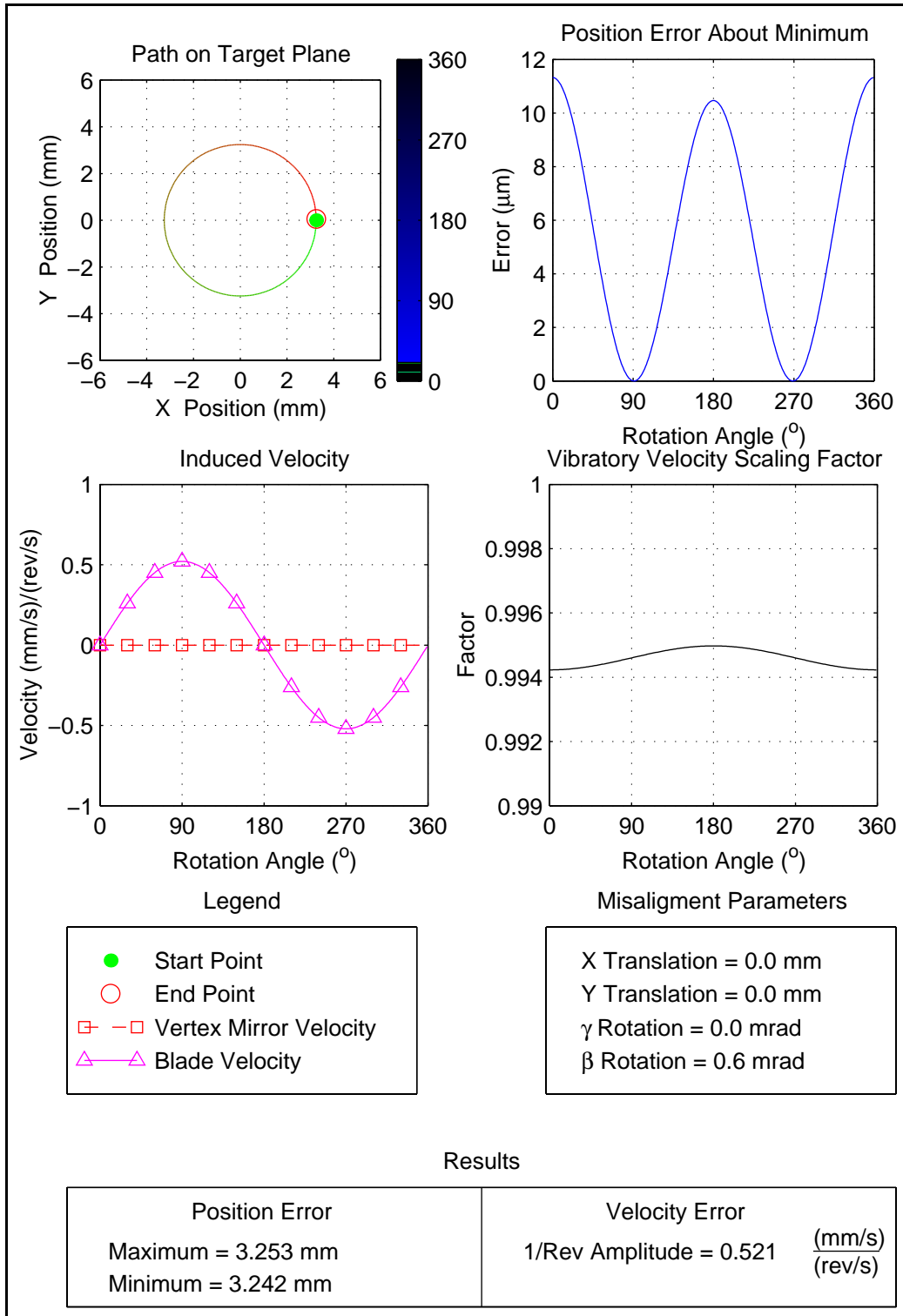


Figure 7.42: Rotational Misalignments, Magnitude Effects, $\beta=0.6$ mrad

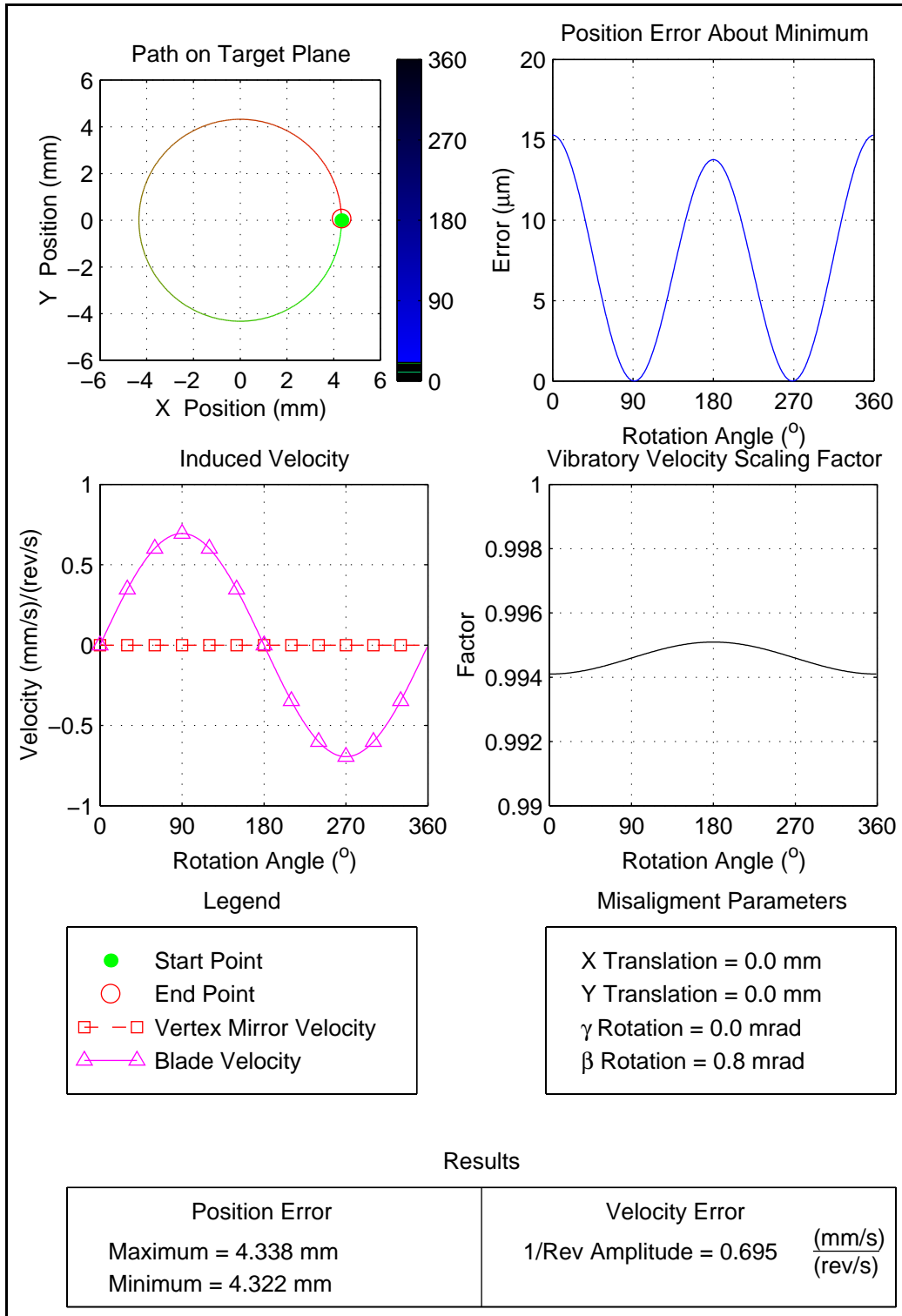


Figure 7.43: Rotational Misalignments, Magnitude Effects, $\beta=0.8$ mrad

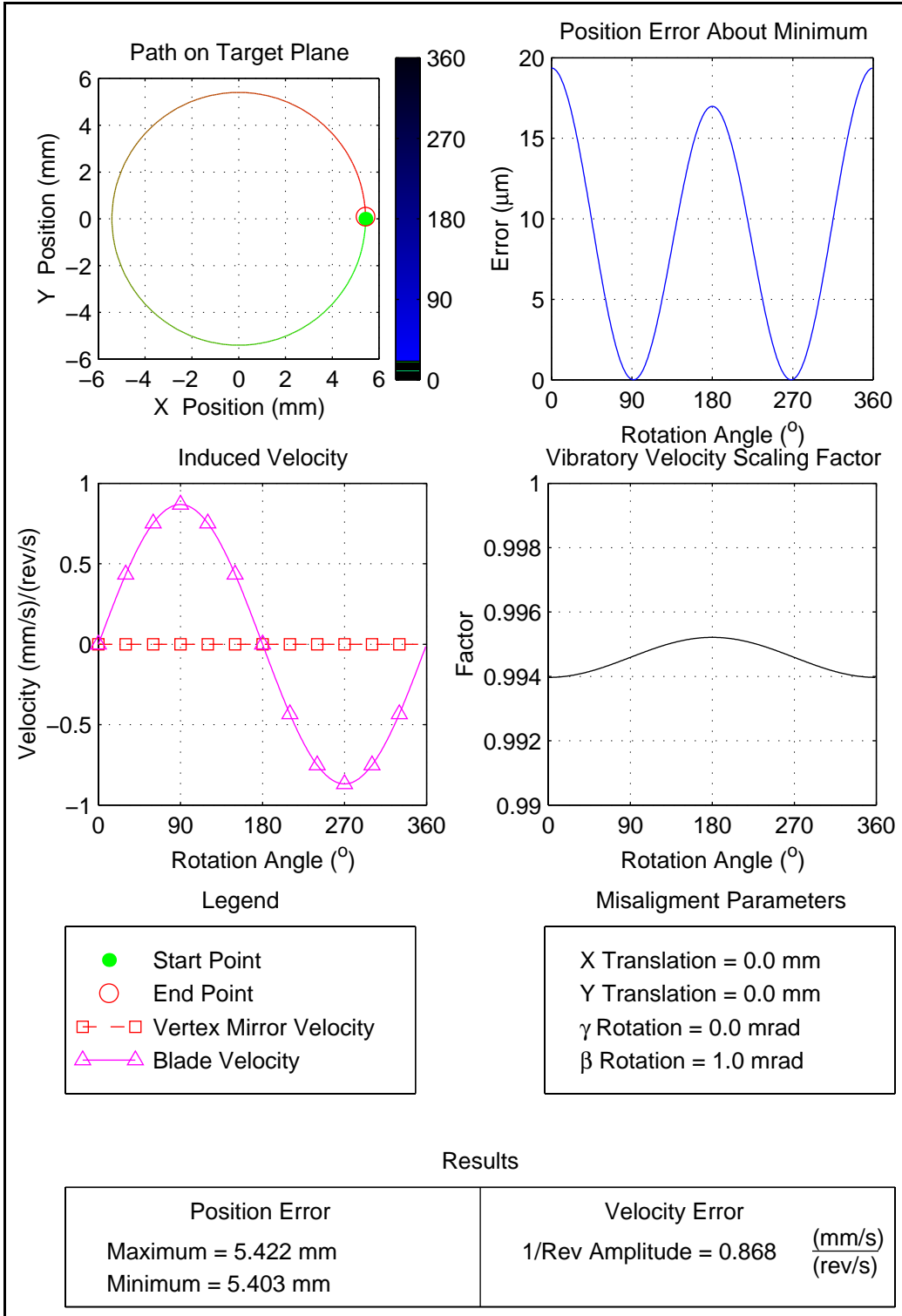


Figure 7.44: Rotational Misalignments, Magnitude Effects, $\beta=1.0$ mrad

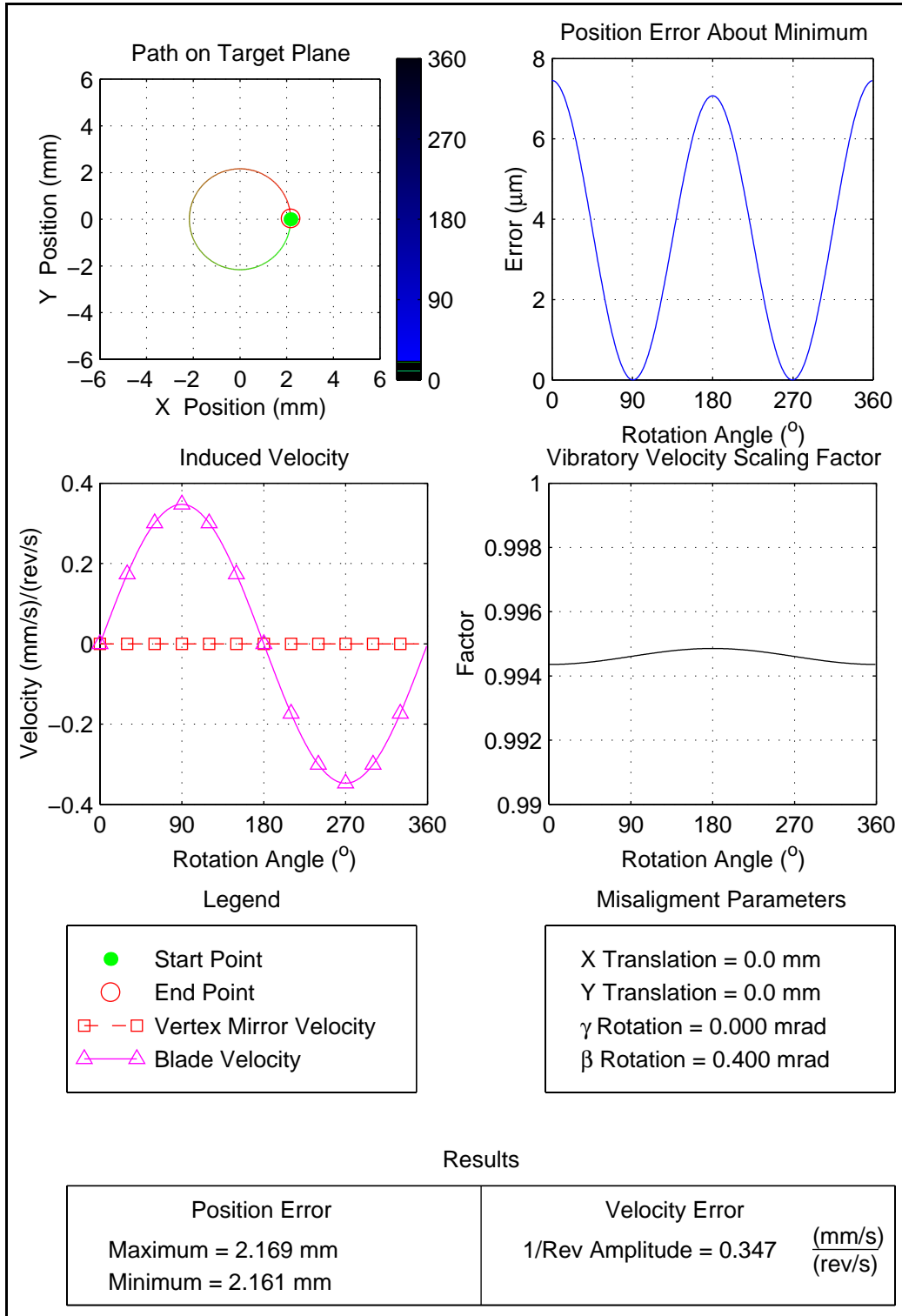


Figure 7.45: Rotational Misalignments, Directional Effects, $\gamma=0.0$ mrad, $\beta=0.4$ mrad

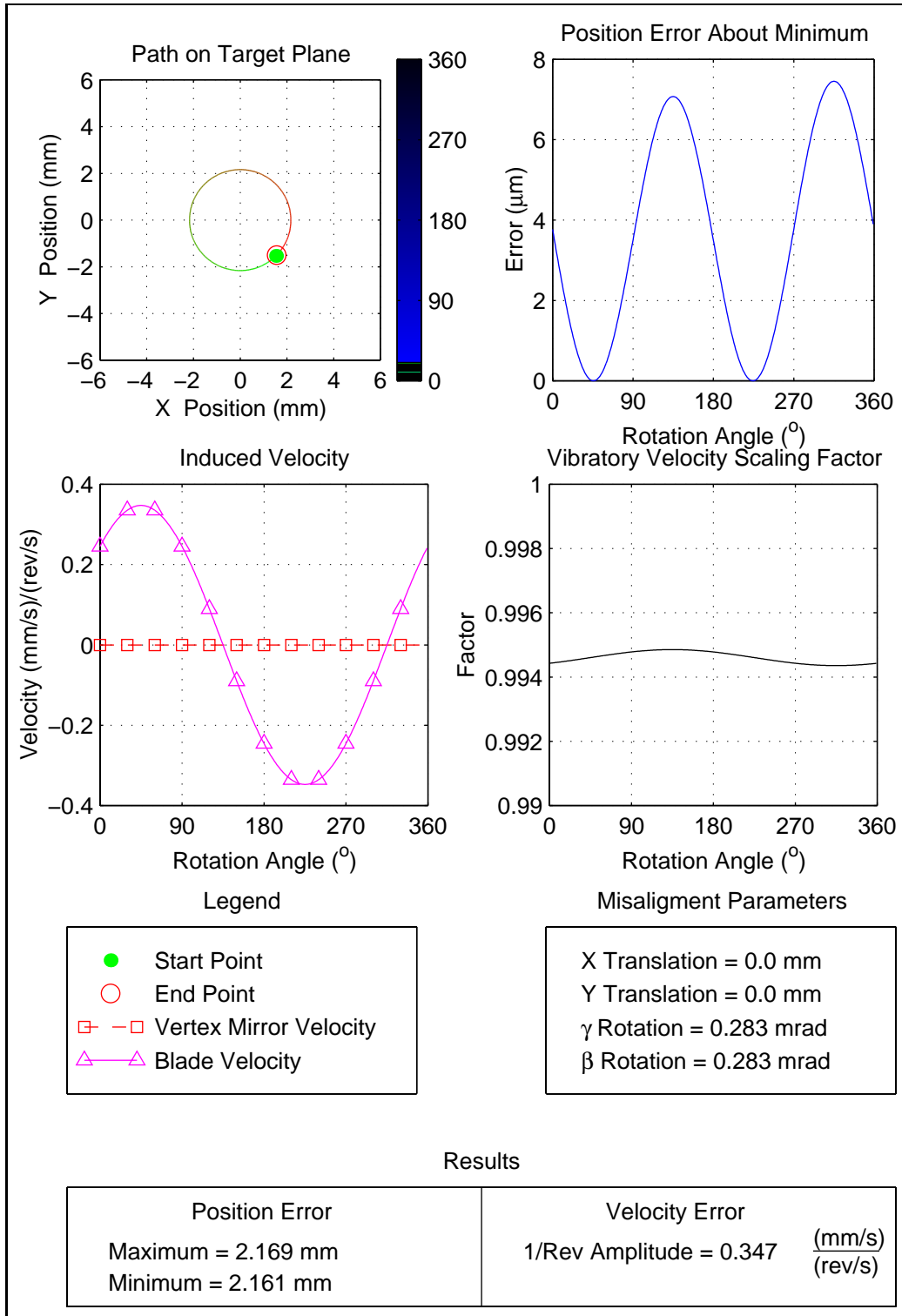


Figure 7.46: Rotational Misalignments, Directional Effects, $\gamma=0.283$ mrad, $\beta=0.283$ mrad

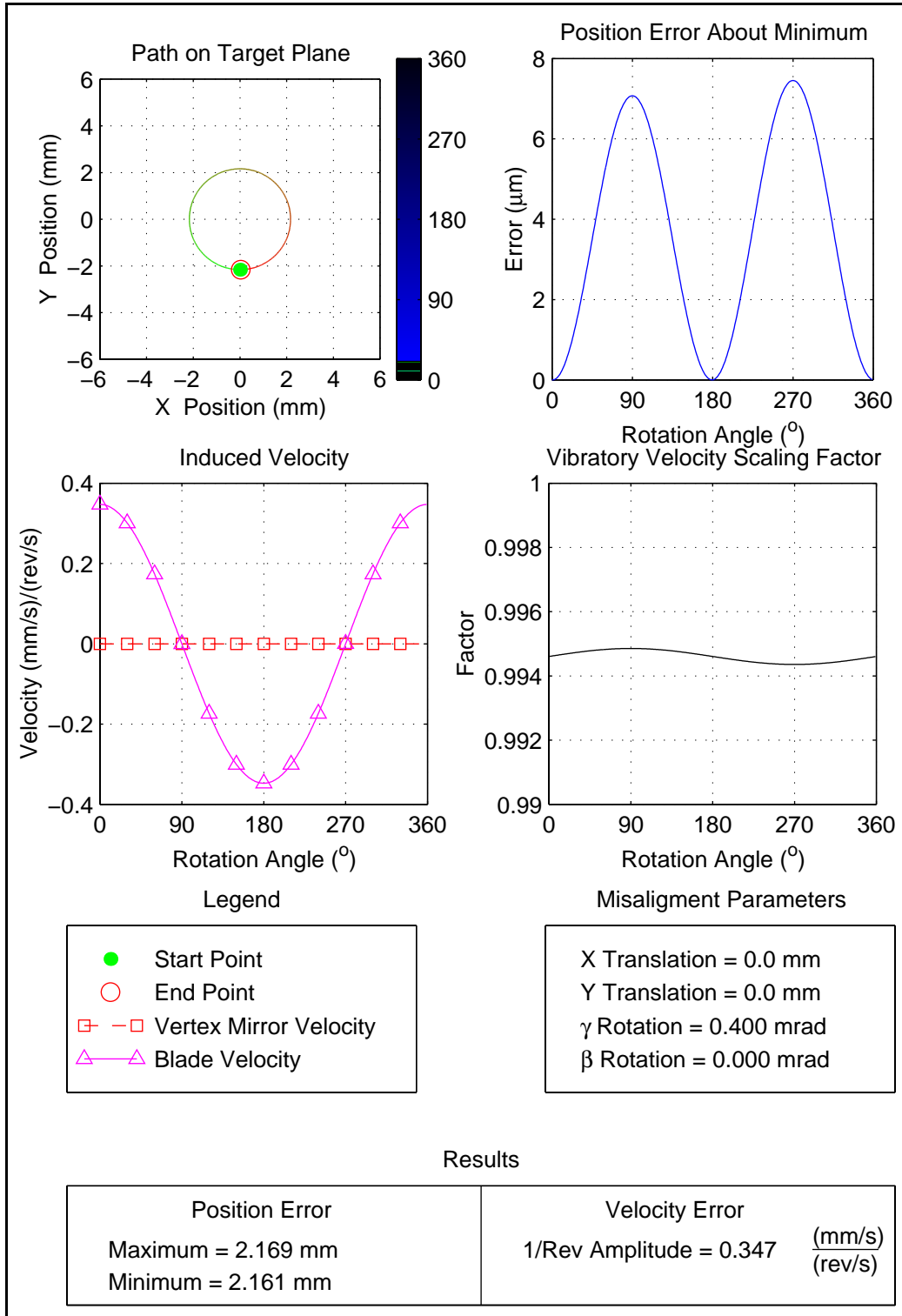


Figure 7.47: Rotational Misalignments, Directional Effects, $\gamma=0.4$ mrad, $\beta=0.0$ mrad

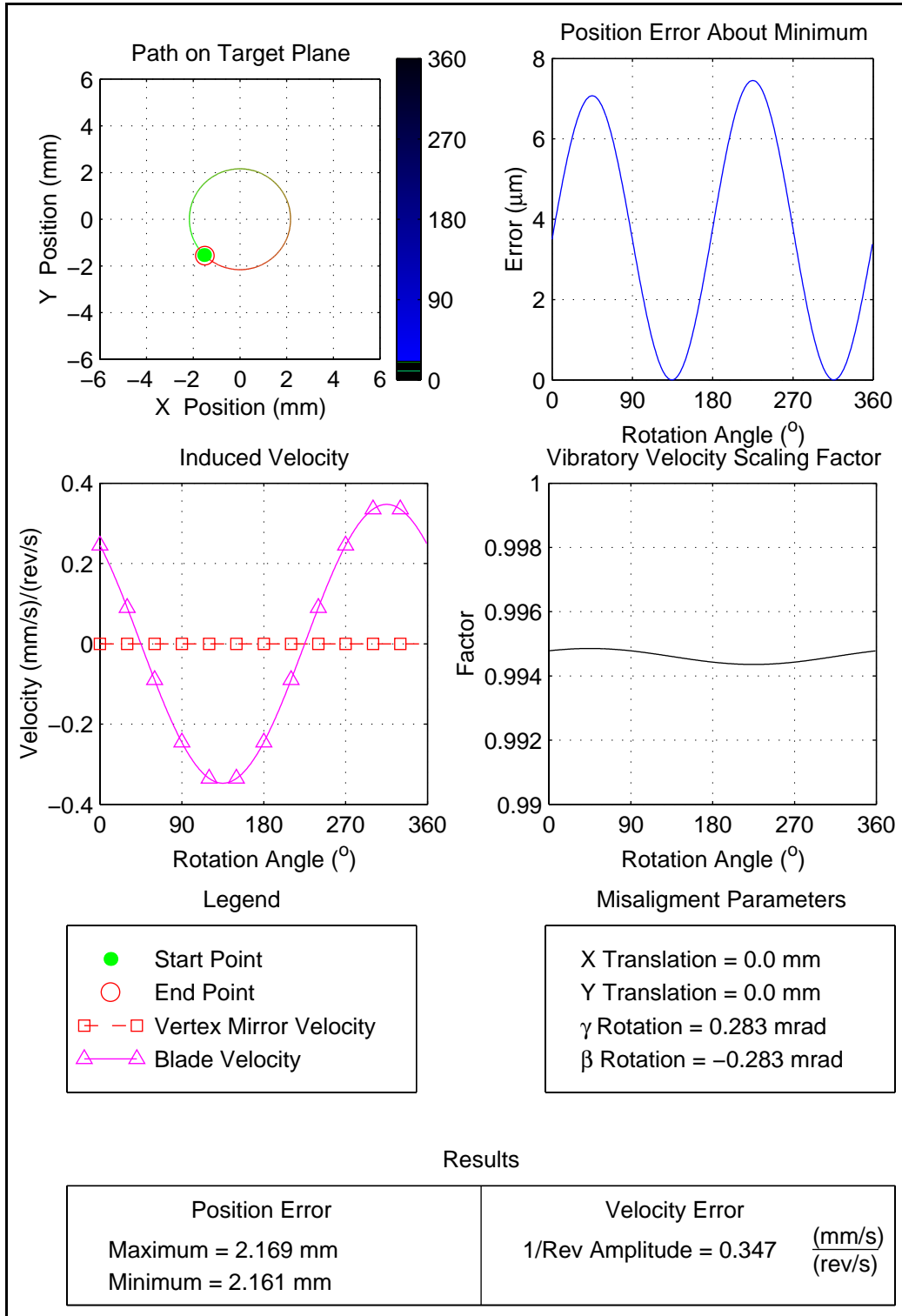


Figure 7.48: Rotational Misalignments, Directional Effects, $\gamma=0.283$ mrad, $\beta=-0.283$ mrad

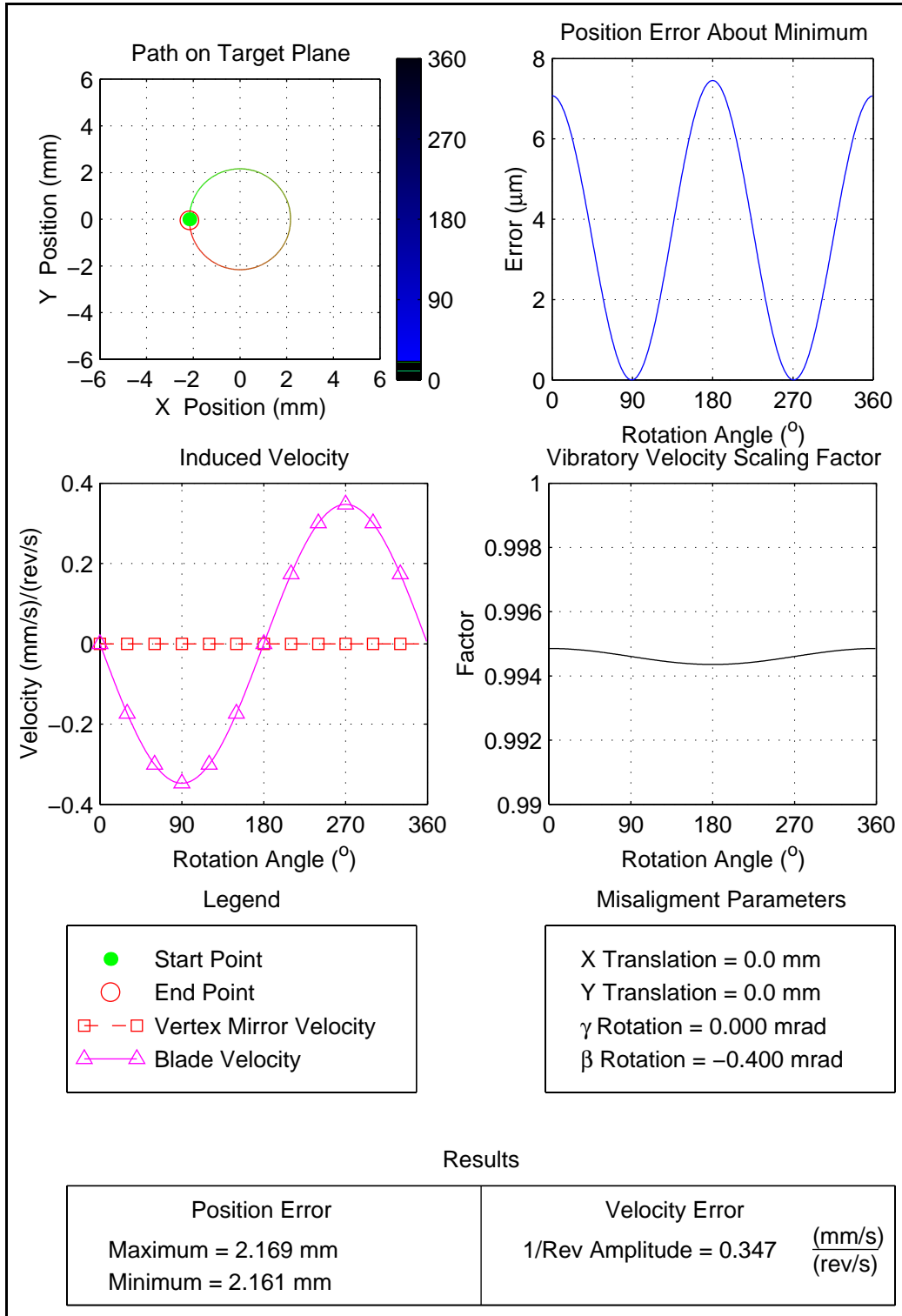


Figure 7.49: Rotational Misalignments, Directional Effects, $\gamma=0.0$ mrad, $\beta=-0.4$ mrad

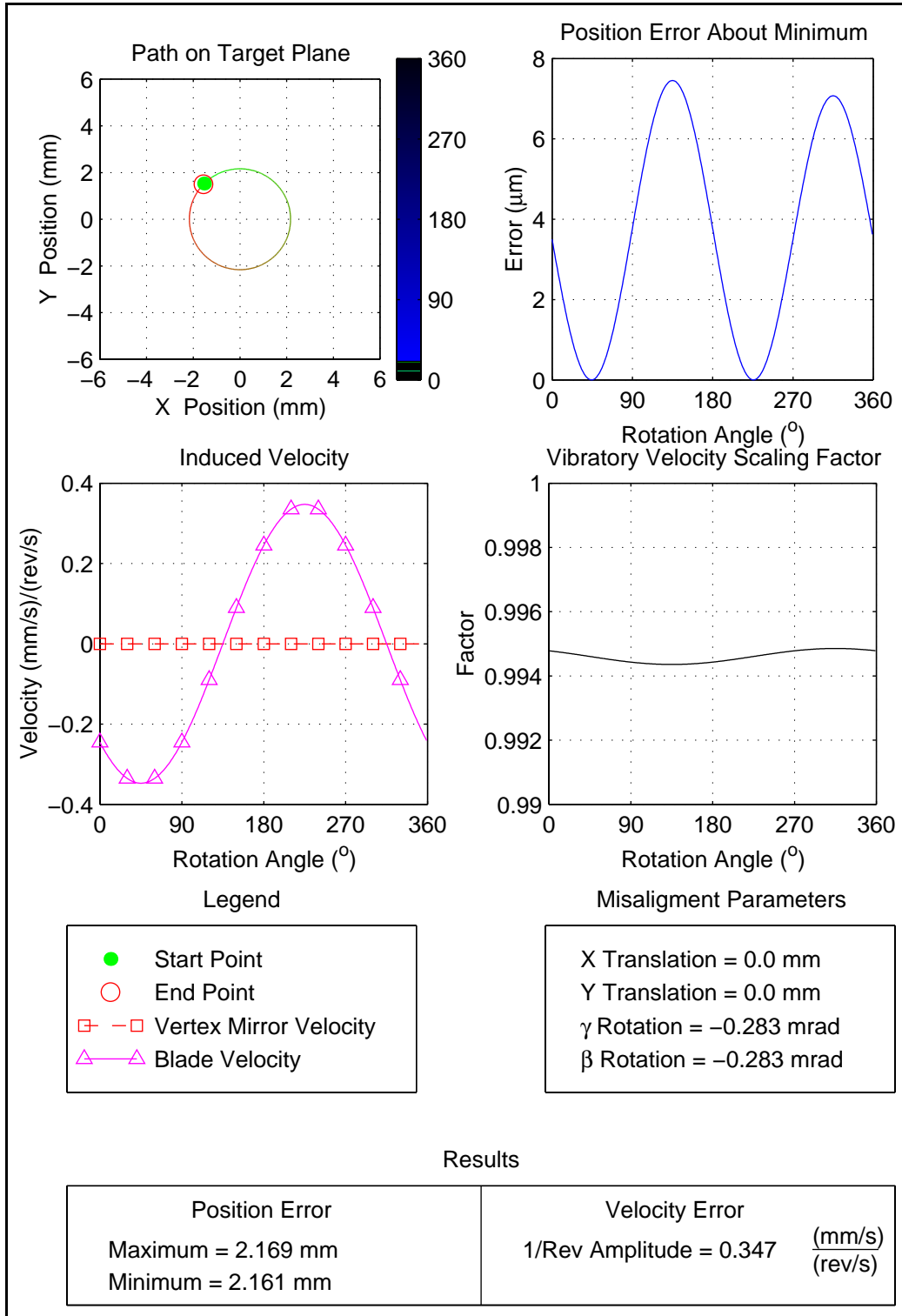


Figure 7.50: Rotational Misalignments, Directional Effects, $\gamma=-0.283$ mrad, $\beta=-0.283$ mrad

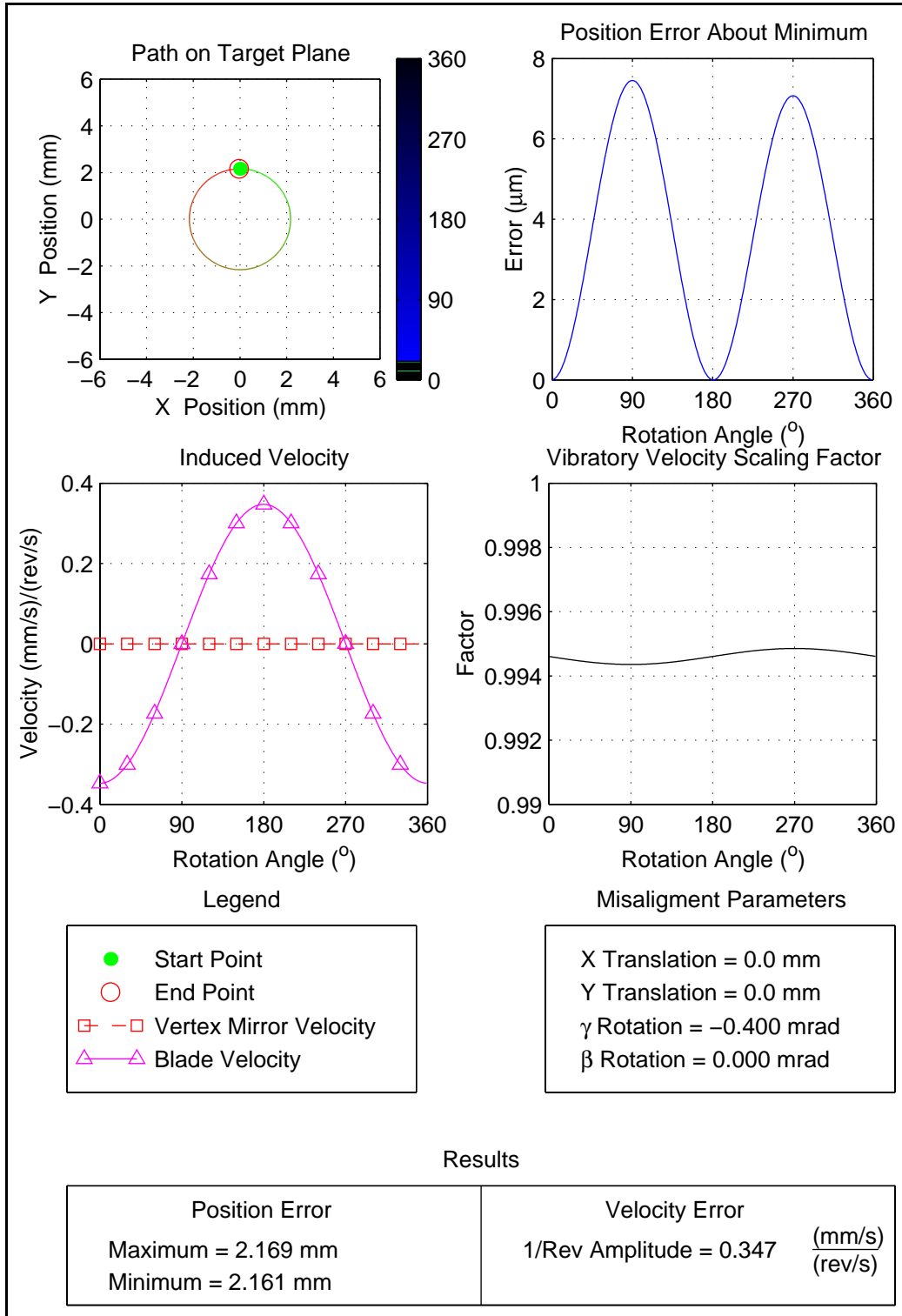


Figure 7.51: Rotational Misalignments, Directional Effects, $\gamma=-0.4$ mrad, $\beta=0.0$ mrad

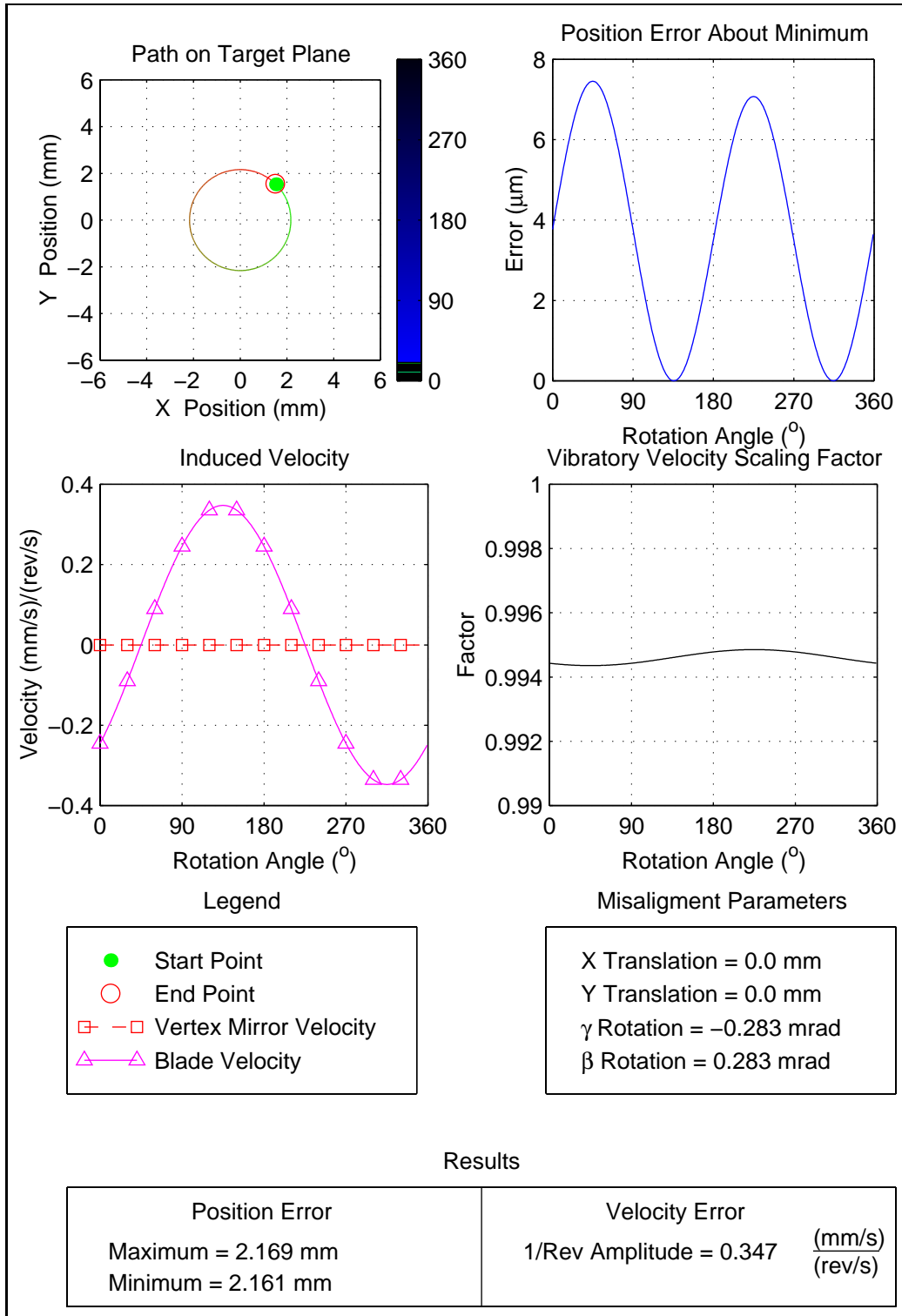


Figure 7.52: Rotational Misalignments, Directional Effects, $\gamma=-0.283$ mrad, $\beta=0.283$ mrad

Table 7.4: Rotational Misalignment Magnitude Effects

Case	Rotations		Position Errors		Velocity Errors	
	β (mrad)	γ (mrad)	Minimum (mm)	Variation (μm)	Induced (mm/s)/(rev/s)	Vibratory Scaling Factor
1	-1.0	0	5	7	0.868	0.994
2	-0.8	0	4	5	0.695	0.994
3	-0.6	0	3	4	0.521	0.994
4	-0.4	0	2	3	0.347	0.994
5	-0.2	0	1	1	0.174	0.994
6	0	0	0	0	0	0.994
7	0.2	0	1	1	0.174	0.994
8	0.4	0	2	3	0.347	0.994
9	0.6	0	0	0	0.521	0.994
10	0.8	0	1	1	0.695	0.994
11	1.0	0	2	3	0.868	0.994

7.4.2 Experimental Verification

To verify the effects of rotational misalignments, a series of experiments were performed. Varying levels of rotational misalignment were introduced into the test rig and the position and velocity errors measured.

The test rig's configuration allows for rotation about the y axis of the ideal alignment frame. The rotational misalignments are introduced through differential translation of the two linear slideways that support the rotating rig. To introduce rotations about the vertical line that passes through the vertex of the laser path, both the front and rear slideways must be adjusted. The amount of required translation needed to introduce rotation about this line was calculated based on the distance between the two slideways. Figure 7.53 shows the relationship between linear translation of each slideway and rotation angle of the structure.

Based on the dimensions of the system, to introduce a pure rotational misalignment about the line x-x the ratio of the translations of the rear and front slideways is 4.14. Since the

Table 7.5: Rotational Misalignment Directional Effects

Case	Rotations		Position Errors		Velocity Errors	
	β (mrad)	γ (mrad)	Minimum (mm)	Variation (μm)	Induced (mm/s)/(rev/s)	Vibratory Scaling Factor
1	0.4	0	5	7	0.347	0.994
2	0.283	0.283	4	5	0.347	0.994
3	0	0.4	3	4	0.347	0.994
4	-0.283	0.283	2	3	0.347	0.994
5	0	-0.4	1	1	0.347	0.994
6	-0.283	-0.283	0	0	0.347	0.994
7	-0.4	0	1	1	0.347	0.994
8	0.283	-0.283	2	3	0.347	0.994

micrometer stages are marked in 0.01mm increments, the required ratio was rounded to 4. While this introduces a small translation along with the desired rotation, the magnitude is small enough to be ignored. Table 7.4.2 summarizes the amount each slideway was translated and the corresponding rotation and translation of the test rig.

For each angular misalignment, the position and velocity errors were measured. The position errors were measured by rotating the blade by hand through a full revolution. The velocity errors were measured with the motor driving the blade at approximately 10 revolutions per second.

The measured velocity shows the expected behavior, with the measured velocity changing with varying levels of rotational misalignment. One interesting result is that the minimum velocity did not occur for the assumed zero rotational misalignment case as predicted by the simulations. Instead, as shown in Figure 7.58, the minimum velocity occurs at approximately 0.2 mrad of rotational misalignment.

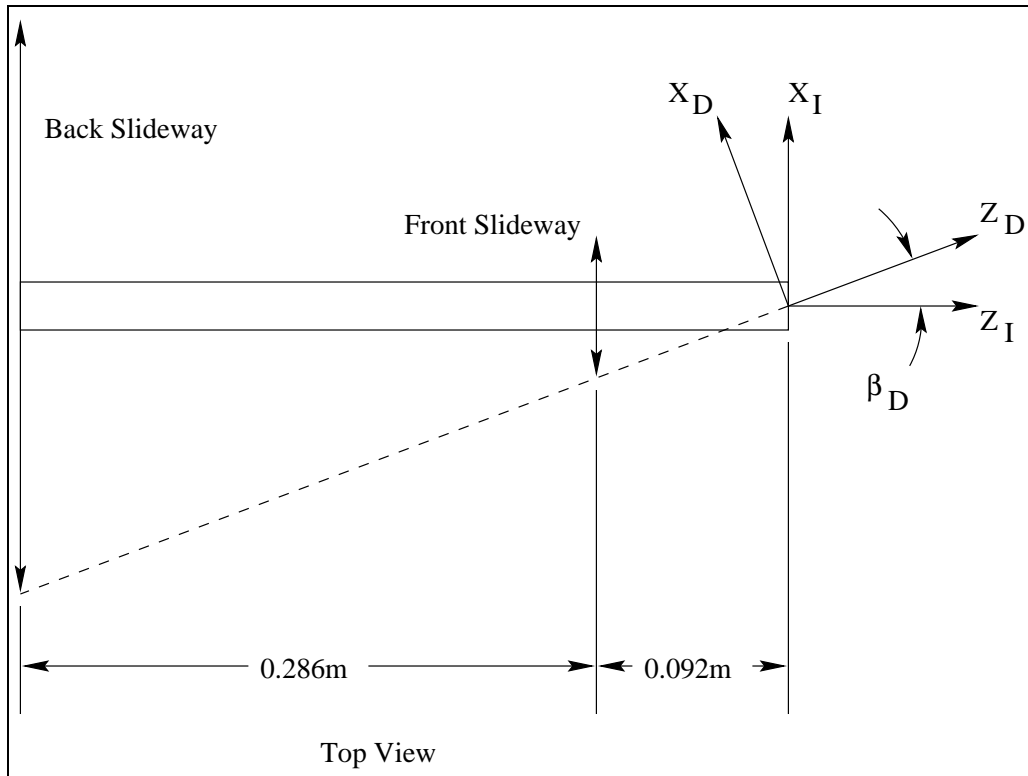


Figure 7.53: Rotational Misalignments

7.4.3 Analytical Verification of Rotational Misalignment Effects

There are two possible explanations for this discrepancy. First, it is possible that the assumed ideal alignment case had some residual rotational misalignment. Second, it is possible that this effect is caused by the speckle noise, similar to the effect seen for the translational misalignment case.

Closed Form Solution with Simplified Model

The simulations result show that rotational misalignments introduce both position and velocity errors. The amount of these errors can be approximated based on the simplified model of the self-tracker. Recall that in the simplified model of the ideal alignment case, the vertex

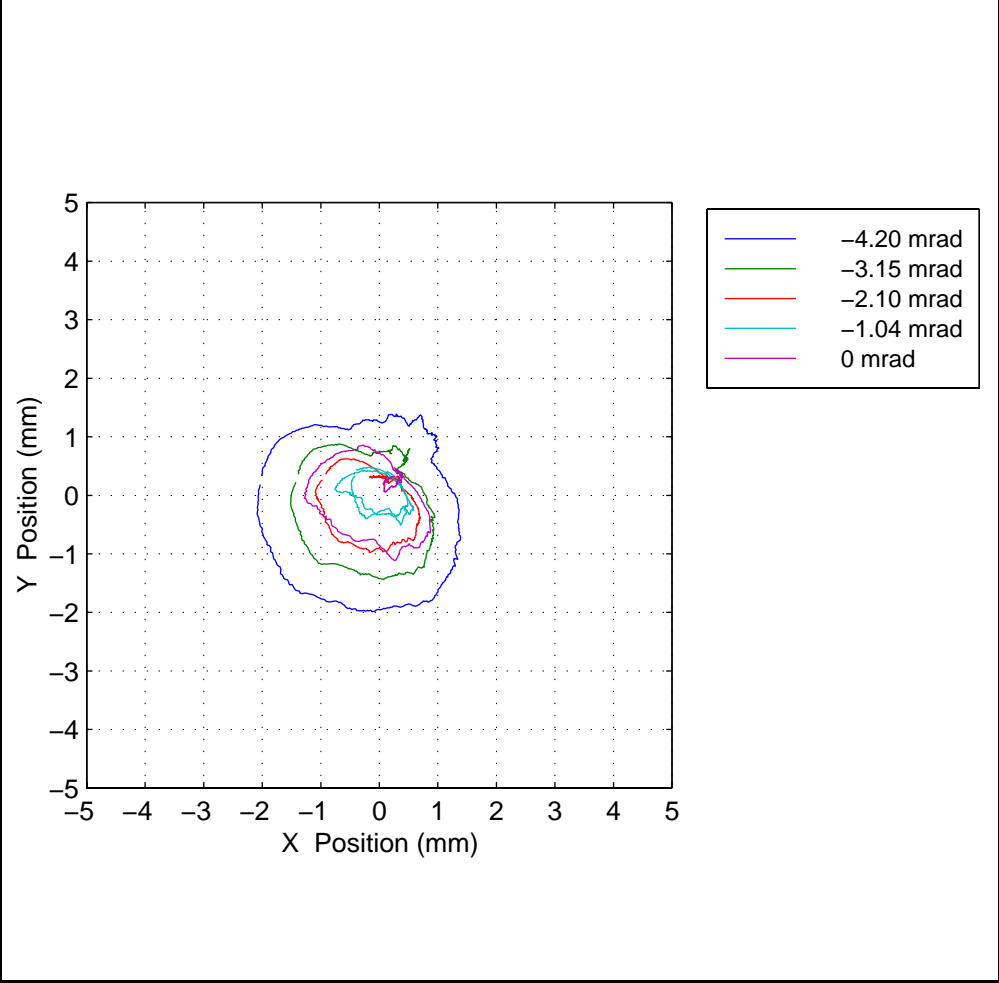


Figure 7.54: Measured Position Errors for Negative Rotational Misalignments

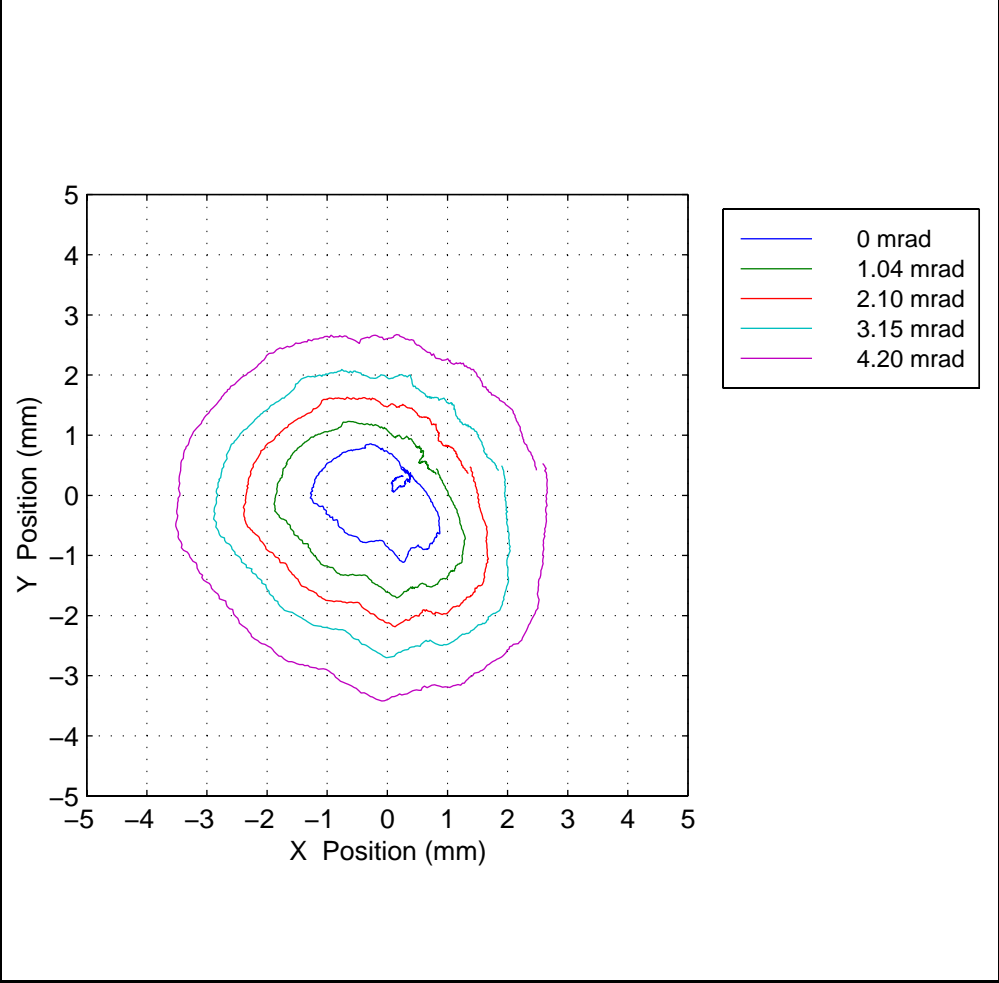


Figure 7.55: Measured Position Errors for Positive Rotational Misalignments

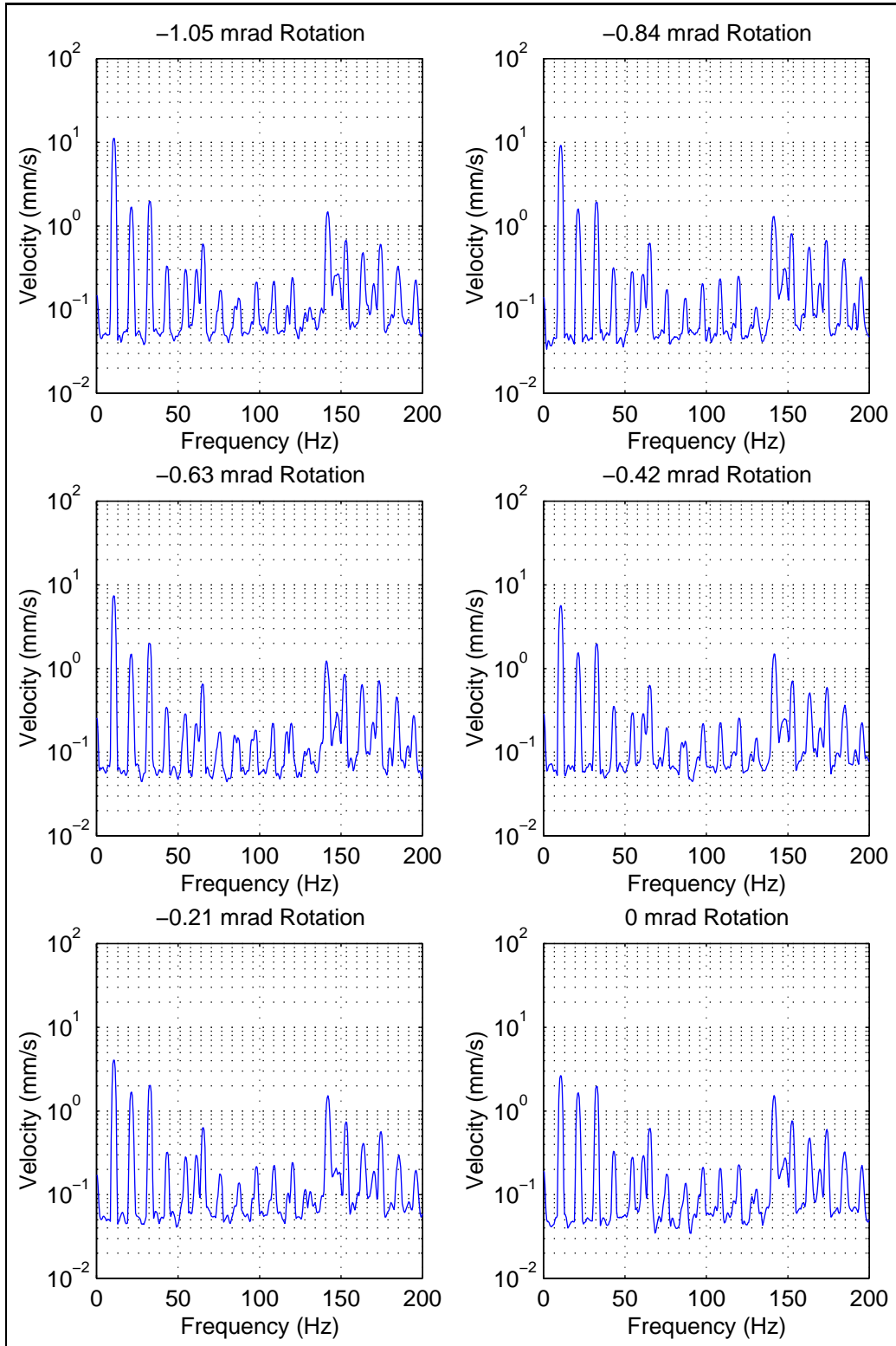


Figure 7.56: Measured Velocity Errors for Negative Rotational Misalignments

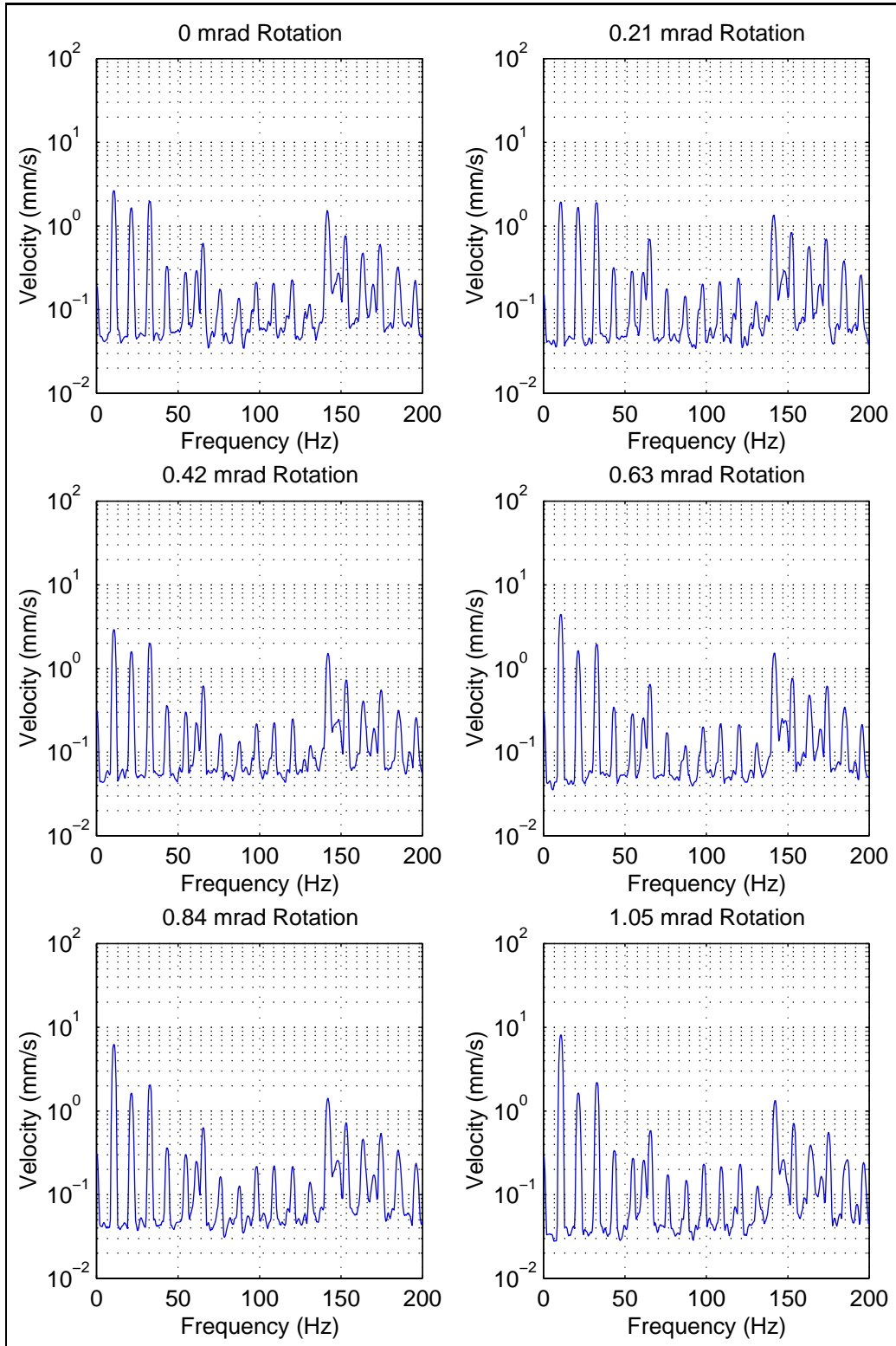


Figure 7.57: Measured Velocity Errors for Positive Rotational Misalignments

Table 7.6: Slideway Translations and Rotations

Case	Front (mm)	Rear (mm)	Rotation (mrad)	Translation (μm)
1	0.10	0.40	-1.05	3.39
2	0.08	0.32	-0.84	2.71
3	0.06	0.24	-0.63	2.04
4	0.04	0.16	-0.42	1.36
5	0.02	0.08	-0.21	0.68
6	0.00	0.00	0.00	0.00
7	-0.02	-0.08	0.21	-0.68
8	-0.04	-0.16	0.42	-1.36
9	-0.06	-0.24	0.63	-2.04
10	-0.08	-0.32	0.84	-2.71
11	-0.10	-0.40	1.05	-3.39

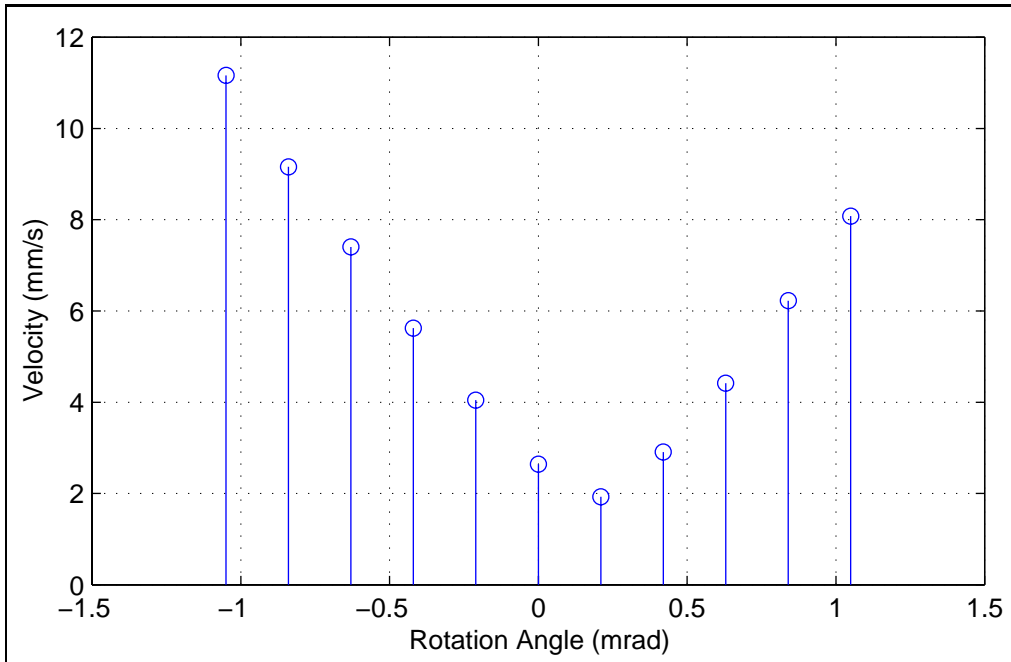


Figure 7.58: Once Per Rev Measured Velocity for Rotational Misalignments

of the laser cone remains fixed and the vertex angle is constant. For rotational misalignments the vertex location remains fixed but the vertex angle changes. A secondary effect is to introduce an additional tilt on the blade. However this effect can be neglected since it is small relative to the effect of the changing vertex angle. With this assumption, the position error can be estimated based on the simplified model shown in Figure 7.59.

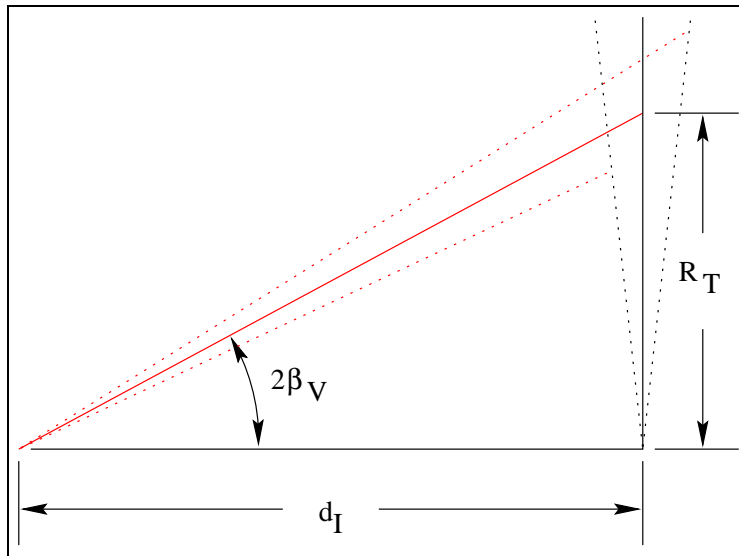


Figure 7.59: Simplified Model for Rotational Misalignments

This shows that the vertex angle, which for the ideal alignment case is constant with a value of $2\beta_V$, will take on values of $2\beta_V \pm 2\phi$. The location of the measurement point will be

$$R_M = d_I \cdot \tan(2\beta_V \pm 2\phi) \quad (7.15)$$

Applying the trigonometric identity for the tangent of the sum and differences of angles

$$\tan(\alpha \pm \beta) = \frac{\tan(\alpha) \pm \tan(\beta)}{1 \mp \tan(\alpha)\tan(\beta)} \quad (7.16)$$

Table 7.7: Rotational Misalignment Position Errors

Case	Rotations β (mrad)	Position Errors	
		Simulation (mm)	Simplified Model (mm)
1	-1.0	5	5.4
2	-0.8	4	4.3
3	-0.6	3	3.2
4	-0.4	2	2.1
5	-0.2	1	1.1
6	0	0	0
7	0.2	1	1.1
8	0.4	2	2.1
9	0.6	3	3.2
10	0.8	4	4.3
11	1.0	5	5.4

and noting that the term

$$\tan(\alpha)\tan(\beta) \ll 1 \tag{7.17}$$

the position error can be approximated as

$$\epsilon = d_I \cdot \tan(2\phi) \tag{7.18}$$

where 2ϕ is the additional angular rotation due to the angular misalignment.

Applying this result to the simulation cases, where $d_I = 2.687m$, the position errors due to the rotational misalignments are calculated and compared to the simulation results, with the results summarized in Table 7.4.3.

These results show that the simplified model provides a conservative estimate of the position error without the added complexity of the simulation.

The simplified model can also be used to approximate the velocity error for rotational misalignments. As shown in Figure 7.60, a rotational misalignment will cause a component of

the blade's rigid body motion to be projected onto the laser beam plane defined as

$$V'_B = r \cdot \omega \cdot \sin(\beta_D) \tag{7.19}$$

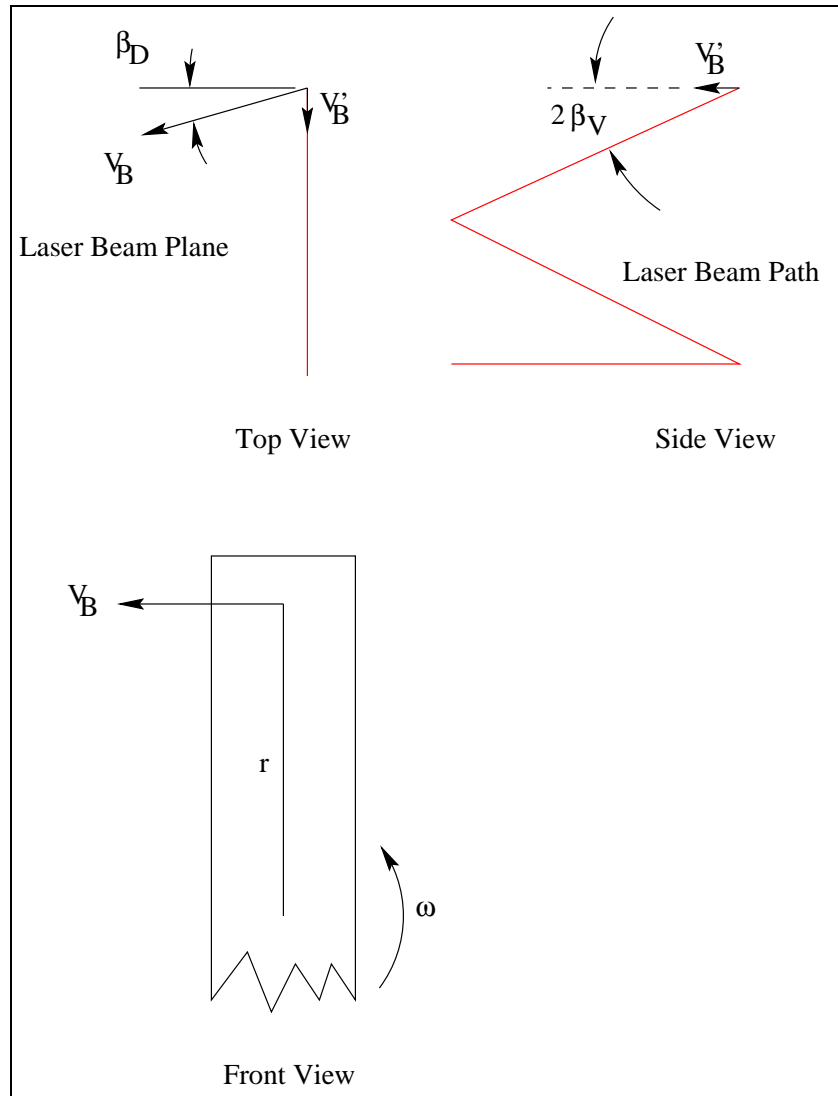


Figure 7.60: Velocity Error for Rotational Misalignments

The projection of this component along the laser beam path results in

Table 7.8: Rotational Misalignment Velocity Errors

Case	Rotations β (mrad)	Velocity Errors	
		Simulation (mm/s)/(rev/s)	Simplified Model (mm/s)/(rev/s)
1	-1.0	0.868	0.878
2	-0.8	0.695	0.708
3	-0.6	0.521	0.527
4	-0.4	0.347	0.351
5	-0.2	0.174	0.176
6	0	0	0
7	0.2	0.174	0.176
8	0.4	0.347	0.351
9	0.6	0.521	0.527
10	0.8	0.695	0.708
11	1.0	0.868	0.878

$$V_B'' = r \cdot \omega \cdot \sin(\beta_D) \cdot \cos(2\beta_V) \quad (7.20)$$

and expression which can be used to approximate the velocity error due to rotational misalignments. Applying this expression to the simulation cases, the velocity errors are calculated and compared to the simulation results and summarized in Table 7.4.3

These results confirm that the simplified model provides a conservative estimate of the velocity errors resulting from rotational misalignments.

7.5 Combined Static Displacement and Rotation

The previous sections illustrated the individual effects of translational and rotational misalignments. These results were based on the occurrence of one of the misalignments. In

general, both of these types of misalignments may be present and the combined effects must be characterized. Since translational and rotational misalignments introduce position and velocity errors through different mechanisms, it is expected that the concept of superposition can be applied to predict the effects of combinations of these misalignments. Thus the goal of this section is to verify that the concept of superposition can be applied.

Unlike the previous cases, the effects of combined misalignments are studied based on the simulation only. This is done for two reasons. First, experimental results can only be obtained for a few specific combinations due to limitations in the test rig. Additionally, since the model has been shown to accurately predict the effects of misalignments, it is more efficient to use the simulations. Secondly, whereas the simulation results for the individual misalignments were verified with simple analytical models, the complexity of combined misalignments makes this approach much more difficult. Therefore, the combined effects of translational and rotational misalignments will be studied using the simulation.

7.5.1 Simulation Results

Since there are a multitude of combinations of translational and rotational misalignments that can be considered, a method must be developed to select a small set of combinations that illustrate the combined effects. The misalignment conditions selected for simulation were selected to illustrate two concepts; first, that the concept of superposition can be applied to finding the effects of combined misalignments, and secondly, that combinations of misalignments can mask the effects of individual misalignments.

One set of simulation was designed to illustrate the concept of superposition, consisted of combinations of the previous translational and rotational misalignments. A single rotational misalignment was introduced along with different translational misalignments.

The results of these simulations are shown in Figures 7.61 through 7.68 with the results

summarized in Table 7.5.1

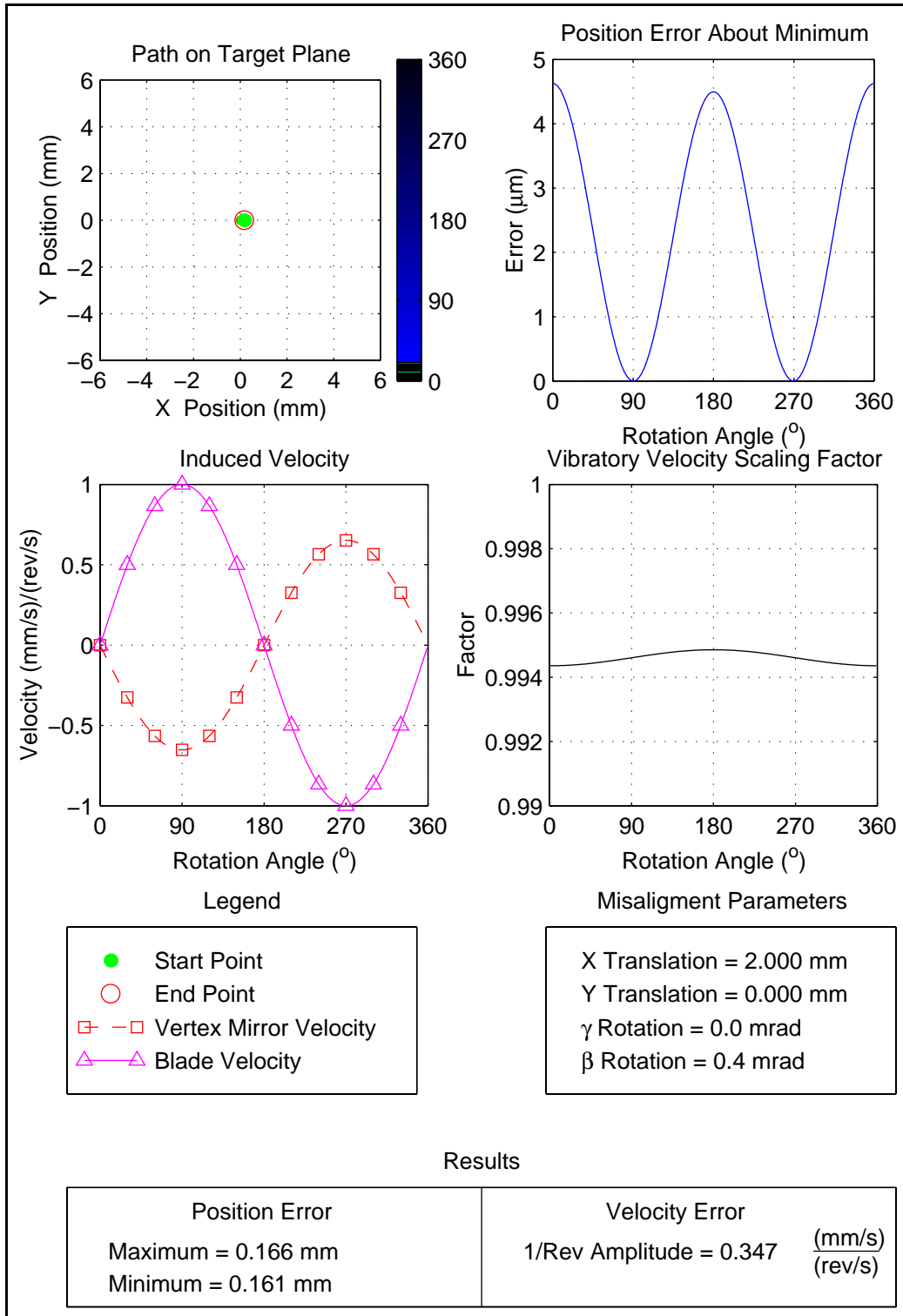


Figure 7.61: Combined Misalignments, $\beta=0.4$ mrad, $d_X=2$ mm, $d_Y=0$ mm

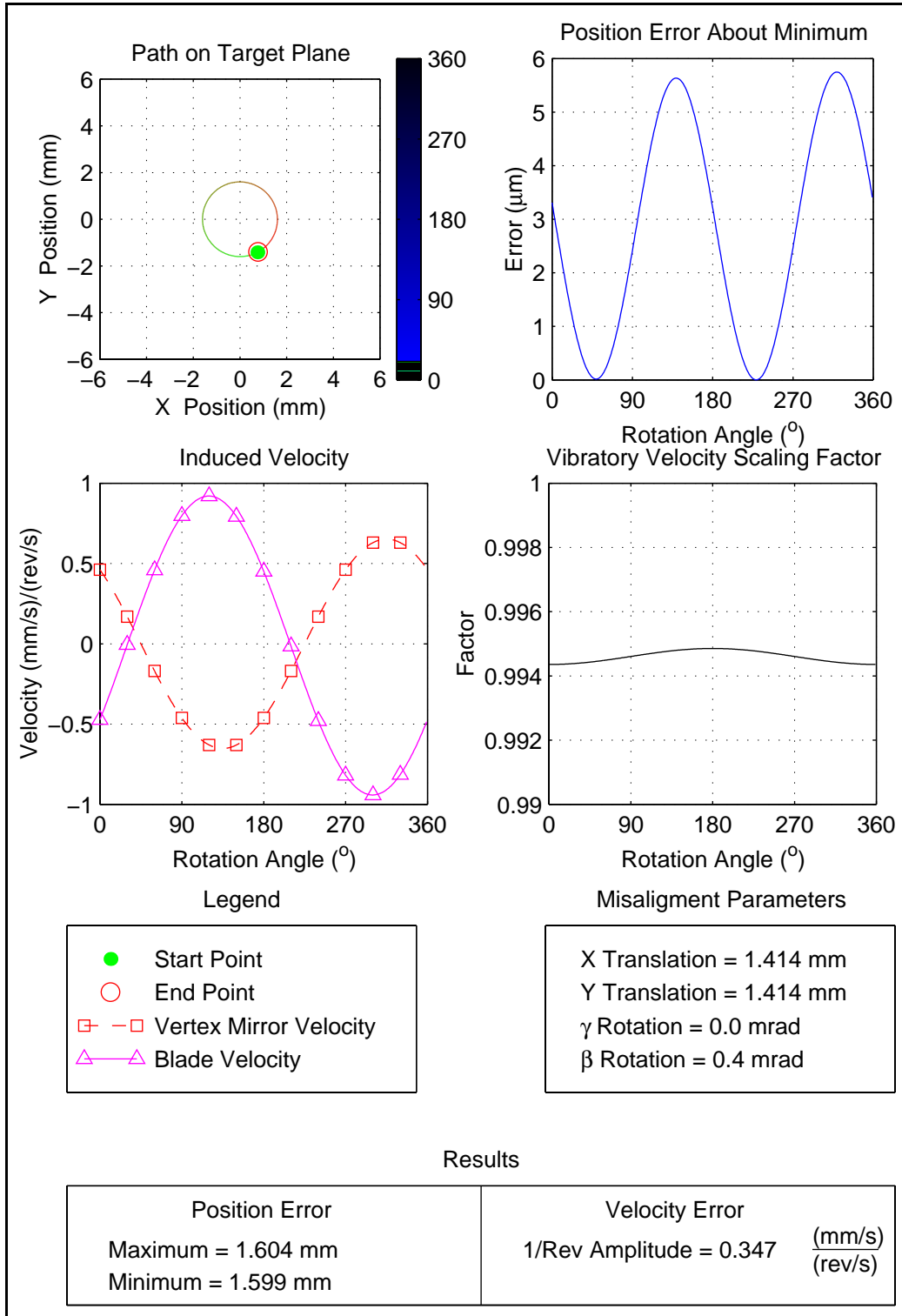


Figure 7.62: Combined Misalignments, $\beta=0.4$ mrad, $d_x=1.414$ mm, $d_y=1.414$ mm

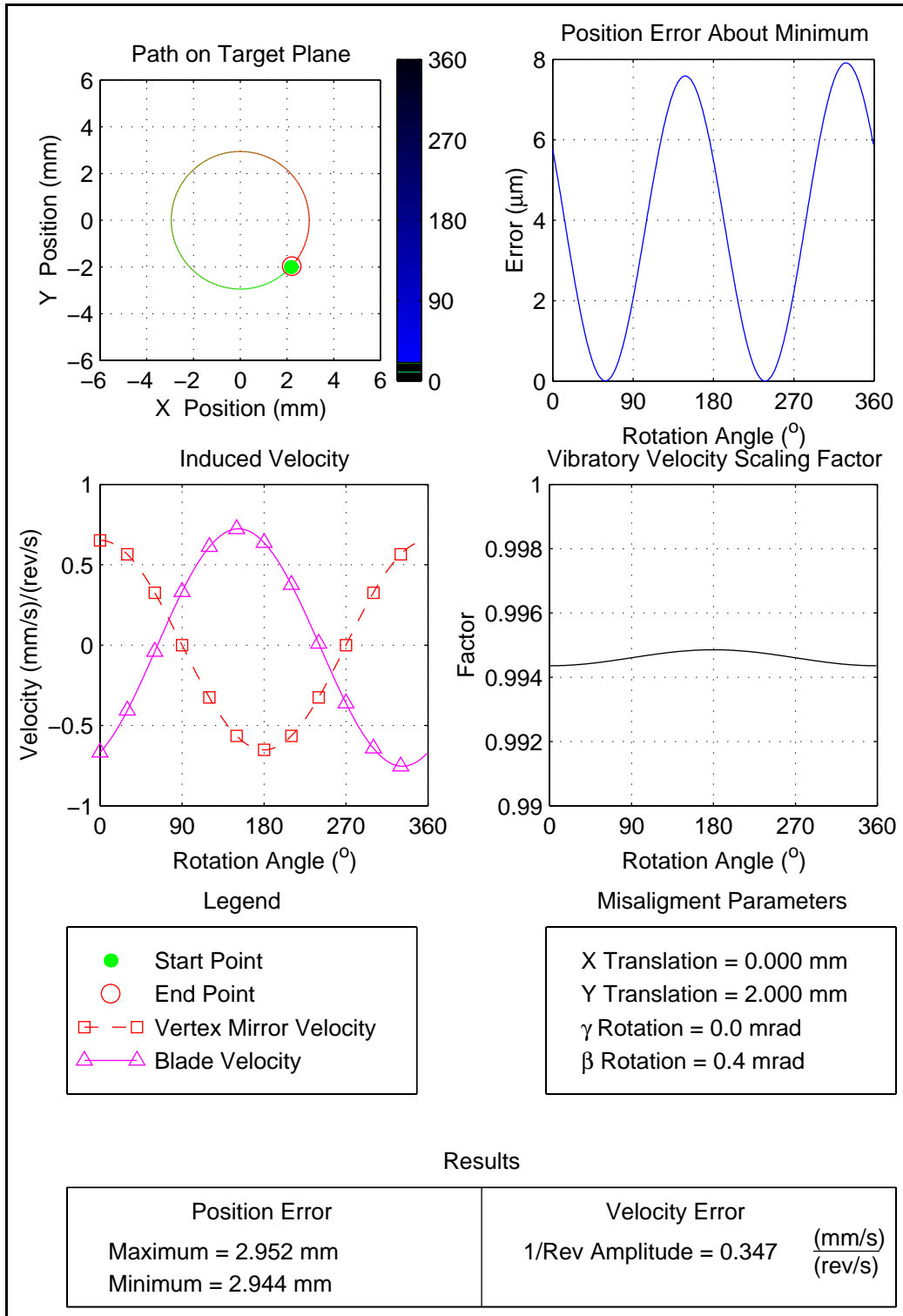


Figure 7.63: Combined Misalignments, $\beta=0.4$ mrad, $d_X=0$ mm, $d_Y=2$ mm

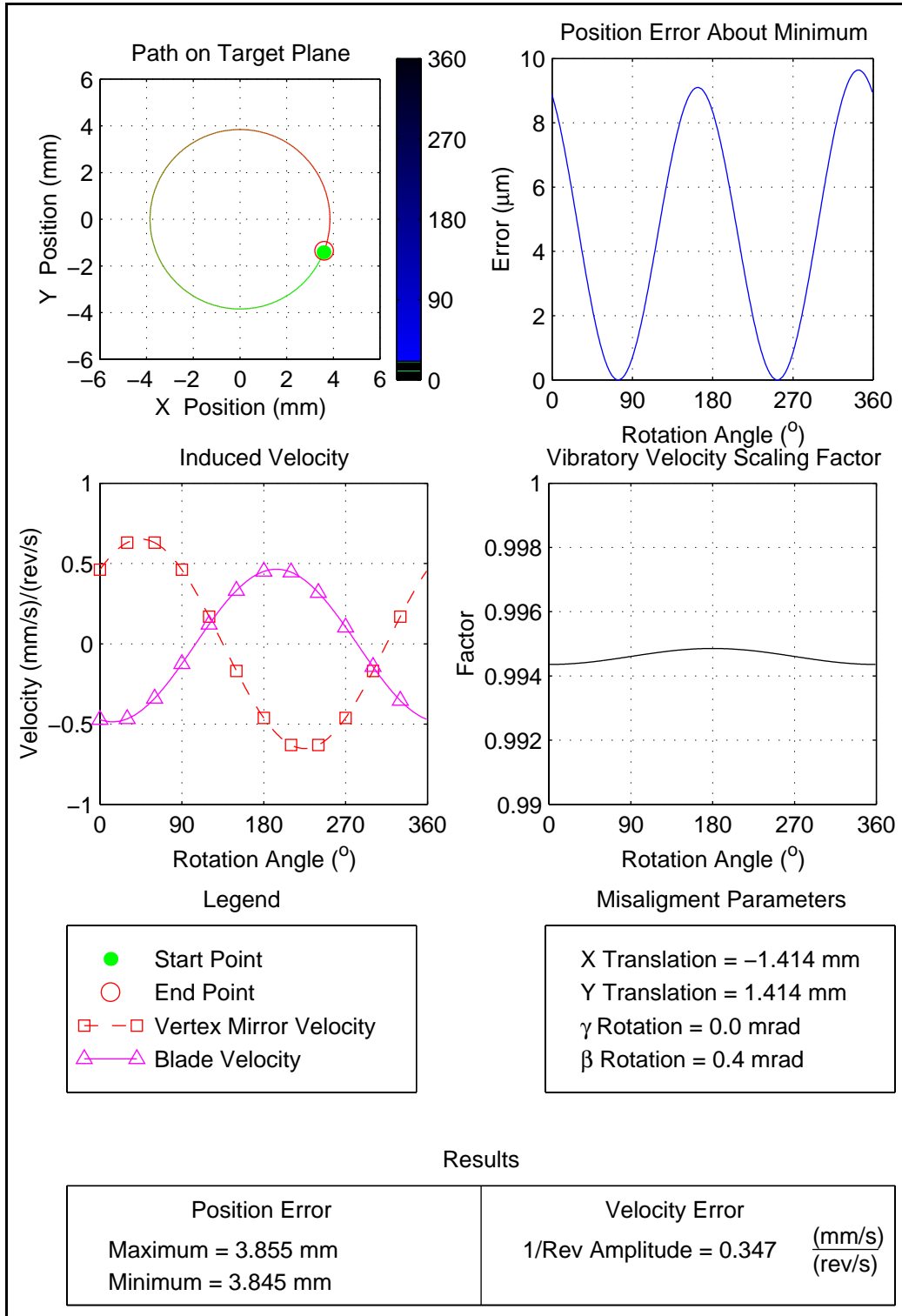


Figure 7.64: Combined Misalignments, $\beta=0.4$ mrad, $d_X=-1.414$ mm, $d_Y=1.414$ mm

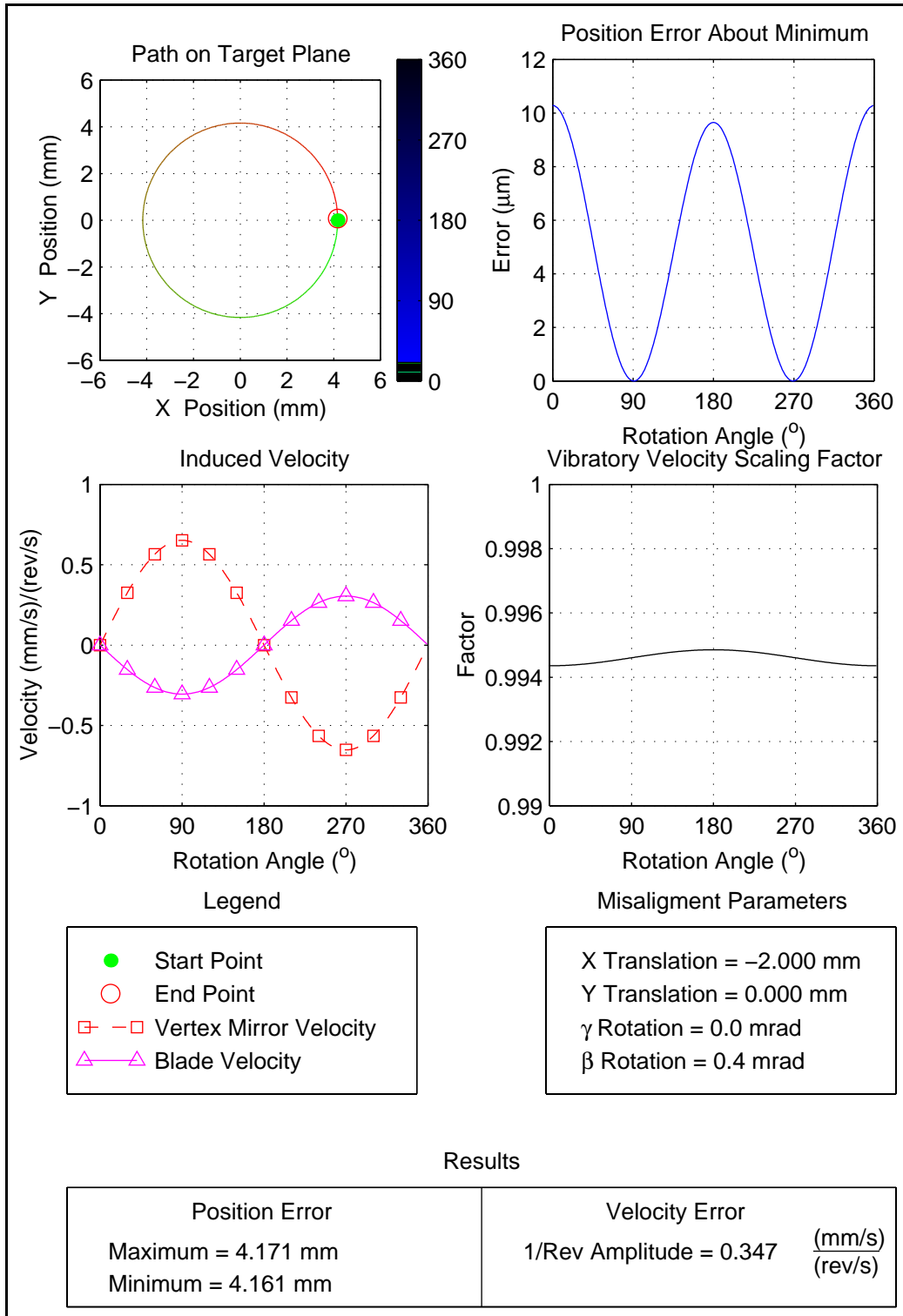


Figure 7.65: Combined Misalignments, $\beta=0.4$ mrad, $d_X=-2$ mm, $d_Y=0$ mm

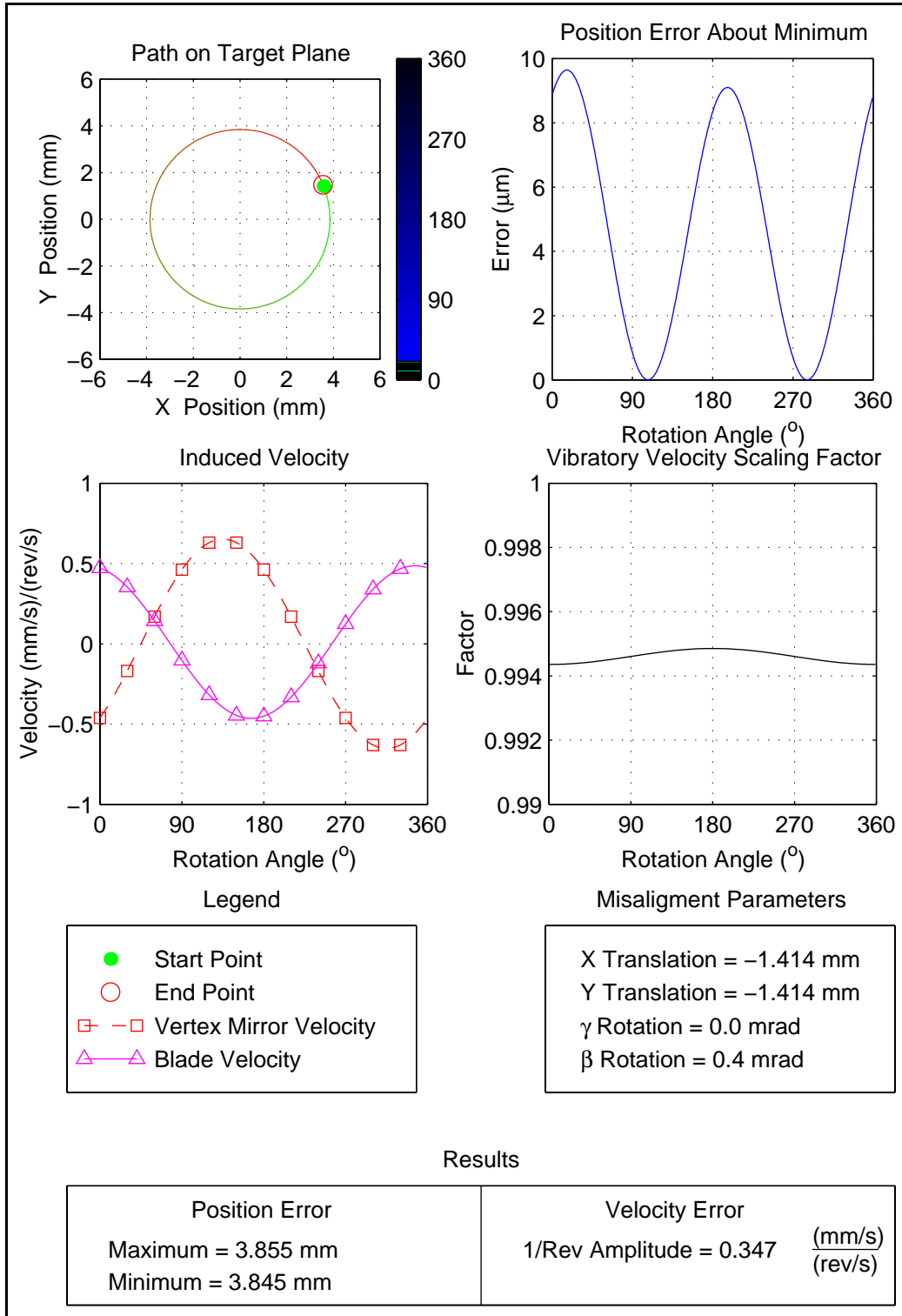


Figure 7.66: Combined Misalignments, $\beta=0.4$ mrad, $d_X=-1.414$ mm, $d_Y=-1.414$ mm

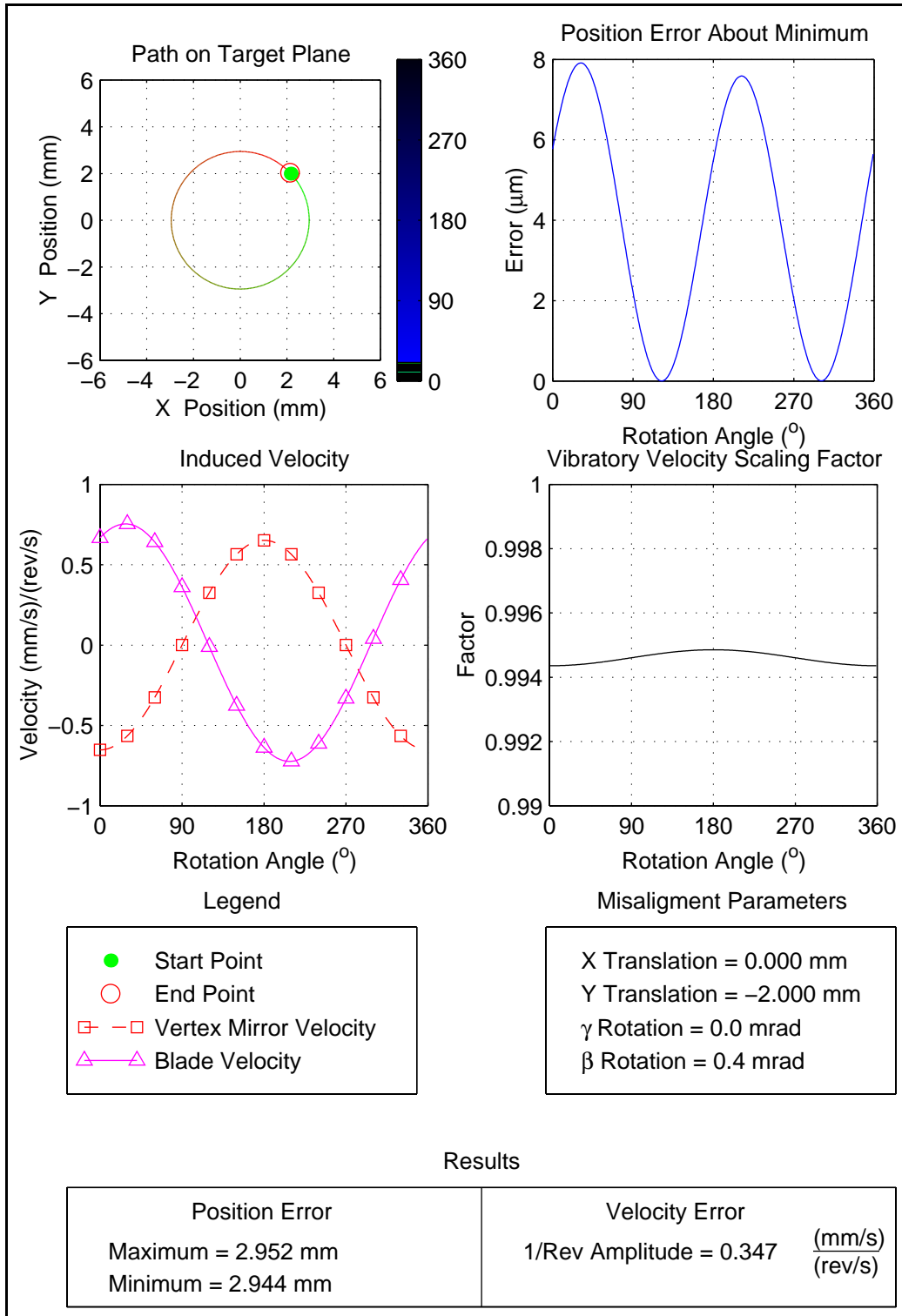


Figure 7.67: Combined Misalignments, $\beta=0.4$ mrad, $d_X=0$ mm, $d_Y=-2$ mm

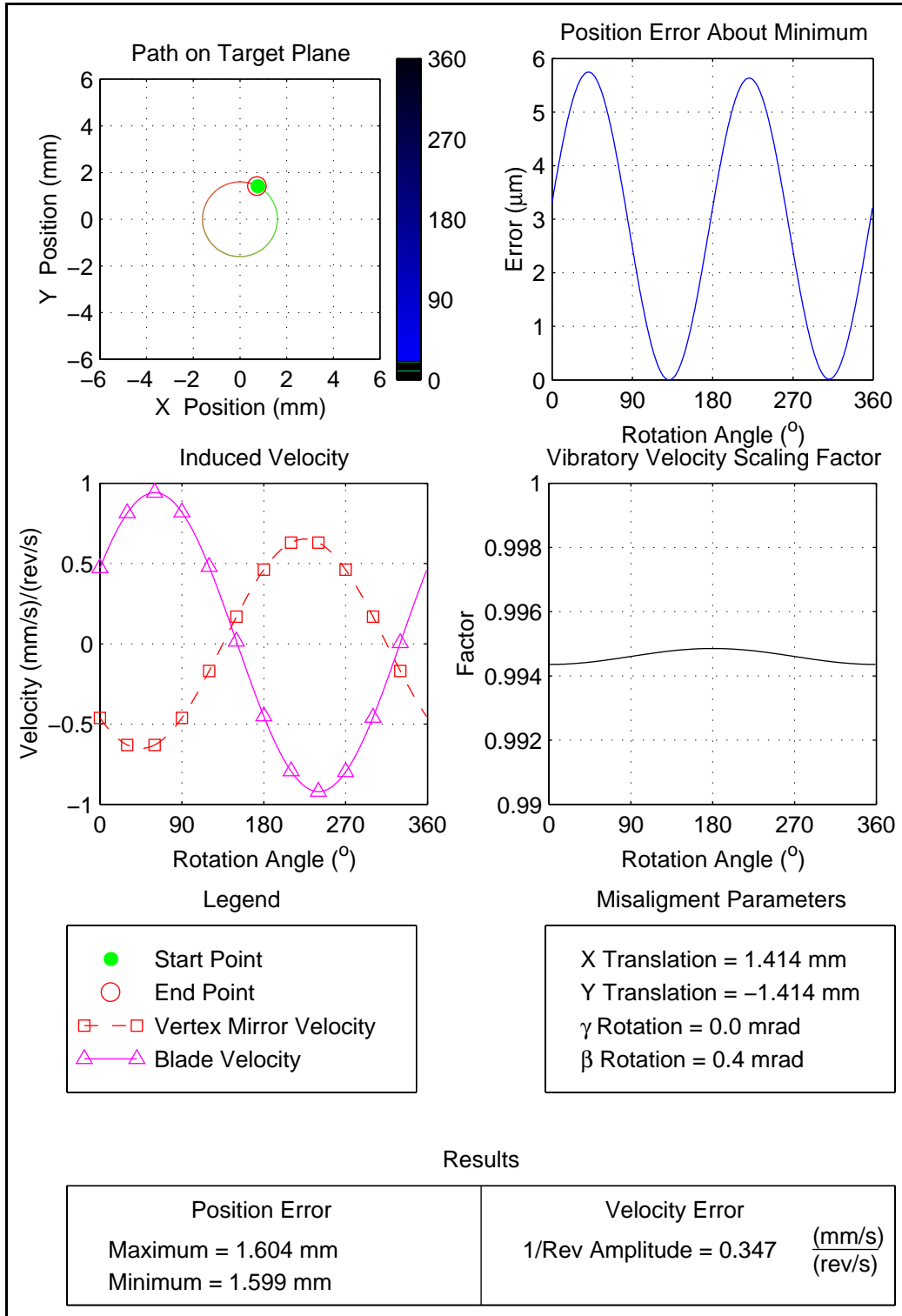


Figure 7.68: Combined Misalignments, $\beta=0.4$ mrad, $d_X=1.414$ mm, $d_Y=-1.414$ mm

Table 7.9: Combined Translational and Rotational Misalignment Effects

Case	Rotations		Translations		Position Errors		Velocity Errors	
	β (mrad)	γ (mrad)	d_x (mm)	d_y (mm)	Minimum (mm)	Variation (μm)	Induced $\frac{\text{mm/s}}{\text{rev/s}}$	Scaling Factor
1	0.4	0	2	0	0.161	4.5	0.347	0.994
2	0.4	0	1.414	1.414	1.599	5.5	0.347	0.994
3	0.4	0	0	2	2.944	8	0.347	0.994
4	0.4	0	-1.414	1.414	3.845	10	0.347	0.994
5	0.4	0	-2	0	4.161	10.5	0.347	0.994
6	0.4	0	-1.414	-1.414	3.845	10	0.347	0.994
7	0.4	0	0	-2	2.944	8	0.347	0.994
8	0.4	0	1.414	-1.414	1.599	5.5	0.347	0.994

These results show that combinations of translational and rotational misalignments can be predicted through the principle of superposition. In each case, the position error is equal to the vector sum of the individual position errors. Similarly, the velocity errors consists solely of the contribution from the rotational misalignment since the translational misalignments introduce no velocity error. A second result of these findings is that it is possible to counteract the effects of one type of misalignment with another type and reduce the position error to near zero. However, this technique can not be used to reduce the velocity errors resulting from rotational misalignments.

7.6 Summary

The effects of static misalignments of the self-tracker on tracking and velocity error have been studied. Simulation results, experimental data, and simplified models produced the following results. First, for the configurations studied, it was shown that translational misalignments introduce position errors, but no net velocity error. The position errors are approximately equal to the amount of translational misalignment. Secondly, rotational misalignments in-

roduce both position and velocity errors. Each of these can be approximated based on simplified models of the self tracker system. Last, the effects of combinations of translational and rotational misalignments can be approximated through superposition of the effects of the individual translational and rotational misalignment. Application of the principle of superposition showed that certain combinations of translational and rotational misalignments can reduce the position errors to undetectable levels. However, no combination of translational and rotational misalignments can reduce the velocity error to undetectable levels. Thus, the self-tracker is susceptible to both types of misalignments, yet only rotational misalignments hamper the use of the laser vibrometer.

Chapter 8

Conclusions

A self-tracking laser vibrometry system has been developed, modeled and characterized. The model predicts the position and velocity errors arising from static misalignments. These predictions are verified by experimental measurements and simplified models of the self-tracker.

8.1 Self-Tracker Capabilities

The results show that the self-tracker is capable of tracking a single point with no position or velocity errors under the ideal alignment conditions. Translational misalignments introduce position and velocity errors that can be predicted using a simplified system model. Similarly, rotational misalignments also introduce position and velocity errors that can be predicted with the simplified models. Combinations of translational and rotational misalignments can be predicted using the concept of superposition. It is also shown that the position error can be reduced to near undetectable levels for combinations of translational and rotational misalignments. However there is no combination of translational and rotational misalignments

that reduce the velocity errors to undetectable levels.

8.2 Recommendations for Future Work

This work has presented a novel approach for laser vibrometry on rotating structures and described the effects of static misalignment on position and velocity errors. Several areas still need to be addressed.

The system presented here is limited to radial scanning. The next step is to develop a method for easily implementing circumferential scanning. Another area for investigation is the development of signal processing techniques for handling the case where the structure is obscured along part of its path.

While this work only addressed specific cases of static misalignment, there are a number of other misalignment cases that can be studied. These include dynamic misalignments and misalignments of each component of the self-tracker. Additionally, a robust procedure for aligning the system components needs to be developed.

Bibliography

Anton, H., 1987, *Elementary Linear Algebra*, John Wiley & Sons.

Beeck, M. A., 1988, "Pulsed Holographic Vibration Analysis on High-Speed Rotating Objects: Fringe Formation, Recording Techniques, and Practical Applications," *Holographic Techniques and Applications*, Vol. 1026, pp. 186–195.

Bucher, I., Schmiechen, P., Robb, D. A., and Ewins, D. J., 1994, "A Laser-Based Measurement System for Measuring the Vibration on Rotating Discs," *Vibration Measurements*, Vol. 2358, pp. 398–408.

Castellini, P. and Santolini, C., 1996, "Vibration Measurements on Blades of Naval Propeller Rotating in Water," *SPIE*, Vol. 2868, pp. 186–194.

Craig, J. J., 1989, *Introduction to Robotics Mechanics and Controls*, Addison-Wesley.

Dainty, J. C., ed., 1984, *Laser Speckle and Related Phenomena*, Springer-Verlag.

Denman, M., Halliwell, N. A., and Rothberg, S. J., 1995, "Laser Vibrometry: The Effect of Speckle Size on Doppler Signal Phase and Amplitude Modulation," *Design Engineering Technical Conferences*, Vol. 3, pp. 1387–1397.

Denman, M., Halliwell, N. A., and Rothberg, S. J., 1996, "Speckle Noise Reduction in Laser Vibrometry: Experimental and Numerical Optimisation," *SPIE*, Vol. 2868, pp. 12–21.

Drain, L. E., 1980, *The Laser Doppler Technique*, John Wiley & Sons.

Drain, L. E., Speake, J. H., and Moss, B. C., 1977, "Displacement and Vibration Measurement by Laser Interferometry," *First European Conference on Optics Applied to Metrology*, Vol. 136, pp. 52–57.

Drouin, B., 1996, "Holographic Vibratory Analysis of Steam Turbine Blades," *SPIE*, Vol. 2868, pp. 400–411.

Fowles, G., 1987, *Introduction to Modern Optics*, John Wiley & Sons.

Gasvik, K., 1968, *Optical Metrology*, Holt, Rinehart, and Winston, Inc.

Halliwell, N. A., 1996, "The Laser Torsional Vibrometer: A Step Forward in Roating Machinery Diagnostics," *Journal of Sound and Vibration*, Vol. 190, No. 3, pp. 399–418.

Kadambi, J. R., Quinn, R. D., and Adams, M. L., 1989, "Turbomachinery Blade Vibration and Dynamic Stress Measurements Utilizing Nonintrusive Techniques," *Transactions of the ASME*, Vol. 111, pp. 468–474.

Kulczyk, W. K. and Davis, Q. V., 1973a, "Laser Doppler Instrument for Measurement of Vibration of Moving Turbine Blades," *Proceedings of IEEE*, Vol. 120, No. 9, pp. 1017–1023.

Kulczyk, W. K. and Davis, Q. V., 1973b, "Signal-to-Noise Ratio in Laser Doppler Systems," *Proceedings of IEEE*, Vol. 120, No. 9, pp. 1024–1029.

Lesne, J.-L., Fervier, T., Triquigneaux, P., and Floc'h, C. L., 1985, "Vibratory Analysis of a Rotating Bladed Disk Using Holographic Interferometry and Laser Vibrometry," *SPIE-Optics in Engineering Measurement*, Vol. 599, pp. 74–79.

Lopez-Dominguez, J. C., 1994, "Reconstruction of 3-D Structural Dynamic Response Fields: An Experimental Laser-Based Approach with Statistical Emphasis," Ph.D. Thesis, Virginia Polytechnic Institute and State University.

- Maddux, G. E., 1997, "Work Plan for High Cycle Fatigue Instrumentation Subtask," WPAFB Document-Personal Correspondence with Dr. Andy Barker.
- Meirovitch, L., 1967, *Analytical Methods in Vibrations*, MacMillan.
- Reinhardt, A. K., Kadambi, J. R., and Quinn, R. D., 1994, "Laser Vibrometry Measurements of Rotating Blade Vibrations," *Transactions of the ASME-ITGI*, Vol. 9, pp. 453–461.
- Rothberg, S. J., Baker, J. R., and Halliwell, N. A., 1989, "Laser Vibrometry: Pseudo-Vibrations," *Journal of Sound and Vibration*, Vol. 135, No. 3, pp. 516–522.
- Rothberg, S. J. and Halliwell, N. A., 1994, "Vibration Measurements on Rotating Machinery Using Laser Doppler Velocimetry," *Transactions of the ASME*, Vol. 116, pp. 326–331.
- Rothberg, S. J. and Halliwell, N. A., 1995, "Application of Laser Vibrometry to Vibration Measurements on Rotating Components," *Design Engineering Technical Conferences*, Vol. 3, pp. 1425–1434.
- Rothberg, S. J. and Halliwell, N. A., 1996, "Optics Measures Vibration in Rotating Machines," *Noise and Vibration Worldwide*, Vol. 27, No. 7, pp. 7–9.
- Standbridge, A. B. and Ewins, D. J., 1994, "Measurement of Translational and Angular Vibration Using a Scanning Laser Doppler Vibrometer," *SPIE*, Vol. 2358, pp. 37–46.
- Stetson, K. A., 1978, "The Use of an Image Derotator in Hologram Interferometry and Speckle Photography of Rotating Objects," *Experimental Mechanics*, Vol. 18, pp. 67–73.
- Strean, R. F., Mitchell, L. D., and Barker, A. J., 1996, "Global Noise Characteristics of a Laser Doppler Vibrometer, Part I: Theory," *SPIE*, Vol. 2868, pp. 2–11.
- Takai, N., Iwai, T., and Asakura, T., 1983, "Correlation Distance of Dynamic Speckles," *Applied Optics*, Vol. 22, No. 1, pp. 170–177.
- Tsuruta, T. and Itoh, Y., 1970, "Holographic Interferometry for Rotating Subject," *Applied Physics Letters*, Vol. 7, No. 2, pp. 85–87.

Wlezien, R. W., Miu, D. K., and Kibens, V., 1984, "Characterization of Rotating Flexible Disks Using a Laser Doppler Vibrometer," *Optical Engineering*, Vol. 23, No. 4, pp. 436–442.

Young, M., 1986, *Optics and Lasers*, Springer-Verlag.

Vita

Richard A. Lomenzo, Jr. was born on May 10, 1969 in New Orleans, Louisiana. After graduating from Clover Hill High School in Midlothian, Virginia, he studied Aerospace Engineering at Virginia Tech and graduated with a Bachelor of Science Degree in 1991. He continued his education at Virginia Tech in the Mechanical Engineering Department and received his Master of Science in 1994. Following completion of his Master's Degree, he began work on his Doctor of Philosophy, also in Virginia Tech's Mechanical Engineering Department. Throughout his graduate studies, he served as a Graduate Teaching Assistant for the Mechanical Engineering Department's undergraduate laboratory course, earning the admiration of innumerable students. Upon completion of his Doctorate, he plans to work at Pratt & Whitney's Large Military Engines Division in West Palm Beach, Florida.

Permanent Address: 4500 Tall Hickory Drive
Midlothian VA 23113

This dissertation was typeset with $\text{\LaTeX} 2_{\epsilon}$ ¹ by the author.

¹ $\text{\LaTeX} 2_{\epsilon}$ is an extension of \LaTeX . \LaTeX is a collection of macros for \TeX . \TeX is a trademark of the American Mathematical Society. The macros used in formatting this dissertation were written by Dinesh Das, Department of Computer Sciences, The University of Texas at Austin.